

## ABSTRACT

Title of Document: PERFORMANCE ASSESSMENT OF MEMS  
GYROSCOPE AND SHOCK DURABILITY  
EVALUATION OF SAC305-X SOLDERS FOR  
HIGH TEMPERATURE APPLICATIONS

Chandradip Pravinbhai Patel,  
Doctor of Philosophy, 2014

Directed By: Associate Professor F. Patrick McCluskey,  
Department of Mechanical Engineering

Recent advances in MEMS technology have resulted in relatively low cost MEMS gyroscopes. Their unique features compared to macro-scale devices, such as lighter weight, smaller size, and lower power consumption, have made them popular in many applications with environmental conditions ranging from mild to harsh. This dissertation aims to address a gap in the literature on MEMS gyroscopes by investigating the effects of elevated temperatures on the performance of MEMS gyroscopes.

MEMS gyroscopes are characterized at room and elevated temperatures for both stationary and rotary conditions. During the test, MEMS gyroscopes are subjected to five thermal cycles at each of four temperature ranges (viz. 25°C to 85°C, 25°C to 125°C, 25°C to 150°C and 25°C to 175°C). A model is developed in MATLAB Simulink to simulate the temperature effect on the MEMS gyroscope.

Simulation results show good agreement with experimental results and confirm that Young's modulus and damping coefficient are the dominant factors responsible for temperature-dependent bias at elevated temperatures.

Solder interconnects are one of the weakest elements in MEMS devices. Thus, the reliability of solder interconnects is separately studied in this dissertation. Though SAC305 (96.5%Sn3.0%Ag0.5%Cu) is the industry preferred solder in combined thermal cycling and shock/drop environments, it exhibits better thermal cycling reliability than drop/shock reliability. One of the ways to improve the drop/shock reliability of SnAgCu solders is by microalloy addition of various dopants such as Mn, Ce, Ti, Y, Ge, Bi, Zn, In, Ni, Co etc. Thus, the second part of this dissertation aims to evaluate the shock durability of SAC305 and SAC305-X (where X refers to two different concentrations of Mn and Ce dopants).

High temperature isothermal aging tests are conducted on selected solders using QFN44, QFN32 and R2512 package types at 185°C and 200°C up to 1000 hours. Isothermal aging test results showed that interfacial IMC growth reduction can be achieved by microalloy addition of selected dopants in SAC305 on both copper and nickel leaded package types. Shock durability of selected solders is examined on as-reflowed and thermally aged test boards. Mechanical shock is performed using a custom shock machine that utilizes a shock pulse of 500G with 1.3 millisecond duration. The shock test results showed that the mechanical shock reliability of SAC305 was significantly improved for both as-reflowed and thermally aged test boards by microalloy addition of one of the selected dopants in SAC305.

PERFORMANCE ASSESSMENT OF MEMS GYROSCOPE AND SHOCK  
DURABILITY EVALUATION OF SAC305-X SOLDERS FOR HIGH  
TEMPERATURE APPLICATIONS

By

Chandradip Pravinbhai Patel

Dissertation submitted to the Faculty of the Graduate School of the  
University of Maryland, College Park, in partial fulfillment  
of the requirements for the degree of  
Doctor for Philosophy  
2014

Advisory Committee:  
Associate Professor Patrick McCluskey, Chair  
Professor Abhijit Dasgupta  
Associate Professor Miao Yu  
Senior Research Scientist Dr. Michael Osterman  
Professor Neil Goldsman

© Copyright by  
Chandradip Pravinbhai Patel  
2014



## **Dedication**

To my grandfather Mr. Ratanshibhai Patel, father Mr. Pravinbhai Patel, mother Mrs. Devikaben Patel, and brother Mr. Ananddeep Patel for their unconditional love, constant support and encouragement throughout my life.

## **Acknowledgements**

First and foremost, I would like to thank my PhD advisor Prof. Patrick McCluskey for giving me the opportunity to do this research. I am indebted to his guidance, encouragement and support throughout my PhD study. I would also like to thank Prof. Abhijit Dasgupta, Dr. Michael Osterman, Prof. Miao Yu and Prof. Neil Goldsman for serving in my dissertation committee and also proving insightful discussions, valuable guidance and feedback for my research.

I would like to thank all current and former members of Prof. McCluskey's research group for proving friendly, motivating and enjoyable work environment. Thanks to Hannes Greve, Ali Moeini, Sumeer Khanna, David Squille, Subramani Manoharan, Jennifa Li, Robert Boettcher, Michael Crandall, Kyle Smith, Nicholas Jankowski, Lauren Boteler and Douglas DeVoto. Special thanks go to Hannes Greve for helping me with the board design and to Ahmed Idris and Tommy Ji for helping me with cross-sectioning work.

I would also like to thank all current and former students (too many to name), faculty and staff at CALCE for proving advise, support and good memories. Thanks Carlos Morillo for helping with nano-indentation measurement. Thanks to Subhasis Mukherjee and Ranjith Kumar for their help and suggestions.

Special thanks go to CPE/PWA team at Schlumberger especially Francis Dupouy, Mark Kostinovsky and Glen Schilling for providing technical inputs for the experiment and help me to realize the practical aspect of my research work. I also need to thank CALCE and Schlumberger for the use of test equipment and facilities to successfully complete this research. In addition, I am also grateful to the Maryland

Industrial Partnership Program, TRX Systems, CALCE and Schlumberger for providing financial support for this research. My heartiest thank to all the member of the Mechanical Engineering department and the University of Maryland for creating wonderful environment that helped me to grow personally and professionally.

Lastly, I would like to thank my parents, brother and grandfather for their love, encouragement and continuous support towards my endeavors.

# Table of Contents

|  |     |
|--|-----|
| Dedication .....   | ii  |
| Acknowledgements .....   | iii |
| Table of Contents .....  | v   |
| List of Tables .....   | ix  |
| List of Figures .....  | xi  |
| 1. Introduction.....   | 1   |
| 1.1. Advantages and Applications of MEMS Vibratory Gyroscope .....   | 1   |
| 1.2. Research Motivation .....   | 3   |
| 1.3. Previous Work on Examination of Temperature Effects on the MEMS Gyroscope and Its Reliability Concern ..... | 5   |
| 1.4. Research Objectives .....   | 10  |
| 1.5. Dissertation Outline .....  | 11  |
| 2. Effects of Elevated Temperatures on the Performance of the MEMS Vibratory Gyroscope .....                     | 13  |
| 2.1. Introduction.....   | 13  |
| 2.2. Experimental Set-up and Test Procedure.....   | 14  |
| 2.2.1. Stationary Test .....   | 16  |
| 2.2.2. Rotary Test.....  | 19  |
| 2.3. Results and Analysis .....  | 22  |
| 2.3.1. Stationary Test Results: .....  | 23  |
| 2.3.2. Rotary Test Results: .....  | 32  |
| 2.4. Conclusions.....  | 42  |
| 3. Simulation of Temperature Effect on the Performance of a MEMS Gyroscope .....                                 | 44  |
| 3.1. Introduction.....   | 44  |
| 3.2. Working Principle .....   | 44  |
| 3.3. MEMS Gyroscope Motion Equations.....  | 47  |
| 3.4. Simulink Model .....  | 49  |
| 3.5. Simulation Results at Room Temperature .....  | 53  |
| 3.6. Simulation over a Wider Temperature Range .....   | 55  |
| 3.7. Model Validation .....  | 62  |
| 3.7.1. Examination of Model Validation within the Manufacturer's Recommended Temperature Range .....             | 62  |
| 3.7.2. Examination of Model Validation beyond the Manufacturer's Recommended Temperature Range .....             | 66  |
| 3.8. Conclusions.....  | 70  |
| 4. High Temperature Reliability of Solder – Literature Review .....  | 72  |
| 4.1. Effects of High Temperature on Lead-free Solder .....   | 73  |
| 4.1.1. Interfacial Intermetallic Growth .....  | 73  |
| 4.1.2. Coarsening of Bulk Intermetallic.....   | 74  |
| 4.1.3. Void Formation.....   | 76  |
| 4.2. High Temperature Reliability of Lead-free Solder.....   | 77  |
| 4.2.1. High Temperature Thermal Cycling Reliability Test .....   | 77  |

|        |   |     |
|--------|---|-----|
| 4.2.2. | High Temperature Mechanical Drop/Shock Reliability Test .....   | 79  |
| 4.3.   | A Technique to Improve Drop/Shock Reliability of SnAgCu Solders.....  | 82  |
| 4.4.   | Advantages of Mn dopant in SnAgCu Solder.....   | 84  |
| 4.4.1. | Drop/Shock Reliability Improvement.....   | 84  |
| 4.4.2. | Interfacial IMC Growth Reduction and its Possible Mechanism .....   | 85  |
| 4.4.3. | Effects on Melting Behavior .....   | 86  |
| 4.4.4. | Effects on Undercooling .....   | 87  |
| 4.4.5. | Effects on Mechanical Property .....  | 88  |
| 4.5.   | Advantage of Ce dopant in SnAgCu Solder .....   | 89  |
| 4.5.1. | Drop/Shock Reliability Improvement.....   | 89  |
| 4.5.2. | Interfacial IMC Growth Reduction and its Possible Mechanism .....   | 90  |
| 4.5.3. | Effects on Melting Behavior .....   | 91  |
| 4.5.4. | Effects on Microstructure .....   | 92  |
| 4.5.5. | Effects on Mechanical Property .....  | 94  |
| 4.6.   | Research Gap .....  | 95  |
| 5.     | Experimental Selections.....  | 96  |
| 5.1.   | Solder Selection .....  | 96  |
| 5.2.   | Component Selection .....   | 98  |
| 5.3.   | Printed Circuit Board (PCB) Design and Fabrication.....   | 101 |
| 5.4.   | Printed Circuit Board (PCB) Reflow Assembly:.....   | 104 |
| 5.5.   | Test Board Inspection after Reflow Assembly .....   | 106 |
| 5.6.   | Printed Wiring Assembly.....  | 107 |
| 6.     | Design of Experiment, Test Equipment and Monitoring Systems .....   | 110 |
| 6.1.   | Aging Test.....   | 110 |
| 6.1.1. | Design of Experiment (DOE) for Aging Test.....  | 111 |
| 6.1.2. | Test Equipment and Measurement Systems for Aging Test.....  | 113 |
| 6.1.3. | Cross-sectioning, ESEM, IMC Measurement, EDS and WDS Procedure<br>113   |     |
| 6.2.   | Mechanical Shock Reliability Test .....   | 115 |
| 6.2.1. | Design of Experiment (DOE) for Mechanical Shock Test .....  | 116 |
| 6.2.2. | Test Equipment and Measurement Systems for Mechanical Shock Test<br>117   |     |
| 6.2.3. | Failure Criteria for Mechanical Shock Test.....   | 119 |
| 7.     | Effects of Mn and Ce Dopant on the Microstructure and Mechanical Properties<br>of SAC305 Solder. ....   | 121 |
| 7.1.   | Microstructure Analysis.....  | 121 |
| 7.1.1. | Number of $\beta$ -tin Grains.....  | 121 |
| 7.1.2. | Size of $\text{Ag}_3\text{Sn}$ IMC Particles, Number of $\beta$ -tin Dendrites, Area Fraction<br>of Eutectic Region and Area Fraction of $\beta$ -tin Dendrites ..... | 125 |
| 7.2.   | Mechanical Properties of Solders .....  | 135 |
| 8.     | Interfacial Intermetallic Growth during Isothermal Aging at 185°C and 200°C on<br>QFN44 and QFN32 Packages .....  | 138 |
| 8.1.   | Interfacial Intermetallic Formation during Reflow on QFN Packages.....  | 139 |
| 8.2.   | Effect of Isothermal Aging on QFN Package .....   | 140 |
| 8.2.1. | The Growth of Interfacial Intermetallic Layers during Isothermal Aging<br>141   |     |

|          |  |     |
|----------|--|-----|
| 8.2.2.   | Void Creation and Coalescence at the Interface during Isothermal Aging                                     | 141 |
| 8.3.     | QFN44 - Cu <sub>6</sub> Sn <sub>5</sub> IMC Growth and %Voiding during 185°C Aging                         | 146 |
| 8.4.     | QFN44 - Cu <sub>6</sub> Sn <sub>5</sub> IMC Growth and %Voiding during 200°C Aging                         | 154 |
| 8.5.     | QFN32 - Cu <sub>6</sub> Sn <sub>5</sub> IMC Growth and %Voiding during 185°C Aging                         | 164 |
| 8.6.     | QFN32 - Cu <sub>6</sub> Sn <sub>5</sub> IMC Growth and %Voiding during 200°C Aging                         | 167 |
| 8.7.     | Conclusions  | 171 |
| 9.       | Interfacial Intermetallic Formation and Growth during Isothermal Aging at 185°C and 200°C on R2512 Package | 173 |
| 9.1.     | R2512 – Interfacial IMC Growth on the Component and the Board side during 185°C Aging                      | 175 |
| 9.2.     | R2512 – Interfacial IMC Growth on Component and Board side during 200°C Aging                              | 183 |
| 9.2.1.   | Evolution of Ni Layer Consumption during 200°C Aging   | 185 |
| 9.2.2.   | Board Side Interfacial IMC Thickness Measurement   | 188 |
| 9.3.     | EDS and WDS Analysis on High Mn Solder Sample  | 197 |
| 9.3.1.   | EDS Analysis Result  | 197 |
| 9.3.1.1. | Point Scan Analysis  | 197 |
| 9.3.1.2. | Line Scan Analysis   | 199 |
| 9.3.2.   | WDS Analysis Result  | 202 |
| 9.4.     | Conclusions  | 205 |
| 10.      | Mechanical Shock Reliability Test  | 208 |
| 10.1.    | QFN44 - Mechanical Shock Test Results after Thermal Aging at 185°C and 200°C                               | 210 |
| 10.1.1.  | Discussion on QFN44 Mechanical Shock Test Results  | 218 |
| 10.2.    | QFN32 - Mechanical Shock Test Results after Thermal Aging at 185°C and 200°C                               | 221 |
| 10.2.1.  | Discussion on QFN32 Mechanical Shock Test Results  | 230 |
| 10.3.    | QFP256 - Mechanical Shock Test Results after Thermal Aging at 185°C and 200°C                              | 233 |
| 10.4.    | R2512 and R2010 - Mechanical Shock Test Results after Thermal Aging at 185°C and 200°C                     | 235 |
| 10.4.1.  | R2512 Mechanical Shock Test Results after Thermal Aging at 185°C and 200°C                                 | 236 |
| 10.4.2.  | R2010 Mechanical Shock Test Results after Thermal Aging at 185°C and 200°C                                 | 239 |
| 10.5.    | Time=0 Test Boards - Mechanical Shock Test Results   | 240 |
| 10.6.    | Failure Analysis   | 243 |
| 10.6.1.  | SAC305 Solder  | 243 |
| 10.6.2.  | Low Mn Solder  | 245 |
| 10.6.3.  | High Mn Solder   | 247 |
| 10.6.4.  | Low Ce Solder  | 248 |
| 10.6.5.  | High Ce Solder   | 250 |
| 10.7.    | Conclusions  | 251 |
| 11.      | Contributions  | 254 |
|          | Appendix-A   | 256 |

|                 |     |
|-----------------|-----|
| Appendix-B..... | 265 |
| References..... | 275 |

## List of Tables

|   |     |
|---|-----|
| Table 1-1: Summary of Previous Work on Various Temperature Ranges Examined by Researchers.....  | 6   |
| Table 2-1: Temperature-dependent Bias Value of Five Thermal Cycles from 25°C to 125°C.....  | 27  |
| Table 2-2: Average Temperature-dependent Bias of all Nine Gyroscopes from 25°C to 125°C.....  | 27  |
| Table 2-3: Mean and Standard Deviation of Five Stationary Baseline Tests.....   | 32  |
| Table 2-4: Angular Velocity and Temperature Dependent Bias of Five Rotary Thermal Cycles from 25°C to 125°C.....  | 37  |
| Table 2-5: Average Temperature-dependent Bias of all Nine Gyroscopes from 25°C to 125°C during 60°/s angular rotation.....                                | 37  |
| Table 2-6: Mean and Standard Deviation of Rotary Baseline Test.....   | 42  |
| Table 3-1: MEMS Gyroscope's Parameters and Simulation Result at Ambient Condition (Angular Velocity = 60°/s, Temperature=25°C, Pressure= 1 atm).....      | 54  |
| Table 3-2: Average Angular Velocity Output of the ADIS16250 MEMS Gyroscope from 25°C to 85°C.....   | 63  |
| Table 3-3: Temperature-dependent Bias Value of ADIS16250 from 25°C to 85°C ( $\Delta T = 60^\circ C$ ) at 0, 60, 120 and 240 deg/s Angular Rotations..... | 65  |
| Table 3-4: Comparison of Simulation and Experimental Temperature-dependent Bias Value of ADIS16250 from 25°C to 85°C.....                                 | 66  |
| Table 3-5: Comparison of Simulation and Experimental Temperature-dependent Bias value of ADIS16255 from 25°C to 125°C.....                                | 69  |
| Table 4-1: Previous Studies of Mechanical Drop/Shock Reliability.....   | 79  |
| Table 5-1: Details on various package types selected in this study.....   | 100 |
| Table 6-1: Polishing Steps for QFN44 and QFN32.....   | 114 |
| Table 6-2: Polishing Steps for R2512.....   | 114 |
| Table 7-1: Total Number of $\beta$ -tin Grains in Each Side of Solder Joint in QFN44 and QFN32.....   | 124 |
| Table 7-2: % Change in Microstructure Attributes of Modified SAC305 Solders Compared to SAC305.....   | 135 |
| Table 10-1: Weibull Parameters for QFN44 - 400 hours of Aging at 185°C.....   | 212 |
| Table 10-2: Kruskal-Wallis Test - QFN44 (400 hours of Aging at 185°C).....  | 212 |
| Table 10-3: Weibull Parameters for QFN44 - 1000 hours of Aging at 185°C.....  | 213 |
| Table 10-4: Kruskal-Wallis Test - QFN44 (1000 hours of Aging at 185°C).....   | 213 |
| Table 10-5: Weibull Parameters for QFN44 - 400 hours of Aging at 200°C.....   | 215 |
| Table 10-6: Kruskal-Wallis Test - QFN44 (400 hours of Aging at 200°C).....  | 215 |
| Table 10-7: Weibull Parameters for QFN44 - 1000 hours of Aging at 200°C.....  | 217 |
| Table 10-8: Kruskal-Wallis Test - QFN44 (1000 hours of Aging at 200°C).....   | 217 |
| Table 10-9: QFN44 - Characteristic Life Comparison.....   | 219 |
| Table 10-10: Weibull Parameters for QFN32 - 400 hours of Aging at 185°C.....  | 223 |
| Table 10-11: Kruskal-Wallis Test – QFN32 (400 hours of Aging at 185°C).....   | 223 |
| Table 10-12: Weibull Parameters for QFN32 - 1000 hours of Aging at 185°C.....   | 225 |
| Table 10-13: Kruskal-Wallis Test – QFN32 (1000 hours of Aging at 185°C).....  | 225 |



|  |     |
|--|-----|
| Table 10-14: Weibull Parameters for QFN32 - 400 hours of Aging at 200°C .....  | 227 |
| Table 10-15: Kruskal-Wallis Test – QFN32 (400 hours of Aging at 200°C) .....   | 227 |
| Table 10-16: Weibull Parameters for QFN32 - 1000 hours of Aging at 200°C .....   | 229 |
| Table 10-17: Kruskal-Wallis Test – QFN32 (1000 hours of Aging at 200°C) .....  | 229 |
| Table 10-18: QFN32 - Characteristic Life Comparison .....  | 231 |
| Table 10-19: QFP256 - Mechanical Shock Test Result Summary after 400 and 1000<br>hours of Aging at 185°C and 200°C ..... | 235 |
| Table 10-20: R2512 - Mechanical Shock Test Result Summary after 400 and 1000<br>hours of Aging at 185°C and 200°C .....  | 236 |
| Table 10-21: R2010 - Mechanical Shock Test Result Summary after 400 and 1000<br>hours of Aging at 185°C and 200°C .....  | 239 |
| Table 10-22: Failure Summary of various Package Types (Time=0) during 600,000<br>Mechanical Shocks .....                 | 241 |
| Table 10-23: Failure of various Package Types (Time=0) during 100,000 Mechanical<br>Shocks .....                         | 241 |
| Table 0-1: Temperature dependent bias values of five stationary thermal cycles from<br>25°C to 125°C .....               | 257 |
| Table 0-2: Mean and Standard Deviation of Stationary Baseline Test .....   | 258 |
| Table 0-3: Angular velocity and temperature dependent bias of five rotary thermal<br>cycles from 25°C to 125°C .....     | 259 |
| Table 0-4: Mean and Standard Deviation of Rotary Baseline Test .....   | 260 |
| Table 0-5: Temperature dependent bias values of five stationary thermal cycles from<br>25°C to 125°C .....               | 261 |
| Table 0-6: Angular velocity and temperature dependent bias of five rotary thermal<br>cycles from 25°C to 125°C .....     | 263 |
| Table 0-7: Mean and Standard Deviation of Rotary Baseline Test .....   | 264 |

## List of Figures

|  |    |
|--|----|
| Figure 2-1: Schematic of MEMS Gyroscope Package .....  | 14 |
| Figure 2-2: Experimental Approach for MEMS Gyroscope Performance<br>Characterization at High Temperature.....  | 16 |
| Figure 2-3: Stationary Test Sequence for Evaluating Effects of Elevated<br>Temperatures on the MEMS Gyroscope.....   | 17 |
| Figure 2-4: Stationary Baseline Test Setup. ....   | 18 |
| Figure 2-5: Stationary Thermal Test Setup.....   | 19 |
| Figure 2-6: Rotary Test Sequence for Evaluating Elevated Temperature Effect on the<br>Performance of MEMS Gyroscope.....   | 20 |
| Figure 2-7: Rotary Baseline Test Setup. ....   | 21 |
| Figure 2-8: Rotary Thermal Test Setup. ....  | 22 |
| Figure 2-9: First Stationary Baseline Test Result: (a) Raw Angular Rate Data; (b)<br>Filtered Angular Rate Data with Window size = 100. (Mean=0.01°/s, STD=0.44).....              | 23 |
| Figure 2-10: Stationary Thermal Test Results from 25°C to 85°C (a) Raw Angular<br>Rate Data; (b) Filtered Angular Rate Data with Window size = 100; (c) Die<br>Temperature. ....   | 24 |
| Figure 2-11: Second Stationary Baseline Test Result: (a) Raw Angular Rate Data; (b)<br>Filtered Angular Rate Data with Window size = 100. (Mean= -0.01, STD= 0.48).....            | 25 |
| Figure 2-12: Stationary Thermal Test Result from 25°C to 125°C: (a) Raw Angular<br>Rate Data; (b) Filtered Angular Rate Data with Window size = 100; (c) Die<br>Temperature. ....  | 26 |
| Figure 2-13: Third Stationary Baseline Test Result: (a) Raw Angular Rate Data; (b)<br>Filtered Angular Rate Data with Window size = 100. (Mean= 0.01, STD=0.45).....               | 28 |
| Figure 2-14: Stationary Baseline Test Result from 25°C to 150°C: (a) Raw Angular<br>Rate Data; (b) Filtered Angular Rate Data with Window size = 100; (c) Die<br>Temperature. .... | 29 |
| Figure 2-15: Fourth Stationary Baseline Test Result: (a) Raw Angular Rate Data; (b)<br>Filtered Angular Rate Data with Window-size = 100. (Mean=0.01, STD=0.46).....               | 30 |
| Figure 2-16: Stationary Thermal Test Results from 25°C to 175°C: (a) Raw Angular<br>Rate Data; (b) Filtered Angular Rate Data with Window size = 100; (c) Die<br>Temperature. .... | 31 |
| Figure 2-17: Fifth Stationary Baseline Test Result: (a) Raw Angular Rate Data; (b)<br>Filtered Angular Rate Data with Window-size = 100. (Mean= 0.01, STD=0.44).....               | 32 |
| Figure 2-18: First Rotary Baseline Test Result: (a) Raw Angular Rate Data; (b)<br>Filtered Angular Rate Data with Window size = 100. (Mean= 59.87, STD= 0.84)....                  | 33 |
| Figure 2-19: Rotary Thermal Test Results from 25°C to 85°C: (a) Raw Angular Rate<br>Data; (b) Filtered Angular Rate Data with Window size = 100; (c) Die Temperature.<br>.....     | 34 |
| Figure 2-20: Second Rotary Baseline Test Result: (a) Raw Angular Rate Data; (b)<br>Filtered Angular Rate Data with Window size = 100. (Mean= 59.98, STD= 1.49)....                 | 35 |
| Figure 2-21: Rotary Thermal Test Results from 25°C to 125°C: (a) Raw Angular Rate<br>Data; (b) Filtered Angular Rate Data with Window size = 100; (c) Die Temperature.<br>.....    | 36 |

|  |    |
|--|----|
| Figure 2-22: Third Rotary Baseline Test Result: (a) Raw Angular Rate Data; (b) Filtered Angular Rate Data with Window size = 100. (Mean= 59.92, STD= 0.82)....   | 38 |
| Figure 2-23: Rotary Thermal Test Results from 25°C to 150°C: (a) Raw Angular Rate Data; (b) Filtered Angular Rate Data with Window size = 100; (c) Die Temperature.  | 39 |
| Figure 2-24: Fourth Rotary Baseline Test Result: (a) Raw Angular Rate Data; (b) Filtered Angular Rate Data with Window size = 100. (Mean= 59.99, STD= 1.27)....  | 40 |
| Figure 2-25: Rotary Thermal Test Results from 25°C to 175°C: (a) Raw Angular Rate Data; (b) Filtered Angular Rate Data with Window size = 100; (c) Die Temperature.  | 41 |
| Figure 2-26: Fifth Rotary Baseline Test Result: (a) Raw Angular Rate Data; (b) Filtered Angular Rate Data with Window size = 100. (Mean= 59.79, STD= 1.28)....   | 41 |
| Figure 3-1: Schematic of Two Degree-of-freedom (2-DOF) Mass-spring-damper System.....  | 45 |
| Figure 3-2: Schematic Illustration of MEMS Vibratory Gyroscope .....   | 46 |
| Figure 3-3: Two Proof Mass-spring-damper System.....   | 47 |
| Figure 3-4: Two Degree-of-freedom Mass-spring-damper System Model .....  | 48 |
| Figure 3-5: Simulink Model.....  | 50 |
| Figure 3-6: Displacement of Drive and Sense Comb at 60°/s Angular Rotation (a) Drive Comb Displacement (m) vs. Time (sec) (b) Sense Comb Displacement (m) vs. Time (sec) .....   | 55 |
| Figure 3-7: Capacitance Change (F) vs. Angular Velocity (RPM) .....  | 55 |
| Figure 3-8: (a) Change in Young's Modulus with Temperature from 25°C to 125°C (b) Change in Drive Resonance Frequency with Temperature from 0°C to 140°C. ....   | 57 |
| Figure 3-9: Change in Drive Damping with Temperature from 0°C to 140°C. ....   | 58 |
| Figure 3-10: Capacitance Change with Temperature from 0°C to 140°C.....  | 59 |
| Figure 3-11: Transient Response of the MEMS Gyroscope at 60 °/s Angular Rotation from 0°C to 140°C Temperatures: (a) Drive Displacement (m) vs. Time (s), (b) Sense Displacement (m) vs. Time (s), (c) Magnified View of Window-(a), (d) Magnified View of Window-(b), (e) Magnified View of Window-(c) indicates an Increase in Drive Amplitude with Temperatures, (f) Magnified View of Window-(d) indicates an Increase in Sense Amplitude with Temperatures..... | 60 |
| Figure 3-12: Capacitance Change due to Variation in Angular Velocity from 59.5 °/s to 64.0 °/s.....  | 61 |
| Figure 3-13: Simulated Temperature-Dependent Bias of MEMS Gyroscope at 60°/s Angular Rotation.....   | 61 |
| Figure 3-14: Temperature-dependent Bias of ADIS16250 from 25°C to 85°C at 0, 60, 120 and 240 deg/s Angular Rotations.....  | 64 |
| Figure 3-15: Comparison of Simulation and Experimental Temperature-dependent Bias of ADIS16250 from 25°C to 85°C.....  | 65 |
| Figure 3-16: Experimental Results of ADIS16255 for Five Thermal Cycles from 25°C to 125°C at 60°/s Angular Rotation.....   | 67 |
| Figure 3-17: Simulated Temperature-Dependent Bias from +25°C to +125°C at 60°/s Angular Rotation.....  | 68 |
| Figure 4-1: R2512 - SAC305 Solder Joint on ENIG Board (a) After Reflow (b) After 100 hours at 185°C (c) After 400 hours at 185°C (d) After 1000 hours at 185°C.....  | 76 |

|  |     |
|--|-----|
| Figure 4-2: Drop Test Results of As-reflowed Solders [71] [70] .....   | 83  |
| Figure 5-1: Printed Circuit Board Layout .....   | 102 |
| Figure 5-2: Schematic of PCB layers.....   | 103 |
| Figure 5-3: Primary side of PCB .....  | 103 |
| Figure 5-4: Secondary side of PCB .....  | 103 |
| Figure 5-5: A CAD Simulation on PCB Assembly .....   | 104 |
| Figure 5-6: A General Guideline on Reflow Profile for SnAgCu Solder by Indium Corporation .....  | 105 |
| Figure 5-7: Assembled PCB after Reflow .....   | 105 |
| Figure 5-8: An Enlarge View of Each Package Types after Reflow Assembly .....  | 106 |
| Figure 5-9: X-ray Image of Each Package Types .....  | 107 |
| Figure 5-10: Primary-side of Assembled Test Board .....  | 108 |
| Figure 5-11: Secondary-side of Assembled Test Board .....  | 109 |
| Figure 6-1: Design of Experiment (DOE) for Aging Test.....   | 112 |
| Figure 6-2: Detailed Design of Experiment (DOE) for Aging Test .....   | 112 |
| Figure 6-3: Design of Experiment (DOE) for Mechanical Shock Test .....   | 117 |
| Figure 6-4: A Shock Plate for Testing Two Test Boards at Once .....  | 118 |
| Figure 6-5: Shock Plate Assembly Mounted on Shock Machine .....  | 118 |
| Figure 6-6: Shock Profile for Mechanical Shock Test.....   | 118 |
| Figure 6-7: Package Failure during Mechanical Shock Testing (a) QFN44 Failed at 7665 Shocks (b) QFN32 Failed at 12020 Shocks (c) QFP256 Failed at 55310 Shocks (Note: Package Resistance is in Ohm Unit).....                  | 120 |
| Figure 7-1: Cross-polarized Images of Left and Right Side of Solder Joint in QFN44 Package (a) SAC305, (b) Low Mn, (c) High Mn, (d) Low Ce, (e) High Ce .....  | 123 |
| Figure 7-2: Cross-polarized Images of Left and Right Side of Solder Joint in QFN32 Package: (a) SAC305, (b) Low Mn, (c) High Mn, (d) Low Ce, (e) High Ce .....   | 124 |
| Figure 7-3: Average Number of $\beta$ -tin Grains of Various Solders Observed in QFN44 and QFN32.....  | 125 |
| Figure 7-4: ESEM Image at 2500x Magnification of Various Solders in QFN32 Package: (a) SAC305, (b) Low Mn, (c) High Mn, (d) Low Ce, (e) High Ce .....  | 126 |
| Figure 7-5: ESEM Image at 2500x Magnification of Various Solders in QFN44 Package (a) SAC305, (b) Low Mn, (c) High Mn, (d) Low Ce, (e) High Ce .....   | 127 |
| Figure 7-6: (a) ESEM Image of Solder at 7000x Magnification (b) Selected Ag-Sn IMC Particles in the Solder Bulk .....  | 129 |
| Figure 7-7: (a) ESEM Image of Solder at 7000x Magnification (b) Selected Region for $\beta$ -tin Dendrites.....  | 130 |
| Figure 7-8: Column (a) ESEM Image at 7000x Magnification, Column (b) Detected Ag <sub>3</sub> Sn IMC Particles, and Column (c) Selected $\beta$ -tin Lobes: (A) SAC305, (B) Low Mn, (C) High Mn, (D) Low Ce, (E) High Ce ..... | 132 |
| Figure 7-9: Mean Length and Width of Ag-Sn IMC Particles for Solders.....  | 132 |
| Figure 7-10: Area Fraction of Eutectic Region.....   | 133 |
| Figure 7-11: Area Fraction of $\beta$ -tin Dendrites .....   | 133 |
| Figure 7-12: Number of $\beta$ -tin dendrites/Lobes .....  | 134 |
| Figure 7-13: Example of Indentations in Solder Bulk .....  | 136 |
| Figure 7-14: Elastic Modulus of Various Solders.....   | 137 |
| Figure 7-15: Hardness of Various Solders.....  | 137 |

|   |     |
|---|-----|
| Figure 8-1: An ESEM Image of QFN44 and QFN32 after Reflow .....   | 139 |
| Figure 8-2: Left and Right Solder Joint of QFN44.....   | 140 |
| Figure 8-3: Interfacial IMC Formation on QFN Package during Reflow (SAC305 – Time=0) .....  | 140 |
| Figure 8-4: Interfacial IMC Growth and Void Creation during Isothermal Aging (SAC305 - 185°C/100 hours).....  | 142 |
| Figure 8-5: Interfacial IMC Growth and Void Coalescing during further Isothermal Aging (SAC305 - 185°C/600 hours).....  | 143 |
| Figure 8-6 Cu <sub>6</sub> Sn <sub>5</sub> IMC Layer Thickness Measurement (a) Length of the Horizontal Cu <sub>6</sub> Sn <sub>5</sub> IMC Layer used for Measurement (b) ESEM Image at 2500x Magnification for Average Cu <sub>6</sub> Sn <sub>5</sub> IMC Layer Thickness Measurement..... | 144 |
| Figure 8-7: ESEM Image of Solder Joint Indicating Length Measurement Marks for % voiding Calculation.....   | 145 |
| Figure 8-8: QFN44 - Cu <sub>6</sub> Sn <sub>5</sub> IMC Layer Growth Summary during 185°C Aging...  | 146 |
| Figure 8-9: QFN44 - %Voiding Measurements during 185°C Aging .....  | 147 |
| Figure 8-10: QFN44 - SAC305 Solder Joint (a) After Reflow, (b) After 100 hours/185°C Aging, (c) After 1000 hours/185°C Aging.....   | 149 |
| Figure 8-11: QFN44 - SAC305+0.05%Mn Solder Joint (a) After Reflow, (b) After 100 hours/185°C Aging, (c) After 1000 hours/185°C Aging.....   | 150 |
| Figure 8-12: QFN44 - SAC305+0.17%Mn Solder Joint (a) After Reflow, (b) After 100 hours/185°C Aging, (c) After 1000 hours/185°C Aging.....   | 151 |
| Figure 8-13: QFN44 - SAC305+0.07%Ce Solder Joint (a) After Reflow, (b) After 100 hours/185°C Aging, (c) After 1000 hours/185°C Aging.....   | 152 |
| Figure 8-14: QFN44 - SAC305+0.13%Ce Solder Joint (a) After Reflow, (b) After 100 hours/185°C Aging, (c) After 1000 hours/185°C Aging.....   | 153 |
| Figure 8-15: QFN44 - Cu <sub>6</sub> Sn <sub>5</sub> IMC Growth Summary during 200°C Aging .....  | 154 |
| Figure 8-16: Ni layer consumption phenomenon in QFN44 package, a demonstration using SAC305 solder joint at various time intervals under 200°C aging.....   | 156 |
| Figure 8-17: QFN44 - %Voiding Measurements during 200°C Aging .....   | 158 |
| Figure 8-18: QFN44 - SAC305 Solder Joint (a) After 100 hours/200°C Aging, (b) After 1000 hours/200°C Aging .....  | 160 |
| Figure 8-19: QFN44 - SAC305+0.05%Mn Solder Joint (a) After 100 hours/200°C Aging, (b) After 1000 hours/200°C Aging.....   | 161 |
| Figure 8-20: QFN44 - SAC305+0.17%Mn Solder Joint (a) After 100 hours/200°C Aging, (b) After 1000 hours/200°C Aging.....   | 162 |
| Figure 8-21: QFN44 - SAC305+0.07%Ce Solder Joint (a) After 100 hours/200°C Aging, (b) After 1000 hours/200°C Aging.....   | 163 |
| Figure 8-22: QFN44 - SAC305+0.13%Ce Solder Joint (a) After 100 hours/200°C Aging, (b) After 1000 hours/200°C Aging.....   | 164 |
| Figure 8-23: QFN32 - Cu <sub>6</sub> Sn <sub>5</sub> IMC Growth Summary during 185°C Aging .....  | 165 |
| Figure 8-24: QFN32 - %Voiding Measurements during 185°C Aging .....   | 166 |
| Figure 8-25: QFN32 - Cu <sub>6</sub> Sn <sub>5</sub> IMC Growth Summary during 200°C Aging .....  | 168 |
| Figure 8-26: (a) SAC305+0.07%Ce Solder Joint after 1000 hours of Aging at 200°C, (b) Magnified View of Consumed Ni Layer.....   | 169 |
| Figure 8-27: QFN32 - %Voiding Measurements during 200°C Aging .....   | 170 |

|   |     |
|---|-----|
| Figure 9-1: A Left and a Right Solder Joint of R2512 after Reflow (SAC305 – Time=0) .....   | 174 |
| Figure 9-2: (a) Interfacial IMCs (b) bulk IMCs formation after Reflow on R2512 Package (SAC305 – Time=0) .....  | 174 |
| Figure 9-3: Regions of IMC Layer on the Component and Board Side for Calculating Interfacial IMC Layer Thickness .....  | 175 |
| Figure 9-4: R2512 - Component Side Ni <sub>3</sub> Sn <sub>4</sub> Interfacial IMC Growth Summary during 185°C Aging .....  | 176 |
| Figure 9-5: R2512 – Board Side (Ni,Cu) <sub>3</sub> Sn <sub>4</sub> Interfacial IMC Growth Summary during 185°C Aging .....   | 176 |
| Figure 9-6: R2512 - SAC305 Solder Joint (a) After Reflow, (b) Solder Interfaces after 1000 hours/185°C Aging, (c) Solder Bulk after 1000 hours/185°C Aging .....  | 179 |
| Figure 9-7: R2512 - SAC305+0.05%Mn Solder Joint (a) After Reflow, (b) Solder Interfaces after 1000 hours/185°C Aging, (c) Solder Bulk after 1000 hours/185°C Aging .....  | 180 |
| Figure 9-8: R2512 - SAC305+0.17%Mn Solder Joint (a) After Reflow, (b) Solder Interfaces after 1000 hours/185°C Aging, (c) Solder Bulk after 1000 hours/185°C Aging .....  | 181 |
| Figure 9-9: R2512 - SAC305+0.07%Ce Solder Joint (a) After Reflow, (b) Solder Interfaces after 1000 hours/185°C Aging, (c) Solder Bulk after 1000 hours/185°C Aging .....  | 182 |
| Figure 9-10: R2512 - SAC305+0.13%Ce Solder Joint (a) After Reflow, (b) Solder Interfaces after 1000 hours/185°C Aging, (c) Solder Bulk after 1000 hours/185°C Aging .....   | 183 |
| Figure 9-11: R2512 - Component Side Ni <sub>3</sub> Sn <sub>4</sub> Interfacial IMC Growth Summary during 200°C Aging .....   | 184 |
| Figure 9-12: R2512 - Board side Interfacial IMC evolution for SAC305 Solder joint, (a) After Reflow, (b) After 100 hours/200°C Aging, (c) After 200 hours/200°C Aging, (d) After 400 hours/200°C Aging, (e) After 600 hours/200°C Aging, (f) After 1000 hours/200°C Aging ..... | 187 |
| Figure 9-13: R2512- EDS Point Analysis on Board Side IMC Layers (SAC305 Solder, 1000 hours/ 200°C Aging) .....  | 188 |
| Figure 9-14: R2512 – Board Side Ni-Cu-Sn Interfacial IMC Growth Summary during 200°C Aging .....  | 189 |
| Figure 9-15: R2512 - SAC305 Solder Joint (a) After 100 hours/200°C Aging, (b) After 1000 hours/200°C Aging .....  | 191 |
| Figure 9-16: R2512 – SAC305 (a) Left Solder Joint (b) Right Solder Joint after 1000 hours/200°C Aging .....   | 191 |
| Figure 9-17: R2512 - SAC305+0.05%Mn Solder Joint (a) After 100 hours/200°C Aging, (b) After 1000 hours/200°C Aging .....  | 192 |
| Figure 9-18: R2512 – SAC305+0.05%Mn (a) Left Solder Joint (b) Right Solder Joint after 1000 hours/200°C Aging .....   | 192 |
| Figure 9-19: R2512 - SAC305+0.17%Mn Solder Joint (a) After 100 hours/200°C Aging, (b) After 1000 hours/200°C Aging .....  | 193 |
| Figure 9-20: R2512 – SAC305+0.17%Mn (a) Left Solder Joint (b) Right Solder Joint after 1000 hours/200°C Aging .....   | 193 |

|   |     |
|---|-----|
| Figure 9-21: R2512 - SAC305+0.07%Ce Solder Joint (a) After 100 hours/200°C Aging, (b) After 1000 hours/200°C Aging.....   | 194 |
| Figure 9-22: R2512 – SAC305+0.07%Ce (a) Left Solder Joint (b) Right Solder Joint after 1000 hours/200°C Aging .....   | 195 |
| Figure 9-23: R2512 - SAC305+0.13%Ce Solder Joint (a) After 100 hours/200°C Aging, (b) After 1000 hours/200°C Aging.....   | 196 |
| Figure 9-24: R2512 – SAC305+0.13%Ce (a) Left Solder Joint (b) Right Solder Joint after 1000 hours/200°C Aging .....   | 196 |
| Figure 9-25: R2512 – (a) Locations of Point Scan Analysis, (b) Elemental Spectrum of X3 Location (c) Measurement of Mn Dopant by Weight% (High Mn Solder after 1000 hours/200°C Aging) .....  | 198 |
| Figure 9-26: R2512 - Location of Line Scan Analysis and Reference Line for EDS Technique (High Mn Solder after 1000 hours/200°C aging).....   | 200 |
| Figure 9-27: R2512 - EDS Line Scan Measurement Results (a) Compiled Elemental Plot with Line Scan and Reference Line (b) Elemental Plot of Mn (c) Elemental Plot of Ni (d) Elemental Plot of Sn (e) Elemental Plot of P (f) Elemental Plot of Ag (g) Elemental Plot of Cu (h) Combined Elemental Plot of All Elements (High Mn Solder after 1000 hours/200°C Aging) ..... | 201 |
| Figure 9-28: R2512 - Elemental Plot of Mn during EDS Line Scan Analysis (High Mn Solder after 1000 hours/200°C Aging).....  | 202 |
| Figure 9-29: R2512 - Location of Line Scan Analysis for WDS Technique (High Mn Solder after 1000 hours/200°C aging).....  | 203 |
| Figure 9-30: R2512 - WDS Line Scan Measurement Results. Elements are ordered as follow Ni, Mn, Sn, P, Cu and Ag (High Mn Solder after 1000 hours/200°C aging) .....   | 204 |
| Figure 9-31: R2512 - Elemental Plot of Mn during WDS Line Scan Analysis (a) Raw Signal (b) Refined Signal (High Mn Solder after 1000 hours/200°C Aging).....  | 204 |
| Figure 10-1: Mechanical Shock Testing Outline .....   | 209 |
| Figure 10-2: QFN44 Weibull Plot - 400 hours of Aging at 185°C.....  | 211 |
| Figure 10-3: QFN44 Weibull Plot - 1000 hours of Aging at 185°C.....   | 213 |
| Figure 10-4: QFN44 Weibull Plot - 400 hours of Aging at 200°C.....  | 215 |
| Figure 10-5: QFN44 Weibull Plot - 1000 hours of Aging at 200°C.....   | 217 |
| Figure 10-6: QFN44 - Characteristic Life after 400 and 1000 hours of Aging at 185°C and 200°C.....  | 220 |
| Figure 10-7: QFN44 – Cu <sub>6</sub> Sn <sub>5</sub> IMC Thickness after 400 and 1000 hours of Aging at 185°C and 200°C.....  | 220 |
| Figure 10-8: QFN44 – %Voiding after 400 and 1000 hours of Aging at 185°C and 200°C.....   | 221 |
| Figure 10-9: QFN32 Weibull Plot - 400 hours of Aging at 185°C.....  | 223 |
| Figure 10-10: QFN32 Weibull Plot - 1000 hours of Aging at 185°C.....  | 225 |
| Figure 10-11: QFN32 Weibull Plot - 400 hours of Aging at 200°C.....   | 227 |
| Figure 10-12: QFN32 Weibull Plot - 1000 hours of Aging at 200°C.....  | 229 |
| Figure 10-13: QFN32 - Characteristic Life after 400 and 1000 hours of Aging at 185°C and 200°C.....   | 232 |
| Figure 10-14: QFN32 – Cu <sub>6</sub> Sn <sub>5</sub> IMC Thickness after 400 and 1000 hours of Aging at 185°C and 200°C.....   | 232 |

|   |     |
|---|-----|
| Figure 10-15: QFN32 – %voiding after 400 and 1000 hours of Aging at 185°C and 200°C.....  | 233 |
| Figure 10-16: R2512 – Ni-Cu-Sn Board Side Interfacial IMC Thickness after 400 and 1000 hours of Aging at 185°C and 200°C.....   | 238 |
| Figure 10-17: R2512 – (Ni,Cu) <sub>3</sub> Sn <sub>4</sub> Component Side Interfacial IMC Thickness after 400 and 1000 hours of Aging at 185°C and 200°C .....  | 238 |
| Figure 10-18: Interfacial IMC Thickness Measurement after Reflow of QFN44 Cu <sub>6</sub> Sn <sub>5</sub> IMC on Component Side, QFN32 Cu <sub>6</sub> Sn <sub>5</sub> IMC on Component Side, R2512 (Ni,Cu) <sub>3</sub> Sn <sub>4</sub> IMC on Board Side, R2512 (Ni,Cu) <sub>3</sub> Sn <sub>4</sub> IMC on Component Side..... | 242 |
| Figure 10-19: SAC305 Solder Failure during Mechanical Shock Test (a) QFN44 – 1000 hours/200°C Aging (b) Additional QFN44 - 1000 hours/200°C Aging (c) R2512 - 1000 hours/200°C Aging (d) Magnified view of R2512 Crack.....   | 245 |
| Figure 10-20: SAC305+0.05%Mn Solder Failure during Mechanical Shock Test (a) QFN44 – 1000 hours/200°C Aging (b) Additional QFN44 - 1000 hours/200°C Aging (c) R2512 - 1000 hours/200°C Aging (d) Magnified view of R2512 Crack.....   | 247 |
| Figure 10-21: SAC305+0.17%Mn Solder Failure during Mechanical Shock Test (a) QFN44 – 1000 hours/200°C Aging (b) Additional QFN44 - 1000 hours/200°C Aging .....   | 248 |
| Figure 10-22: SAC305+0.07%Ce Solder Failure during Mechanical Shock Test (a) QFN44 – 1000 hours/200°C Aging (b) Additional QFN44 - 1000 hours/200°C Aging (c) R2512 - 1000 hours/200°C Aging (d) Magnified view of R2512 Crack.....   | 250 |
| Figure 10-23: SAC305+0.13%Ce Solder Failure during Mechanical Shock Test (a) QFN44 – 1000 hours/200°C Aging (b) Additional QFN44 - 1000 hours/200°C Aging (c) R2512 - 1000 hours/200°C Aging (d) Magnified view of R2512 Crack.....   | 251 |
| Figure 0-1: (a) Stationary thermal test results from 25°C to 85°C; (b) Mean of angular rate data with window size = 100; (c) Thermal cycles from 25°C to 85°C.....  | 256 |
| Figure 0-2: (a) Stationary thermal test results from 25°C to 125°C; (b) Mean of angular rate data with window size = 100; (c) Thermal cycles from 25°C to 125°C.....  | 256 |
| Figure 0-3: (a) Stationary thermal test results from 25°C to 150°C; (b) Mean of angular rate data with window size = 100; (c) Thermal cycles from 25°C to 150°C.....  | 257 |
| Figure 0-4: (a) Stationary thermal test results from 25°C to 175°C; (b) Mean of angular rate data with window size = 100; (c) Thermal cycles from 25°C to 175°C.....  | 258 |
| Figure 0-5: (a) Rotary thermal test results from 25°C to 85°C; (b) Mean of angular rate data with window size = 100; (c) Thermal cycles from 25°C to 85°C.....  | 258 |
| Figure 0-6: (a) Rotary thermal test results from 25°C to 125°C; (b) Mean of angular rate data with window size = 100; (c) Thermal cycles from 25°C to 125°C.....  | 259 |
| Figure 0-7: (a) Rotary thermal test results from 25°C to 150°C; (b) Mean of angular rate data with window size = 100; (c) Thermal cycles from 25°C to 150°C.....  | 259 |
| Figure 0-8: (a) Rotary thermal test results from 25°C to 175°C; (b) Mean of angular rate data with window size = 100; (c) Thermal cycles from 25°C to 175°C.....  | 260 |
| Figure 0-9: (a) Stationary thermal test results from 25°C to 85°C; (b) Mean of angular rate data with window size = 100; (c) Thermal cycles from 25°C to 85°C.....  | 260 |
| Figure 0-10: (a) Stationary thermal test results from 25°C to 125°C; (b) Mean of angular rate data with window size = 100; (c) Thermal cycles from 25°C to 125°C.....   | 261 |
| Figure 0-11: (a) Stationary thermal test results from 25°C to 150°C; (b) Mean of angular rate data with window size = 100; (c) Thermal cycles from 25°C to 150°C.....   | 261 |



|   |     |
|---|-----|
| Figure 0-12: (a) Stationary thermal test results from 25°C to 175°C; (b) Mean of angular rate data with window size = 100; (c) Thermal cycles from 25°C to 175°C. | 262 |
| Figure 0-13: (a) Rotary thermal test results from 25°C to 85°C; (b) Mean of angular rate data with window size = 100; (c) Thermal cycles from 25°C to 85°C.       | 262 |
| Figure 0-14: (a) Rotary thermal test results from 25°C to 125°C; (b) Mean of angular rate data with window size = 100; (c) Thermal cycles from 25°C to 125°C.     | 263 |
| Figure 0-15: (a) Rotary thermal test results from 25°C to 150°C; (b) Mean of angular rate data with window size = 100; (c) Thermal cycles from 25°C to 150°C.     | 263 |
| Figure 0-16: (a) Rotary thermal test results from 25°C to 175°C; (b) Mean of angular rate data with window size = 100; (c) Thermal cycles from 25°C to 175°C.     | 264 |
| Figure 0-1: QFN32 - SAC305 Solder Joint (a) After Reflow, (b) After 100 hours/185°C Aging, (c) After 1000 hours/185°C Aging                                       | 265 |
| Figure 0-2: QFN32 - SAC305+0.05%Mn Solder Joint (a) After Reflow, (b) After 100 hours/185°C Aging, (c) After 1000 hours/185°C Aging                               | 266 |
| Figure 0-3: QFN32 - SAC305+0.17%Mn Solder Joint (a) After Reflow, (b) After 100 hours/185°C Aging, (c) After 1000 hours/185°C Aging                               | 267 |
| Figure 0-4: QFN32 - SAC305+0.07%Ce Solder Joint (a) After Reflow, (b) After 100 hours/185°C Aging, (c) After 1000 hours/185°C Aging                               | 268 |
| Figure 0-5: QFN32 - SAC305+0.13%Ce Solder Joint (a) After Reflow, (b) After 100 hours/185°C Aging, (c) After 1000 hours/185°C Aging                               | 269 |
| Figure 0-6: QFN32 - SAC305 Solder Joint (a) After Reflow, (b) After 100 hours/200°C Aging, (c) After 1000 hours/200°C Aging                                       | 270 |
| Figure 0-7: QFN32 - SAC305+0.05%Mn Solder Joint (a) After Reflow, (b) After 100 hours/200°C Aging, (c) After 1000 hours/200°C Aging                               | 271 |
| Figure 0-8: QFN32 - SAC305+0.17%Mn Solder Joint (a) After Reflow, (b) After 100 hours/200°C Aging, (c) After 1000 hours/200°C Aging                               | 272 |
| Figure 0-9: QFN32 - SAC305+0.07%Ce Solder Joint (a) After Reflow, (b) After 100 hours/200°C Aging, (c) After 1000 hours/200°C Aging                               | 273 |
| Figure 0-10: QFN32 - SAC305+0.13%Ce Solder Joint (a) After Reflow, (b) After 100 hours/200°C Aging, (c) After 1000 hours/200°C Aging                              | 274 |

# **1. Introduction**

MEMS (Microelectromechanical System) inertial sensors, like the accelerometer and the gyroscope, have gained much attention in the past few years. MEMS accelerometers alone possess the second-largest sales volume after MEMS pressure sensors [1]. Recently, the MEMS gyroscope also became popular after the success of the MEMS accelerometer.

The MEMS gyroscope is a sensor that measures the rate of change of an angular position. There are some similarities and differences between MEMS vibratory gyroscopes and MEMS accelerometers. In the majority of the cases, both devices use suspended proof mass to measure the physical quantity, like, linear acceleration in the case of an accelerometer, or Coriolis acceleration, which is proportional to an angular velocity, in the case of a MEMS gyroscope. The MEMS accelerometer has a suspended proof mass that moves only in the presence of change in external linear acceleration. In contrast, the MEMS gyroscope has a proof mass that starts vibrating at its resonance in the drive direction when connected to the power supply, and the proof mass moves in the sense direction only during angular rotation.

## **1.1. Advantages and Applications of MEMS Vibratory Gyroscope**

There are different varieties of gyroscopes with different designs and working principles that can be broadly classified into three different categories: spinning mass gyroscopes, optical gyroscopes and vibratory gyroscopes [2]. Out of these gyroscopes, vibratory gyroscopes, which use vibrating elements to sense the angular rotation, have gained much attention.

The reason behind the success of the MEMS vibratory gyroscope compared to other gyroscopes is that no rotating parts are involved that require bearing, which increases device reliability. In addition, when compared to macro-scale gyroscopes, MEMS vibrating gyroscopes also possess other benefits such as reduction in their significant size, weight and cost. With advances in fabrication technologies lowering their cost, MEMS gyroscope sensors are being used in an ever wider variety of applications such as automotive, consumer electronics, Industries, avionics/military etc.

The automotive applications are vehicle stability control, rollover detection, load leveling/suspension control, anti-lock brake and collision avoidances system. A consumer electronic market is the largest consumer of the rate grade MEMS gyroscope for applications like image stabilization in cellphones and video cameras, computer input devices, handheld computing devices, game controllers, virtual reality gear, sports equipment, and robots. Industrial applications include motion control of hydraulic equipment or robots, platform stabilization of heavy machinery, and yaw rate control of wind-power plants. Finally, avionics/military uses precise MEMS gyroscopes for applications like missile guidance, platform stabilization of avionics, stabilization of pointing systems for antennas, and unmanned air vehicles or land vehicles.

One of the recent applications of the MEMS gyroscope is for navigation and tracking where high sensitivity and performance stability are key requirements. The navigation system based on inertial sensors has shown many advantages when compared to commonly used GPS technology. Such examples include locating an object near or inside a building, underground, or in dense urban areas where GPS does not work

effectively. Because of the high noise levels generated by GPS signals in such conditions resulting from single attenuation and reflection, the navigation and tracking system based on inertial sensors is a good alternative. In the majority of cases, an inertial navigation unit (INU) consists of an accelerometer, a gyroscope and a compass. The linear and angular positions are determined by integrating the respective accelerations from accelerometer and gyroscope. Due to this integration process, any errors in the sensor measurement are accumulated with time which degrades the performance of the inertial navigation system. If these errors are not compensated, then the accelerometer and gyroscope introduce an error in the navigation proportional to the square and cube of the elapsed time, respectively.

## **1.2. Research Motivation**

The low cost of MEMS gyroscopes has resulted in their use in many applications where environmental conditions exist from mild to harsh. These severe environments include high mechanical shock, high frequency vibration, high frequency acoustic environment, high temperature etc. Despite their widespread use, the performance of the MEMS vibratory gyroscope in harsh environments is still under question.

While some studies have been conducted to understand the effects of high mechanical shock [3]–[6], high-frequency vibration [7],[8], and high-frequency acoustic environment [9]–[11], the effects of elevated temperatures especially temperatures that are beyond manufacturer’s recommended temperature range have not been well researched.

Performance stability and long-term reliability are the greatest challenges for commercialization of MEMS gyroscopes. Their vast uses in different applications require them to function from medium to harsh environments, making their performance more dependent on environmental conditions. Therefore, it is necessary to examine the performance and long-term reliability of MEMS gyroscope.

Due to the high demand of MEMS gyroscopes in consumer electronics, a majority of available commercial-off-the-shelf (COTS) gyroscopes have limited operating temperature ranges from  $-40^{\circ}\text{C}$  to  $+85^{\circ}\text{C}$  [12]–[15]. In many applications like automotive, deep-water energy exploration, down-hole drilling tool navigation, high-temperature industrial applications etc., the MEMS gyroscope sensor experiences temperatures that are beyond the manufacturer's recommended temperature range.

Most of the reported gyroscopes are fabricated from silicon or poly-silicon material, whose material properties are temperature dependent. Variations in temperature of the MEMS structure affects the dynamic system parameters due to temperature-dependent Young's modulus, temperature-dependent damping coefficient and thermally induced localized stresses. MEMS vibrating gyroscope measures an angular velocity via comb structure displacement measurement, which can be on the order of micrometers to nanometers. High sensitivity to small changes in displacement causes the MEMS gyroscope sensor to be affected if any of the system parameters change at elevated temperature conditions. Thus, examining the effects of elevated temperatures on the MEMS gyroscope performance is very critical.

### **1.3.Previous Work on Examination of Temperature Effects on the MEMS Gyroscope and Its Reliability Concern**

MEMS gyroscope research has substantially increased over the last couple of years. It is believed that this research growth was due to advancement in MEMS fabrication technology that has allowed MEMS manufacturers to come up with various unique designs. Many companies have emerged and entered the market to deliver low-cost gyroscopes. With continuous design evolution of the MEMS gyroscope to improve its sensitivity and performance, the efforts on examining performance and long-term reliability of the MEMS gyroscope in high temperature environments has not been explored.

One of the earliest studies to understand temperature effects on the MEMS gyroscope was performed by researchers at the JPL (Jet Propulsion Lab). Shcheglov et al. [16] and Ferguson et al. [17] at the JPL found that the resonance frequency of the MEMS gyroscope linearly decreases with increases in temperature. Ferguson et al. [17] also found that no hysteresis exists in both resonance frequency and Q factor when the gyroscope was subjected from 35°C to 65°C at stationary conditions. Because of the limited temperature range (35°C to 65°C) examined at a stationary condition in the literature [17], this study recommended exploring the performance of the MEMS gyroscope over a wider temperature range and also under rotary conditions.

Other studies also observed similar linear dependency of resonance frequency with temperature [18][19][20][21][22]. Table 1-1 shows the summary of previous studies conducted to examine temperature effects on the MEMS gyroscope.

Table 1-1: Summary of Previous Work on Various Temperature Ranges Examined by Researchers.

| Authors           | Year | Temp Range    | Authors         | Year | Temp Range    |
|-------------------|------|---------------|-----------------|------|---------------|
| Zhang et al. [18] | 2009 | -20°C to 20°C | Xia et al. [19] | 2009 | -40°C to 60°C |
| Zhu et al. [23]   | 2009 | -20°C to 60°C | Liu et al. [20] | 2008 | -40°C to 40°C |
| Wu et al. [24]    | 2008 | -30°C to 70°C | Hou et al.[21]  | 2011 | 30°C to 60°C  |
| Hou et al. [22]   | 2011 | -40°C to 60°C | Feng et al.[25] | 2011 | -35°C to 55°C |

Some of the studies shown in Table 1-1 also explored the temperature compensation method. In general, it is clear from Table 1-1 that all previous studies examined temperature effect on the MEMS gyroscope with a limited range from -40°C to 70°C. Thus, there is a need to examine the effects of elevated temperature on the performance of the MEMS gyroscope.

Studies shown in Table 1-1 confirm that temperature is the dominant source of error in the MEMS gyroscope. Temperature affects the performance of the MEMS gyroscope by various factors. These factors include Young’s modulus, damping coefficient, thermal expansion and coefficient of thermal expansion (CTE) mismatch.

**Young’s modulus:**

Temperature influences the Young’s modulus of the material that changes beam stiffness and deviates resonance frequencies of MEMS gyroscope [18], [20], [22].

**Damping coefficient:**

Air damping is the dominant energy loss mechanism in MEMS resonators when operated close to atmosphere pressure [26]. Feng et.al [27] experimentally calculated

the Q-factor of the MEMS gyroscope from 238K to 328K. They found that the Q-factor decreases with increase in temperature from 238K to 328K.

**Thermal expansion:**

Temperature causes expansion of the beams that may change capacitance between two comb fingers by altering space between them.

**CTE mismatch:**

The CTE mismatch between silicon and glass substrate produces thermal stress in the MEMS gyroscope that leads to change in resonance frequency [22]. In addition, the CTE mismatch between MEMS package and board also causes thermally induced package stress that compromises the MEMS gyroscope reliability.

In order to analyze the effect of above temperature-dependent factors on the MEMS gyroscope, analytical and numerical methods were developed to simulate the behavior of the MEMS gyroscope either at room temperature or at elevated temperatures [29–32].

Some of these methods that simulate the temperature effects on the MEMS gyroscope have considered only one temperature-dependent variable [18],[31]. For example, the temperature simulation model developed in literature [32] only considered change in Young's modulus due to temperature variation.

Other methods utilized complex numerical techniques [28],[30] and these methods are not experimentally validated [20]. For example, Liu et al. [20] conducted thermal numerical simulation that showed that temperature fluctuation from -40°C to +40°C causes slight deviation in gyroscope output due to Young's modulus and thermal



deformation. The developed simulation model was not validated with experimental results.

From the current literature, it is clear that there is a need to identify the dominating temperature-dependent factors responsible to performance change of the MEMS gyroscope under temperature variation. In addition, there is a need to develop an experimentally validated simulation model that can consider more than one temperature-dependent variable in order to accurately simulate the temperature effects on MEMS gyroscope.

Reliability of the MEMS gyroscope is governed by many factors. In general, the MEMS package has a significant impact on its long-term reliability [32]. A dominant reliability issue in MEMS devices is the package induced stress. This package induced stress can affect many sub-components of the MEMS gyroscope system including proof mass, substrate, solder interconnects, package lead etc. Any failure in these sub-components will lead to failure of the MEMS gyroscope device. Thus, it is necessary to examine the long-term reliability of weak sub-component to improve the reliability of the MEMS gyroscope device.

In general, MEMS gyroscopes are fabricated from silicon material that exhibits no plastic deformation or creep below 500°C. Silicon also possesses good fatigue properties and, thus, it can last millions of cycles without failure. Due to such excellent mechanical properties of silicon, proof mass and substrate of the MEMS gyroscope can survive much longer than other sub-components of the MEMS gyroscope such as solder interconnects, package lead etc.

The literature shows that solder joints are one of the weakest sub-components of the MEMS gyroscope system. Yeh et al. [33] and Lu et al. [33], [34] conducted finite element thermal fatigue analysis of the MEMS gyroscope, which revealed that the maximum equivalent plastic strain was observed in the outer corner solder ball that resulted in solder interconnect failure when thermally cycled from -40°C to 125°C. In addition, Cui et al. [35] also found that solder joints in the MEMS gyroscope are the weakest points that can fracture and fail easily, and thus influence the reliability of the MEMS gyroscope under high-G load conditions.

The above cited literature confirms that solder interconnects of a MEMS gyroscope are the weakest sub-components of the MEMS gyroscope system. Thus, examining and enhancing the reliability of solder interconnects is necessary to improve the long-term reliability of the MEMS gyroscope system.

Many SnAgCu based commercial solders are available in the market. Some of the commonly used SnAgCu based solders include SAC105 (98.5%Sn1%Ag0.5%Cu), SAC205 (97.5%Sn2%Ag0.5%Cu), SAC305 (96.5%Sn3%Ag0.5%Cu), SAC405 (95.5%Sn4%Ag0.5%Cu), Sn3.5Ag (96.5%Sn3.5%Ag), Sn0.7Cu (99.3%Sn0.7%Cu) etc. SnAgCu containing high levels of Ag (viz. SAC305 and SAC405), are known to exhibit inferior resistance to mechanical loads like shock/drop and vibration. Thus, SAC105 solder, that contains only 1% of Ag, is recommended for better mechanical fatigue resistance. However, reduction in Ag content also reduces creep resistance of solder which compromises its thermal fatigue reliability, as SAC405 solder exhibits far better thermal fatigue reliability than SAC105 solder. Because of these two extremes, SAC305 solder that contains 3% Ag is considered to be an optimum and

thus became the industry standard in applications where both thermal and mechanical fatigue resistance are necessary.

Though SAC305 solder is an optimum choice for combined thermal fatigue and mechanical shock/drop loading environments, the thermal fatigue resistance of SAC305 is better than its resistance to mechanical loads, which limit its performance in harsh environment applications.

Recently, it has been found that the drop/shock reliability of SnAgCu solder can be improved by addition of small amount of fourth element (dopant). Some of these dopants have the ability to suppress the growth of interfacial intermetallic compound (IMC) during isothermal aging. This approach has shown very promising results on SAC105, a low Ag solder; however, the effect of dopant on SAC305 to improve its drop/shock reliability has not been well examined, especially after exposure to high temperatures.

#### **1.4. Research Objectives**

The research objectives of this dissertation are as follows:

- Examination of the effects of elevated temperature on the performance of the MEMS gyroscope and identify the temperature-dependent factors that dominate in a high temperature environment.
  - Quantify the MEMS gyroscope performance over a wider temperature range

- Development of a simulation model to identify the dominating-temperature dependent factors in a high temperature environment and correlate simulation results with experimental results
- Assessment of dopants that minimize the growth of interfacial IMCs in SAC305 solder to improve mechanical drop/shock reliability under high temperature environments.
  - Identification and selection of dopants based on thorough literature search
  - Assessment of interfacial IMC growth under high temperature isothermal aging on selected SAC305 and SAC305-X solders
  - Assessment of shock reliability of SAC305 and SAC305-X solders before and after high temperature isothermal aging
  - Correlation between interfacial IMC growth and shock reliability degradation of SAC305 and SAC305-X solders

## **1.5. Dissertation Outline**

Chapter 1 provides the introduction, background and motivation for the research presented in this dissertation. Chapter 2 presents the test matrix and discusses effects of elevated temperature on the performance of the MEMS gyroscope. In chapter 3, an analytical model is developed to simulate temperature effect on the MEMS gyroscope. Simulation and experimental results are compared to determine the dominant temperature-dependent factor(s) responsible for temperature-dependent bias observed at elevated temperatures. Chapter 4 provides motivation and literature

search on the high temperature reliability of solders. Chapter 5 discusses various experimental selections including solders, components and PCB material for examining shock durability of SAC305 and SAC305+X solders. The design of experiment, test equipment and monitoring systems for solder testing is summarized in chapter 6. The result of microstructural examination and mechanical properties evaluation of selected solders are presented in chapter 7. Interfacial intermetallic growth during isothermal aging at 185°C and 200°C on QFNs and R2512 package types are presented in chapter 8 and chapter 9, respectively. Chapter 10 shows detailed mechanical shock reliability results of SAC305 and SAC305+X solder performed on as-reflowed and thermally aged at 185°C and 200°C. Finally, chapter 11 summarizes the research contribution resulting from this dissertation.

## **2. Effects of Elevated Temperatures on the Performance of the MEMS Vibratory Gyroscope**

### **2.1. Introduction**

In this chapter, we discuss the development of a test protocol to assess the effects of elevated temperatures on the performance of a MEMS gyroscope. Due to the high demand for MEMS gyroscopes in consumer electronics, commercially available off-the-shelf MEMS gyroscopes have limited operating temperature ranges from  $-40^{\circ}\text{C}$  to  $+85^{\circ}\text{C}$ . However, due to the interest in examining the effects of elevated temperatures on MEMS gyroscopes, wider temperature ranges specifically beyond the manufacturer's recommended temperature range, were selected for the assessment.

The MEMS gyroscope used in this study is a programmable low-power single-axis digital gyroscope (ADIS16255) procured from Analog Devices Inc. This commercial-off-the-shelf (COTS) gyroscope comes in a laminate-based land grid array (LGA) package with  $11\text{ mm} \times 11\text{ mm} \times 5.5\text{ mm}$  dimensions. A schematic of ADIS16255 package is shown in Figure 2-1. This gyroscope features an integrated temperature sensor that detects the temperature of the die during operation, and on-chip signal processing that calibrates and compensates angular velocity measurement output within the temperature range of  $-40^{\circ}\text{C}$  to  $+85^{\circ}\text{C}$ . The manufacturer's specified operating temperature range for ADIS16255 was from  $-40^{\circ}\text{C}$  to  $+85^{\circ}\text{C}$ . An evaluation board (ADISUSBZ) designed by Analog Devices Inc. was used for recording the output from ADIS16255. The output of the MEMS gyroscope includes

angular velocity in degrees/second ( $^{\circ}/s$ ) and MEMS die temperature in degrees Celsius ( $^{\circ}C$ ).

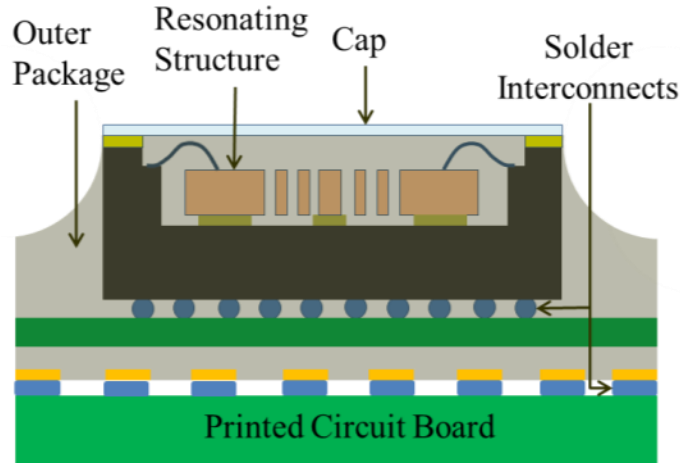


Figure 2-1: Schematic of MEMS Gyroscope Package

## 2.2. Experimental Set-up and Test Procedure

An experimental test procedure was developed to examine the effects of elevated temperatures on a MEMS gyroscope at stationary and rotary conditions. Since the selected MEMS gyroscope indicates nearly zero  $^{\circ}/s$  angular velocity output at a stationary condition, it was necessary to subject the MEMS gyroscope to rotary conditions to collect non-zero angular velocity output. During the rotary test, the MEMS gyroscope was subjected to a  $60^{\circ}/s$  or 10 revolutions per second (rpm) angular rotation by placing it on the center of a homemade precise turntable. The turntable was fabricated using precise motor assuring 0.65 arc-sec positioning resolution. It can maintain precise angular rotation up to  $\pm 500$  rpm.

During the experiment at stationary and rotary conditions, the performance of the MEMS gyroscope was analyzed at ambient and elevated temperatures. The measurement of the MEMS gyroscope at ambient temperature established the

baseline. The baseline tests at stationary and rotary conditions are referred to as a stationary baseline test (SBT) and rotary baseline test (RBT), respectively. For elevated temperature/thermal test, the MEMS gyroscope was subjected to four temperature ranges from 25°C to 85°C, from 25°C to 125°C, from 25°C to 150°C, and from 25°C to 175°C. Such thermal tests performed at stationary and rotary conditions are referred to as a stationary thermal test (STT) and rotary thermal test (RTT), respectively. The reason for selecting these temperature ranges was to cover wider elevated temperature conditions to examine a MEMS gyroscope's performance within and beyond manufacturer's recommended temperature limits. Since the selected MEMS gyroscope was only recommended to operate up to high temperature of +85°C, any temperature beyond +85°C may affect the performance of the MEMS gyroscope and also cause permanent damage. In order to evaluate the maximum temperature limit and check if the short-term exposure to the MEMS gyroscope at elevated temperature ranges caused any permanent damage, it was decided to subject the MEMS gyroscope to five thermal cycles at each selected temperature range. It was also necessary to observe the MEMS gyroscope's performance before and after five thermal cycles to record any permanent shift in the MEMS gyroscope's output. Thus, for both stationary and rotary conditions, a baseline test was conducted first, followed by five thermal cycles test. The primary purpose of conducting the baseline test was to observe the sensor characteristics before temperature cycling to allow for later comparison. These baseline tests were performed at room temperature conditions. An overview of the experimental approach is shown in Figure 2-2. A total of nine individual single-axis MEMS gyroscope sensors were analyzed in this test.



The objective of this experimental exercise was to examine the performance bias caused by the elevated temperature exposure, which is stated here as a temperature-dependent bias. Performance bias refers to the level of the output signal of the MEMS gyroscope that is not related to the input quantity sensed by the gyroscope sensor, such as when a MEMS gyroscope produces non-zero angular velocity output at a stationary condition.

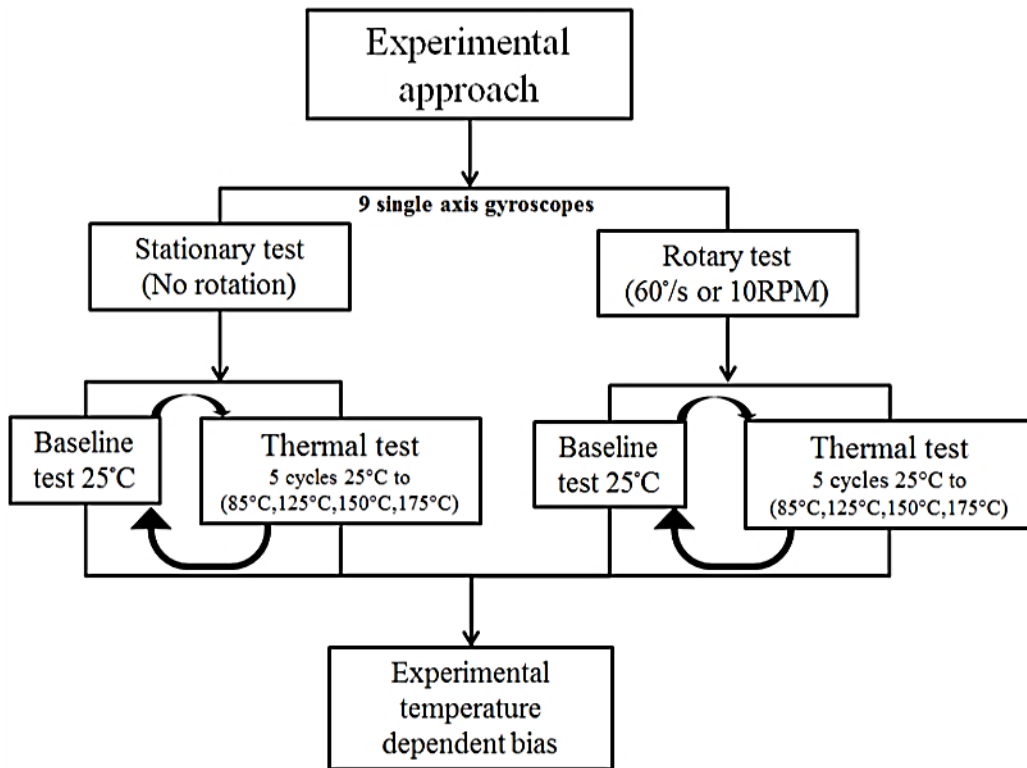


Figure 2-2: Experimental Approach for MEMS Gyroscope Performance Characterization at High Temperature

### 2.2.1. Stationary Test

As the name suggests, a stationary test was performed at the stationary condition. The MEMS gyroscope was mounted on a stationary table and its performance was evaluated at room and elevated temperatures by conducting stationary baseline and

stationary thermal tests, respectively. The detailed test sequence for the stationary test is shown in Figure 2-3.

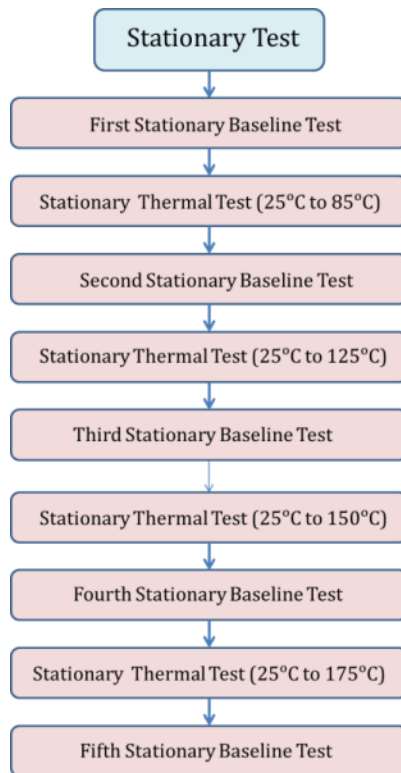


Figure 2-3: Stationary Test Sequence for Evaluating Effects of Elevated Temperatures on the MEMS Gyroscope.

The MEMS gyroscope sensor was securely attached to the stationary table using high temperature tape. The evaluation board and ADIS16255\_Eval\_Rev\_1 software were used for collecting the output from the MEMS gyroscope. A palmtop was also used for data storage purposes. The test setup for the stationary baseline tests is shown in Figure 2-4. One end of the evaluation board was connected to the MEMS gyroscope whereas the other end was connected to the USB port of a palmtop.

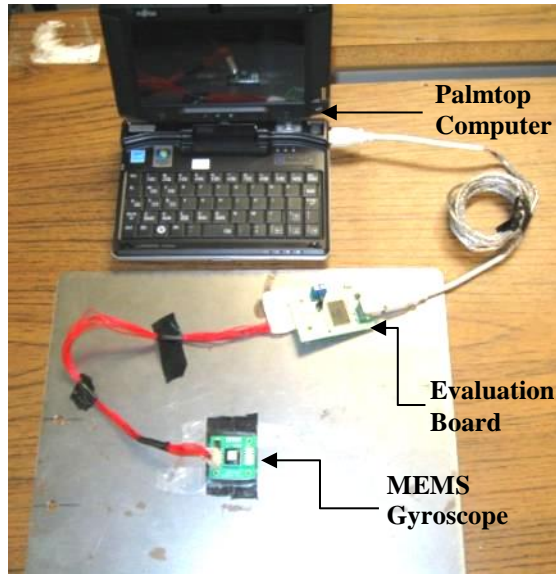


Figure 2-4: Stationary Baseline Test Setup.

Initially, the first stationary baseline test was performed at room temperature to establish a baseline condition for the MEMS gyroscope. The first stationary baseline test was conducted until 10,000 data points were acquired. After analyzing the MEMS gyroscope output signals from the first stationary baseline test, it was subjected to five thermal cycles from 25°C to 85°C. In order to achieve thermal cycling conditions, a Temptronic Thermostream air system was used. This apparatus has the capability to supply a constant temperature air stream at a wide temperature range from -75°C to 225°C. The gyroscope was placed under and at the center of the glass hood of the Temptronic Thermostream apparatus such that it was directly exposed to hot air flowing from the nozzle at 5 standard cubic feet per minute (SCFM). The test set-up for stationary thermal test is shown in Figure 2-5.

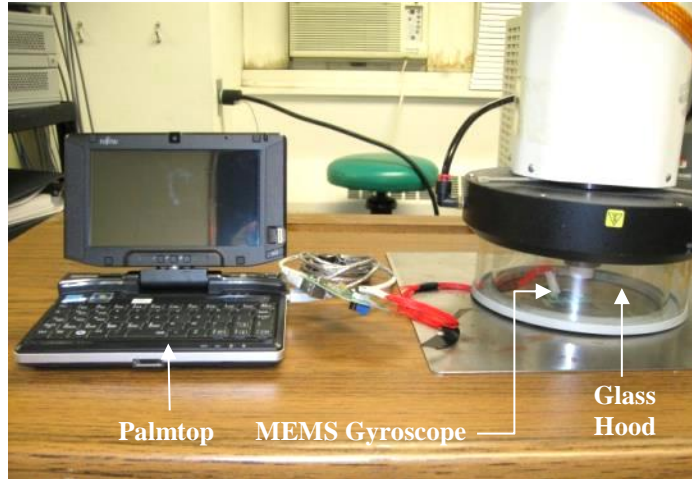


Figure 2-5: Stationary Thermal Test Setup.

After completing five thermal cycles from 25°C to 85°C, the MEMS gyroscope was subjected to a second stationary baseline test to check if the MEMS gyroscope experienced any permanent shift in its output due to exposure to the five thermal cycles from 25°C to 85°C. This test sequence was repeated to complete remaining baseline and thermal tests at stationary conditions, as shown previously in Figure 2-3.

### **2.2.2. Rotary Test**

A rotary test was performed by subjecting the MEMS gyroscope to a constant angular rotation of 60°/s or 10 revolutions per minute (rpm) using a precise turntable. The MEMS gyroscope was mounted on the center of a turntable, and its performance was evaluated at room and elevated temperatures by conducting rotary baseline and rotary thermal tests, respectively. The test sequence of RBT and RTT for the rotary test is shown in Figure 2-6.

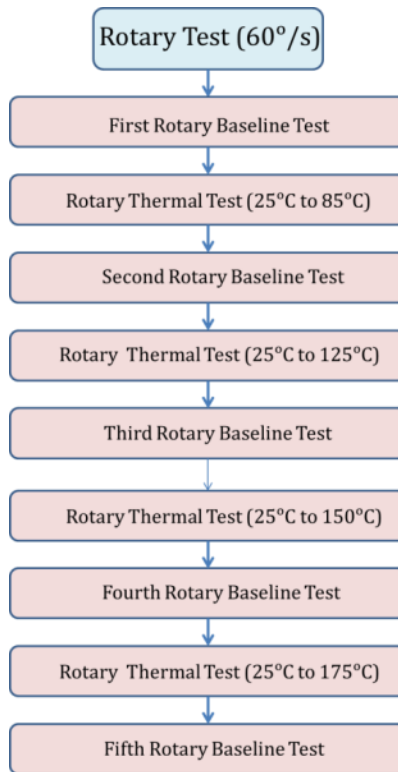


Figure 2-6: Rotary Test Sequence for Evaluating Elevated Temperature Effect on the Performance of MEMS Gyroscope.

For RBT and RTT, the MEMS gyroscope was securely attached to the center of a turntable using high temperature tape. The evaluation board and ADIS16255\_Eval\_Rev\_1 software were used to collect the output from the MEMS gyroscope. The palmtop was mounted onto the turntable using a vertical brace. Care was exercised in placing and mounting the palmtop to avoid vibration during turntable rotation.

The test setup for the rotary baseline test is shown in Figure 2-7. Initially, the first rotary baseline test was performed by subjecting the MEMS gyroscope to 60°/s rotational velocity at room temperature. The test was conducted until 10,000 data points were acquired.

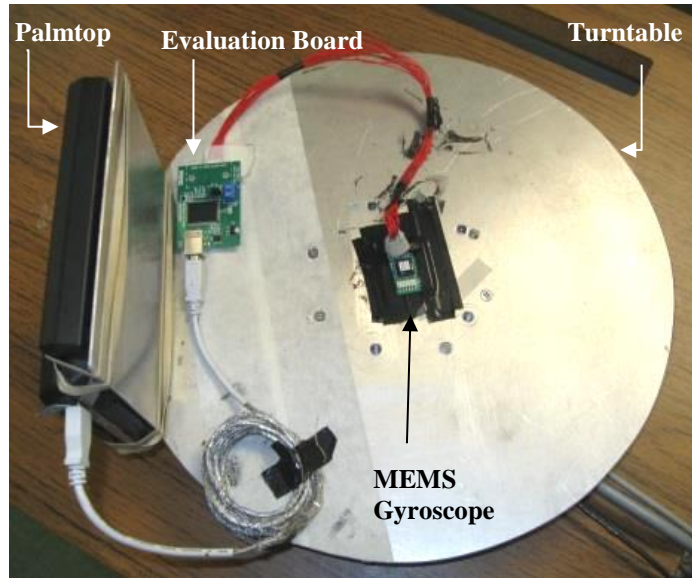


Figure 2-7: Rotary Baseline Test Setup.

After analyzing the MEMS gyroscope output signals from the first rotary baseline test, the MEMS gyroscope was subjected to five thermal cycles from 25°C to 85°C at 60°/s rotational velocity. For the rotary thermal test, the entire rotating platform was placed under the glass hood of the Temptronic Thermostream apparatus such that the gyroscope faced hot air directly flowing from the nozzle at 5 SCFM. This arrangement for the rotary thermal test is shown in Figure 2-8.

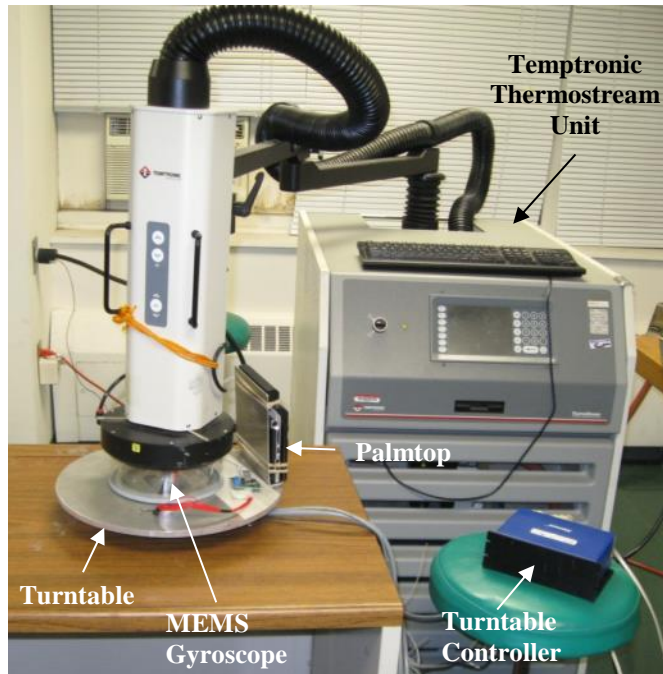


Figure 2-8: Rotary Thermal Test Setup.

After completing rotary thermal cycles from 25°C to 85°C, the MEMS gyroscope along with a rotary table was brought to ambient conditions and a second rotary baseline test was conducted in room temperature condition at 60°/s rotational velocity. This test sequence was repeated to complete remaining baseline and thermal tests for rotary test as shown previously in Figure 2-6.

### 2.3. Results and Analysis

In this section, collected MEMS gyroscope results from stationary and rotary tests performed at ambient and elevated temperature conditions are discussed in detail. A total of nine individual MEMS gyroscopes were examined in this study. Since all nine gyroscopes showed similar behavior, for simplicity, the results from the first gyro, Unit-A, are used here to describe the elevated temperature effects on the performance of the MEMS gyroscope. The results of other MEMS gyroscopes are summarized in Appendix-A.

### 2.3.1. Stationary Test Results:

The first stationary baseline test was conducted to observe the gyroscope sensor output at room temperature. The plot in Figure 2-9 shows the gyroscope output for the first 10,000 angular velocity measurements at room temperature conditions.

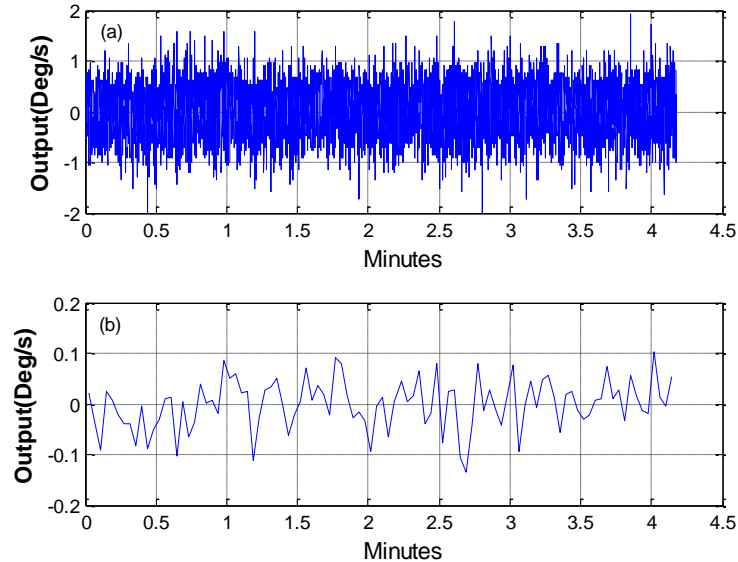


Figure 2-9: First Stationary Baseline Test Result: (a) Raw Angular Rate Data; (b) Filtered Angular Rate Data with Window size = 100. (Mean=0.01°/s, SD=0.44)

Plot-(a) in Figure 2-9 shows the raw data of the angular velocity during the first stationary baseline test. The scattering of data was easily analyzed by grouping (averaging) each set of 100 data points into a single point, which is shown in plot (b) of Figure 2-9. The selection of 100 data points as the “window size,” or the reduced level of resolution, was driven by a tradeoff between noise reduction and loss of signal. The mean and standard deviation of the raw angular rate data for the first stationary baseline test were 0.01°/s and 0.44°/s, respectively.

After the first stationary baseline test, the sensor was then subjected to five thermal cycles from 25°C to 85°C. Figure 2-10 includes three different plots representing raw



angular velocity data (plot-(a)), filtered angular velocity with window size 100 (plot-(b)), and die temperature (plot-(c)).

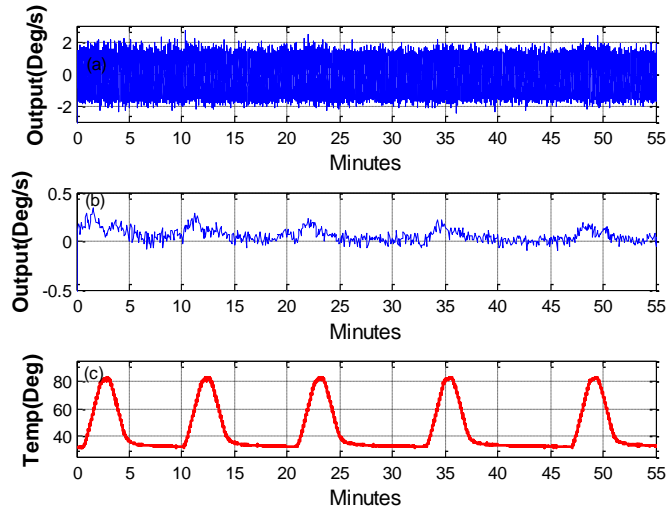


Figure 2-10: Stationary Thermal Test Results from 25°C to 85°C (a) Raw Angular Rate Data; (b) Filtered Angular Rate Data with Window size = 100; (c) Die Temperature.

When the raw angular velocity data (plot-(a)) are compared with die temperature (plot-(c)), the performance variation due to temperature change from 25°C to 85°C is less apparent. However, after filtering the raw angular rate data, the effect of temperature on an increase in bias is visible, as shown in plot-(b). Since the MEMS gyroscope uses internal temperature calibration to compensate for a temperature-dependent bias from -40°C to 85°C, only a small increase in temperature-dependent bias was observed from 25°C to 85°C. The observed temperature dependent bias was within 0.3°/s from 25°C to 85°C, which was agreed well with the manufacturer's suggested temperature bias (bias temperature coefficient = 0.005°/s/°C). This confirms that the MEMS gyroscope performed well within the manufacturer's recommended temperature range.

The slight increase in the temperature dependent bias appears only when the temperature reaches its peak value of 85°C. The noise level returns to its normal level when the temperature returns to room temperature. This observation suggests that there wasn't any permanent shift or degradation in the MEMS gyroscope output as a result of the five thermal cycles from 25°C to 85°C. Thus, the short-term durability of the MEMS gyroscope was preserved during this test.

Next, a second stationary baseline test was conducted to observe the gyroscope output at room temperature. The plot in Figure 2-11 shows the sensor output for the first 10,000 angular velocity measurements at room temperature condition. The mean and standard deviation of the raw data for the secondary stationary baseline test were -0.01°/s and 0.48°/s, respectively. This confirms that there was not any observable shift in the MEMS gyroscope output from the first stationary baseline test.

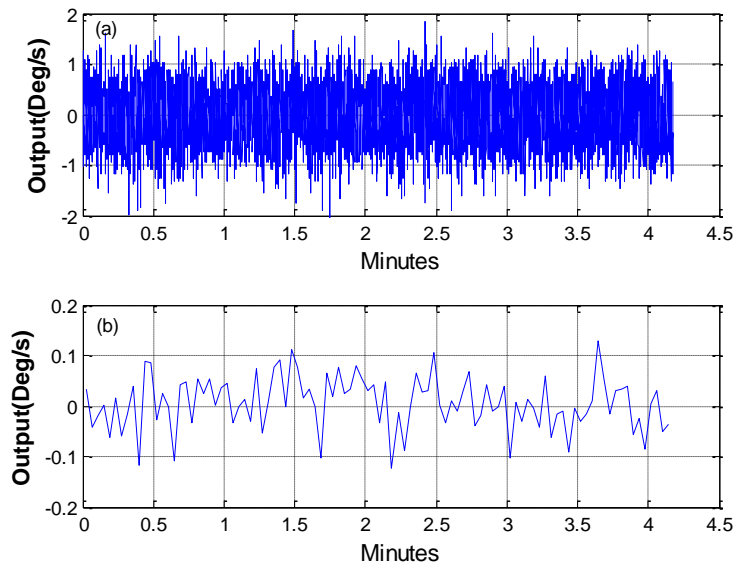


Figure 2-11: Second Stationary Baseline Test Result: (a) Raw Angular Rate Data; (b) Filtered Angular Rate Data with Window size = 100. (Mean= -0.01, STD= 0.48)

After completing the second stationary baseline test, the MEMS gyroscope was subjected to a higher temperature range. The MEMS gyroscope was subjected to five

thermal cycles from 25°C to 125°C. The results of the stationary thermal test from 25°C to 125°C are shown in Figure 2-12.

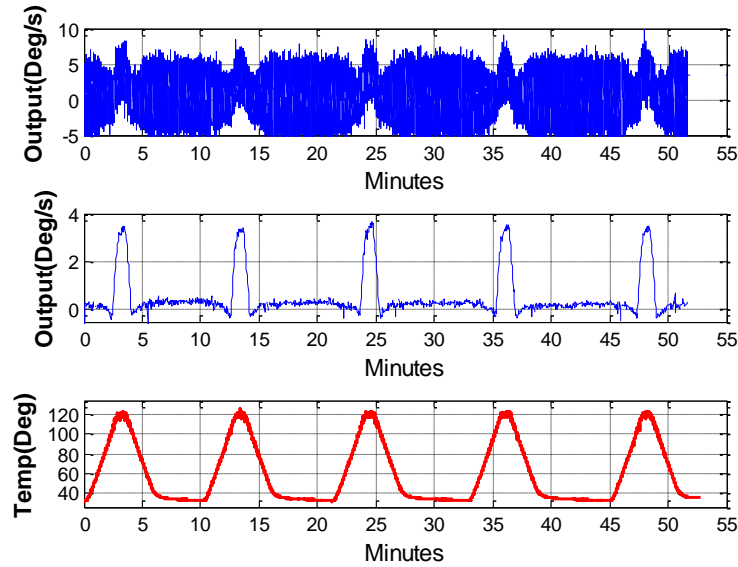


Figure 2-12: Stationary Thermal Test Result from 25°C to 125°C: (a) Raw Angular Rate Data; (b) Filtered Angular Rate Data with Window size = 100; (c) Die Temperature.

Looking at the plot-(a) of Figure 2-12, it can be concluded that the noise level increased with an increase in temperature. After filtering the angular velocity data, an important phenomenon was observed. Plot-(b) shows that a temperature-dependent bias was increased with the increase in temperature. It is essential to notice that there was a sudden change in temperature-dependent bias that occurred when the temperature went above 85°C. This bias was not related to any change in motion since the MEMS gyroscope was at stationary condition during the test. The bias again returned to its normal value when the temperature dropped below 85°C.

It can also be observed that all five thermal cycles resulted in a similar increase in temperature-dependent bias. No evidence of permanent degradation or hysteresis can

be observed. Table 2-1 summarizes the temperature-dependent bias value for each thermal cycle. The average bias turned out to be 3.30°/s.

Table 2-1: Temperature-dependent Bias Value of Five Thermal Cycles from 25°C to 125°C.

| <b>Temperature Cycle</b> | <b>Temperature<br/>Dependent Bias<br/>(°/s)</b> |
|--------------------------|---|
| First cycle              | 3.30  |
| Second cycle             | 3.20  |
| Third cycle              | 3.45  |
| Fourth cycle             | 3.30  |
| Fifth cycle              | 3.25  |
| <b>Average</b>           | <b>3.30</b>                                     |

Similar to Gyroscope Unit-A, the remaining eight gyroscopes also showed similar behavior when subjected from 25°C to 125°C. A summary of the average temperature-dependent bias of all nine gyroscopes from 25°C to 125°C is shown in Table 2-2. The calculated average temperature-dependent bias for all nine gyroscopes is 3.28°/s.

Table 2-2: Average Temperature-dependent Bias of all Nine Gyroscopes from 25°C to 125°C

| <b>Gyroscope</b> | <b>Average<br/>Temperature<br/>Dependent Bias<br/>(°/s)</b> |
|------------------|---|
| Unit – A         | 3.30  |
| Unit – B         | 3.26  |
| Unit – C         | 3.28  |
| Unit – D         | 3.27  |
| Unit – E         | 3.29  |
| Unit – F         | 3.30  |
| Unit – G         | 3.29  |
| Unit – H         | 3.26  |
| Unit – I         | 3.27  |
| <b>Average</b>   | <b>3.28</b>   |

The above results indicate the very interesting behavior of the MEMS gyroscope from 25°C to 125°C. Since all nine MEMS gyroscopes showed a similar increase in temperature-dependent bias from 25°C to 125°C, a temperature compensation algorithm can be developed to compensate for the temperature effects on the MEMS gyroscope up to 125°C. In so doing, the MEMS gyroscope can be used for applications up to a max temperature of 125°C without losing its performance.

After completing the thermal test from 25°C to 125°C, a third stationary baseline test was conducted to observe the gyroscope sensor output. The plot in Figure 2-13 shows the sensor output for the first 10,000 angular velocity measurements at room temperature conditions. The mean and standard deviation of the raw data for the third stationary baseline test were 0.01°/s and 0.45°/s, respectively. This confirms that there was not any observable shift in the MEMS gyroscope output from the first and second stationary baseline tests.

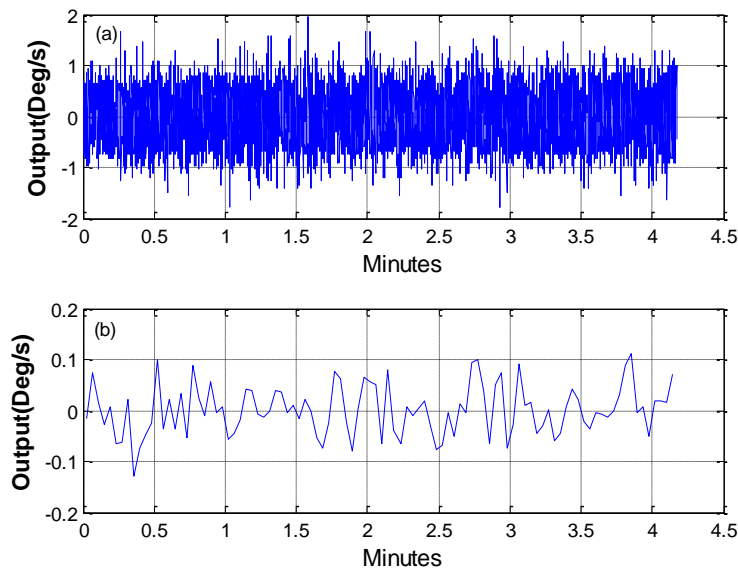


Figure 2-13: Third Stationary Baseline Test Result: (a) Raw Angular Rate Data; (b) Filtered Angular Rate Data with Window size = 100. (Mean= 0.01, STD=0.45)

After completing the third stationary baseline test, the MEMS gyroscope was again subjected to an even higher temperature. This time, the thermal cycle temperature was raised to 25°C to 150°C. The result of the stationary thermal test from 25°C to 150°C is shown in Figure 2-14. Plot-(a) and plot-(b) of Figure 2-14 indicate a significant increase in the temperature-dependent bias from 25°C to 150°C. During the temperature increase, it was observed that the angular velocity output of the MEMS gyroscope initially increased and then started to descend at the peak temperature. Such behavior of the MEMS gyroscope was identical for all five temperature cycles from 25°C to 150°C. It was also noticed that the MEMS gyroscope did not show any kind of permanent shift in its output due to exposure to five thermal cycles with 150°C peak temperature. The output of the MEMS gyroscope again returned to normal value along with a decrease in temperature to room temperature condition.

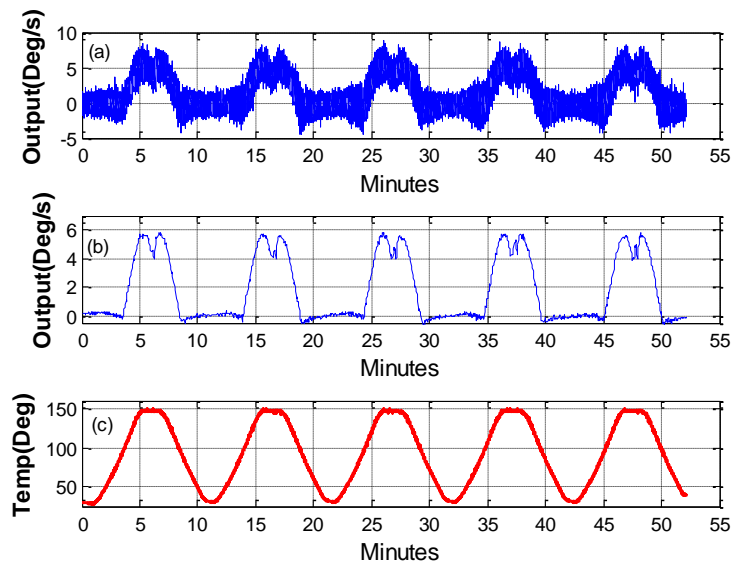


Figure 2-14: Stationary Baseline Test Result from 25°C to 150°C: (a) Raw Angular Rate Data; (b) Filtered Angular Rate Data with Window size = 100; (c) Die Temperature.

After completing the stationary thermal test from 25°C to 150°C, a fourth stationary baseline test was conducted to observe the gyroscope sensor output. The plot in

Figure 2-15 shows sensor output for the first 10,000 angular velocity measurements at room temperature conditions. The mean and standard deviation of raw data for the fourth stationary baseline test were 0.01°/s and 0.46°/s, respectively. This confirms that there was not any observable shift in the MEMS gyroscope output due to short-term elevated temperature exposure from the previous stationary thermal test.

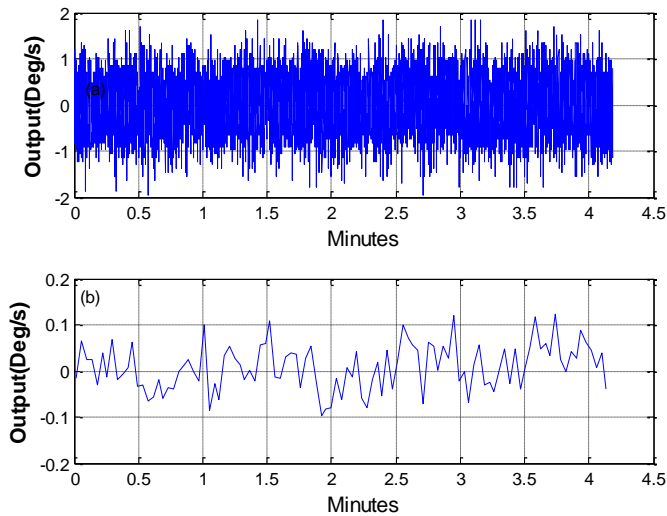


Figure 2-15: Fourth Stationary Baseline Test Result: (a) Raw Angular Rate Data; (b) Filtered Angular Rate Data with Window-size = 100. (Mean=0.01, STD=0.46)

After completing the fourth stationary baseline test, the MEMS gyroscope was again subjected to an even higher temperature from 25°C to 175°C. The results of a stationary thermal test from 25°C to 175°C are shown in Figure 2-16. Here, the effect of a decrease in MEMS gyroscope output at elevated temperature was quite significant. It was also noticed that the MEMS gyroscope did not show any kind of permanent shift in its output due to exposure to five thermal cycles with 150°C peak temperature. The output of the MEMS gyroscope again returned to normal value along with a decrease in temperature to room temperature conditions.

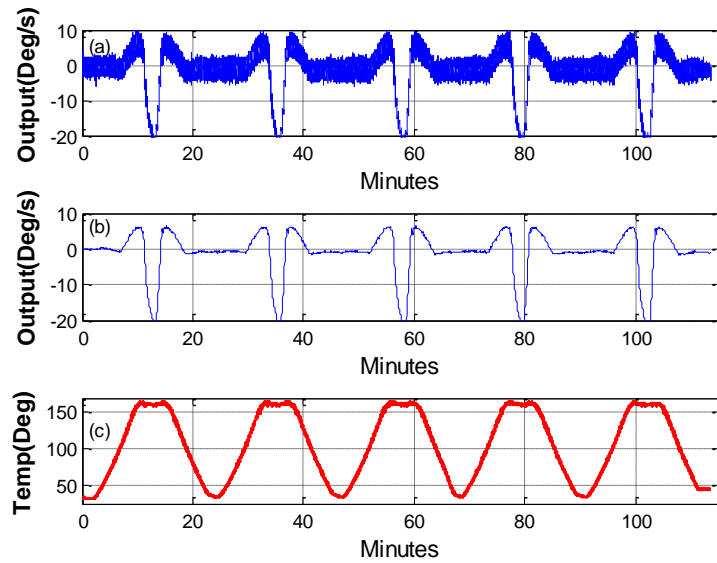


Figure 2-16: Stationary Thermal Test Results from 25°C to 175°C: (a) Raw Angular Rate Data; (b) Filtered Angular Rate Data with Window size = 100; (c) Die Temperature.

After completing the stationary thermal test from 25°C to 175°C, a fifth stationary baseline test was conducted to observe the gyroscope sensor output for any permanent shift that occurred due to the previous stationary thermal test. The plot in Figure 2-17 shows sensor output for the first 10,000 angular velocity measurements at room temperature conditions. The mean and standard deviation of the raw data for the fifth stationary baseline test were 0.01°/s and 0.46°/s, respectively.



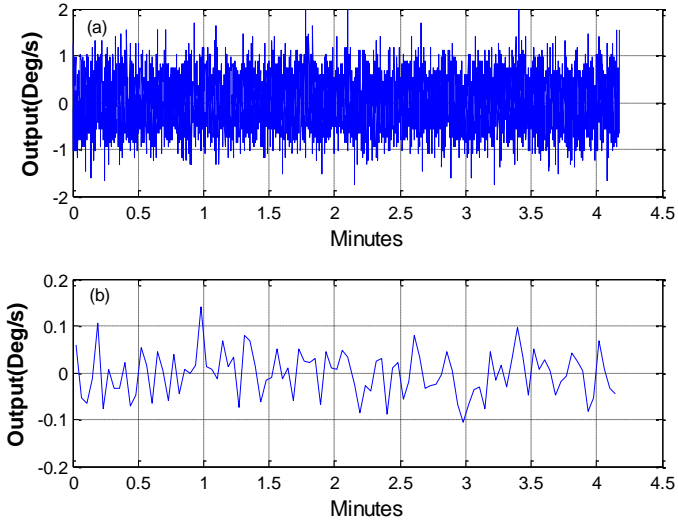


Figure 2-17: Fifth Stationary Baseline Test Result: (a) Raw Angular Rate Data; (b) Filtered Angular Rate Data with Window-size = 100. (Mean= 0.01, STD=0.44)

The mean and standard deviation of all five stationary baseline tests are summarized in Table 2-3. Since there was no significant difference in the mean and standard deviation values among these tests, it can be concluded that the MEMS gyroscope did not show any kind of permanent shift in its output due to short-term thermal cycle exposure during stationary thermal tests.

Table 2-3: Mean and Standard Deviation of Five Stationary Baseline Tests

| No | Tests                           | Mean ( $^{\circ}/s$ ) | Standard Deviation ( $^{\circ}/s$ ) |
|----|---------------------------------|-----------------------|-------------------------------------|
| 1  | First stationary baseline test  | 0.01                  | 0.44                                |
| 2  | Second stationary baseline test | -0.01                 | 0.48                                |
| 3  | Third stationary baseline test  | 0.01                  | 0.45                                |
| 4  | Fourth stationary baseline test | 0.01                  | 0.46                                |
| 5  | Fifth stationary baseline test  | 0.01                  | 0.45                                |

### 2.3.2. Rotary Test Results:

The baseline and thermal tests conducted for rotary test were identical to the baseline and thermal tests conducted for the stationary test, except that the MEMS gyroscope

was subjected to a 60°/s angular rotation using a precise turntable. In real applications, a MEMS gyroscope is always subjected to non-stationary condition. Thus, the rotary test conditions simulate the real usage condition of a MEMS gyroscope better than stationary test conditions.

First, the rotary baseline test was conducted to observe the gyroscope output during 60°/s angular rotation at room temperature. The plot in Figure 2-18 shows the MEMS gyroscope output for the first 10,000 angular velocity measurements at room temperature condition. Plot-(a) and plot-(b) in Figure 2-18 show raw and filtered data of angular velocity during the first rotary baseline test. The mean and standard deviation of raw data for the first rotary baseline test were 59.87°/s and 0.84°/s, respectively.

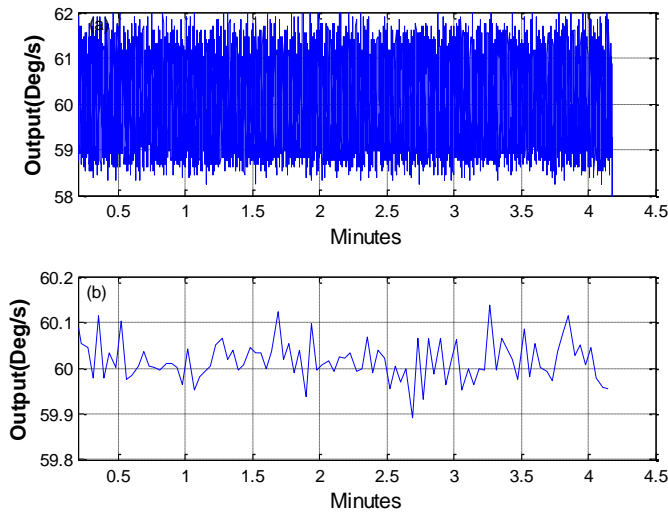


Figure 2-18: First Rotary Baseline Test Result: (a) Raw Angular Rate Data; (b) Filtered Angular Rate Data with Windowsize = 100. (Mean= 59.87, STD= 0.84)

After the first rotary baseline test, the MEMS gyroscope sensor was then subjected to five thermal cycles from 25°C to 85°C. Figure 2-19 shows three different plots representing raw angular velocity data (plot-(a)), filtered angular velocity with windowsize 100 (plot-(b)), and die temperature (plot-(c)).

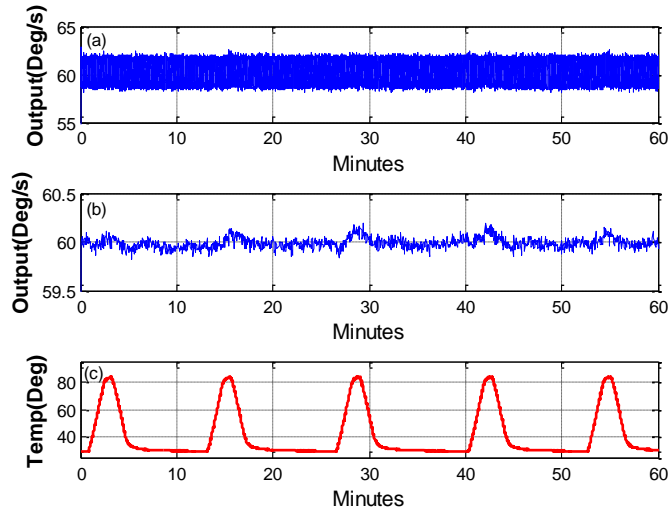


Figure 2-19: Rotary Thermal Test Results from 25°C to 85°C: (a) Raw Angular Rate Data; (b) Filtered Angular Rate Data with Window size = 100; (c) Die Temperature.

When raw angular velocity data (plot-(a)) is compared with die temperature (plot-(c)), performance variation due to temperature change from 25°C to 85°C is less apparent. However, after filtering the raw angular rate data, the effect of temperature on an increase in bias is visible, as shown in plot-(b). Since the MEMS gyroscope uses internal temperature calibration to compensate temperature-dependent bias from -40°C to 85°C, only a small increase in temperature-dependent bias was observed from 25°C to 85°C. The observed temperature dependent bias at 60°/s angular rotation was within 0.3°/s from 25°C to 85°C, which agreed well with the manufacturer's suggested temperature bias (bias temperature coefficient = 0.005°/s/°C). Such an observation is similar to the stationary thermal test result from 25°C to 85°C. This confirms that the MEMS gyroscope performed well within the manufacturer's recommended temperature range at both stationary and rotary conditions.

The slight increase in the dependent bias appears only when the temperature reaches its peak value of 85°C. The noise level returns to its normal level when the

temperature returns to room temperature. This observation suggests that there was not any permanent shift or degradation in the MEMS gyroscope output as a result of five thermal cycles from 25°C to 85°C. Thus, the short-term durability of the MEMS gyroscope was preserved during the rotary thermal test.

Next, the second rotary baseline test was conducted to observe the gyroscope sensor output at room temperature. The plot in Figure 2-20 shows the sensor output for the first 10,000 angular velocity measurements at room temperature conditions. The mean and standard deviation of raw data for the second rotary baseline test were 59.98°/s and 1.49°/s respectively. This confirms that there was not any significant shift in the MEMS gyroscope output from the first rotary baseline test.

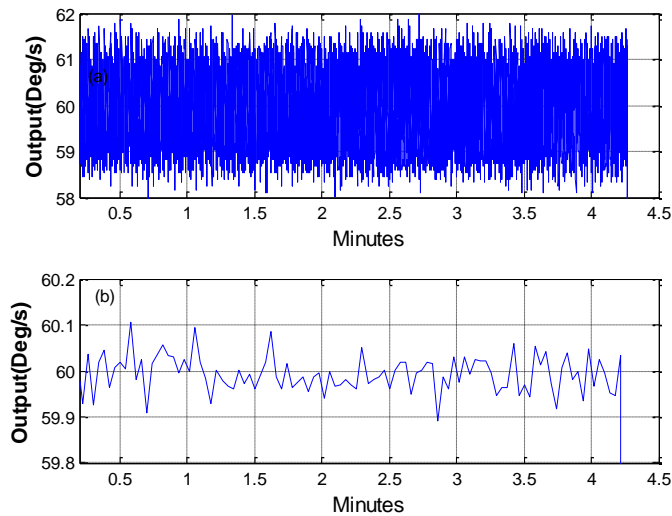


Figure 2-20: Second Rotary Baseline Test Result: (a) Raw Angular Rate Data; (b) Filtered Angular Rate Data with Window size = 100. (Mean= 59.98, STD= 1.49)

After completing the second rotary baseline test, the MEMS gyroscope was again subjected to a higher temperature range. The MEMS gyroscope was subjected to five thermal cycles from 25°C to 125°C. The results of the rotary thermal test from 25°C to 125°C are shown in Figure 2-21.

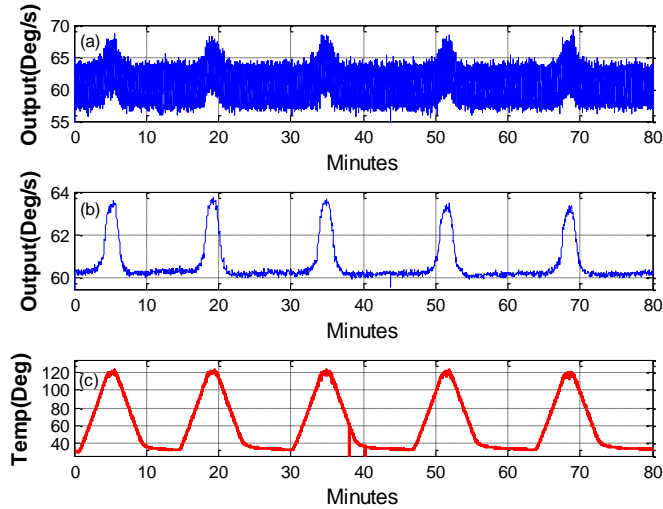


Figure 2-21: Rotary Thermal Test Results from 25°C to 125°C: (a) Raw Angular Rate Data; (b) Filtered Angular Rate Data with Window size = 100; (c) Die Temperature.

Looking at the plot-(a) of Figure 2-21, it can be concluded that the noise level increased with an increase in temperature. After filtering the angular velocity data, an important phenomenon was observed. Plot-(b) shows that a temperature-dependent bias was increased with the increase in temperature. It is essential to notice that there was a sudden change in temperature-dependent bias that occurred when temperature went above 85°C. This bias was not related to any change in motion since the MEMS gyroscope was rotated at a constant 60°/s angular rotation during the test. The bias again returned to its normal value with the temperature dropping below 85°C. Such behavior of the MEMS gyroscope was similar to the stationary thermal test from 25°C to 125°C.

It was also observed that all five thermal cycles resulted in a similar increase in the temperature-dependent bias. No evidence of permanent degradation or hysteresis was observed. Table 2-4 shows the temperature-dependent bias for each thermal cycle. The average bias was 3.26°/s.

Table 2-4: Angular Velocity and Temperature Dependent Bias of Five Rotary Thermal Cycles from 25°C to 125°C.

| <b>Temperature Cycle</b> | <b>Observed Angular Velocity (Deg/s) At 125 °C</b> | <b>Temperature Dependent Bias (°/s)</b> |
|--------------------------|--|---|
| First cycle              | 63.3   | 3.3                                     |
| Second cycle             | 63.4   | 3.4                                     |
| Third cycle              | 63.3   | 3.3                                     |
| Fourth cycle             | 63.2   | 3.2                                     |
| Fifth cycle              | 63.1   | 3.1                                     |
| Avg.                     | 63.26  | 3.26                                    |

Similar to Gyroscope Unit-A, the remaining eight gyroscopes also showed similar behavior when subjected from 25°C to 125°C at 60°/s angular rotation. A summary of the average temperature-dependent bias of all nine gyroscopes from 25°C to 125°C is shown in Table 2-5. The calculated average temperature-dependent bias for all nine gyroscopes was 3.27°/s.

Table 2-5: Average Temperature-dependent Bias of all Nine Gyroscopes from 25°C to 125°C during 60°/s angular rotation

| <b>Gyroscope</b> | <b>Average Temperature Dependent Bias (°/s)</b> |
|------------------|---|
| Unit – A         | 3.26  |
| Unit – B         | 3.27  |
| Unit – C         | 3.28  |
| Unit – D         | 3.30  |
| Unit – E         | 3.27  |
| Unit – F         | 3.26  |
| Unit – G         | 3.26  |
| Unit – H         | 3.25  |
| Unit – I         | 3.28  |
| <b>Average</b>   | 3.27  |

Similar to a stationary thermal test from 25°C to 125°C, the above results indicate very interesting behavior of the MEMS gyroscope. Since all nine MEMS gyroscopes showed a similar increase in temperature-dependent bias from 25°C to 125°C at 60°/s

angular rotation. A temperature compensation algorithm can be developed to compensate for the temperature effects on the MEMS gyroscope up to 125°C. Doing so, the MEMS gyroscope can be used for applications up to a max temperature of 125°C without losing its performance.

After completing the rotary thermal test from 25°C to 125°C, a third rotary baseline test was conducted to observe the gyroscope sensor output. The plot in Figure 2-22 shows the sensor output for the first 10,000 angular velocity measurements at room temperature conditions. The mean and standard deviation of raw data for the third rotary baseline test were 59.92°/s and 0.82°/s, respectively. This confirms that there was not any significant shift in the MEMS gyroscope output from the first and second rotary baseline tests.

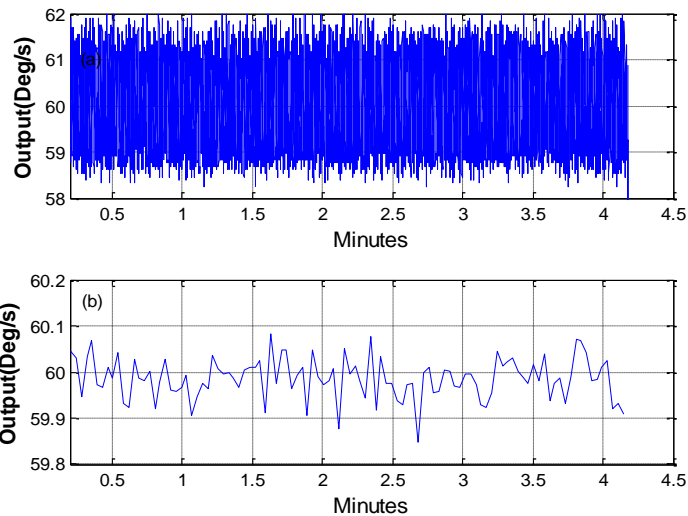


Figure 2-22: Third Rotary Baseline Test Result: (a) Raw Angular Rate Data; (b) Filtered Angular Rate Data with Window size = 100. (Mean= 59.92, STD= 0.82)

After completing the third rotary baseline test, the MEMS gyroscope was again subjected to an even higher temperature. This time, the thermal cycling temperature range was raised to 25°C to 150°C. The result of rotary thermal test from 25°C to 150°C is shown in Figure 2-23. Plot-(a) and plot-(b) of Figure 2-23 indicate a

significant increase in the temperature-dependent bias from 25°C to 150°C. During the temperature increase, it was observed that the angular velocity output of the MEMS gyroscope initially increased and then started to descend at the peak temperature. Such behavior of the MEMS gyroscope was identical for all five temperature cycles from 25°C to 150°C. It was also noticed that the MEMS gyroscope did not show any kind of permanent shift in its output due to exposure to the five thermal cycles with a 150°C peak temperature. The output of the MEMS gyroscope again returned to its normal value along with a decrease in temperature to room temperature conditions.

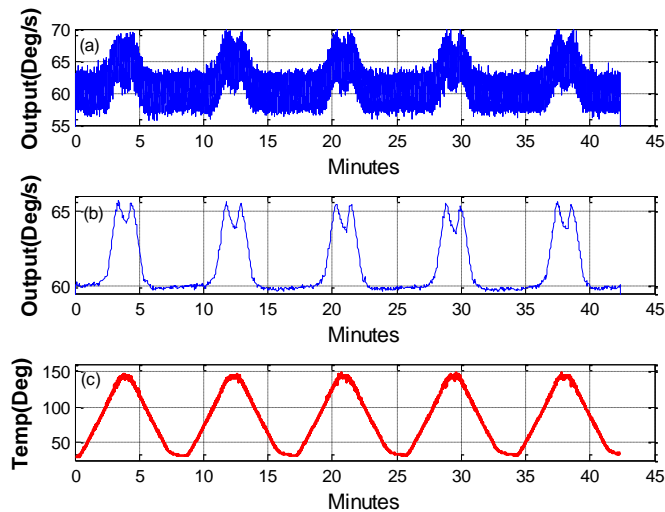


Figure 2-23: Rotary Thermal Test Results from 25°C to 150°C: (a) Raw Angular Rate Data; (b) Filtered Angular Rate Data with Window size = 100; (c) Die Temperature.

After completing the rotary thermal test from 25°C to 150°C, a fourth rotary baseline test was conducted to observe the gyroscope sensor output. The plot in Figure 2-24 shows sensor output for the first 10,000 angular velocity measurements at room temperature conditions. The mean and standard deviation of raw data for the fourth rotary baseline test were 59.99°/s and 1.27°/s, respectively. This confirms that there



was not any significant shift in the MEMS gyroscope output due to short-term elevated temperature exposure from previous rotary baseline tests.

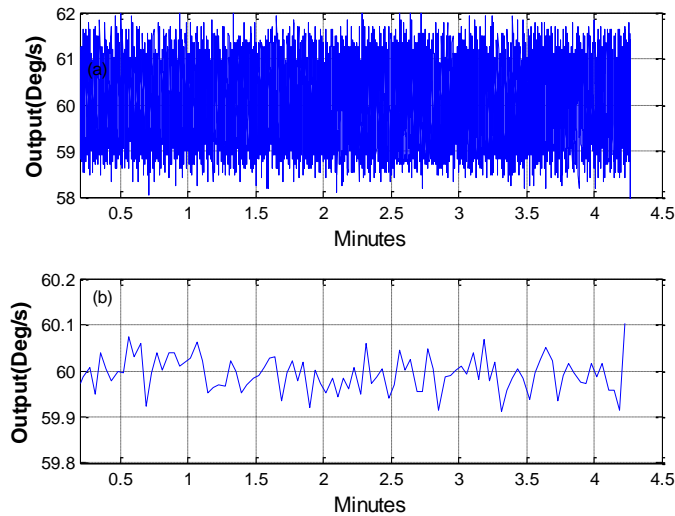


Figure 2-24: Fourth Rotary Baseline Test Result: (a) Raw Angular Rate Data; (b) Filtered Angular Rate Data with Windowsize = 100. (Mean= 59.99, STD= 1.27)

After completing the fourth rotary baseline test, the MEMS gyroscope was again subjected an even to wider temperature range from 25°C to 175°C. The results of the rotary thermal test from 25°C to 175°C are shown in Figure 2-25. Here, the effects of a decrease in the MEMS gyroscope output at an elevated temperature were quite significant. It was also noticed that the MEMS gyroscope did not show any kind of permanent shift in its output due to exposure to five thermal cycles with 150°C peak temperature. The output of the MEMS gyroscope again returned to normal value along with a decrease in temperature to room temperature conditions. Such behavior of the MEMS gyroscope was similar to stationary thermal test from 25°C to 175°C.

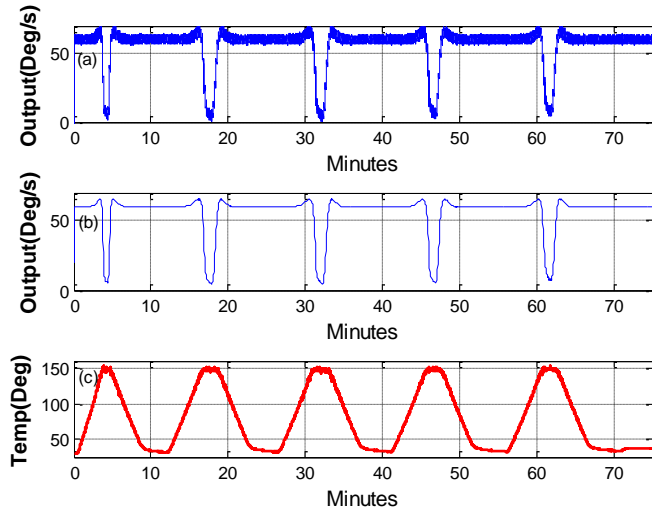


Figure 2-25: Rotary Thermal Test Results from 25°C to 175°C: (a) Raw Angular Rate Data; (b) Filtered Angular Rate Data with Window size = 100; (c) Die Temperature.

After completing the rotary thermal test from 25°C to 175°C, a fifth rotary baseline test was conducted to observe the gyroscope sensor output. The plot in Figure 2-26 shows sensor output for the first 10,000 angular velocity measurements at room temperature conditions. The mean and standard deviation of raw data for the fifth rotary baseline test were 59.79°/s and 1.28°/s, respectively.

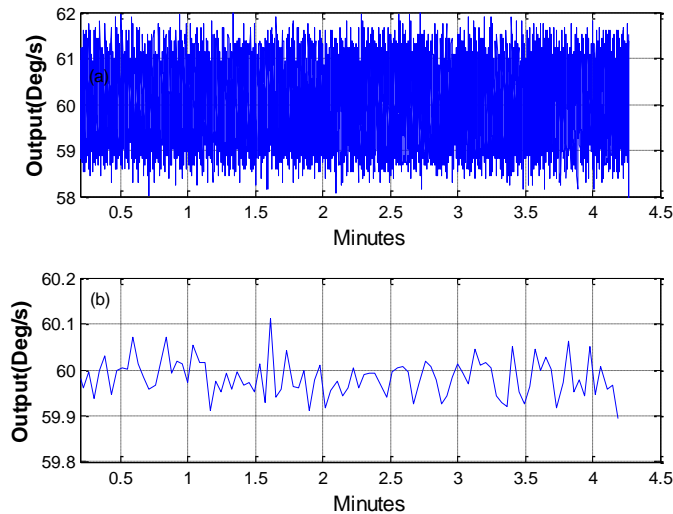


Figure 2-26: Fifth Rotary Baseline Test Result: (a) Raw Angular Rate Data; (b) Filtered Angular Rate Data with Window size = 100. (Mean= 59.79, STD= 1.28)

The summary of the mean and standard deviation of all rotary baseline tests are summarized in Table 2-6. Since there was no significant difference among the mean

and standard deviation values among these tests, it can be concluded that the MEMS gyroscope did not show any kind of damage or permanent shift in output due to short term elevated thermal cycle exposure during the rotary tests.

Table 2-6: Mean and Standard Deviation of Rotary Baseline Test

| No | Tests                       | Mean (°/s) | Standard Deviation (°/s) |
|----|-----------------------------|------------|--------------------------|
| 1  | First Rotary baseline test  | 59.87      | 0.84                     |
| 2  | Second Rotary baseline test | 59.98      | 1.49                     |
| 3  | Third Rotary baseline test  | 59.68      | 0.82                     |
| 4  | Fourth Rotary baseline test | 59.99      | 1.27                     |
| 5  | Fifth Rotary baseline test  | 59.79      | 1.28                     |

## 2.4. Conclusions

This study has resulted in many interesting findings. The following conclusions can be made from this study:

- A new test protocol has been developed for evaluating the effects of elevated temperatures on the performance of MEMS gyroscopes operated within and beyond manufacturer’s recommended temperature range.
- No permanent change or hysteresis in the performance was observed on the MEMS gyroscope after exposure to five thermal cycles at various temperature ranges during stationary and rotary thermal tests. This was again verified from baseline tests performed after each thermal test at stationary and rotary conditions.

- A temperature increase caused similar performance changes to the MEMS gyroscope during the stationary thermal test and the rotary thermal test over wider temperature ranges.
- The MEMS gyroscope showed a small increase in temperature-dependent bias when exposed to a temperature range of 25°C to 85°C at stationary and rotary conditions. Such small increase in the temperature-dependent bias was well within the manufacturer's specification.
- There was a significant increase in the angular velocity measured by the gyroscope with temperature when the gyroscope was operated from 25°C to 125°C. This did not correspond to any actual change in the angular velocity either at stationary or rotatory conditions. For nine individual MEMS gyroscopes, the average temperature-dependent bias at stationary and rotary conditions from 25°C to 125°C turned out to be 3.28°/s and 3.27°/s, respectively. If the observed temperature-dependent bias from 25°C to 125°C was compensated, the MEMS gyroscope could be used in applications where temperature goes to 125°C.
- When a MEMS gyroscope was subjected to 150°C or beyond, it was observed that the angular velocity output of the MEMS gyroscope initially increased and then started to descend at peak temperature. Further analysis is required to investigate such behavior of MEMS gyroscope at or beyond 150°C to enable the reliable application of MEMS gyroscopes in high temperature environments. However, this was outside the scope of current research.

### **3. Simulation of Temperature Effect on the Performance of a MEMS Gyroscope**

#### **3.1. Introduction**

This chapter describes a method to simulate temperature effects on the performance of a MEMS gyroscope. Initially, the working principle of the MEMS gyroscope is described. Based on the characteristic equations of motion for a MEMS vibratory gyroscope, a model is developed to simulate its performance at an ambient condition. Thereafter, the effects of temperature-dependent factors are considered to simulate temperature effects on the performance of the MEMS gyroscope. In order to check the validation of the developed model, the experiment is conducted to characterize the MEMS gyroscope's performance within the manufacturer's recommended temperature range. In addition, to find the validity limit of the simulation model beyond the manufacturer's recommended temperature range, simulation results are also compared with previously conducted experimental results over a wider elevated temperature range.

#### **3.2. Working Principle**

A MEMS vibratory gyroscope can be simply visualized as a two degree-of-freedom (2-DOF) mass-spring-damper system as shown in Figure 3-1. At the core, it has a vibrating mass or a proof mass. The proof mass is suspended above the substrate by use of flexible beams, which also work as mechanical springs. The proof mass is subjected to vibration at resonance frequency by use of an electrostatic force that causes movement of a proof mass in the drive direction. When the gyroscope sensor

experiences an angular rotation, a Coriolis force is induced in the direction orthogonal to both the drive direction (x) and the angular rotation axis (z). This rotation induced Coriolis force causes energy transfer between the drive mode and the sense mode. The movement of a proof mass caused by the Coriolis force in the sense direction (y) is proportional to the angular rotation applied and can be measured with differential capacitance techniques using interdigitated comb electrodes. An example of schematic view of the MEMS gyroscope that utilizes interdigitated comb electrodes as sense combs is shown in Figure 3-2.

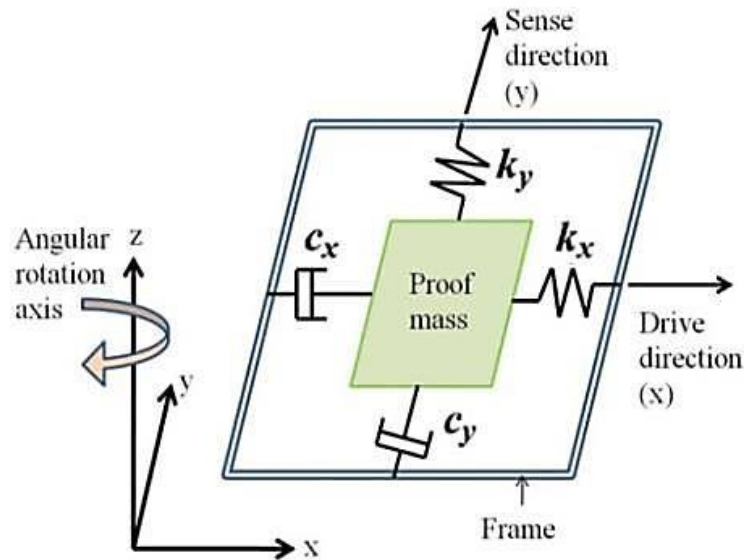


Figure 3-1: Schematic of Two Degree-of-freedom (2-DOF) Mass-spring-damper System

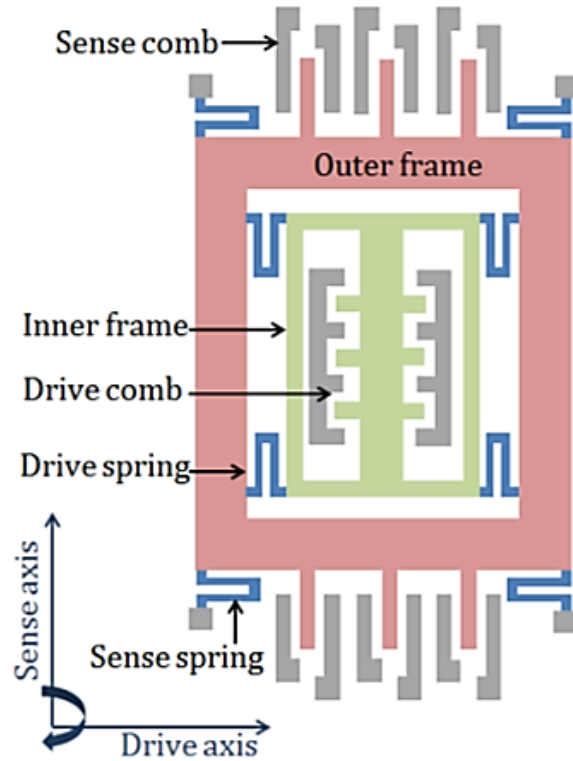


Figure 3-2: Schematic Illustration of MEMS Vibratory Gyroscope

There are many ways to increase device output. One of the ways is to vibrate the drive and sense mode at a resonance that increases the device output and hence its sensitivity. On the other hand, increasing device sensitivity makes the MEMS gyroscope more vulnerable to the external parameters like temperature, pressure, vibration, and shock that shift the natural frequency, introduce quadrature errors and alter device output [36]. Thus, in most of the cases, MEMS gyroscopes are designed to have sense-mode slightly shifted from the drive-mode to improve robustness and thermal stability.

Various designs have been explored to make MEMS gyroscopes more robust. One such design is shown in Figure 3-3 where two proof masses are placed on either side and are driven in opposite directions. During rotation, Coriolis force induced on the two proof masses are also in opposite directions. This special arrangement helps to

nullify the external inertial inputs caused by undesirable linear acceleration, vibration and shock. This concept has been widely used in commercial gyroscopes like the ADIS16250 and ADIS16255.

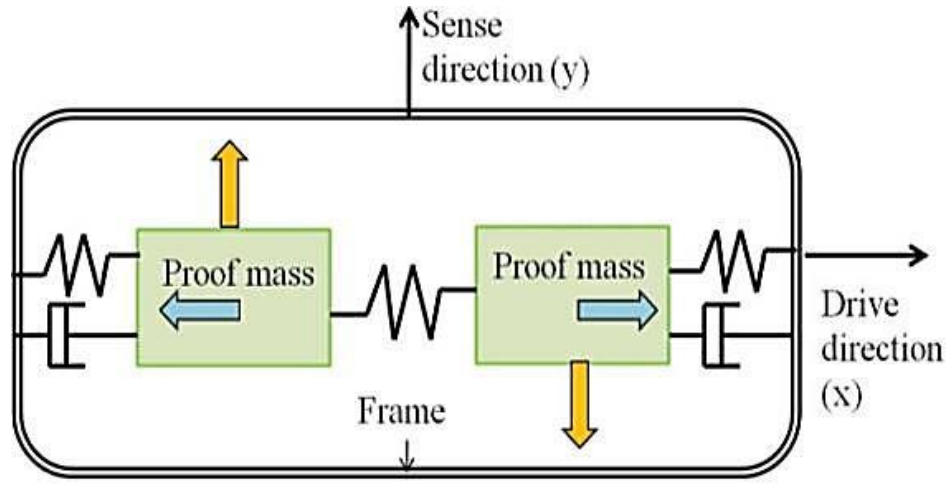


Figure 3-3: Two Proof Mass-spring-damper System

### 3.3.MEMS Gyroscope Motion Equations

In order to derive the equation of motion for a MEMS vibratory gyroscope, the system is represented by a two degree-of-freedom, mass-spring-damper system. Since the gyroscope structure movement is modeled while it rotates, motion equations can be represented based on a stationary frame (gyroscope frame) and a non-stationary frame (inertial frame). The mass-spring-damper system, a gyroscope frame and an inertial frame, is shown in Figure 3-4.



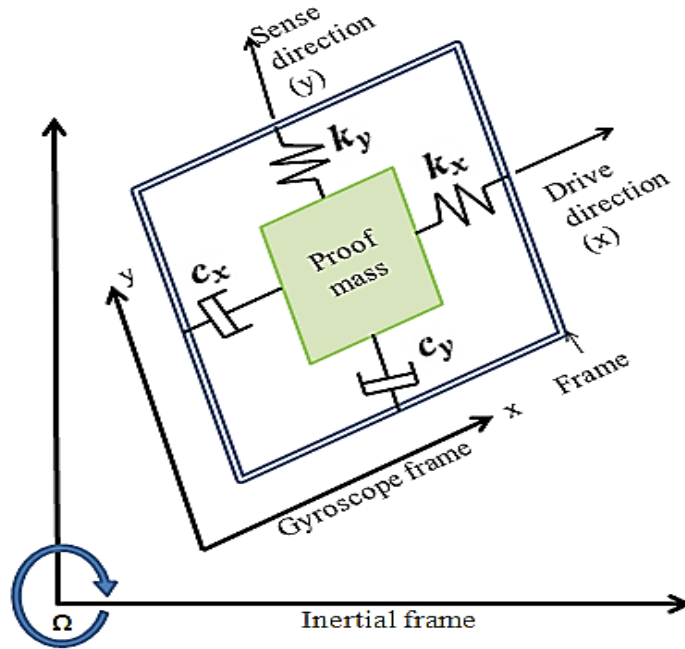


Figure 3-4: Two Degree-of-freedom Mass-spring-damper System Model

The mass-spring-damper system is initially observed with respect to the gyroscope frame. Once the motion equations have been established, these equations are derived with respect to the inertial frame. The equations of motion for the mass-spring-damper system with respect to the gyroscope frame can be represented as:

$$ma_x + c_x v_x + k_x x = F_d \quad \text{A}$$

$$ma_y + c_y v_y + k_y y = 0 \quad \text{B}$$

Where  $m$  is the mass of the vibrating structure,  $c_x$  and  $c_y$  are the damping coefficients in drive and sense direction,  $k_x$  and  $k_y$  are the beam stiffness in drive and sense directions,  $a_x$  and  $a_y$  are the acceleration components and  $v_x$  and  $v_y$  are the velocity components in the drive and sense directions, respectively and  $F_d$  is an electrostatic force applied by drive combs. If these equations are viewed from an inertial frame, they can be represented as,

$$m\ddot{x} + c_x\dot{x} + k_x x = F_d + 2m\Omega\dot{y} \quad \text{C}$$

$$m\ddot{y} + c_y\dot{y} + k_y y = -2m\Omega\dot{x} \quad \text{D}$$

The  $2m\Omega\dot{y}$  and  $2m\Omega\dot{x}$  are the rotation-induced Coriolis terms. When the gyroscope starts vibrating in the drive direction and experiences an external angular rotation, these Coriolis terms cause dynamic coupling between the drive and sense modes of vibration, and because of this coupling, the suspended proof mass starts to vibrate in the sense direction.

### 3.4. Simulink Model

In order to calculate the drive and sense comb displacement from the characteristic equation of motion, it is necessary to solve equations C and D. There are various methods to solve these coupled differential equations. The one used in this research is by using Simulink tool. Simulink is a toolbox in MATLAB for analyzing multi-domain dynamic system. A Simulink model is developed by rearranging equations E and F as shown below.

$$\ddot{x} = \frac{1}{m}(F_d + 2m\Omega\dot{y} - c_x\dot{x} - k_x x) \quad \text{E}$$

$$\ddot{y} = \frac{1}{m}(-2m\Omega\dot{x} - c_y\dot{y} - k_y y) \quad \text{F}$$

From equations E and F, a Simulink model is developed that is shown in Figure 3-5.

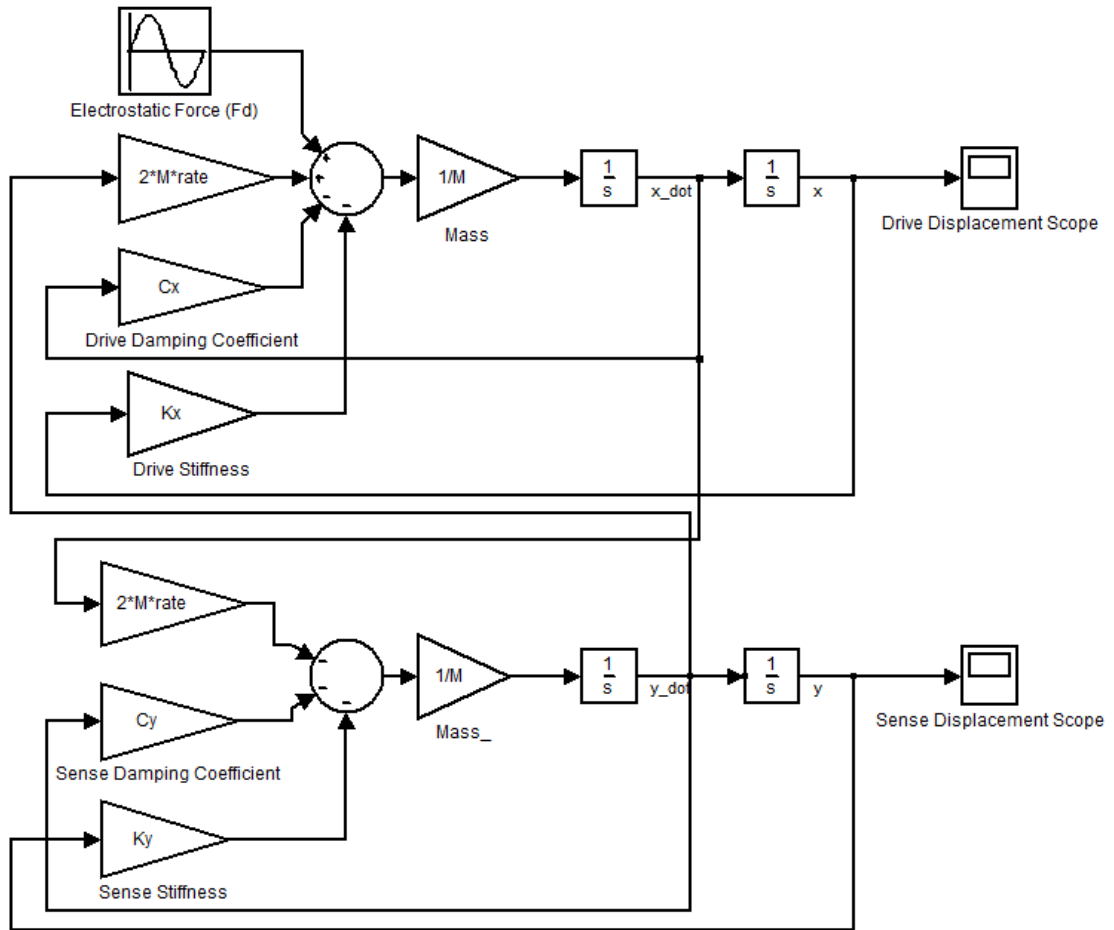


Figure 3-5: Simulink Model

To calculate drive and sense displacement for a specific angular rotation at room temperature through the Simulink model, the values of mass of suspended structure, stiffness in drive and sense directions, the damping coefficient in drive and sense directions and electrostatic force are required. In order to calculate these parameters, equations from the literature were used to calculate the value for these parameters.

The mass of suspended structure ( $M$ ) can be calculated as [37]:

$$M = M_m + M_b + M_c - M_e \quad G$$

Where  $M_m$  is mass of inner and outer frames,  $M_b$  is suspension beam mass,  $M_c$  is drive and sense combs mass and  $M_e$  is etch holes mass.

The drive beam stiffness ( $K_x$ ) and sense beam stiffness ( $K_y$ ) depend on the gyroscope design. Based on the configuration of the MEMS gyroscope examined in this study, the following equations were used to calculate drive beam stiffness ( $K_x$ ) and sense beam stiffness ( $K_y$ ):

$$K_x = K_y = \frac{4 \cdot E \cdot t_{b1} \cdot w_{b1}^3}{l_{b1}^3} + \frac{4 \cdot E \cdot t_{b2} \cdot w_{b2}^3}{l_{b2}^3} \quad \text{H}$$

Where  $E$  is Young's modulus of polysilicon,  $t_{b1}$  and  $t_{b2}$ ,  $w_{b1}$  and  $w_{b2}$ ,  $l_{b1}$  and  $l_{b2}$  are thickness, width and length of beam 1 and beam 2, respectively.

From the mass of suspended structure ( $M$ ), drive beam stiffness ( $K_x$ ) and sense beam stiffness ( $K_y$ ) calculated previously, drive mode frequency ( $f_x$ ) and sense mode frequency ( $f_y$ ) can be calculated as [38]:

$$f_x = \frac{1}{2\pi} \sqrt{\frac{K_x}{M}}, \quad f_y = \frac{1}{2\pi} \sqrt{\frac{K_y}{M}} \quad \text{I}$$

In order to determine the flow regime to calculate the damping coefficient, the Knudsen number ( $K_n$ ) can be calculated as [36] [37]:

$$K_n = \frac{\lambda}{L_c} = \frac{R \cdot T}{\sqrt{2} \cdot \pi \cdot D^2 \cdot N_a \cdot P \cdot L_c} \quad \text{J}$$

Where  $\lambda$  is the mean free path of the gas molecule,  $L_c$  is a characteristic length of flow,  $R$  is a gas constant,  $T$  is ambient temperature,  $D$  is the diameter of the gas molecule,  $N_a$  is Avogadro number, and  $P$  is ambient pressure.

Based on the values of the Knudsen number ( $K_n$ ), the flow regime is determined. Proof mass damping coefficient ( $C_{proof\ mass}$ ) and comb structure damping coefficient ( $C_{comb\ structure}$ ) can be calculated as [36] [37] [39]:

$$C_{proof\ mass} = \frac{\mu \cdot A_{proof\ mass}}{(1 + 2 \cdot K_n) \cdot h} \quad \text{K}$$

Where  $\mu$  is air viscosity,  $A_{proof\ mass}$  is proof mass area,  $K_n$  is the Knudsen number and  $h$  is the gap between proof mass and the substrate.

$$C_{Comb\ structure} = \frac{\mu \cdot N \cdot A_{combs}}{g_c + \lambda} \quad \text{L}$$

Where  $\mu$  is air viscosity,  $N$  is the number of combs,  $A_{combs}$  is the comb area,  $g_c$  is the gap between the comb fingers and  $\lambda$  is the mean free path of the gas molecule ( $K_n^* L_c$ ).

The net damping is the summation of damping of the proof mass and comb structure. Thus, drive damping coefficient ( $C_{drive}$ ) and sense damping coefficient ( $C_{sense}$ ) can be calculated as [36] [37] [39]:

$$\begin{aligned} C_{drive} &= C_{sense} \\ &= C_{proof\ mass} + C_{Comb\ structure} \end{aligned} \quad \text{M}$$

The selected device is actuated by electrostatic combs. Thus, net electrostatic force ( $F_d$ ) can be calculated as [36] [38] [40]:

$$F_d = \frac{2.28 \cdot N \cdot \epsilon \cdot t_c \cdot V_{dc} \cdot V_{ac}}{g_c} \quad \text{N}$$

Where  $N$  is number of the capacitor formed by the comb finger,  $\epsilon$  is permittivity of air,  $V_{dc}$  is DC voltage,  $V_{ac}$  is AC voltage and  $g_c$  is the gap between the comb fingers.

### 3.5.Simulation Results at Room Temperature

Based on the above parameters, a Simulink model can be used to calculate drive and sense comb displacement at room temperature. In many cases, sense combs use interdigitated comb electrodes to measure a differential capacitance that is directly proportional to sense comb displacement. This differential capacitance can be eventually converted with the help of an application specific integrated circuit (ASIC), to a voltage that is measured from the gyroscope output terminal. The differential capacitance or capacitance change ( $\Delta C_b$ ) can be calculated from sense displacement as [37][39]:

$$\Delta C_b = \frac{\epsilon \cdot l_{p_c} \cdot t_c \cdot Y_{sense}}{(g_c)^2} \quad \text{O}$$

Where  $\epsilon$  is the permittivity of air,  $l_{p_c}$  is a comb finger overlap,  $t_c$  is comb finger thickness,  $Y_{sense}$  is a sense displacement,  $g_c$  is the gap between comb fingers.

Based in the construction of MEMS gyroscope used in this research, values of the MEMS gyroscope parameters were calculated from equations G through O . The calculated MEMS gyroscope parameters are summarized in Table 3-1. Using the Simulink model, drive displacement, sense displacement and capacitance change of the MEMS gyroscope at room temperature ( $T=25^\circ\text{C}$ ) and  $60^\circ/\text{s}$  angular rotation were calculated, which are also shown in Table 3-1.

Table 3-1: MEMS Gyroscope's Parameters and Simulation Result at Ambient Condition (Angular Velocity = 60°/s, Temperature=25°C, Pressure= 1 atm)

| Parameters  | Calculated values  |
|---|--------------------|
| Mass of suspended structure ( $M$ )                               | 4 ( $\mu g$ )      |
| Drive beam stiffness ( $K_x$ ) and Sense beam stiffness ( $K_y$ ) | 30.95 ( $N/m$ )    |
| Drive mode frequency ( $f_x$ ) and Sense mode frequency ( $f_y$ ) | 14,000 ( $Hz$ )    |
| Knudsen number ( $K_n$ )  | 0.0334             |
| Proof mass damping coefficient ( $C_{proof\ mass}$ )              | 7.61e-6 ( $Ns/m$ ) |
| Comb structure damping coefficient ( $C_{Comb\ structure}$ )      | 1.37e-7 ( $Ns/m$ ) |
| Drive damping coefficient ( $C_{drive}$ )                         | 7.75e-6 ( $Ns/m$ ) |
| Sense damping coefficient ( $C_{sense}$ )                         | 7.94e-6 ( $Ns/m$ ) |
| Electrostatic force ( $F_d$ )                                     | 4.36e-6 ( $N$ )    |
| Angular velocity ( $\Omega$ )                                     | 60 ( $^\circ/s$ )  |
| Drive displacement ( $X_{drive}$ )                                | 6.39 ( $\mu m$ )   |
| Sense displacement ( $Y_{sense}$ )                                | 6.75 ( $nm$ )      |
| Capacitance change ( $\Delta C_b$ )                               | 7.45e-18 ( $F$ )   |

The time domain response of the drive and sense comb displacement at 60°/s angular rotation and room temperature are shown in Figure 3-6. These results show that the MEMS gyroscope takes around 5 milliseconds to stabilize the output of MEMS gyroscope when subjected to 60°/s constant angular rotation.

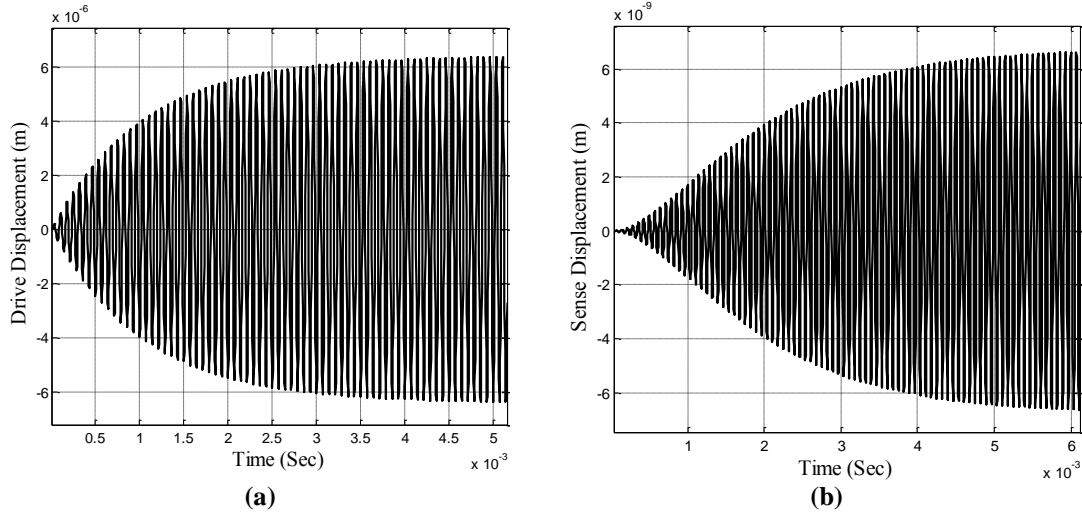


Figure 3-6: Displacement of Drive and Sense Comb at 60°/s Angular Rotation (a) Drive Comb Displacement (m) vs. Time (sec) (b) Sense Comb Displacement (m) vs. Time (sec)

From the Simulink model, output of the MEMS vibratory gyroscope at different angular velocities can be calculated to determine the scale factor. An example is shown in Figure 3-7, where angular velocity was varied from -50 RPM to +50 RPM.

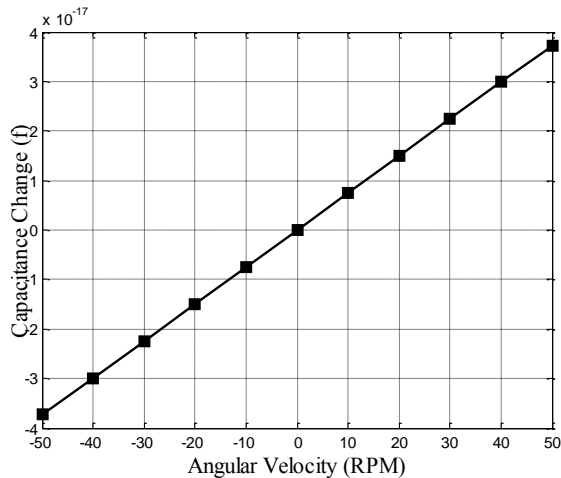


Figure 3-7: Capacitance Change (F) vs. Angular Velocity (RPM)

### 3.6. Simulation over a Wider Temperature Range

The Simulink model can be used to simulate the temperature-dependent characteristic of the MEMS vibratory gyroscope. In recent years, studies have been performed to understand the temperature effects on the MEMS gyroscope's performance. Some of



these studies performed suggest that fluctuation in the ambient temperature of the MEMS vibratory gyroscope results in a performance bias [41]–[45]. Other studies suggest that a prime source of temperature-dependent bias in the MEMS gyroscope is a change in resonance frequency [46]–[48] and Q-factor [25], [49]. Resonance frequency is a function of stiffness that depends on Young’s modulus. A material property, Young’s modulus (E) is a function of temperature, and thus different values of Young’s modulus at different temperatures change the resonance frequency of the vibrating mass. The Q-factor is the ratio of loss of energy to the stored energy in one cycle. A high Q value of an oscillator indicates a lower rate of energy loss relative to the stored energy and thus it depends on the damping coefficient. Thus, different values of damping coefficients at different temperatures change the Q factor of the vibrating mass.

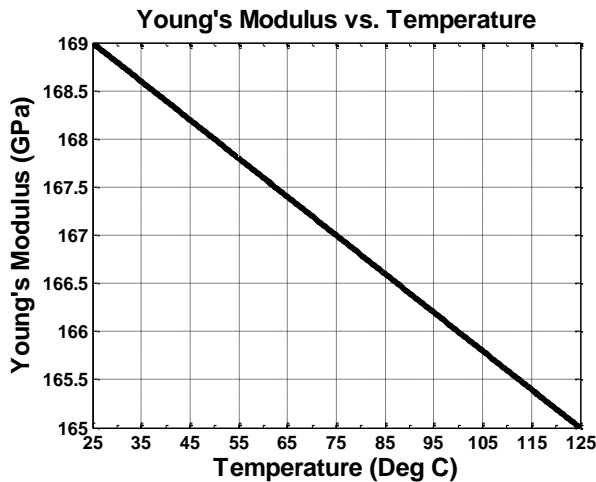
In order to simulate the temperature effects on the MEMS vibratory gyroscope, two factors, found from literature, such as Young’s modulus and damping coefficient, are considered in the simulation.

Many different values of Young’s modulus of polysilicon have been reported in literature [50]. In this study, we have considered the value of Young’s modulus of polysilicon as 169 GPa at +25°C. The mechanical properties of polysilicon depend on temperature and it changes significantly at higher temperatures [51],[52]. The relation between temperature and Young’s modulus of polysilicon reported in the literature [51] is considered in the simulation, which is shown below:

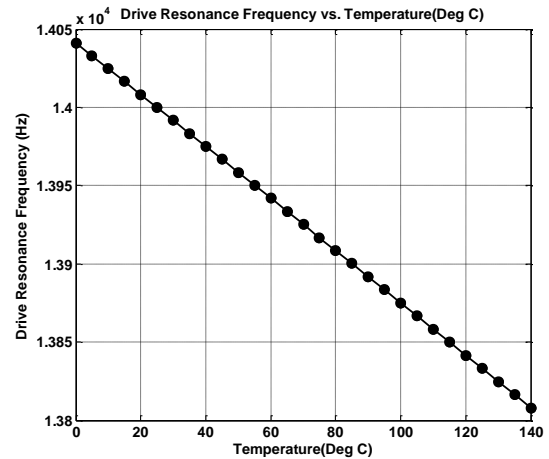
$$E(T) = E_s - A * (T - T_s) \quad \text{P}$$

Where  $E_s$  and  $T_s$  are Young's modulus (GPa) and temperature ( $^{\circ}\text{C}$ ) at ambient condition, respectively. A is the temperature dependent Young's modulus coefficient whose value is 0.04.

Using the equation P, Young's modulus of polysilicon has been calculated from  $25^{\circ}\text{C}$  to  $125^{\circ}\text{C}$  which is shown in Figure 3-8 (a). It is clear that temperature increase of  $100^{\circ}\text{C}$  from  $25^{\circ}\text{C}$  to  $125^{\circ}\text{C}$  resulted reduction in Young's modulus of 4 GPa from 169 GPa to 165 GPa. Such reduction in the Young's modulus of polysilicon affects the drive and the sense resonance frequencies. An example of change in drive resonance frequency from  $0^{\circ}\text{C}$  to  $140^{\circ}\text{C}$  is shown in Figure 3-8 (b).



(a)



(b)

Figure 3-8: (a) Change in Young's Modulus with Temperature from  $25^{\circ}\text{C}$  to  $125^{\circ}\text{C}$   
 (b) Change in Drive Resonance Frequency with Temperature from  $0^{\circ}\text{C}$  to  $140^{\circ}\text{C}$ .

Damping coefficient decreases with temperature increase. The relationship between damping coefficient and temperature can be established from equations K through M which is shown below:

$$C_{drive} = C_{sense} = \frac{\mu A_{Proof\ mass}}{\left(1+2 \left(\frac{RT}{\sqrt{2\pi D^2 N_a P L_c}}\right)h\right)} + \frac{\mu N A_{combs}}{g_c + \left(\frac{RT}{\sqrt{2\pi D^2 N_a P}}\right)}$$

Where  $\mu$  is air viscosity,  $A_{proof\ mass}$  is proof mass area,  $R$  is a gas constant,  $T$  is ambient temperature,  $D$  is the diameter of the gas molecule,  $N_a$  is Avogadro number, and  $P$  is ambient pressure,  $L_c$  is a characteristic length of flow,  $h$  is the gap between proof mass and the substrate,  $N$  is the number of combs,  $A_{combs}$  is the comb area and  $g_c$  is the gap between the comb fingers.

An example of change drive damping from 0°C to 140°C is shown in Figure 3-9 (b).

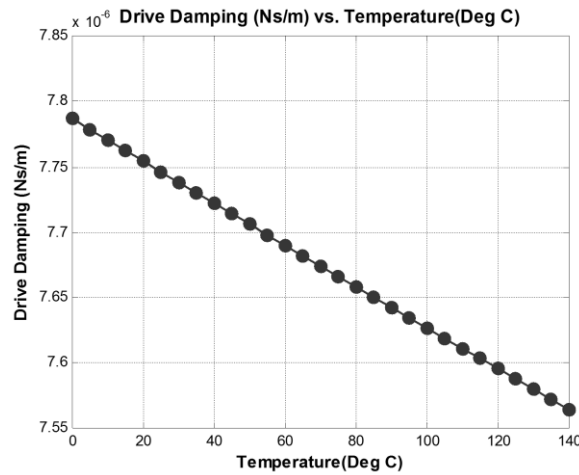


Figure 3-9: Change in Drive Damping with Temperature from 0°C to 140°C.

Using the Simulink model, effect of change in Young’s modulus and damping coefficient at various temperatures were considered to determine capacitance change over the temperatures. An example of calculated capacitance change from 0°C to 140°C is shown in Figure 3-10. Such increase in capacitance over the temperatures was due to larger displacement of drive and sense combs due to change in Young’s modulus and damping coefficient from 0°C to 140°C. The transient response of drive and sense comb displacement are shown in Figure 3-11. The magnified view of the

transient response of drive and sense comb displacement is shown in Figure 3-11-((c), (d), (e), and (f)), which show an increase in drive and sense displacement with temperature increase from 0°C to 140°C. Such increase in the drive and the sense displacement results in higher angular velocity output of a MEMS gyroscope at a constant angular rotation.

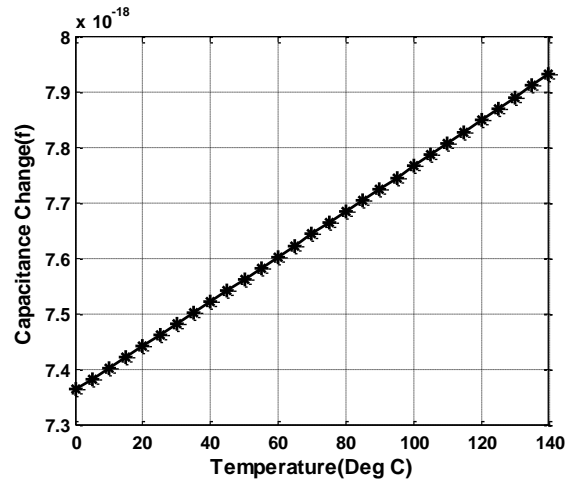
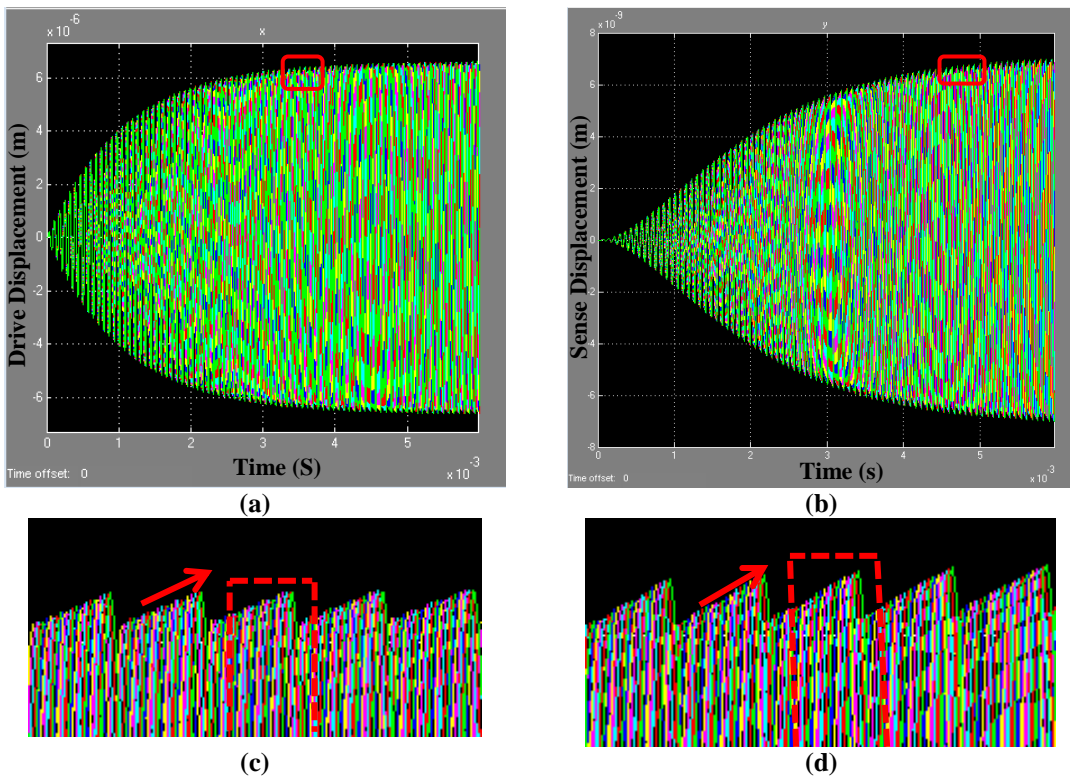


Figure 3-10: Capacitance Change with Temperature from 0°C to 140°C



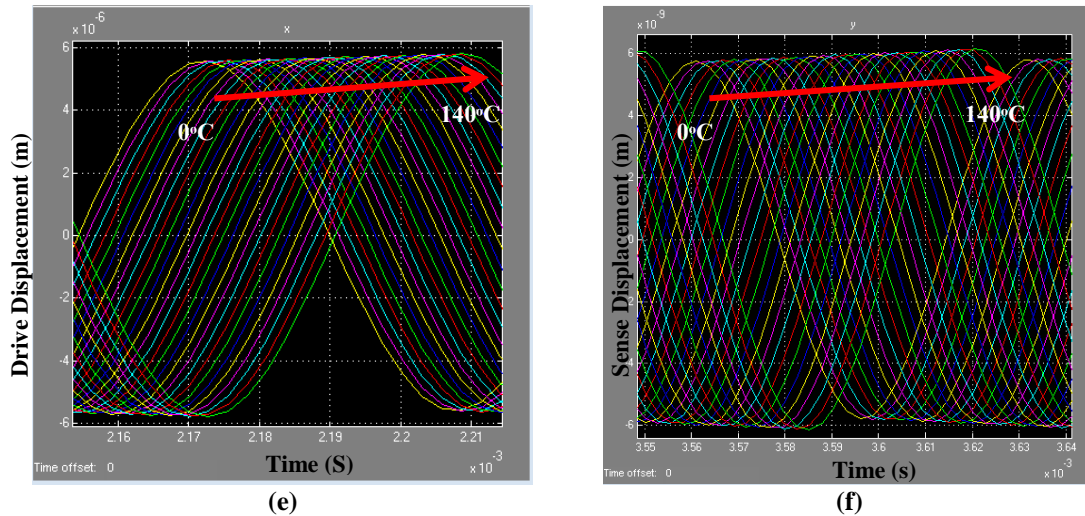


Figure 3-11: Transient Response of the MEMS Gyroscope at 60 °/s Angular Rotation from 0°C to 140°C Temperatures: (a) Drive Displacement (m) vs. Time (s), (b) Sense Displacement (m) vs. Time (s), (c) Magnified View of Window-(a), (d) Magnified View of Window-(b), (e) Magnified View of Window-(c) indicates an Increase in Drive Amplitude with Temperatures, (f) Magnified View of Window-(d) indicates an Increase in Sense Amplitude with Temperatures.

In absence of direction correlation between capacitance change and angular velocity output of the MEMS gyroscope, an indirect approach was followed to establish a correction between angular velocity and temperature.

Using the Simulink model, capacitance change was calculated over a wider input angular velocity of the MEMS gyroscope at room temperature. An example of capacitance change that resulted from input angular velocity increase from 59.5°/s to 64.0°/s is shown in Figure 3-12.

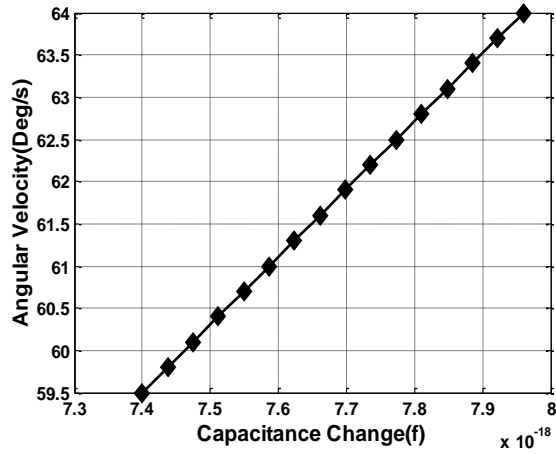


Figure 3-12: Capacitance Change due to Variation in Angular Velocity from 59.5 °/s to 64.0 °/s.

Using the interpolation technique between the results from Figure 3-10 and Figure 3-12, a correlation between angular velocity and temperature was established. An example of this interpolation results for temperature increase from 25°C to 85°C at 60°/s angular rotation is shown in Figure 3-13.

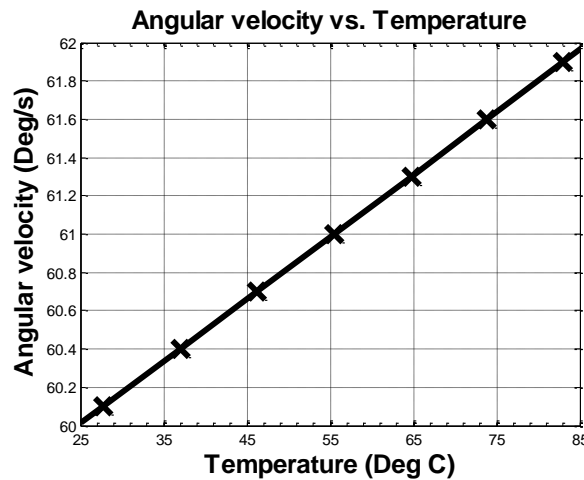


Figure 3-13: Simulated Temperature-Dependent Bias of MEMS Gyroscope at 60°/s Angular Rotation

It is clear from Figure 3-13 that the simulated temperature-dependent bias turned out to be 1.98°/s when the performance of MEMS gyroscope was simulated from 25°C to 85°C at 60°/s angular rotation. Similarly, a wider temperature range can be also used to calculate simulated temperature-dependent bias at any angular rotation speed.

### **3.7. Model Validation**

In order to perform model validation, an experiment was conducted to characterize the MEMS gyroscope's performance within the manufacturer's recommended temperature range. In addition, to find validity limit of the simulation model beyond the manufacturer's recommended temperature range, simulation results were also compared with previously conducted experimental results over a wider elevated temperature range.

#### **3.7.1. Examination of Model Validation within the Manufacturer's Recommended Temperature Range**

In order to examine the validity of the Simulink model within the manufacturer's recommended temperature range, ADIS16250, a single axis MEMS gyroscope, rated from  $-40^{\circ}\text{C}$  to  $+85^{\circ}\text{C}$  was selected for the experiment. ADIS16250 features the same mechanical structure and package design as previously used ADIS16255 single axis MEMS gyroscope. Only the major difference between ADIS16250 and ADIS16255 is that ADIS16250 does not feature internal calibration; whereas, ADIS16255 gyroscope output is internally calibrated and compensated within  $-40^{\circ}\text{C}$  to  $85^{\circ}\text{C}$ . By selecting ADIS16250 gyroscope, it was possible to measure the performance bias due to temperature increase within the manufacturer's recommended temperature range.

For the experiment,  $25^{\circ}\text{C}$  to  $85^{\circ}\text{C}$  temperature range was selected for examining the performance of ADIS16250. This selected temperature range was within the manufacturer's recommended temperature range. The angular velocity output of ADIS16250 was measured at every  $10^{\circ}\text{C}$  temperature intervals from  $25^{\circ}\text{C}$  to  $85^{\circ}\text{C}$  at

0°/s (0 rpm), 60°/s (10 rpm), 120°/s (20 rpm) and 240°/s (40 rpm). At each temperature and angular rotation, the MEMS gyroscope's output was collected for 5 minutes. A precise turntable was used for subjecting the MEMS gyroscope to constant angular rotation. In addition, a tempronic thermostream unit was used to subject ADIS16250 to controlled temperature conditions from 25°C to 85°C. The experimental set-up and data-collection procedure were similar as described in chapter-2 for the ADIS16255 gyroscope.

Table 3-2 shows average angular velocity output of the ADIS16250 MEMS gyroscope from 25°C to 85°C at 0, 60, 120 and 240 deg/s angular rotations. The angular velocity measurement at 25°C establishes the baseline for the measurement at higher temperatures. By subtracting the baseline value from the measurements for each angular velocity exposure, temperature-dependent bias can be calculated, which is shown in Figure 3-14.

Table 3-2: Avarage Angular Velocity Output of the ADIS16250 MEMS Gyroscope from 25°C to 85°C

| <b>Temperature (Deg C)</b> | <b>0 Deg/s</b> | <b>60 Deg/s</b> | <b>120 Deg/s</b> | <b>240 Deg/s</b> |
|----------------------------|----------------|-----------------|------------------|------------------|
| 25 (Baseline)              | 0.85           | 60.77           | 120.66           | 240.41           |
| 35                         | 1.18           | 61.12           | 121.04           | 240.81           |
| 45                         | 1.49           | 61.46           | 121.38           | 241.16           |
| 55                         | 1.79           | 61.80           | 121.74           | 241.54           |
| 65                         | 2.10           | 62.14           | 122.09           | 241.91           |
| 75                         | 2.45           | 62.50           | 122.44           | 242.24           |
| 85                         | 2.80           | 62.79           | 122.75           | 242.55           |



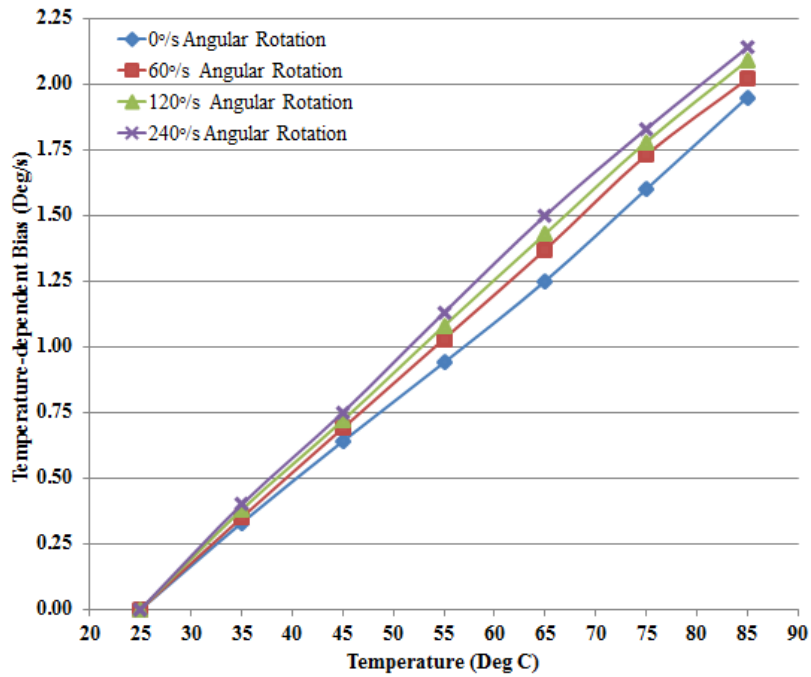


Figure 3-14: Temperature-dependent Bias of ADIS16250 from 25°C to 85°C at 0, 60, 120 and 240 deg/s Angular Rotations

From Figure 3-14, it can be observed that the MEMS gyroscope showed a small increase in temperature-dependent bias with an increase in angular rotation. It is believed that this was due to an external force, such as centrifugal force, excited on the proof mass of MEMS gyroscope with the increase in angular rotation. By subtracting angular velocity measurement at 25°C from 85°C measurement, the magnitude of temperature-dependent bias value of ADIS16250 from 25°C to 85°C ( $\Delta T = 60\text{ }^{\circ}\text{C}$ ) at 0, 60, 120 and 240 deg/s angular rotations can be calculated, which is shown in Table 3-3.

Table 3-3: Temperature-dependent Bias Value of ADIS16250 from 25°C to 85°C ( $\Delta T = 60^\circ\text{C}$ ) at 0, 60, 120 and 240 deg/s Angular Rotations

| Angular Rotation (Deg/s) | Temperature Dependent Bias Value (Deg/s) from 25°C to 85°C |
|--------------------------|--|
| 0°/s Angular Rotation    | 1.95   |
| 60°/s Angular Rotation   | 2.02   |
| 120°/s Angular Rotation  | 2.09   |
| 240°/s Angular Rotation  | 2.14   |

From the Simulink model, the simulated temperature bias can be derived by deducting an angular rotation (i.e, 60°/s) from results shown in Figure 3-13. The comparison of simulation and experimental temperature-dependent bias and its magnitude from 25°C to 85°C is show in Figure 3-15 and Table 3-4, respectively.

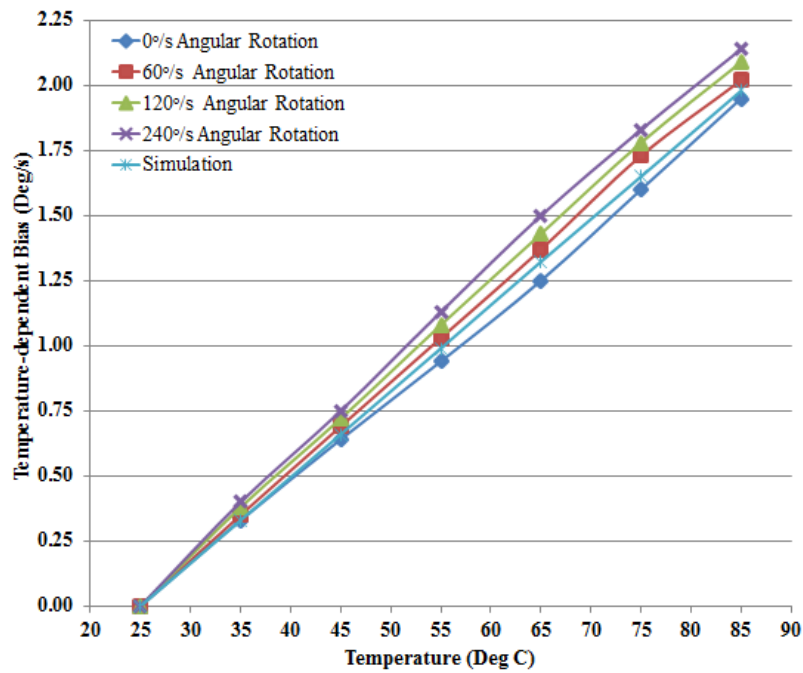


Figure 3-15: Comparison of Simulation and Experimental Temperature-dependent Bias of ADIS16250 from 25°C to 85°C

Table 3-4: Comparison of Simulation and Experimental Temperature-dependent Bias Value of ADIS16250 from 25°C to 85°C

| <b>Experimental/Simulation</b> | <b>Temperature Dependent Bias Value (Deg/s) from 25°C to 85°C</b> |
|--------------------------------|---|
| 0°/s Angular Rotation          | 1.95  |
| 60°/s Angular Rotation         | 2.02  |
| 120°/s Angular Rotation        | 2.09  |
| 240°/s Angular Rotation        | 2.14  |
| Simulation                     | 1.98  |

Figure 3-15 and Table 3-4 show that simulation and experimental results agree fairly well within the manufacturer’s recommended temperature range. The remaining small difference between the simulation and experimental results is likely due to unexamined factors, such as CTE mismatch, thermal expansion, centrifugal force etc., which were neglected to reduce the complexity of the simulation model. The simulation and experimental results confirm that Young’s modulus and damping coefficient are the dominating temperature-dependent factors for the temperature-dependent bias.

### **3.7.2. Examination of Model Validation beyond the Manufacturer’s Recommended Temperature Range**

The validity of the Simulink model outside the manufacturer’s recommended temperature range was also evaluated by comparing simulation results with previously conducted experiments at wider temperature ranges. As discussed in chapter-2, the ADIS16255 single axis MEMS gyroscope was subjected to wider temperature ranges with five thermal cycles from 25°C to 85°C, from 25°C to 125°C, from 25°C to 150°C and from 25°C to 175°C. The manufacturer’s recommended temperature range for ADIS16255 is from -40°C to 85°C. In addition, ADIS16255

gyroscope also features internal calibration that compensates any temperature-dependent variation within  $-40^{\circ}\text{C}$  to  $85^{\circ}\text{C}$ . Therefore, when ADIS16255 was subjected to five thermal cycles from  $25^{\circ}\text{C}$  to  $85^{\circ}\text{C}$ , the MEMS gyroscope did not show any significant increase in temperature-dependent bias due to its compensated output.

When ADIS16255 was subjected to five thermal cycles from  $25^{\circ}\text{C}$  to  $125^{\circ}\text{C}$ , it was found that for nine individual ADIS16255 MEMS gyroscopes, the average temperature-dependent bias at stationary and rotary condition ( $60^{\circ}/\text{s}$  angular rotation) from  $25^{\circ}\text{C}$  to  $125^{\circ}\text{C}$  turned out to be  $3.28^{\circ}/\text{s}$  and  $3.27^{\circ}/\text{s}$ , respectively. For reference, the result of one of the ADIS16255 gyroscopes for five thermal cycles from  $25^{\circ}\text{C}$  to  $125^{\circ}\text{C}$  at  $60^{\circ}/\text{s}$  angular rotation is shown Figure 3-16. At each thermal cycle from  $25^{\circ}\text{C}$  to  $125^{\circ}\text{C}$ , ADIS16255 showed significant increase in temperature-dependent bias when the temperature went beyond  $85^{\circ}\text{C}$  or outside the calibration range and, thus, ADIS16255 showed non-linear behavior of temperature-dependent bias from  $25^{\circ}\text{C}$  to  $125^{\circ}\text{C}$  for all five thermal cycles.

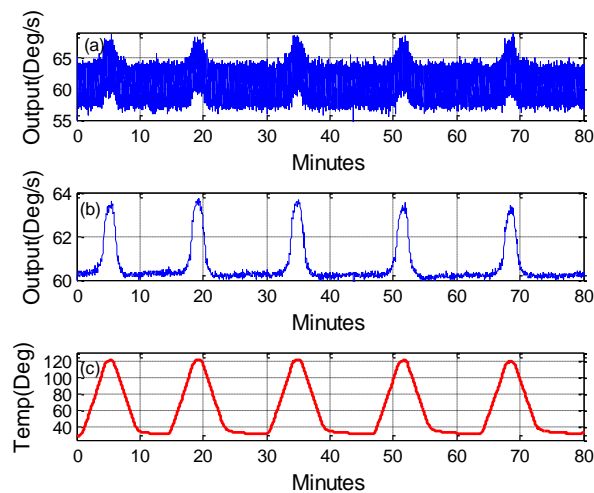


Figure 3-16: Experimental Results of ADIS16255 for Five Thermal Cycles from  $25^{\circ}\text{C}$  to  $125^{\circ}\text{C}$  at  $60^{\circ}/\text{s}$  Angular Rotation

From the Simulink model, the simulated temperature-dependent bias from 25°C to 125°C at 60°/s angular rotation is shown in Figure 3-17. This simulation result shows that when the MEMS gyroscope is exposed to a temperature range from 25°C to 125°C, the simulated temperature-dependent turned out to be is 3.23°/s.

Table 3-5 shows comparison of simulation and experimental temperature-dependent bias value of ADIS16255 from 25°C to 125°C. The simulation and experimental results agree fairly well beyond the manufacturer’s recommended temperature range from 25°C to 125°C. The simulation and experimental results confirm that Young’s modulus and damping coefficient are the dominating temperature-dependent factors for the temperature-dependent bias from 25°C to 125°C. The remaining small difference between the simulation and experimental results is likely due to unexamined factors, such as CTE mismatch, thermal expansion, centrifugal force etc., which were neglected to reduce the complexity of the simulation.

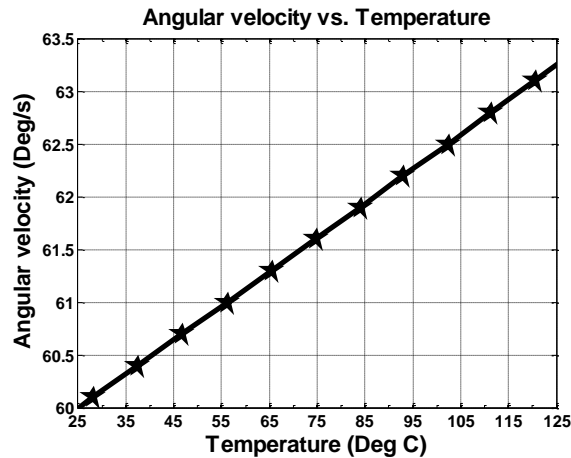


Figure 3-17: Simulated Temperature-Dependent Bias from +25°C to +125°C at 60°/s Angular Rotation

Table 3-5: Comparison of Simulation and Experimental Temperature-dependent Bias value of ADIS16255 from 25°C to 125°C

| <b>Experimental/Simulation</b> | <b>Temperature Dependent Bias Value (Deg/s) from 25°C to 125°C</b> |
|--------------------------------|--|
| Experimental Stationary Bias   | 3.28   |
| Experimental Rotary Bias       | 3.27   |
| Simulated Bias                 | 3.23   |

When the MEMS gyroscope was subjected to 150°C or beyond, it was observed that the angular velocity output of the MEMS gyroscope initially increased and then started to descend at peak temperature. Such behavior of the MEMS gyroscope was unexpected and it is believed that it was not related to change in temperature-dependent parameters such as Young’s modulus, damping coefficient, thermal expansion, CTE mismatch, etc. Some unknown phenomenon took place that requires further research; however, it is beyond the scope of current study. Thus, the developed Simulink model cannot be used to simulate the increasing-decreasing temperature-dependent bias observed during the experiment when the MEMS gyroscope was subjected to 150°C or beyond.

The validation approach indicates that the developed Simulink model fairly well simulates the temperature-dependent characteristic of the MEMS vibratory gyroscope. The simulation results show good agreement with experimental results where temperature-dependent bias of the MEMS gyroscope increase linearly or non-linearly with temperatures within and beyond manufacturer’s recommended temperature range. The validation approach also confirms that Young’s modulus and damping coefficient are the dominating temperature-dependent factors for the

temperature-dependent bias. Thus, when the values of Young's modulus and the damping coefficient at different temperatures are known, the Simulink model can be used to simulate the temperature-dependent characteristic of the MEMS vibratory gyroscope. The developed model cannot be used to simulate decreasing temperature-dependent bias at elevated temperature, which is not due to the variation in temperature-dependent parameters such as Young's modulus and damping coefficient.

### **3.8. Conclusions**

- With the known value of mass, spring stiffness and damping coefficient in the drive and sense direction, the characteristic motion equations of the MEMS vibratory gyroscope can be easily solved by the Simulink model.
- The Simulink model shows a good correlation with experimental results to simulate the temperature-dependent characteristic of the MEMS vibratory gyroscope. Thus, the developed model can be used to get a preliminary idea on the behavior of the MEMS gyroscope prior to executing experimental efforts.
- Simulation results confirm that Young's modulus and damping coefficient are the dominant factors affected by temperature change. It is recommended to design the structure of the MEMS gyroscope robust enough to have these factors minimally effect performance of the MEMS gyroscope.
- The developed model cannot be used to simulate decreasing temperature-dependent bias at elevated temperatures that is not due to the variation in

temperature-dependent parameters such as Young's modulus and damping coefficient.



## **4. High Temperature Reliability of Solder – Literature Review**

Solder joints are a very critical element of electrical and electronic systems as they provide electrical, mechanical and thermal interconnections and pathways. Many applications require that solder joints be robust at high temperatures, including automotive, military, aerospace, and oil and gas exploration electronics, where temperatures can reach up to 200°C. Eutectic Sn/Pb solder cannot be used for these high temperature applications due to its low melting temperature of 183°C. Therefore, high lead-based solders those have high melting temperatures have been used for these applications. Some examples of high lead-based solders are 95Pb-5Sn, 93.5Pb-5.0Sn-1.5Ag and 95.5Pb-2.0Sn-2.5Ag. Although high lead-based solders provide good ductility and fair wetting ability, high temperature industries requiring high temperature electronics are looking for an alternative due to health risk, toxicity, high cost and proposed extensions of RoHS regulation.

Due to the implementation of RoHS regulation that bans use of lead from electrical and electronic components manufactured for standard temperature use after July 1st 2006, the electronic industries have shifted from eutectic Sn/Pb solder to SnAgCu solders. Some of the popular SnAgCu solders are SAC105, SAC305 and SAC405 which have melting/liquidus temperatures near 217°C, higher than the melting temperature of eutectic Sn/Pb solder (183°C). This higher melting temperature of SnAgCu solders presents an opportunity for them to be used for high temperature applications. However, further investigation is needed to determine the reliability of SnAgCu solders under high temperature loading conditions.

This chapter discusses the effects of high temperature on lead-free solders, summarizes the results of previous studies conducted to assess the high temperature reliability of SnAgCu solders and presents a possible way to improve the reliability of SnAgCu solder for high temperature applications.

## **4.1.Effects of High Temperature on Lead-free Solder**

When a lead-free solder joint is exposed to a high temperature environment, three significant changes are noticeable within the solder that can influence the joint's reliability. These three significant changes are interfacial intermetallic growth, coarsening of bulk intermetallics and void formation.

### **4.1.1. Interfacial Intermetallic Growth**

During the reflow process, molten solder reacts chemically with the substrate and initiates the growth of the interfacial intermetallic compound (IMC) layer. The formation of this layer is very important for the structural integrity of the solder joint. However, excessive growth of this interfacial IMC layer creates reliability concerns.

Many studies have been performed to understand the growth of interfacial IMC in various solders [53] [54] [55]. It is known that interfacial IMC layer growth is a diffusion-controlled kinetic phenomenon highly dependent on the temperature [56]. Interfacial IMC layers grow over time and growth accelerates at elevated temperature. The faster growth of interfacial IMC at high temperature can adversely impact the reliability of the solder joints, as it reduces the ductility of the solder joint. Excessive growth of interfacial IMC layers can thus weaken the interface and promote interfacial failure. Thus, a thicker interfacial intermetallic poses reliability concerns.

Many studies confirm that individual interfacial IMC layer growth is due to interdiffusion kinetics as per the following equation [57] [58] [59]:

$$d = d_0 + \sqrt{D * t}$$

Where  $d_0$  is the interfacial IMC thickness after reflow,  $D$  is diffusivity and  $t$  is time. Diffusivity is a temperature dependent process which can be expressed using an Arrhenius-type equation as follows:

$$D = D_0 \exp\left(-\frac{Q}{KT}\right)$$

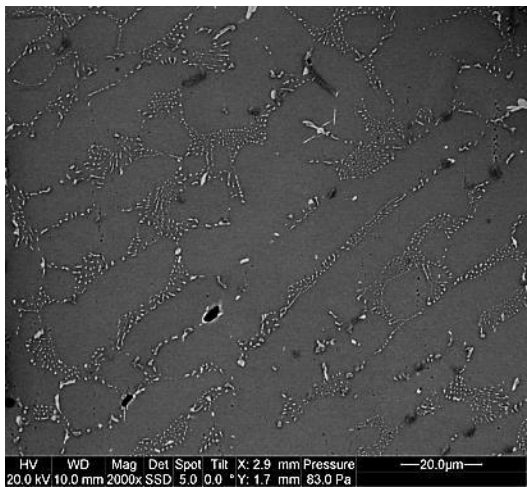
Where  $D_0$  is the diffusivity constant,  $Q$  is the activation energy,  $K$  is Boltzmann's constant, and  $T$  is temperature in Kelvin.

In addition to increasing the thickness of interfacial IMC, high temperature exposure has also been shown to change in the morphology of interfacial IMC. Lee et al. [56] examined eutectic SnPb, Sn3.5Ag, Sn3.8Ag0.7Cu, and Sn0.7Cu solders at 125, 150, and 170°C for 500, 1000 and 1500 hours. It was found that the scallop-type morphology observed after reflow was changed to layer-type morphology after high temperature exposure.

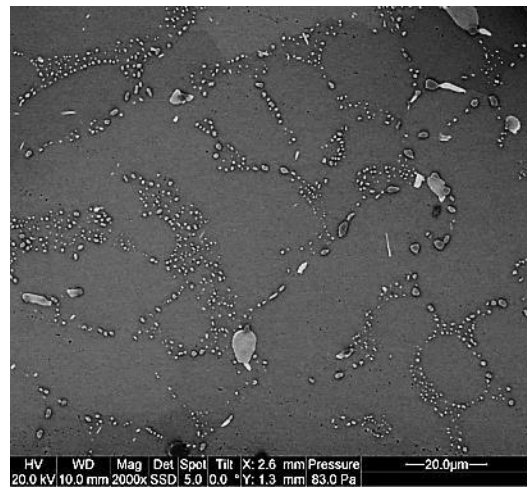
#### **4.1.2. Coarsening of Bulk Intermetallic**

High temperature exposure also leads to the coarsening of intermetallic particles in the solder bulk. Most SnAgCu solders form  $Ag_3Sn$  and  $Cu_6Sn_5$  IMC particles in the solder bulk after reflow. Figure 4-1 (a-d) shows the results of a high temperature exposure test in which an R2512 package was reflowed on an ENIG plated board using SAC305 solder. Due to the presence of gold on the solder pad,  $AuSn_4$  IMC

were formed along with  $\text{Ag}_3\text{Sn}$  and  $\text{Cu}_6\text{Sn}_5$  IMC particles in a Sn-rich matrix after reflow as shown in Figure 4-1 (a). During high temperature, the coarsening of all three IMCs can be seen within 100 hours at  $185^\circ\text{C}$ . The size of all the IMCs further increased during subsequent high temperature exposure after 1000 hours at  $185^\circ\text{C}$  as shown in Figure 4-1 (d). The  $\text{AuSn}_4$  IMC morphology also changed from an acicular (i.e., needle-type) structure after reflow to a laminar (i.e., plate-type) structure during  $185^\circ\text{C}$  temperature exposure. Similar findings on  $\text{AuSn}_4$  IMC growth during isothermal aging have been reported in literature even at lower temperature. Tian et al. [60] investigated a ball grid array (BGA) package reflowed with SAC305 solder on a Au/Ni/Cu solder pad. After reflow, the presence of  $\text{Ag}_3\text{Sn}$ ,  $\text{Cu}_6\text{Sn}_5$  and  $\text{AuSn}_4$  IMCs were found. During isothermal aging at  $150^\circ\text{C}$  up to 120 hours, considerable coarsening in  $\text{AuSn}_4$  IMC took place and its morphology changed from acicular to laminar.



(a)



(b)

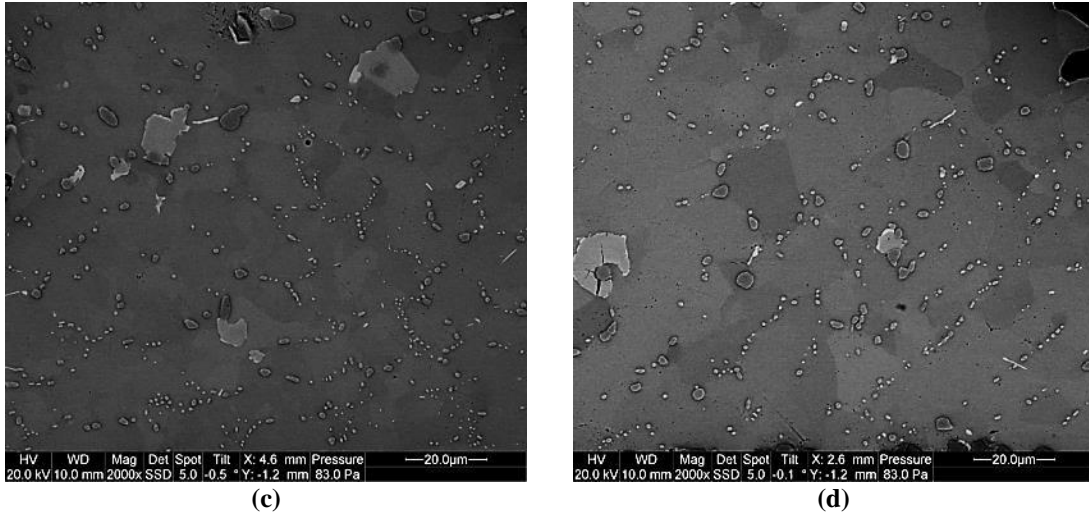


Figure 4-1: R2512 - SAC305 Solder Joint on ENIG Board (a) After Reflow (b) After 100 hours at 185°C (c) After 400 hours at 185°C (d) After 1000 hours at 185°C

SnAgCu solder with a high Ag content also produces large  $\text{Ag}_3\text{Sn}$  platelets. Kim et al. [54] investigated SAC305, SAC357 and SAC396 where Ag content varied from 3.0% to 3.9% by weight. They reported that large  $\text{Ag}_3\text{Sn}$  platelets appear in both SAC357 and SAC396 regardless of the substrate materials. The presence of large  $\text{Ag}_3\text{Sn}$  platelets found to be detrimental as cracks can easily propagate through  $\text{Ag}_3\text{Sn}$  platelets. A shift in fracture mode was also observed from ductile to brittle fracture. It was also recommended that Ag content should be kept below 3.2% to avoid the formation of large  $\text{Ag}_3\text{Sn}$  platelets. Based on this finding, for high temperature applications, SAC305 seems to be preferable to other higher Ag content SnAgCu solder.

#### 4.1.3. Void Formation

In addition to interfacial intermetallic growth and coarsening of bulk intermetallic, high temperature exposure also leads to the formation of Kirkendall voids at the interface between the  $\text{Cu}_3\text{Sn}$  IMC layer and Cu leads or board finishes [61] [62]. The

formation of such voids at the interface can be detrimental to solder joint reliability as voids significantly reduce the interfacial strength, promoting interfacial failure. Kirkendall voids form due to the unbalanced interdiffusion of tin and copper at the interface. Cu has higher diffusivity in Sn compared to Sn diffusivity in Cu. Thus, during migration, vacancies created by Cu atoms are not filled by Sn atoms. Eventually, these vacancies coalesce and form microvoids at the interface or within the  $\text{Cu}_3\text{Sn}$  IMC layer [61]. In this present work, in addition to Kirkendall voids, a unique kind of void was found between the  $\text{Cu}_6\text{Sn}_5$  IMC layer and solder bulk during high temperature exposure, which is discussed in detail in later chapter.

## **4.2.High Temperature Reliability of Lead-free Solder**

This section compiles previous studies on thermal cycling and mechanical shock reliability of various solders under high temperature conditions.

### **4.2.1. High Temperature Thermal Cycling Reliability Test**

The literature on high temperature thermal cycling reliability of lead-free solder is limited. Few studies have examined thermal cycling reliability of solder at where peak temperature ranges from 160°C to 200°C [63][64][65].

One of the earliest attempts to evaluate high temperature thermal cycling reliability of lead-free solder was conducted by the National Center for Manufacturing Science [63]. After performing preliminary assessments on 13 solders, seven lead-free solders were identified for detailed analysis. A variety of components including chip resistors (0805 and 1206), 20 I/O leadless ceramic chip carrier (LCCC), 80 I/O ultra-thin quad flat pack (UTQFP) and 256 I/O ball grid array (BGA) were reflowed using these

seven solders on FR-4 PWB substrates containing imidazole finish. Thermal cycling was performed from -55°C to 160°C. Based on the results from chip resistors and LCCC, it was concluded that SAC405 solder performed as well as or better than Sn3.5Ag solder.

George et al. [64] examined SAC305 and Sn3.5Ag solders under thermal cycling from -40°C to 185°C. Various packages including 256 I/O BGA, 144 I/O BGA, 100 I/O QFP and chip resistors (1210) were assembled on polyimide board featuring ENIG and custom Sn-based finishes. Test results showed that no statistical significant difference in durability was found between SAC305 and Sn3.5Ag solders.

More recently, Crandall [65] investigated four lead-free solders including SAC305 and Sn3.5Ag solders. 256 I/O QFP and chip resistors (2512) were assembled on an ENIG finish polyimide boards. Test boards were subjected to two temperature profiles where the peak temperature exceeded 160°C. It was concluded that SAC305 exhibited superior durability compared to the other three lead-free solders.

From the above studies, it can be concluded that SAC305 and SAC405 are preferred candidates for high temperature thermal fatigue performance. However, SAC305 would be a better choice than SAC405 because Kim et al. [54] showed that formation of large  $\text{Ag}_3\text{Sn}$  platelets detrimental for solder reliability are found in SAC solders with Ag content greater than 3.2%. This might be a reason for better performance of SAC305 than Sn3.5Ag under the thermal cycling condition reported by Crandall [65]. Thus, SAC305 solder seems to be the best pure SAC solder for high temperature thermal fatigue performance.

## 4.2.2. High Temperature Mechanical Drop/Shock Reliability Test

High temperature mechanical drop/shock reliability refers to the mechanical drop/shock reliability of solder examined after high temperature exposure. The majority of the studies performed to examine mechanical drop/shock reliability of solder under high temperature conditions are limited to temperatures below 150°C [66][67][68][69]. The summary of previous studies on mechanical drop/shock reliability of solder with their findings is summarized in Table 4-1:

Table 4-1: Previous Studies of Mechanical Drop/Shock Reliability

| Researchers         | Solder, Substrate, Finish, Package  | Temperature, Duration             | Failure mode  | Findings  |
|---------------------|---|-----------------------------------|---|---|
| Chong et al. [66]   | SAC405 on OSP and ENIG board. FPBGA Package                               | 150°C for 120, 240, and 390 hours | Crack was found at the interface between IMC and copper pad.      | <ul style="list-style-type: none"> <li>- For SAC405/OSP joint, the drop reliability degraded more than 50% after 120 hours at 150°C, and severely reduced to less than five drops after 240 and 390 hours at 150°C due to thicker IMC growth.</li> </ul>            |
| Mattila et al. [67] | CSP (Sn0.2Ag0.4Cu-bumped) assembled on ENIG and OSP FR4 board with SAC387 | 125°C for 500 hours               | Void assisted cracking of component side Cu <sub>3</sub> Sn layer | <ul style="list-style-type: none"> <li>- Significant decrease in drop count was observed after thermal aging exposure.</li> <li>- Presence of Kirkendall voids was observed within Cu<sub>3</sub>Sn layer on component side.</li> <li>- Drop reliability</li> </ul> |



|                 |  |  |   |  |
|-----------------|--|--|---|--|
|                 |  |  |   | was decrease by cracking of Cu <sub>3</sub> Sn layer through Kirkendall voids.   |
| Peng et al [68] | CSP assembled on bare Cu with SAC387   | 100°C and 125°C up to 1000 hours. 150°C up to 200 hours. | Interfacial fracture at the interface of Cu <sub>3</sub> Sn/Cu <sub>6</sub> Sn <sub>5</sub> and Cu <sub>6</sub> Sn <sub>5</sub> /solder on the package side.  | <ul style="list-style-type: none"> <li>- Cracking through interface region was dominant.</li> <li>- Kirkendall voids were observed in the Cu<sub>3</sub>Sn layer but did not directly contribute to drop failures.</li> </ul>  |
| Lee et al [69]  | BGA with electrolytic NiAu finish assembled on OSP finish FR4 with SAC305 on NSMD and SMD pad configuration. | 100°C and 150°C for 500 hours                            | <p>Before aging, for SMD configuration, majority of the failure occurred on the package and the board side interfacial IMCs.</p> <p>After aging, for SMD configuration, crack propagated between (Cu,Ni)<sub>6</sub>Sn<sub>5</sub> IMC and Cu<sub>3</sub>Sn IMC layers on the board side.</p> | <ul style="list-style-type: none"> <li>- NSMD and SMD solder configurations show 53% and 81% degradation, respectively in drop performance after aging at 150°C for 500 hours.</li> <li>- For SMD configuration, board side IMC was the weakest interface after thermal aging.</li> <li>- Shift in failure mode was observed from package side interfacial IMC to board side interfacial IMC.</li> </ul> |

Several conclusions are apparent from the above mechanical drop/shock reliability studies conducted after temperature exposure up to 150°C. First and foremost; mechanical drop/shock load causes brittle fracture at the interfacial IMCs. A thick

interfacial intermetallic formed after temperature exposure poses a reliability risk as it can significantly reduce drop/shock reliability. A failure can occur by crack(s) propagating through various locations including solder/IMC1 interface, IMC1/IMC2 interface, IMC2/solder pad interface, within IMC1, within IMC2 and mixed mode. It is also found that the presence of Kirkendall voids may expedite the crack propagation and cause early failure.

When lead-free solder is subjected to high temperatures (temperatures above 150°C), formation of thicker interfacial IMCs creates an even bigger concern for solder reliability under mechanical shock/drop loading. One of the ways to minimize the degradation of lead-free solder mechanical drop/shock reliability after temperature exposure is by suppressing the growth of interfacial IMCs.

The mechanical drop/shock reliability performance of SnAgCu solders is inferior to the conventional Sn-Pb eutectic solder. This is due to the fact that SnAgCu solders have a higher modulus and a longer stress relaxation time compared to conventional Sn-Pb eutectic solder. Though conventional Sn-Pb eutectic solders exhibit superior mechanical drop/shock reliability, it cannot be used for high temperature applications due to its lower melting temperature. There is however a lack of documentation of high temperature mechanical shock reliability of lead-free solders, especially above 170°C.

As previously discussed in section 4.2.1, SAC305 solder exhibits superior high temperature thermal cycling reliability performance under max temperatures of 185°C and 200°C. However, mechanical drop/shock resistance of SnCuAg solders is poor, especially SAC305. This is a big concern for high temperature applications where

mechanical drop/shock reliability performance is required. Thus, there is a need for improving the mechanical drop/shock reliability performance of SAC305.

### **4.3. A Technique to Improve Drop/Shock Reliability of SnAgCu Solders**

Recently, many researchers have investigated a unique technique to improve the drop/shock reliability of SnAgCu solders. This technique features tailoring the solder interconnect properties by alloying with small amounts of additional elements. A wide variety of alloying elements doped in SnAgCu solders have been investigated including Mn, Ce, Ti, Y, Ge, Bi, Zn, In, Ni, Co etc [70][71][72].

One comprehensive investigations was performed by Liu and Lee [70] [71] who studied effects of various dopants to examine improvement in drop performance. These dopants include Ge, Ni, Mn, Ce, Bi, Y and Ti alloyed alone or in combination to SAC105, a low Ag SnAgCu solder. For comparison, four commercial solders were also examined including SAC305, SAC387, SAC105 and Sn/Pb eutectic solders. BGA packages were assembled on electroplated Ni/Au solder pad using commercial and modified low Ag solders. The number of drops to failure for each solder is shown in Figure 4-2. It can be seen that drop reliability improvement was observed for Mn, Ce, Bi, Y and Ti dopants where Mn and Ce dopants showed higher improvement and Mn outperform compared to other dopants. In addition to the dopant chemistry, concentration also plays major role. There seems to be an optimum concentration amount for the dopants to get the best drop performance as indicated with a dotted line for Mn, Ce and Y dopants shown in Figure 4-2. For Mn, the drop reliability improved with increasing concentration up to 0.13 wt% of manganese. Adding Mn

concentration beyond 0.13 wt% decreased the drop performance. Similar phenomena were also evident for Ce and Y dopants. Looking at the drop performance of commercial solders, high Ag solder including SAC305 and SAC387 performed the poorest, and SAC105 performance was better than SAC305 and SAC387 but much lower than Sn/Pb eutectic solders.

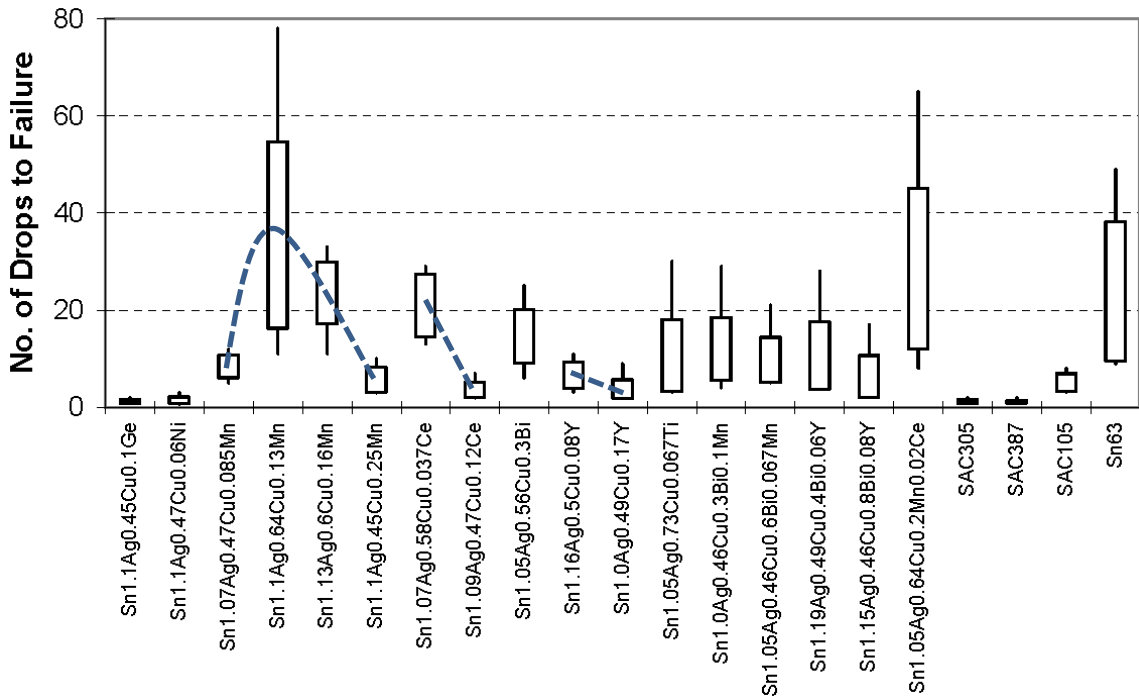


Figure 4-2: Drop Test Results of As-reflowed Solders [71] [70]

Many important conclusions can be made from the results published by Liu and Lee [71] [70]. Clearly, SAC 105 solder has shown better drop performance when alloyed with Mn and Ce dopants. It was also found that an optimal concentration exists for these dopants to achieve superior drop performance. SAC305 solder exhibits poorer drop performance compared to SAC105 solder.

Next section shows the detailed information on the advantages of Mn and Ce dopants in SnAgCu solders.

## **4.4. Advantages of Mn dopant in SnAgCu Solder**

Many researchers have investigated the effects of the addition of a small amount of Mn in various lead-free solders. Effects of Mn dopant in lead-free solders have been summarized for five categories including drop/shock reliability, interfacial IMC growth, melting behavior, undercooling and mechanical properties.

### **4.4.1. Drop/Shock Reliability Improvement**

Liu et al. [73] [74] examined 0.05 wt% Mn doped in SAC105 under drop test conditions. Drop test was performed on as-reflowed and various preconditioned test boards. Compared to SAC105, SAC105+0.05%Mn exhibited drop performance improvement of 20% for as-reflowed, 50% for thermally aged 100 hours at 150°C, 103% for thermally aged 250 hours at 150°C, and 48% for pre-exposed to 250 thermal cycles from -40°C to 125°C.

Liu and Lee [71] also reported superior drop performance by adding 0.13% Mn in low Ag SnAgCu solder. Failure analysis of as-reflowed Sn1.1Ag0.64Cu0.13Mn solder interconnects after drop test revealed the shift in fracture pattern from interfacial failure to increasing mixed-type failure mode. It was also suggested that a shift in failure mode indicates stronger bond strength of the interface.

More interestingly, Liu and Lee [71] [70] found that when 0.085 wt%, 0.13 wt%, 0.16 wt% and 0.25 wt% concentrations of Mn doped in low Ag SAC solder was thermally aged at 150°C for four weeks, higher drop counts were observed for thermally aged compared to the as-reflowed condition for all Mn doped solders. It was also suggested

that drop reliability improvement could be attributed to softening of solder material during thermal aging.

#### **4.4.2. Interfacial IMC Growth Reduction and its Possible Mechanism**

Various studies confirm that trace amount of Mn can help to reduce the growth of interfacial IMCs.

Anderson et al [75] investigated Sn<sub>3.7</sub>Ag<sub>0.6</sub>Cu<sub>0.3</sub>Mn solder on bare Cu under isothermal aging at 150°C up to 1000 hours. They found that Mn was the most effective dopant to suppress the growth of both Cu<sub>3</sub>Sn and Cu<sub>6</sub>Sn<sub>5</sub> intermetallic layers during isothermal aging. In addition, Mn was also able to suppress void formation and coalescence at the interface between Cu<sub>3</sub>Sn and Cu substrate during isothermal aging. Based on the atomic radius and electronegativity, a Darken-Gurry plot was developed to find substitution capability of Mn for Cu atoms. Due to the presence of a higher concentration of Mn within Cu<sub>3</sub>Sn phase and Cu<sub>3</sub>Sn/ Cu<sub>6</sub>Sn<sub>5</sub> interface, it was suggested that Mn tends to substitute Cu into interfacial IMCs. This substitution produces increased lattice-strain in the intermetallic layers and reduces interdiffusion of Sn and Cu to suppress the growth of Cu<sub>3</sub>Sn and Cu<sub>6</sub>Sn<sub>5</sub> intermetallic layers and also void formation and coalescence at the interface between Cu<sub>3</sub>Sn and Cu substrate.

Liu et al. [73] [74] also found reduction in the growth rate of board side and component side interfacial IMC thickness of SAC105+0.05%Mn solder under isothermal aging at 150°C up to 1000 hours. After selectively etching interfacial IMC, it was also found that interfacial IMC particles for doped Mn solder thickened more

slowly than SAC105 solder during 150°C isothermal aging. It was suggested that reduction in the growth rate of interfacial IMC could be due to inclusion of Mn in the interfacial IMC layer.

Liu and Lee [71] reported that they observed a small amount of manganese-containing particles after reflow near the IMC layer on Sn1.1Ag0.64Cu0.13Mn solder joint. As the manganese concentration increased from 0.13 wt% to 0.25 wt%, they also reported an accumulation of Mn-Sn intermetallic particles near IMC layer. With higher concentration of Mn dopant, Sn1.1Ag0.45Cu0.25Mn showed presence of MnSn<sub>2</sub> intermetallic particles in the solder near the board side interfacial intermetallic layer. The reason for Mn atoms migration and accumulation near the interfacial IMC layer in the form of MnSn<sub>2</sub> particles was not given.

Ghosh et al. [76] examined Sn3.64Ag0.7Cu+0.61Mn solder under isothermal aging at 100°C up to 200 hours. They reported that addition of 0.61%Mn exhibited sluggish growth of Cu<sub>6</sub>Sn<sub>5</sub> during isothermal aging.

More recently, Crandall [65] examined Sn2.6%Ag0.8%Cu solder, doped with 0.05%Mn under high temperature isothermal aging at 185°C and 200°C for 1000 hours and 500 hours respectively. He found that the growth rate of board side interfacial IMC was lowest in Mn doped solder compared to SAC305.

#### **4.4.3. Effects on Melting Behavior**

Liu and Lee [71] [70] found that addition of a small amount of Mn has a negligible effect on the melting behavior of SAC105. Though it was demonstrated for low Ag SnAgCu solder, a similar response is expected for addition of a small amount of Mn

on the melting behavior of SAC305. This makes Mn dopant more attractive for high temperature applications.

#### **4.4.4. Effects on Undercooling**

Lin et al. [77] studied SAC105, SAC105+0.15%Mn and SAC105+0.50%Mn solders. They reported that addition of Mn dopant drastically reduces undercooling. The reported undercooling for SAC105+0.15%Mn and SAC105+0.50%Mn solders were 9.5°C and 6.8°C respectively; whereas undercooling for SAC105 was 24.0°C.

Similar observation was also found by other researchers. Kim et al. [78] examined SAC305 and SAC305+0.10%Mn solder. They also found that small addition of Mn in SAC305 remarkably suppresses the undercooling.

Boesenberg [79] conducted a detailed study to examine the undercooling effect of Mn dopant in SnAgCu solder. He examined 0%, 0.01%, 0.05%, 0.10%, 0.15%, 0.20% and 0.25% manganese alloyed in Sn<sub>3.5</sub>Ag<sub>0.95</sub>Cu solder. He found that the addition of a small amount of Mn, even 0.01% Mn, significantly reduced undercooling from 12°C to 4°C and remained near 4°C up to 0.25% concentration of Mn. However, it was also found that 0.01%, 0.05% and 0.10% Mn showed presence of Ag<sub>3</sub>Sn blades or platelets IMCs. Thus, an optimal concentration of Mn exists that suppress the formation of Ag<sub>3</sub>Sn platelets in the solders they examined. Addition of Mn greater than 0.15% in Sn<sub>3.5</sub>Ag<sub>0.95</sub>Cu promoted heterogeneous nucleation and limited Ag<sub>3</sub>Sn blade formation.



#### 4.4.5. Effects on Mechanical Property

Liu and Lee [71] [70] found no change in hardness of bulk solder due to the addition of Mn dopant. Liu et al. [73] [74] also reported that addition of 0.05%Mn in SAC105 did not change tensile strength, yield strength and Young's modulus. However, % elongation or ductility was found to be higher for SAC105+0.05%Mn than SAC105.

In contrast, Kim [78] reported that ultimate tensile strength was slightly increased by doping 0.10 wt% of Mn in SAC305. In addition, they also found significant improvement in ductility for SAC305+0.1%Mn compare to SAC305. It was also reported that Mn also caused fine precipitates within primary  $\beta$ -tin dendrites which was believed to be the reason for higher strength and a significant improvement in ductility.

Lin et al. [77] [80] studied SAC105, SAC105+0.15%Mn and SAC105+0.50%Mn. With the addition of Mn dopant, they reported a reduction in ultimate tensile strength (UTS); however, ductility was improved. In addition, nanoindentation results indicated that SAC105+0.15%Mn and SAC105+0.50%Mn solders exhibited lower elastic modules compare to SAC105. It was also indicated that a reduction in elastic modules of solder might help to improve drop life time.

More recently, Mukherjee et al.[81] [82] investigated time-dependent creep response of SAC105 and SAC105+0.05Mn. They found that that the addition of Mn increases the creep resistance of SAC105 solder by one to two orders of magnitude at the tested stress levels of 2–20 MPa.

It is clear from the above summary that addition of a small amount of Mn in lead-free solder has positive results on improving the properties of lead-free solder. Only limited studies have been performed to assess reliability improvement on Mn doped solders. These limited reliability studies have primarily investigated SAC105, a low Ag SnAgCu solder. However, high silver content solders, such as SAC305 and SAC405, are typically used for high temperature application; it is thus necessary to study effects of manganese in high silver content solder.

#### **4.5. Advantage of Ce dopant in SnAgCu Solder**

It has been observed that a minute amount of Ce addition can greatly enhance the properties of an alloy. Effects of Ce dopant in lead-free solders have been summarized in five categories including drop/shock reliability, interfacial IMC growth, melting behavior, microstructure and mechanical properties.

##### **4.5.1. Drop/Shock Reliability Improvement**

Liu et al. [73] [74] examined 0.02 wt% Ce doped in SAC105 under drop test condition. Drop test was performed on as-reflowed and various preconditioned test boards. Compare to SAC105, SAC105+0.02%Ce exhibited drop performance improvement of 21% for as-reflowed condition, 223% for thermally aged 100 hours at 150°C, 233% for thermally aged 250 hours at 150°C, and 67% for pre-exposed to 250 thermal cycles from -40°C to 125°C.

Liang et al. [83] investigated Sn<sub>2.5</sub>Ag<sub>0.5</sub>Cu (SAC2505) alloyed with 0%, 0.03%, 0.05% and 0.1% concentrations of Ce. Drop testing was performed on as-reflowed and thermally aged test boards at 125°C for 300 hours. For the drop test conducted on

as-reflowed boards, SAC2505+0.03%Ce showed the best drop test performance among all solder. However, drop testing performed after thermal aging at 125°C for 300 hours, SAC2505+0.10%Ce outperformed other solders. In addition, SAC2505+0.10%Ce showed no observable degradation in drop performance after thermal aging compare to as-reflowed condition. 0.03% and 0.05% Ce doped in SAC2505 also showed better drop performance than SAC2505 after thermal aging.

More interestingly, Liu and Lee [71] [70] found that when 0.037 wt% Ce doped in SAC105 solder was thermally aged at 150°C for four weeks, higher drop counts were observed for thermally aged compared to as-reflowed condition for Ce doped solder. It was also suggested that drop reliability improvement could be attributed due to softening of solder material during thermal aging.

#### **4.5.2. Interfacial IMC Growth Reduction and its Possible Mechanism**

Wu et al. [84] examined effect of 0.25% and 0.50% concentrations of combined Ce and La dopants in Sn3.5Ag and Sn0.7Cu solders. Sn3.5Ag and Sn0.7Cu solders were also analyzed for comparison. It was found that the addition of both 0.25% and 0.50% concentrations dopants suppressed the growth of  $\text{Cu}_6\text{Sn}_5$  and  $\text{Cu}_3\text{Sn}$  interfacial IMCs in both Sn3.5Ag and Sn0.7Cu solders during isothermal aging at 170°C up to 1000 hours. Addition of 0.50% concentration of Ce and La resulted in the lowest interfacial IMC thickness. It was suggested that the reason for interfacial IMC reduction during thermal aging was attributed due to fact that Ce and La reacts with Sn near the interface between solder and  $\text{Cu}_6\text{Sn}_5$  IMC and form Sn-(Ce,La) compound. Formation

of Sn-(Ce,La) compound lowers the activity of Sn at the interface and thus reduces the further growth of  $\text{Cu}_6\text{Sn}_5$  and  $\text{Cu}_3\text{Sn}$  IMCs during isothermal aging. This study didn't show the presence of Sn-(Ce,La) compound at the solder/IMC interface. However, It was also mentioned that the size of Sn-(Ce,La) compound would be very small and accumulation can only be observed under a slow cooling solidification.

Law et al. [85] investigated 0.05%, 0.1% and 0.25% concentrations of combined Ce and La dopants in SAC357 on copper coupons. Thermal aging was performed at 170°C for 100, 200, 500 and 1000 hours. It was found that SAC357+X% (Ce and La) showed reduced growth of  $\text{Cu}_6\text{Sn}_5$  and  $\text{Cu}_3\text{Sn}$  interfacial IMCs during isothermal aging. It was suggested that inhibition of interfacial IMCs growth in Ce and La doped solders could be due to lower activity of Sn at the interface due to Sn-(Ce,La) compound formation.

Liu et al. [73] [74] found a reduction in the growth rate of board side interfacial IMC of SAC105+0.02%Ce solder under isothermal aging at 150°C up to 1000 hours. After selectively etching interfacial IMC layer, it was also found that interfacial IMC particles for doped Ce solder thickened slower than SAC105 solder during 150°C isothermal aging. It was speculated that a reduction in the growth rate of interfacial IMC could be due to inclusion of Ce in the interfacial IMC layer.

### **4.5.3. Effects on Melting Behavior**

Chen et al. [86] examined melting behavior of various concentrations of Ce including 0%, 0.025%, 0.05%, 0.1%, 0.25%, 0.5% and 1.0% in SAC387 solder. With the addition of Ce doping in SAC387, liquids temperature remains within 220°C to

225°C. Thus no significant change in melting temperature was observed with addition of Ce dopant in SAC387 solder.

Wu et al. [84] also found a negligible effect from the addition of Ce and La on the melting temperature of Sn3.5Ag solder. The observed melting temperature of Sn3.5Ag+0.25% (Ce,La) and Sn3.5Ag+0.50% (Ce,La) were 220.9°C and 220.8°C respectively, as compared with 221.4°C for Sn3.5Ag solder.

Liu and Lee [71] [70] found that addition of small amount of Ce (0.037 wt%) has a negligible effect on the melting behavior of SAC105 solder.

Above studies show negligible effect of Ce dopant addition in various lead-free solders. This makes Ce dopant more attractive for alloying with solders used for high temperature applications.

#### **4.5.4. Effects on Microstructure**

Chen et al. [87] conducted a detailed study to examine the effect of Ce on the microstructure of SnAgCu solder. They examined 0%, 0.025%, 0.05%, 0.1%, 0.25%, 0.5% and 1.0% concentrations of Ce in SAC387 solder. With the addition of Ce,  $\beta$ -tin dendrite refinement was observed. Further analysis showed that Ce atoms aggregated on the boundaries of primary  $\beta$ -tin dendrites and formed a web-like structure surrounding  $\beta$ -tin dendrites. Since the atomic radius of Ce (0.183 nm) is around 33% larger than Sn (0.141 nm), Ce is less likely to play a role in a solid solution strengthening by replacing Sn atoms. Instead, Ce atoms accumulate at the high energy region such as the boundaries of  $\beta$ -tin dendrites. Thus, aggregation of Ce on the

boundaries of primary  $\beta$ -tin dendrite was observed which led to refinement of primary  $\beta$ -tin dendrite during solidification.

Wu et al. [84][88][89][90] investigated effects of Ce and La on various lead-free solders including SnZn, SnAg and SnCu. They found that the addition of Ce and La in lead-free solders refines  $\beta$ -tin dendrite and decreases the size of  $\text{Ag}_3\text{Sn}$  and  $\text{Cu}_6\text{Sn}_5$  IMCs in solder bulk. Such behavior of Ce and La is due to the fact that Ce and La are active (surface-active) elements and they accumulate at the interface of various phases during solidification. The absorption of these surface active elements decreases the surface energy which reduces the further growth of the interface of phase during solidification which leads to refinement of the microstructure. In addition, Ce has higher affinity for Sn than for Cu and Ag in the solder matrix. Thus, effect of decrease in the size of  $\beta$ -tin dendrite is more apparent with addition of Ce and La.

Law et al. [85] investigated SAC357 doped with 0.05%, 0.1% and 0.25% concentrations of combined Ce and La dopants. They found that the addition of Ce and La reduced  $\beta$ -tin dendrite size. The size of dendrites reduced from 10 to 20 microns for SAC357 to 5 to 10 microns for SAC357+0.25% (Ce and La). An additional phase containing Ce and La was not detected due to the small amount of dopant and due to its fine dispersion. In addition, they also found that 0.1% concentration for La and Ce resulted in the best wetting behavior. An excessive amount of Ce and La concentration (0.25%) deteriorated the benefit of these dopants on wetting behavior.

#### 4.5.5. Effects on Mechanical Property

As the microstructure of solder is refined by the addition of Ce dopant, it is foreseen that mechanical properties will also improve.

Chen et al. [87] examined 0%, 0.025%, 0.05%, 0.1%, 0.25%, 0.5% and 1.0% concentrations of Ce in SAC387 solder. They found that 0.1%Ce in SAC387 resulted in the highest creep-rupture life. Adding concentration of Ce more than 0.1% deteriorated creep performance and SAC387+1.0%Ce resulted in the lowest creep-rupture life. The ultimate tensile strength was increased slightly. Ductility was also increased for Ce concentration from 0.025% to 0.25%. However, adding higher concentration above 0.25% resulted in a significantly lower ductility. Compared to SAC387, addition of 0.025%, 0.05%, 0.1%, 0.25%, 0.5% and 1.0% concentrations of Ce resulted in an improvement in elastic modulus of 1.2%, 1.8%, 8.9%, 36.6%, 45.8%, and 55.7%, respectively.

Wu et al. [88][89][90] reported that addition of 0.25% and 0.50% Ce and La in SnCu, SnAg and SnZn solders resulted in an increase in UTS of about 23%, 15% and 18%, respectively. It was also reported that the addition of 0.25% and 0.50% Ce and La to various solders also resulted in a reduction in the elongation or ductility. Reduction in elongation or ductility could be due to the formation of hard Ce or La bearing particles. In addition, significant improvement in creep performance was observed with addition of Ce and La dopants.

Liu and Lee [71] [70] found no change in hardness of bulk solder due to the addition of Ce dopant.

It is clear from the above summary that addition of small amount of Ce in lead-free solder improves the properties of lead-free solder. However, only limited studies have been conducted to assess reliability improvement on Ce doped solders. These limited reliability studies have primarily investigated SAC105, a low Ag SnAgCu solder. However, high silver content solders, such as SAC305 and SAC405, are typically used for high temperature application; it is thus necessary to study effects of Ce in high silver content solder.

#### **4.6. Research Gap**

The literature cited above suggests that small amounts of Mn and Ce added to various lead-free solders offer significant improvement in solder properties, thus resulting in substantial improvement in drop reliability. However, there is a lack of a systematic evaluation of Mn and Ce dopant in SAC305 solder. Since SAC305 solder has shown superior high temperature thermal cycling reliability, Mn and Ce are the potential dopants which can be alloyed in SAC305 solder to improve its drop/shock performance without affecting melting temperature of SAC305 solder. If Mn and Ce dopants also show drop/shock performance improvement in SAC305 solder, a suitable lead-free solder alloy can be available for high temperature applications that exhibits both high temperature thermal fatigue and mechanical drop/shock reliability to replace currently used high lead based solders for applications with operation temperature up to 200°C.



## 5. Experimental Selections

This chapter describes various experimental selections decision made for this research. After careful literature search of potential dopants, Mn and Ce dopants were selected to examine in this study. The detail information on solder selection, component selection, printed circuit board (PCB) design and fabrication, PCB reflow assembly, test board inspection and printed wiring assembly (PWA) are discussed in following sections.

### 5.1.Solder Selection

Many SnAgCu based commercial solders are available in the market. Some of the commonly used SnAgCu based solders include SAC105 (98.5%Sn1%Ag0.5%Cu), SAC205 (97.5%Sn2%Ag0.5%Cu), SAC305 (96.5%Sn3%Ag0.5Cu), SAC405 (95.5%Sn4%Ag0.5%Cu), Sn3.5Ag (96.5%Sn3.5%Ag), Sn0.7Cu (99.3%Sn0.7%Cu) etc. SnAgCu containing high levels of Ag (viz. SAC305 and SAC405) are known to exhibit inferior resistance to mechanical loads like shock/drop and vibration. Thus, SAC105 solder, that contains only 1% of Ag, is recommended for better mechanical fatigue resistance. However, reduction in Ag content also reduces creep resistance of solder which compromises its thermal fatigue reliability as SAC405 solder exhibits far better thermal fatigue reliability than SAC105 solder. Because of these two extremes, SAC305 solder that contains 3% Ag is considered to be an optimum and thus became industry standard in applications where both thermal and mechanical fatigue resistance are necessary. For this reason SAC305 solder was selected as a baseline solder.

Though SAC305 solder is an optimum choice for combined thermal fatigue and mechanical shock/drop loading environments, the thermal fatigue resistance of SAC305 is better than its resistance to mechanical loads, which limit its performance in harsh environment applications. Thus, the goal of this research is to find a combination of dopant and its concentration which result in better performance than SAC305 in combined high temperature thermal fatigue and mechanical shock loading. Based on positive results observed in literature where Mn and Ce dopants reduce interfacial intermetallic growth during thermal aging and improve mechanical drop reliability when added to SAC105 solder, two different concentrations of these dopants are selected for comparison in this study.

Commercially available SAC305 that contains 96.5% Sn, 3.0% Ag and 0.5% Cu (by weight) was manufactured for this study by Indium Corporation. This paste used no clean flux, type-3 (mesh size -325/+500 lines-per-inch, average size = 36 micron) solder paste particle size and 89% metal load. Four additional solder pastes were also used each containing one of two different concentrations of either Mn or Ce dopants in SAC305. For manganese doped SAC305 solders, the two different concentrations of Mn dopant were 0.05% and 0.17% by weight. While for cerium doped SAC305 solders, the two different concentrations of Ce dopant were 0.07% and 0.13% by weight. These four custom pastes also used no clean flux, type-3 (mesh size - 325/+500 lines-per-inch, average size = 36 micron) solder paste particle size and 89% metal load which was same as SAC305 baseline solder.

In summary, following five solders were considered for comparison in this study:

- (1) SAC305

(2) SAC305+0.05%Mn

(3) SAC305+0.17%Mn

(4) SAC305+0.07%Ce

(5) SAC305+0.13%Ce

In order to simplify further discussion, the selected solders in this study will be labelled as shown below:

(1) SAC305 (SAC305)

(2) Low Mn (SAC305+0.05%Mn)

(3) High Mn (SAC305+0.17%Mn)

(4) Low Ce (SAC305+0.07%Ce)

(5) High Ce (SAC305+0.13%Ce)

## **5.2.Component Selection**

It is known that the amount of time a solder joint takes to fail depends on package type (i.e. leaded or lead-less), package size (i.e. big or small), package-lead material, and package-lead finish. Based on package-lead material and package-lead finish, the interface between solder and package results in different kinds of interfacial intermetallic layers after reflow that have different effects on the time-to-failure for a solder joint. Thus, in order to have comprehensive understanding of the correlation among type of interfacial IMCs at package/solder interface, package size, solder material and their effects on solder reliability, five package types were selected in this study.

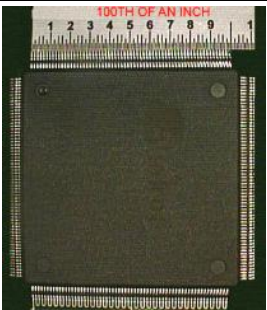
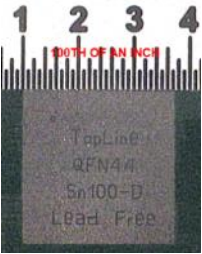

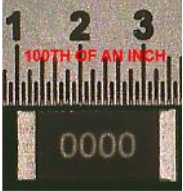

These five packages were a quad-flat pack – 256 (QFP256), two quad-flat no-lead package types (viz. 44 pad (QFN44), and 32 pad (QFN32)), and two surface mount resistors (viz. 2512 (R2512) and 2010 (R2010)). All five packages were dummy components used for solder evaluation purposes. QFP256, QFN44 and QFN32 feature daisy chained dummy die inside the package to simulate a functional die in a real package and are used in the electrical and electronic industries in order to measure resistance continuity during solder testing. The QFP-256, QFN44 and QFN32 leads were also aligned with copper traces on the board to form continuous circuit path.

The QFP256 package has gullwing leads made of copper and plated with matte tin finish. During reflow, the matte tin finish dissolves in the solder which then forms a tin-copper interfacial intermetallic between the copper base metal of the gullwing lead and bulk solder. QFN44 and QFN32 packages do not have protruding leads but feature a big pad at the center underneath the package and many small terminal pads on the periphery of the central pad made of copper and plated with matte tin finish. Similar to QFP256, during reflow, QFN44 and QFN32 form tin-copper interfacial intermetallic layers between the copper pads and bulk solder. R2512 and R2010 have nickel terminals plated in matte tin. During reflow, both resistors form nickel-tin interfacial intermetallic layers between the terminal pads and the bulk solder, which is different from QFP256, QFN44 and QFN32. More details on these packages are summarized in Table 5-1.

Depending on package type, package size, package-lead material and package-lead finish, packages were expected fail at different time intervals. QFP256 features

gullwing leads which minimize stress and strain on the solder joint due to its compliance behavior. QFN44, QFN32, R2512 and R2010 lack any protruded lead and thus cause the solder joint to experience more stress and strain compared to leaded package like QFP256, which results in early solder joint failure. More specifically, QFN44 and QFN32 packages were bigger than R2512 and R2010 packages and featured smaller solder volume per solder joint. It is thus expected that QFN44 and QFN32 packages will fail more rapidly than R2512 and R2010 packages.

Table 5-1: Details on various package types selected in this study

| Package Type               | QFP256   | QFN44  | QFN32   | R2512  | R2010  |
|----------------------------|--|--|---|--|--|
| Package Image              |  |  |  |  |  |
| Length (mm)                | 28.00  | 7.00   | 5.00  | 6.35   | 5.08   |
| Width (mm)                 | 28.00  | 7.00   | 5.00  | 3.20   | 2.54   |
| Thickness (mm)             | 3.93   | 1.00   | 1.00  | 0.65   | 0.56   |
| # of pins                  | 256  | 44   | 32  | 2  | 2  |
| Pitch (mm)                 | 0.4  | 0.5  | 0.5   | -  | -  |
| Lead/pad/terminal material | Copper   | Copper   | Copper  | Nickel   | Nickel   |
| Lead/pad/terminal plating  | Matte tin  | Matte tin  | Matte tin   | Matte tin  | Matte tin  |

| Supplier          | Practical components         | Topline         | Topline         | Practical components | Practical components |
|-------------------|------------------------------|-----------------|-----------------|----------------------|----------------------|
| Supplier part no. | A-QFP256-28mm-.4mm-2.6-DC-Sn | QFN44M.5-T-DE-D | QFN32T.5-T-DE-D | 2512SMR-PL-4K-Sn-0   | 2010SMR-PL-4K-Sn-0   |

### 5.3. Printed Circuit Board (PCB) Design and Fabrication

A schematic and layout for the printed circuit board (PCB) was created using KiCAD open-source software. Due to space constraints, fewer large QFP256 packages were used on the test board than for the smaller QFNs and resistors. The PCB layout consists of two QFP256, eight R2512, eight R2010, four QFN44 and four QFN32 as shown in Figure 5-1. Each package was connected with a separate daisy chain configuration to a common ground forming 26 individual daisy chained connections on each test board. All packages were placed on the primary side of the PCB only. The secondary side of the board features via and copper traces for the circuit connection. For QFP256, QFN44 and QFN32 packages, test pads were placed near each side of the package to identify the location for a solder joint failure after testing. The PCB layout was designed with redundant common grounds such that any package can be removed from the PCB without affecting circuit continuity of other packages on the board. 14 non-plated mounting holes with diameter of 0.125" were added on the border of the PCB board. These mounting holes facilitate assembling two 0.25" thick aluminum frames attached together on top and bottom side of the PCB with 14 nut-bolt assemblies. These aluminum frames provide additional rigidity to the PCB to increase its reliability under harsh environment testing which was also representative of field condition usages of electronic assemblies in harsh environment applications. An additional 28 non-plated drilled holes were placed near the

monitoring wire region to facilitate the attachment of monitoring wires with a strain relieving mounting system.

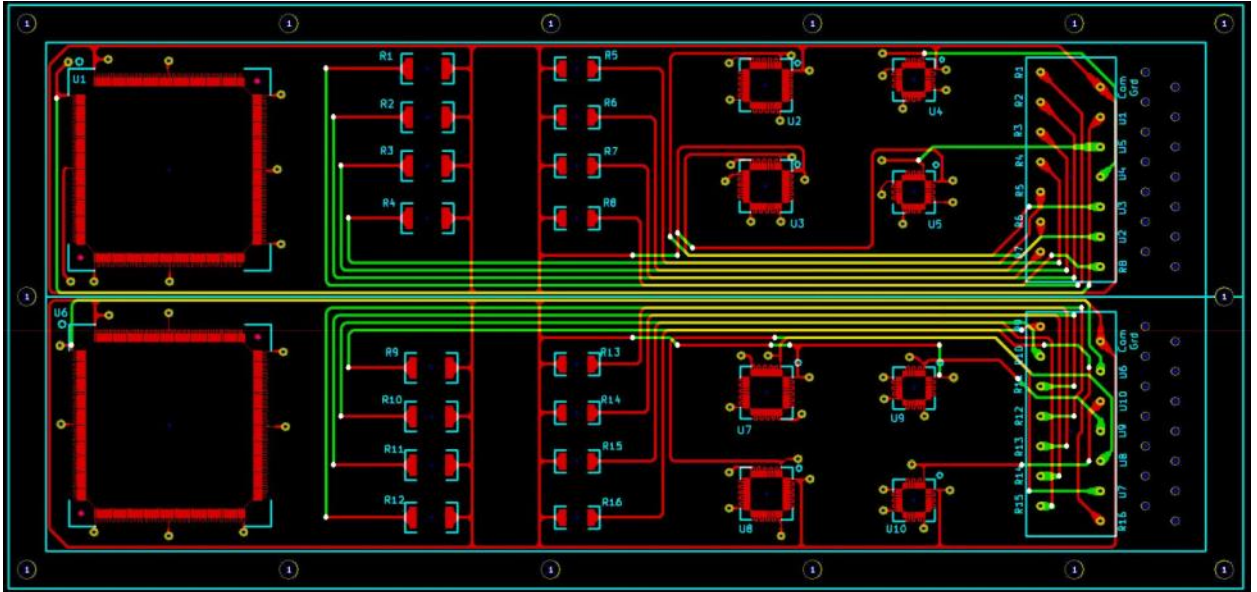


Figure 5-1: Printed Circuit Board Layout

The goal of this study was to examine solder performance under harsh environments including high temperature aging and mechanical shock. Since high temperature is a concern for PCB material, it was thus necessary to fabricate the PCB with a polymer featuring high resistance to thermal degradation under high temperature. Polyimide was selected as the PCB fabrication material due to its higher glass transition temperature ( $T_g$ ) of 260°C compared to conventional FR-4. PCB layout files in Gerber format were sent to the PCB manufacturer for fabrication. The PCB was constructed from two layers of polyimide board and then plated with electroless nickel immersion gold (ENIG) finish. ENIG was selected as the solder pad finish due to its success in literature as a diffusion barrier to minimize the growth of board side interfacial IMC during thermal aging and thermal cycling. The schematic of

polyimide PCB layers is shown in Figure 5-2. The primary and secondary side of fabricated PCB is shown in Figure 5-3 and Figure 5-4, respectively.

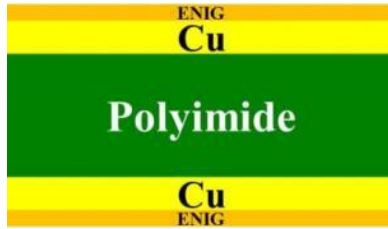


Figure 5-2: Schematic of PCB layers

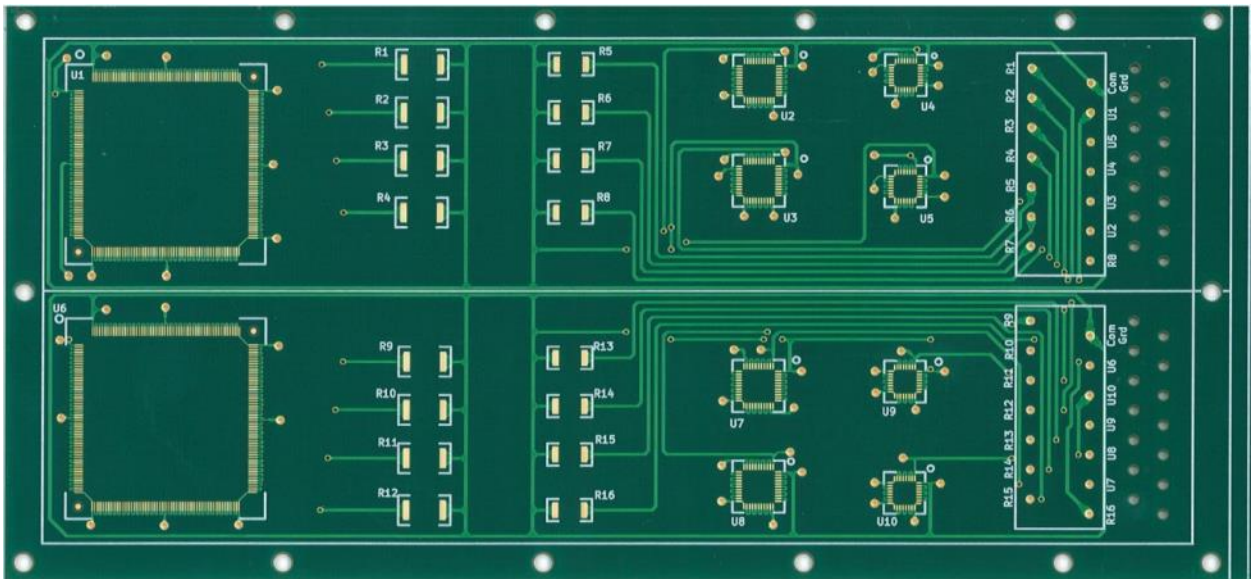


Figure 5-3: Primary side of PCB

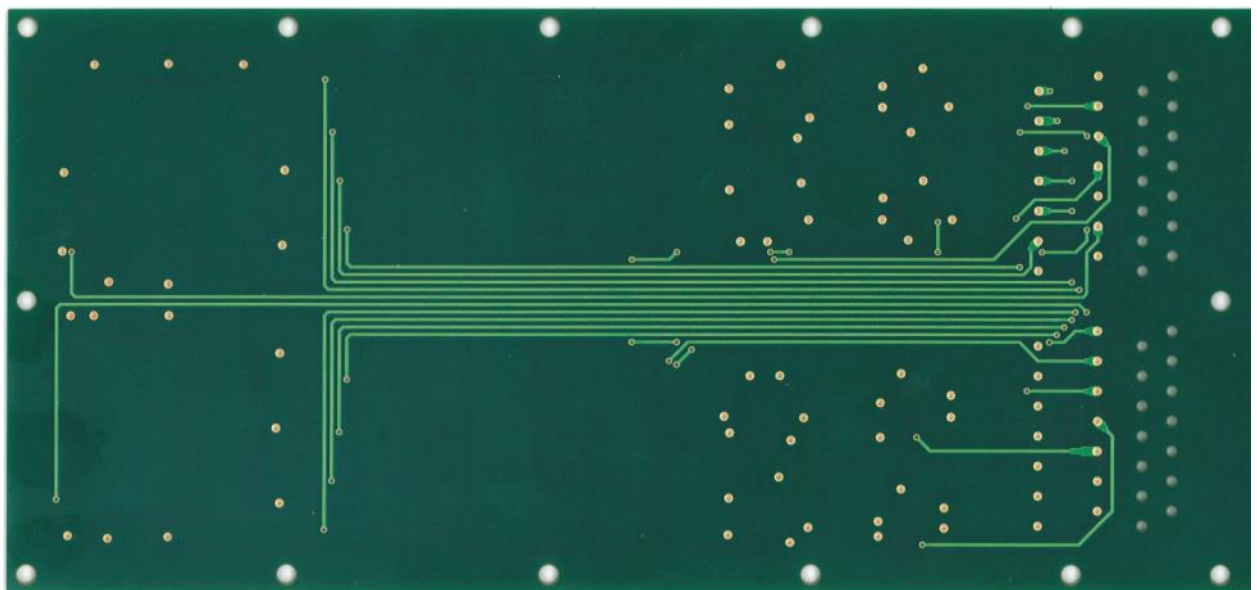


Figure 5-4: Secondary side of PCB



## 5.4. Printed Circuit Board (PCB) Reflow Assembly:

PCB reflow assembly was carried out by Schlumberger Technology Center in Sugar Land, TX, using stencil printing to apply the solder paste and a pick and place machine for accurate package location. A CAD simulation of the PCB assembly, shown in Figure 5-5, was developed to verify the placement of all packages on the board.

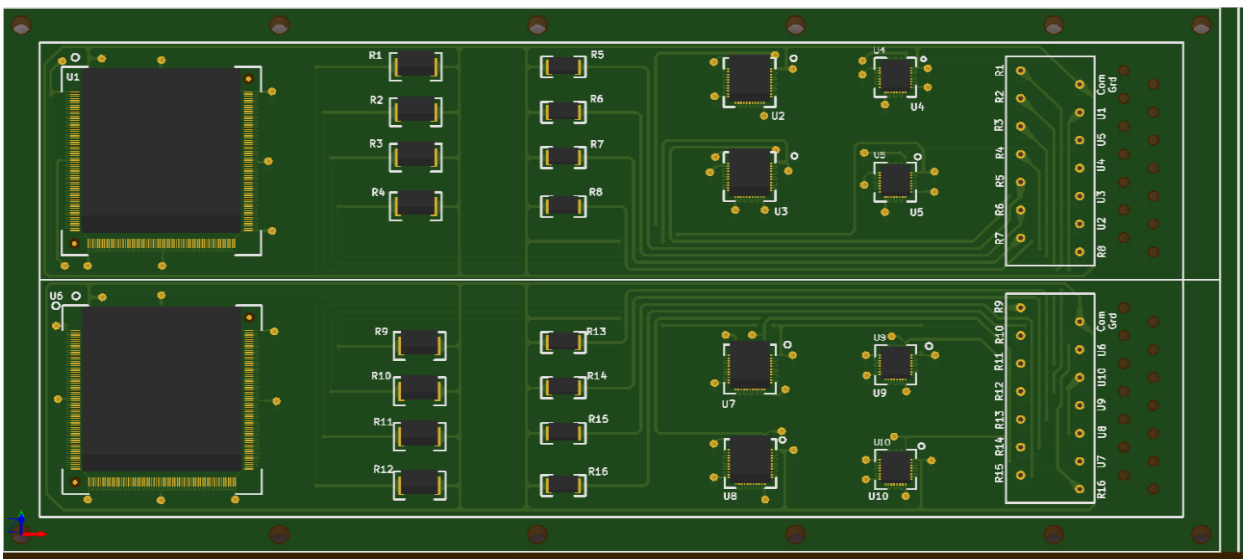


Figure 5-5: A CAD Simulation on PCB Assembly

There were 110 PCB boards which were assembled with five solder pastes that include SAC305, Low Mn, High Mn, Low Ce and High Ce. 22 boards were assembled with each solder paste in a convection reflow oven. The non-commercial solder pastes that were doped with Mn and Ce trace elements do not have an optimum reflow profile. However, the amount of Mn and Ce trace element in SAC305 is low enough that it has negligible effect on the melting temperature range of SAC305 base material (217°C to 220°C). Literature [91] confirms that when SAC105 (low Ag SnAgCu solder) was doped with various concentrations of Mn and Ce (0.10%Mn, 0.13%Mn, 0.16%Mn, 0.02%Ce and 0.037%Ce), the melting behavior of modified

SAC105 solders in comparison to SAC105 were unaffected. All five solder pastes were reflowed with a peak temperature between 245°C and 250°C, based on a general profile provided by Indium Corporation as shown in Figure 5-6 for the reflow of lead-free SnAgCu solder paste with melting point approximately around 217°C. The assembled PCB after reflow is shown in Figure 5-7. An enlarged view of each package type is shown with scale in Figure 5-8.

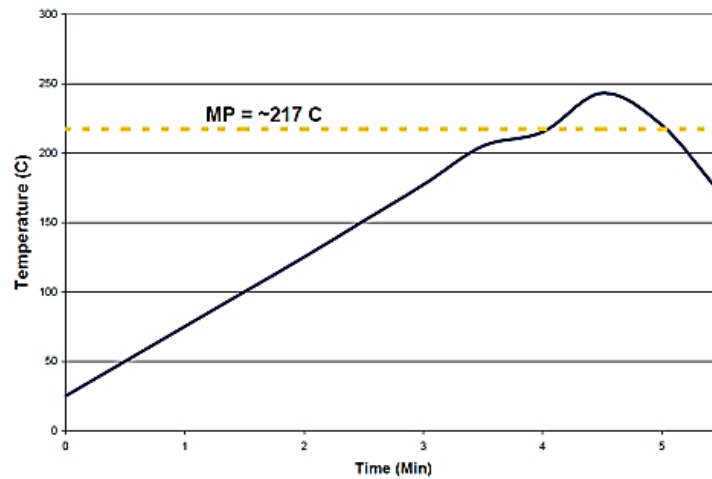


Figure 5-6: A General Guideline on Reflow Profile for SnAgCu Solder by Indium Corporation

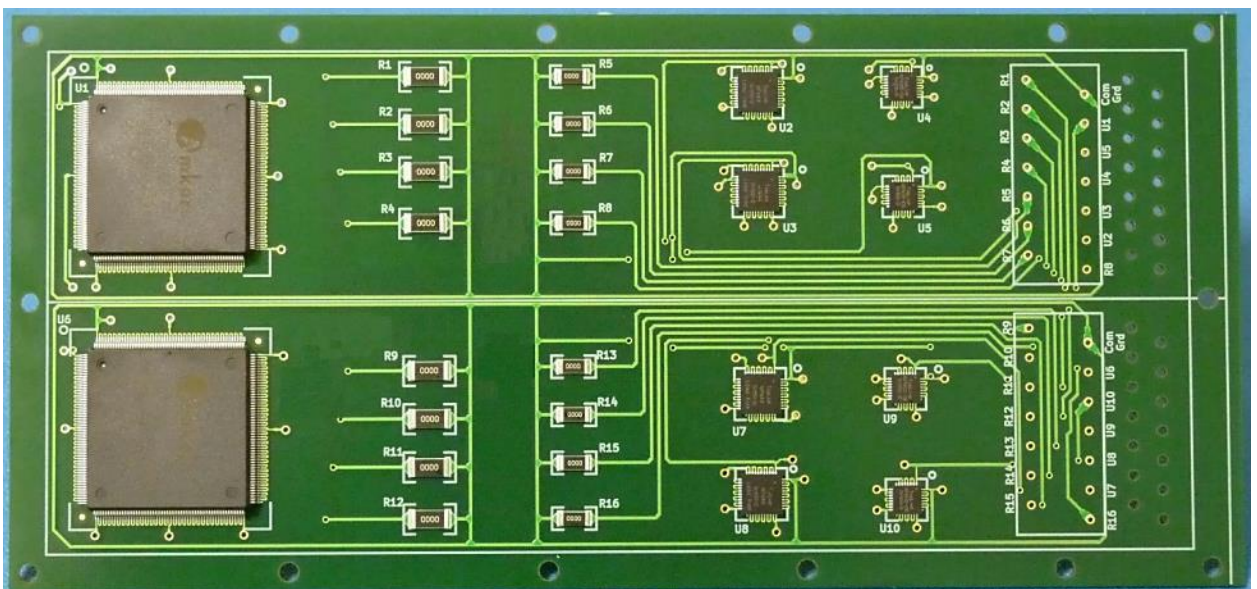


Figure 5-7: Assembled PCB after Reflow

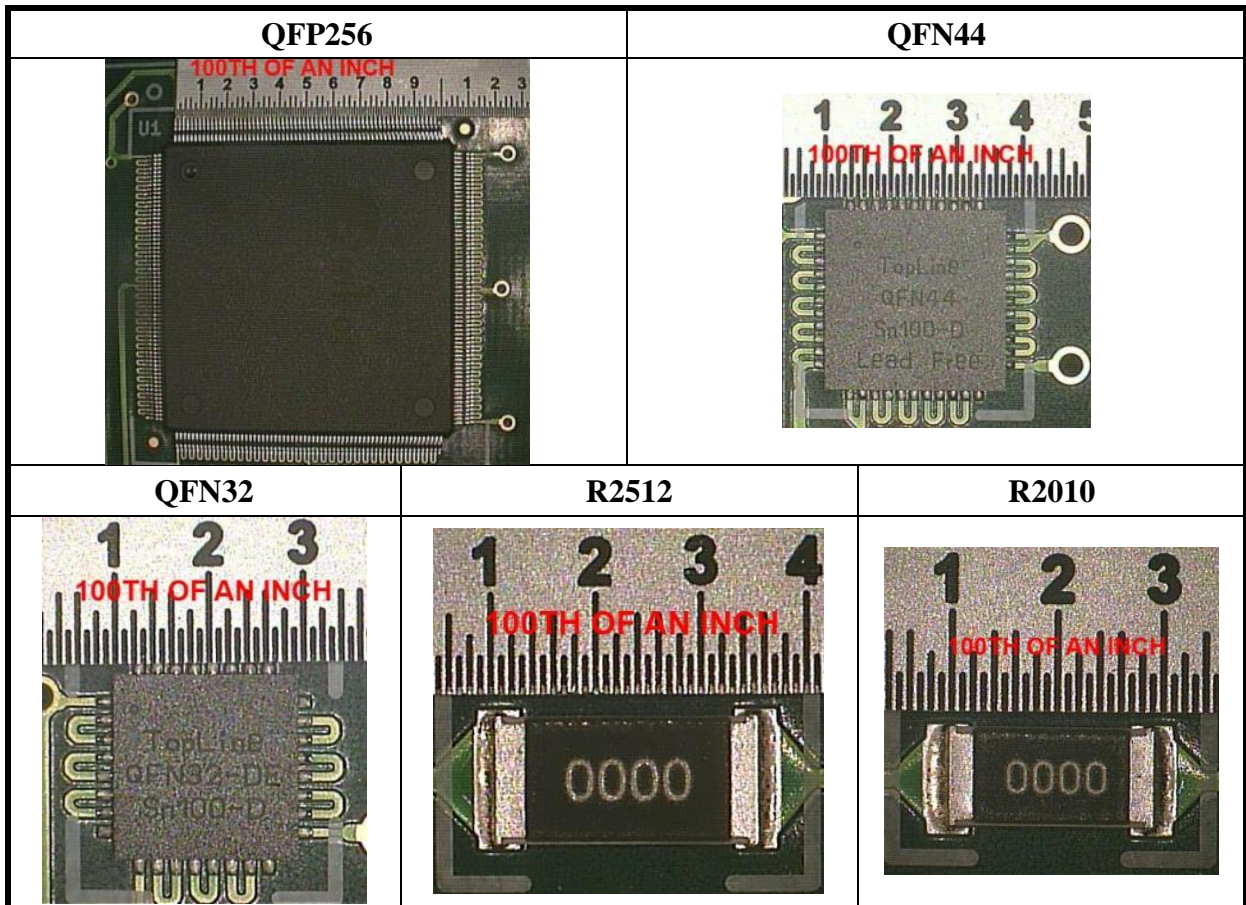


Figure 5-8: An Enlarge View of Each Package Types after Reflow Assembly

### 5.5. Test Board Inspection after Reflow Assembly

All 110 test boards were first visually inspected after reflow assembly for any missing packages or misaligned packages. No such abnormalities were found. Test boards were then inspected for continuity by probing with a multimeter. During this exercise, it was found that QFP256, QFN44, QFN32, R2512 and R2010 packages resulted in 10.0  $\Omega$ , 1.0  $\Omega$ , 0.8  $\Omega$ , 0.35  $\Omega$ , and 0.33  $\Omega$  circuit resistance respectively after reflow assembly. All test boards were also inspected using X-ray for the presence of voids. A sample X-ray image for all package types is shown in Figure 5-9. It was found that the void percentage for all packages was less than 25%, meeting IPC-A-610D voiding acceptability criteria [92].

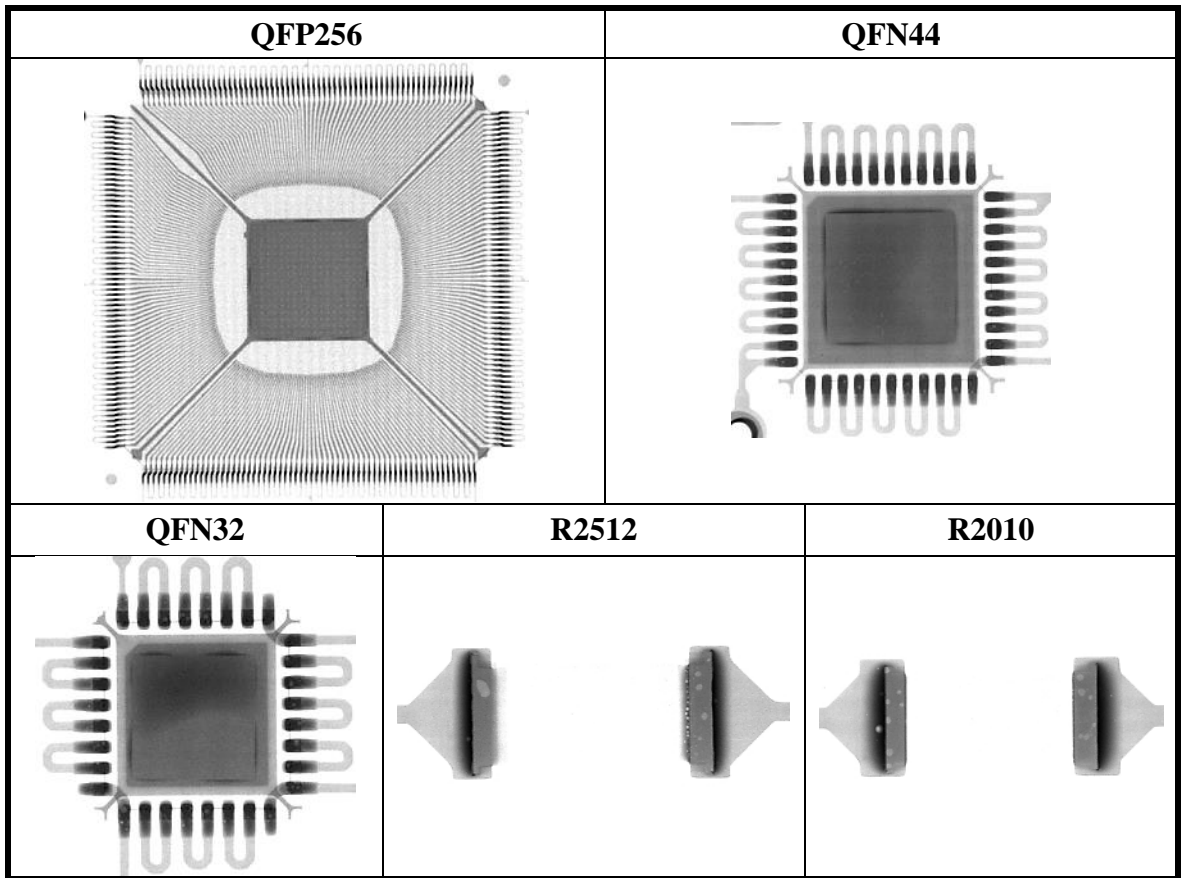


Figure 5-9: X-ray Image of Each Package Types

## 5.6. Printed Wiring Assembly

In order to complete last stage of the board assembly process, test boards were mounted in-between top and bottom aluminum frames with 14 nuts and bolts, as shown in Figure 5-10 and Figure 5-11. High temperature Teflon coated wires were used for in-situ resistance monitoring during test. A strain relieving mounting method was used to attach monitoring wires to the test boards to minimize any additional stress and strain during testing. Eutectic SnAg solder (MP = 221°C) in wire form was used to attach monitoring wires to ENIG plated plated-through-holes (PTH) on the test boards. The other end of the monitoring wires was connected to D-Sub connector which was later connected to a data collection system for in-situ monitoring. Glass



tape was used to secure the monitoring wires which also provided wear and tear protection during testing. Finally, the monitoring wire region was potted with an epoxy on primary (top) and secondary (bottom) side to provide additional rigidity to monitoring wires during testing.

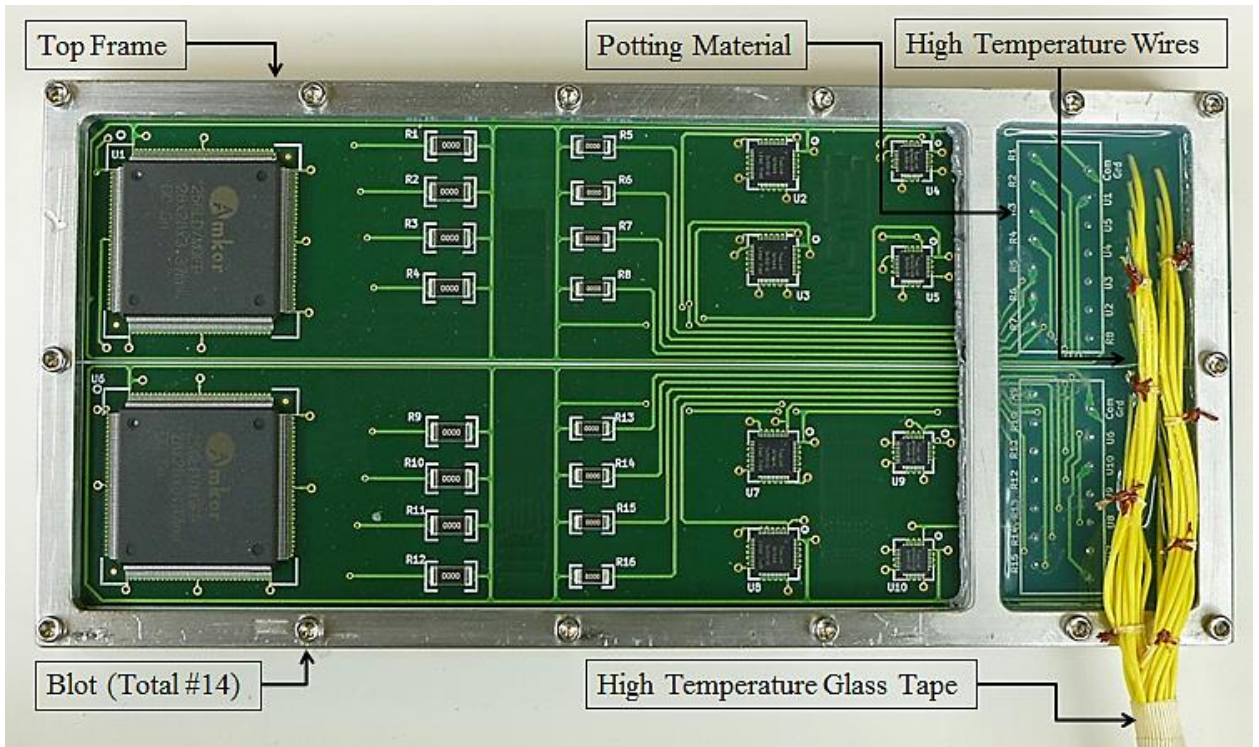


Figure 5-10: Primary-side of Assembled Test Board

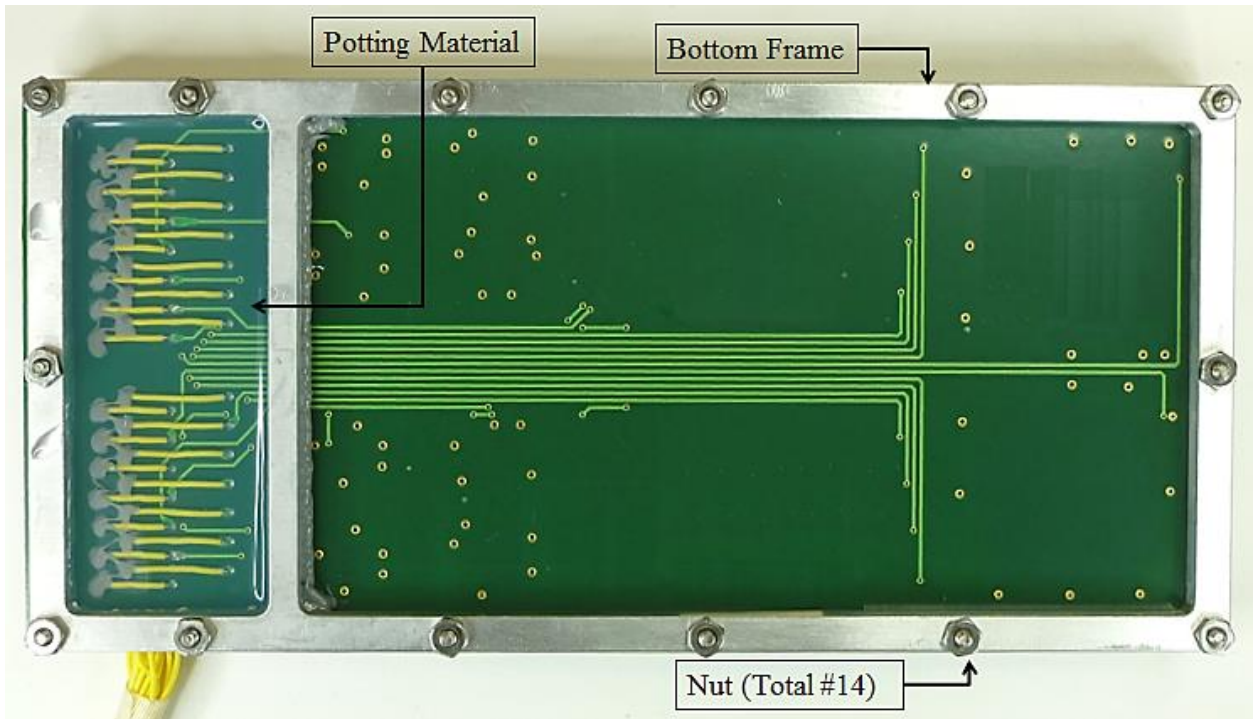


Figure 5-11: Secondary-side of Assembled Test Board

## **6. Design of Experiment, Test Equipment and Monitoring Systems**

The design of experiments matrix, test equipment, and monitoring system were designed for the investigation and assessment of the reliability of lead-free solders exposed to high temperature thermal stress (viz. isothermal aging) and mechanical stress (viz. mechanical shock) with the goal of determining the most reliable solder in these environments. SAC305 solder is known to perform well in thermal fatigue but suffers under mechanical loads, and thus the goal here was to find a combination of a dopant and its concentration that when added to SAC305 will result in better performance under both high temperature mechanical stress loading. Two tests were thus developed for this purpose. The first test was a high temperature isothermal aging test and the second test was reliability test utilizing mechanical shock stress conditions.

All solder pastes used in this study were non-eutectic solders with melting temperature ranges between  $\sim 217^{\circ}\text{C}$  and  $\sim 220^{\circ}\text{C}$ . Two aging temperature conditions above  $150^{\circ}\text{C}$  were selected (viz.  $185^{\circ}\text{C}$  and  $200^{\circ}\text{C}$ ). The selection of these temperatures was based on field conditions observed in high temperature applications such as oil and gas well drilling where electronics can be exposed to such high temperatures during operations.

### **6.1. Aging Test**

The isothermal aging test was conducted at  $185^{\circ}\text{C}$  and  $200^{\circ}\text{C}$  up to 1000 hours. The aging test temperatures were very close to melting temperature range ( $\sim 217^{\circ}\text{C}$  to

~220°C) of the selected solders. The homologous temperatures (i.e. the ratio of operating temperature of solder in Kelvin scale to the melting temperature of solder in Kelvin Scale), at 185°C and 200°C for the selected solders were  $T_{H(185^{\circ}\text{C})} = 0.935$  and  $T_{H(200^{\circ}\text{C})} = 0.965$  respectively (Note: Due to onset of melting at the liquidus temperature of 217°C, it was considered as the melting temperature for the selected solders the homologous temperature calculation). Due to such high homologous temperatures, significant diffusion and formation of thick interfacial IMCs were expected in the solder joint.

### **6.1.1. Design of Experiment (DOE) for Aging Test**

The purpose of the isothermal aging test was to determine the growth of interfacial IMCs for selected solders. Out of five package types selected in this study, three (viz. QFP256, QFN44 and QFN32) had copper lead/pad plated with matte tin finish and soldered to ENIG plated board. During reflow, these package types resulted in Cu-Sn based interfacial IMCs on the component side and Ni-Sn based interfacial IMC on the board side, which grew further during isothermal aging. Two package types (viz. R2512 and R2010) had nickel terminals plated with matte tin finish and soldered to ENIG plated board. During reflow Ni-Sn based interfacial IMCs form on both component and board side on resistor packages, which also grew further during isothermal aging. This study captured the growth of Cu-Sn and Ni-Sn interfacial IMCs on component side and Ni-Sn interfacial IMC on board side from selected package types. In order to have optimum package types for analysis to cover all interfacial IMCs of interest, QFN44 and QFN 32 packages were selected for the aging test to be representative of Cu-Sn interfacial IMCs on component side and Ni-Sn



interfacial IMC on board side, while R2512 package was selected for aging test to be representative of Ni-Sn interfacial IMCs on both component and board side.

Six aging time intervals were selected for each of the two aging tests. These intervals were 0 hour (baseline), 100 hours, 200 hours, 400 hours, 600 hours and 1000 hours. Time=0 (0 hour) condition after reflow assembly was used as a baseline for both aging tests. The design of experiment (DOE) for the isothermal aging test is shown in Figure 6-1 and Figure 6-2. Two solder joints for each selected package types at various aging intervals were examined for IMC thickness measurement.

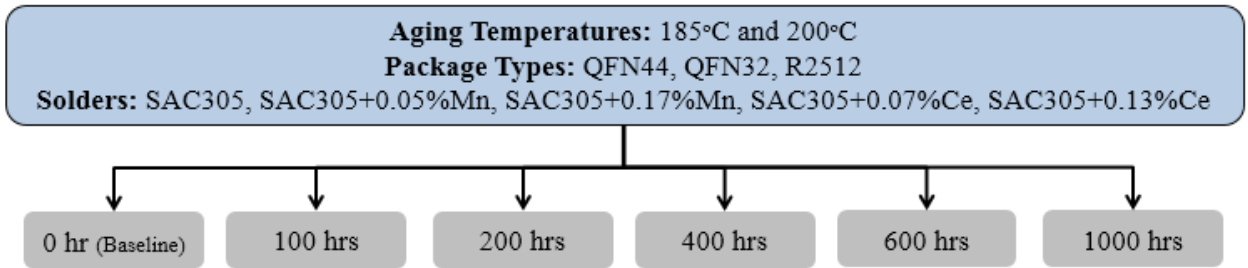


Figure 6-1: Design of Experiment (DOE) for Aging Test

| Package Type | Solder  | Baseline | 185 Deg C Aging |         |         |         |          | 200 Deg C Aging |         |         |         |          |
|--------------|---------|----------|-----------------|---------|---------|---------|----------|-----------------|---------|---------|---------|----------|
|              |         | 0 Hr     | 100 Hrs         | 200 Hrs | 400 Hrs | 600 Hrs | 1000 Hrs | 100 Hrs         | 200 Hrs | 400 Hrs | 600 Hrs | 1000 Hrs |
| QFN44        | SAC305  | X        | X               | X       | X       | X       | X        | X               | X       | X       | X       | X        |
|              | Low Mn  | X        | X               | X       | X       | X       | X        | X               | X       | X       | X       | X        |
|              | High Mn | X        | X               | X       | X       | X       | X        | X               | X       | X       | X       | X        |
|              | Low Ce  | X        | X               | X       | X       | X       | X        | X               | X       | X       | X       | X        |
|              | High Ce | X        | X               | X       | X       | X       | X        | X               | X       | X       | X       | X        |
| QFN32        | SAC305  | X        | X               | X       | X       | X       | X        | X               | X       | X       | X       | X        |
|              | Low Mn  | X        | X               | X       | X       | X       | X        | X               | X       | X       | X       | X        |
|              | High Mn | X        | X               | X       | X       | X       | X        | X               | X       | X       | X       | X        |
|              | Low Ce  | X        | X               | X       | X       | X       | X        | X               | X       | X       | X       | X        |
|              | High Ce | X        | X               | X       | X       | X       | X        | X               | X       | X       | X       | X        |
| R2512        | SAC305  | X        | X               | X       | X       | X       | X        | X               | X       | X       | X       | X        |
|              | Low Mn  | X        | X               | X       | X       | X       | X        | X               | X       | X       | X       | X        |
|              | High Mn | X        | X               | X       | X       | X       | X        | X               | X       | X       | X       | X        |
|              | Low Ce  | X        | X               | X       | X       | X       | X        | X               | X       | X       | X       | X        |
|              | High Ce | X        | X               | X       | X       | X       | X        | X               | X       | X       | X       | X        |

Figure 6-2: Detailed Design of Experiment (DOE) for Aging Test

### **6.1.2. Test Equipment and Measurement Systems for Aging Test**

Two Despatch benchtop convection ovens were used to conduct isothermal aging tests. One benchtop oven was programmed to run at 185°C and the second was programmed to run at 200°C, each for 1000 hours. Prior to testing, both ovens were assessed for temperature stability by placing three thermocouples inside each oven for two days (48 hours). Temperature data were collected at every 30 seconds using an Agilent 34970A multiplexer unit. It was found in-situ temperatures for both ovens were within the range of 0°C and +2°C of the targeted temperature, meeting IPC-9701A standard guideline for isothermal aging test [93]. Prior to aging, samples for each selected package type were carefully removed from the test boards using a diamond circular saw and then placed in various containers labeled with aging time interval for aging test. Since samples were separated from test boards prior to aging, no in-situ monitoring was performed for these samples during isothermal aging test.

### **6.1.3. Cross-sectioning, ESEM, IMC Measurement, EDS and WDS**

#### **Procedure**

After removing samples at various time intervals from aging tests, samples were cold mounted in 1.25" diameter cups with mixture of epoxy resin and epoxy hardener. Samples were then removed from mounting cups and manually ground on 240, 400 and 600 grit silicon carbide grinding papers until an area of interest was reached. After ensuring the surface was free of voids and large scratches, samples were prepared using Buehler Automet 250 auto-polisher which can hold up to six samples at once. Based on many trials, two different polishing methods were developed for

QFNs and resistors. Step by step procedure of polishing steps for QFN44 and QFN32 is shown in Table 6-1, and for R2512 is shown in Table 6-2.

Table 6-1: Polishing Steps for QFN44 and QFN32

| Polishing Material   | Time (mins) | Load (lbs) | Base Speed (rpm) | Head Speed (rpm) | Base and Head Direction | Fluid           |
|--|-------------|------------|------------------|------------------|-------------------------|-----------------|
| 800 Grit Adhesive SiC Paper  | 5           | 1          | 150              | 50               | CW                      | Regular Water   |
| 1200 Grit Adhesive SiC Paper   | 5           | 1          | 150              | 50               | CW                      | Regular Water   |
| Ultrasonic for 10 minutes  |             |            |                  |                  |                         |                 |
| 3 $\mu\text{m}$ Diamond Suspension (Glycol Based Polycrystalline) (Polishing Cloth: Final-A) | 4           | 1          | 100              | 50               | CW                      | Deionized Water |
| Ultrasonic for 10 minutes  |             |            |                  |                  |                         |                 |
| 1 $\mu\text{m}$ Diamond Suspension (Glycol Based Polycrystalline) (Polishing Cloth: Final-A) | 4           | 1          | 100              | 50               | CW                      | Deionized Water |
| Ultrasonic for 10 minutes  |             |            |                  |                  |                         |                 |
| 0.05 $\mu\text{m}$ Colloidal Alumina Suspension (Polishing Cloth: Final-A)                   | 2-3         | 1          | 100              | 50               | CCW                     | Deionized Water |
| Ultrasonic for 10 minutes  |             |            |                  |                  |                         |                 |

Table 6-2: Polishing Steps for R2512

| Polishing Material   | Time (mins) | Load (lbs) | Base Speed (rpm) | Head Speed (rpm) | Base and Head Direction | Fluid           |
|--|-------------|------------|------------------|------------------|-------------------------|-----------------|
| 800 Grit Adhesive SiC Paper  | 5           | 1          | 150              | 50               | CW                      | Regular Water   |
| 1200 Grit Adhesive SiC Paper   | 5           | 1          | 150              | 50               | CW                      | Regular Water   |
| Ultrasonic for 10 minutes  |             |            |                  |                  |                         |                 |
| 1 $\mu\text{m}$ Alumina Suspension (De-Agglomerated) (Polishing Cloth: Spec-Cloth)   | 4           | 1          | 100              | 50               | CW                      | Deionized Water |
| Ultrasonic for 10 minutes  |             |            |                  |                  |                         |                 |
| 0.3 $\mu\text{m}$ Alumina Suspension (De-Agglomerated) (Polishing Cloth: Spec-Cloth) | 4           | 1          | 100              | 50               | CW                      | Deionized Water |
| Ultrasonic for 10 minutes  |             |            |                  |                  |                         |                 |
| 0.05 $\mu\text{m}$ Colloidal Alumina Suspension (Polishing Cloth: Final-A)           | 2-3         | 1          | 100              | 50               | CCW                     | Deionized Water |
| Ultrasonic for 10 minutes  |             |            |                  |                  |                         |                 |

After completion of grinding and polishing, all samples were analyzed using an environmental scanning electron microscope (ESEM). For QFN44 and QFN32, around 10 images for each solder joint on each samples were captured at 2500x magnification. Due to large solder joint area, 10 images for each solder joint on R2512 samples were captured at 2000x magnification. These images captured the entire interfacial IMCs on component and board side of a package and later were used for determining an average interfacial IMC thickness. All 10 images were used for the measurement to capture thickness variation across the interfacial layer. Two image processing software packages, Image-J and XTDocument, were used for calculating average interfacial IMC thickness. Using the software, the total area of an interfacial IMC was measured first and then divided by horizontal distance to calculate an average interfacial IMC thickness. A total of 20 measurements were obtained and averaged to get the sample average interfacial IMC thickness. Standard deviation of these 20 measurements was also measured to find the variations among the total measurements. Apart from an average thickness of interfacial IMC, wavelength dispersive spectroscopy (WDS) and energy dispersive spectroscopy (EDS) analysis were also performed to confirm the stoichiometric composition of interfacial IMCs and to study the distribution of dopants within solder bulk and interfacial IMCs.

## **6.2.Mechanical Shock Reliability Test**

This test was selected to evaluate mechanical shock reliability of the selected solders. In order to study the effects of high temperature isothermal aging on the mechanical shock reliability of solders, mechanical shock was performed on un-aged and thermally aged test boards.

### **6.2.1. Design of Experiment (DOE) for Mechanical Shock Test**

Two temperature intervals and three time intervals were used for mechanical shock testing. These two temperatures were 185°C and 200°C (same as the aging test), and the three time intervals were 0 hour, 400 hours and 1000 hours. 0 hour (Time=0) condition represents test boards after reflow. It was decided to test two boards per solder for every selected interval. This means, a total of 50 test boards (two boards per solder for five solders = 10 test boards total at each interval) were tested for time=0, 400 hours/185°C, 1000 hours/185°C, 400 hours/200°C and 1000 hours/200°C intervals. The design of experiments for the mechanical shock testing is shown in Figure 6-3. Due to high temperature exposure during isothermal aging and thermal cycling tests, interdiffusion rates will be high, resulting in thick interfacial IMCs. It is hypothesized that these thick interfacial intermetallics will cause solder failure to occur more quickly in mechanical shock testing. To avoid any catastrophic failures due to high G forces, a lower G-level was preferable for mechanical shock testing. Thus it was decided to use a shock pulse of 500G with 1.3 millisecond duration for mechanical shock testing. A total of 100,000 mechanical shocks were performed on all aged test boards. For 0 hour of aging (Time=0) condition, it was decided to test until 600,000 mechanical shocks.

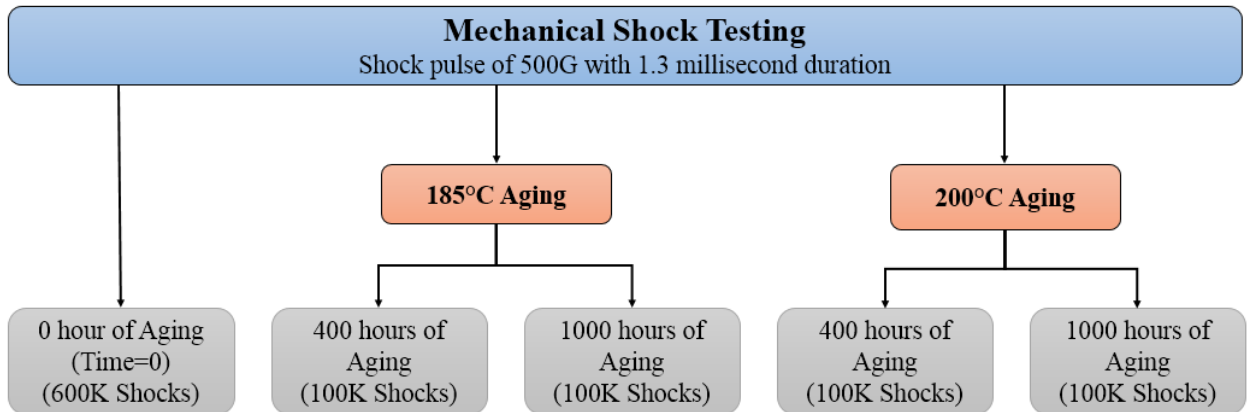


Figure 6-3: Design of Experiment (DOE) for Mechanical Shock Test

## 6.2.2. Test Equipment and Measurement Systems for Mechanical Shock Test

A custom shock machine was used in this study. The two test boards designated for each solder were tested together. In order to mount two test boards on the shock machine, a shock plate was designed with holes drilled on inside which were identical to the holes on the top and bottom of the aluminum frame of the test board. The shock plate also featured eight mounting holes on outside to mount the shock plate onto the shock machine. The designed shock plate is shown in Figure 6-4. After mounting two boards on the shock plate, the shock plate assembly was mounted on mechanical test machine using eight bolts as shown in Figure 6-5. An accelerometer was attached on the shock plate at the center near the front edge of the shock plate. The shock machine was set up to record a shock pulse of 500G with 1.3 millisecond duration on this accelerometer. A typical shock pulse profile recorded by this accelerometer during mechanical shock testing is shown in Figure 6-6. Three additional accelerometers were also used at various locations on shock machine during the testing for feedback control purpose.

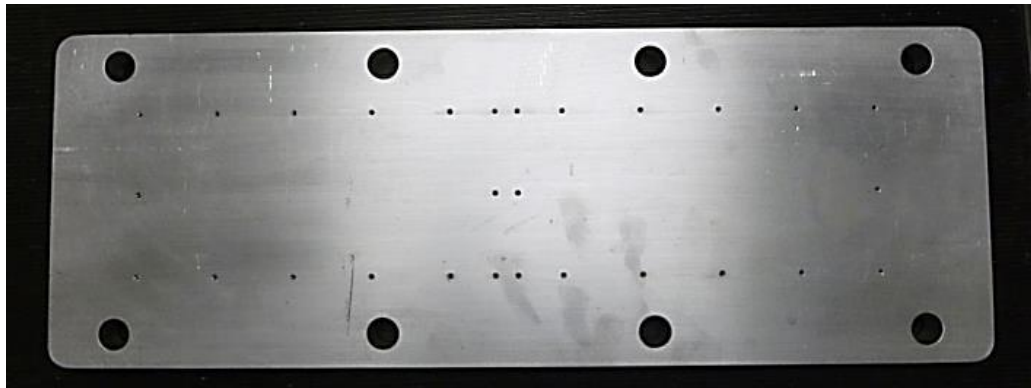


Figure 6-4: A Shock Plate for Testing Two Test Boards at Once

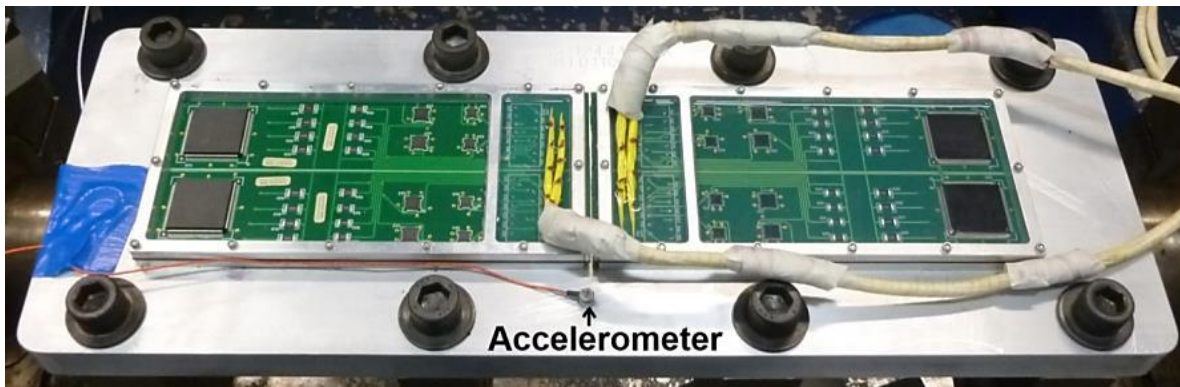


Figure 6-5: Shock Plate Assembly Mounted on Shock Machine

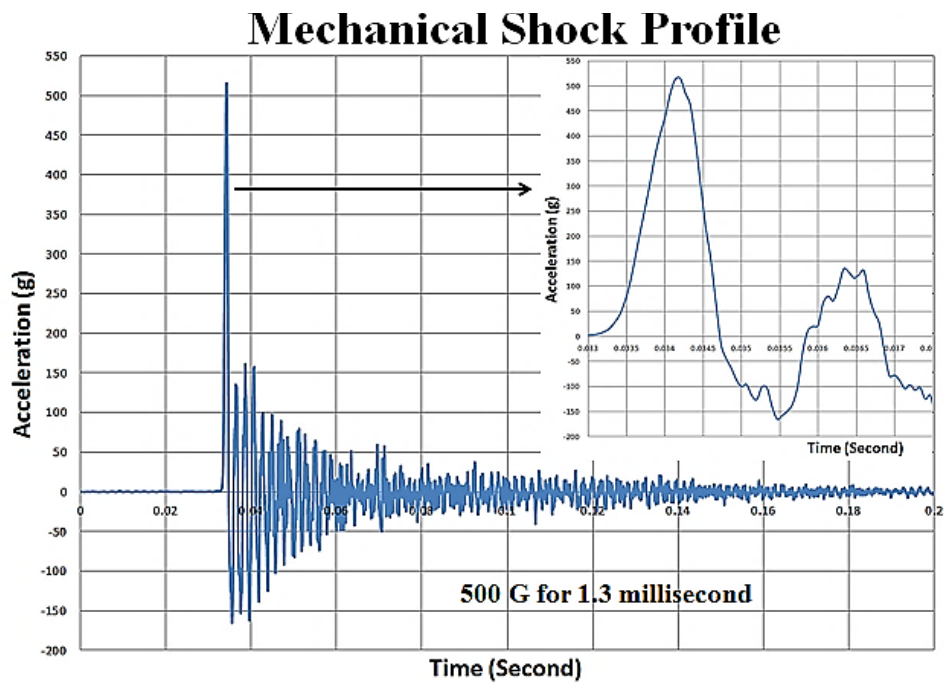


Figure 6-6: Shock Profile for Mechanical Shock Test

During mechanical shock testing, in-situ resistances of all packages on the two test boards were monitored using an Agilent 34970A multiplexer unit. One shock takes around two seconds to complete one cycle. Based on the limitation of the data collection system, in-situ resistance data were recorded every 10 seconds or every five shocks. The test was continued until 100,000 mechanical shocks were completed on the two test boards. This process was repeated to complete 100,000 mechanical shocks on 40 aged test boards and 600,000 mechanical shocks on 10 un-aged test boards.

### **6.2.3. Failure Criteria for Mechanical Shock Test**

In-situ resistance of all packages on the test board was monitored to determine solder joint failure. The failure criterion was developed based on the guideline provided by IPC/JEDEC-9703 [94] (Mechanical Shock Test Guidelines for Solder Joint Reliability) and JESD-B111 [95] (Board Level Drop Test Method of Components for Handheld Electronic Products). A solder joint was considered to be failed at the first indication of package resistance above 100 ohms followed by three such indications during five subsequent shocks. An example of package failure during mechanical shock testing is shown in Figure 6-7 where QFN44, QFN32 and QFP256 failed at 7665, 12020 and 55310 shocks, respectively.



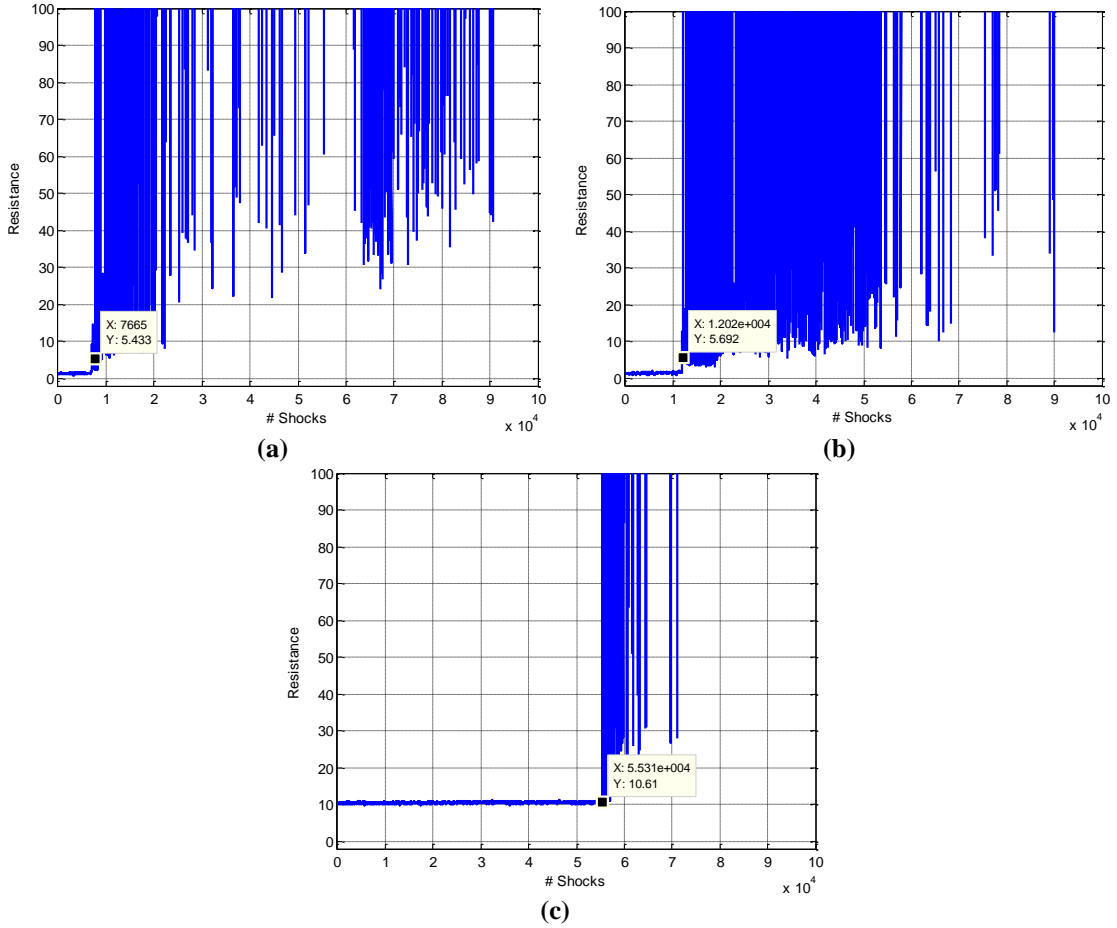


Figure 6-7: Package Failure during Mechanical Shock Testing (a) QFN44 Failed at 7665 Shocks (b) QFN32 Failed at 12020 Shocks (c) QFP256 Failed at 55310 Shocks (Note: Package Resistance is in Ohm Unit).

## **7. Effects of Mn and Ce Dopant on the Microstructure and Mechanical Properties of SAC305 Solder.**

This chapter discusses the effects of additions of Mn and Ce on microstructure and mechanical properties of SAC305 solder that were observed in this study. As-reflowed QFN44 and QFN32 package types for all five solders (SAC305, Low Mn, High Mn, Low Ce and High Ce) were cold mounted, cross-sectioned and polished for examining microstructure and characterizing mechanical properties.

Microstructure of the solder was examined by comparing five attributes. These attributes were number of  $\beta$ -tin grains, size of  $\text{Ag}_3\text{Sn}$  IMC particles, number of  $\beta$ -tin dendrites, area fraction of eutectic region and area fraction of  $\beta$ -tin dendrites. Mechanical properties of the solder were investigated by comparing elastic modulus and hardness of the bulk solder.

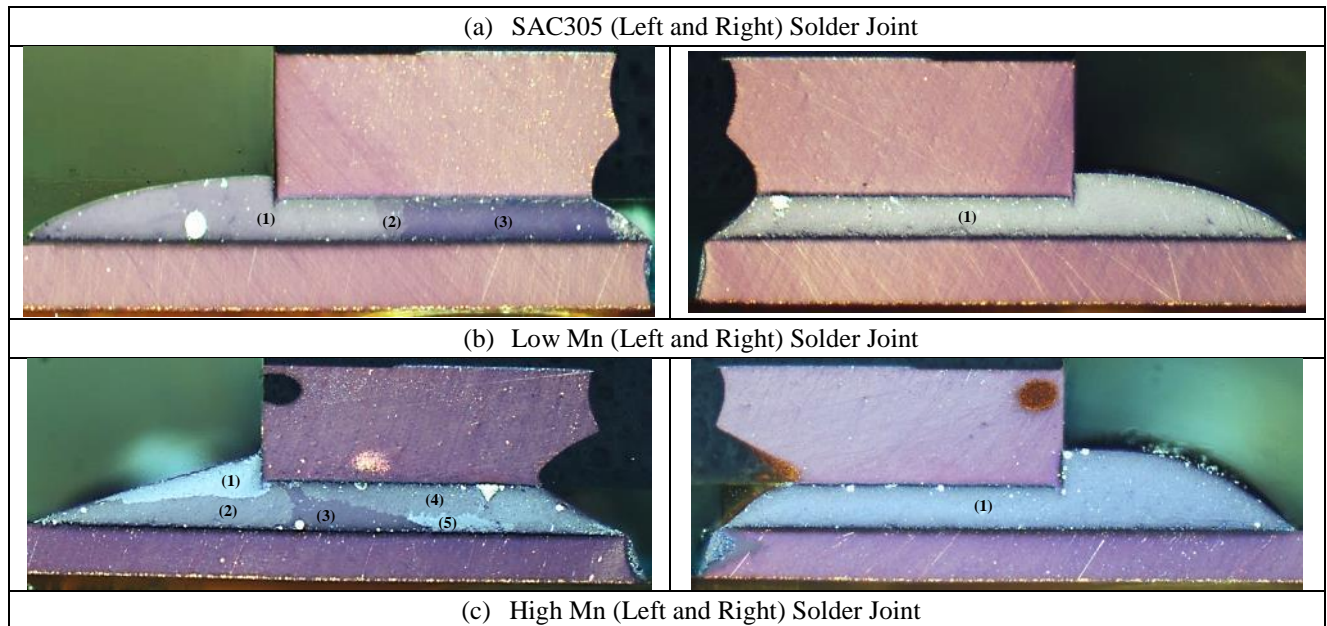
### **7.1. Microstructure Analysis**

The details on microstructure analysis including number of  $\beta$ -tin grains, size of  $\text{Ag}_3\text{Sn}$  IMC particles, number of  $\beta$ -tin dendrites, area fraction of eutectic region and area fraction of  $\beta$ -tin dendrites are discussed below.

#### **7.1.1. Number of $\beta$ -tin Grains**

In order to find the number of  $\beta$ -tin grains in the solder joint, Leica DMEP polarizing microscope system was used. Both left and right side of solder joint on QFN44 and QFN32 were examined to find total number of  $\beta$ -tin grains for all five solders.

Figure 7-1 and Figure 7-2 show the cross-polarized image of left and right side of solder joint in QFN44 and QFN32, respectively. Each individual grain is marked with a number. It is important to note that in addition to large grains of  $\beta$ -tin in each in solder joint, the presence of a few small grains is also found. Due to their smaller sizes, they were difficult to distinguish and count for analysis. Thus, such small grains were not considered in this analysis. In addition to  $\beta$ -tin grains, circular or elliptical bright spots can be seen within the solder joint. These bright spots are process voids that occurred during reflow assembly. The summary of total number of  $\beta$ -tin grains in each side of solder joint in QFN44 and QFN32 is shown in Table 7-1. Figure 7-3 shows average number of  $\beta$ -tin grains of five solders observed in QFN44 and QFN32. It is clear from Figure 7-3 that addition of Mn and Ce dopant in SAC305 increases total number of  $\beta$ -tin grains.



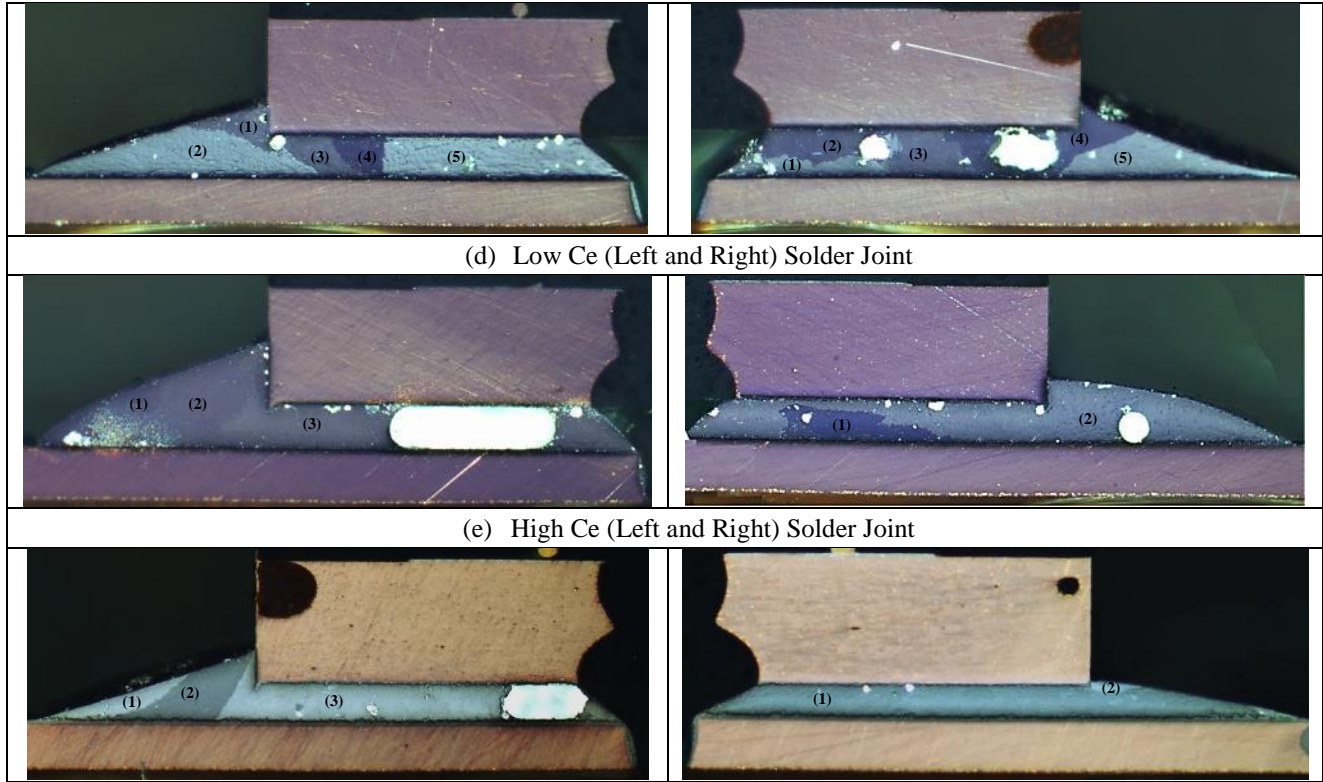
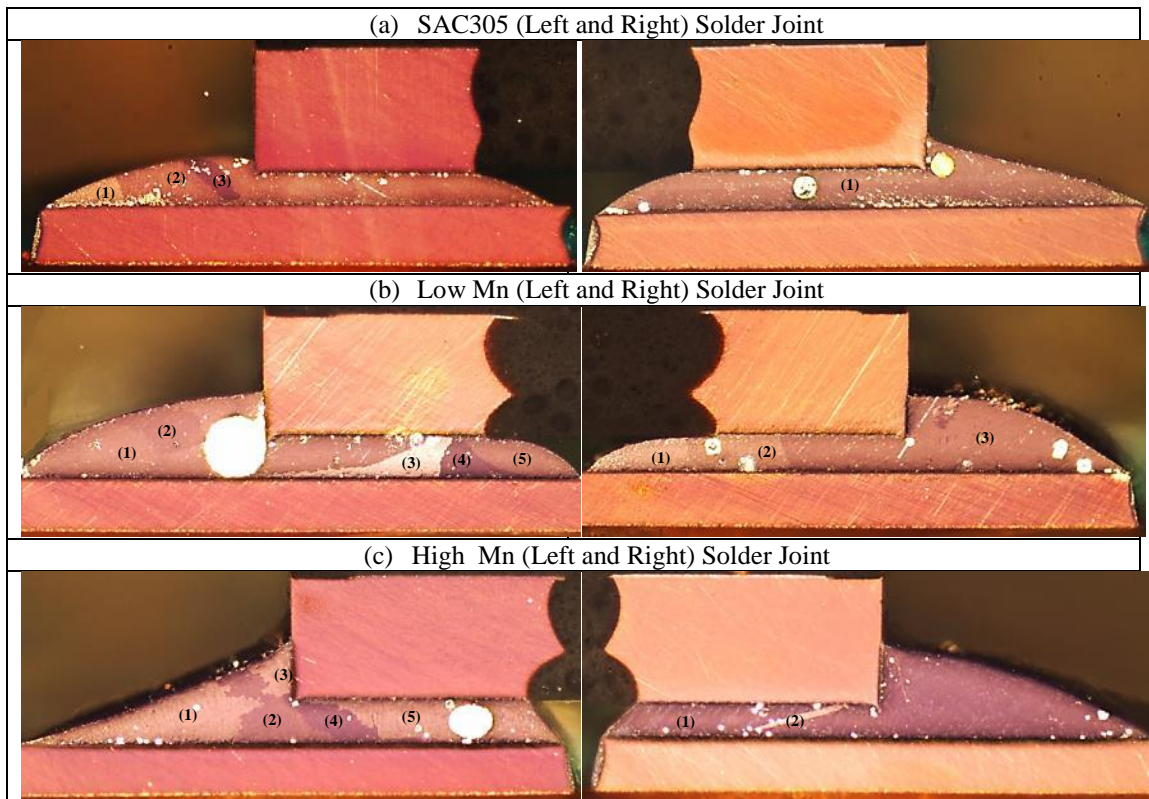


Figure 7-1: Cross-polarized Images of Left and Right Side of Solder Joint in QFN44 Package (a) SAC305, (b) Low Mn, (c) High Mn, (d) Low Ce, (e) High Ce



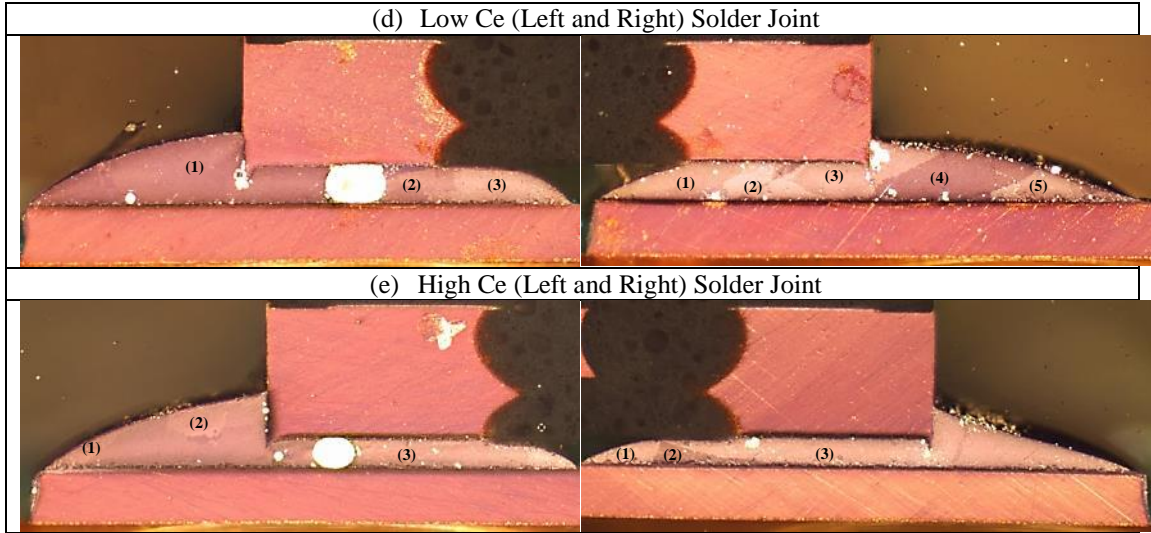


Figure 7-2: Cross-polarized Images of Left and Right Side of Solder Joint in QFN32 Package: (a) SAC305, (b) Low Mn, (c) High Mn, (d) Low Ce, (e) High Ce

Table 7-1: Total Number of  $\beta$ -tin Grains in Each Side of Solder Joint in QFN44 and QFN32

|                             | SAC305   |           | SAC305+<br>0.05%Mn |           | SAC305+<br>0.17%Mn |           | SAC305+<br>0.07%Ce |           | SAC305+<br>0.13%Ce |           |
|-----------------------------|----------|-----------|--------------------|-----------|--------------------|-----------|--------------------|-----------|--------------------|-----------|
|                             | Left Pad | Right Pad | Left Pad           | Right Pad | Left Pad           | Right Pad | Left Pad           | Right Pad | Left Pad           | Right Pad |
| <b>QFN44<br/>(Time = 0)</b> | 3        | 1         | 5                  | 1         | 5                  | 5         | 3                  | 2         | 3                  | 2         |
| <b>QFN32<br/>(Time = 0)</b> | 3        | 1         | 5                  | 3         | 5                  | 2         | 3                  | 5         | 3                  | 3         |



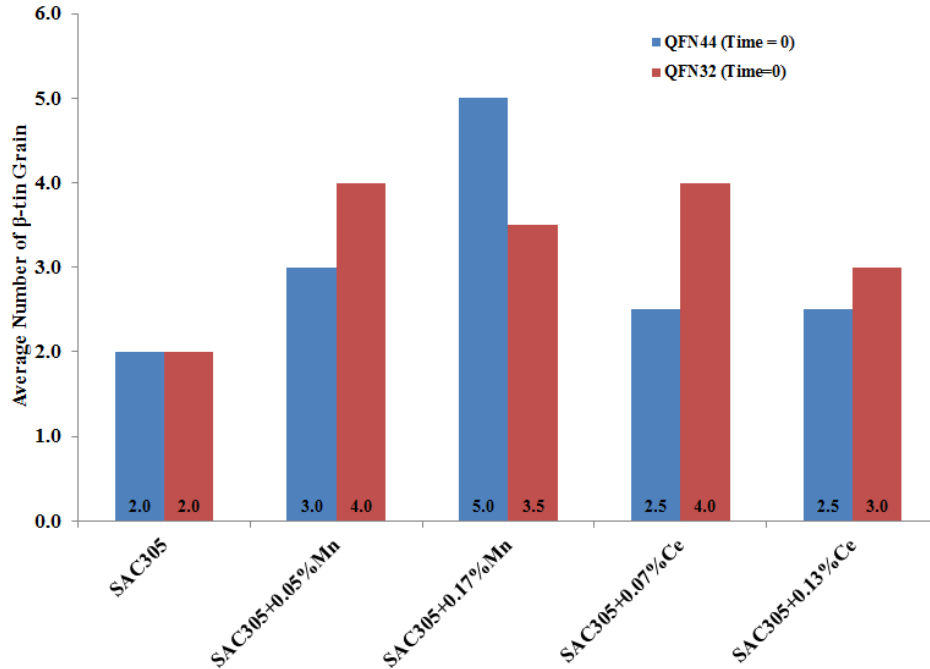


Figure 7-3: Average Number of  $\beta$ -tin Grains of Various Solders Observed in QFN44 and QFN32

### 7.1.2. Size of $\text{Ag}_3\text{Sn}$ IMC Particles, Number of $\beta$ -tin Dendrites, Area Fraction of Eutectic Region and Area Fraction of $\beta$ -tin Dendrites

An ESEM image (at 2500x magnification) of solder bulk microstructure for each of the five solders for QFN32 and QFN44 packages is shown in Figure 7-4 and Figure 7-5, respectively. By comparing microstructure of solders in QFN32 and QFN44, it can be seen that microstructure for the same solder alloy looks similar in both QFN32 and QFN44 package types. Thus, as expected, the size of QFN package has no obvious effect on the microstructure of solder alloy. It is also noticeable that dendrite in Mn modified SAC305 solders seem larger and the dendrites in Ce modified SAC305 solders seem more elongated than for pure SAC305 solder.

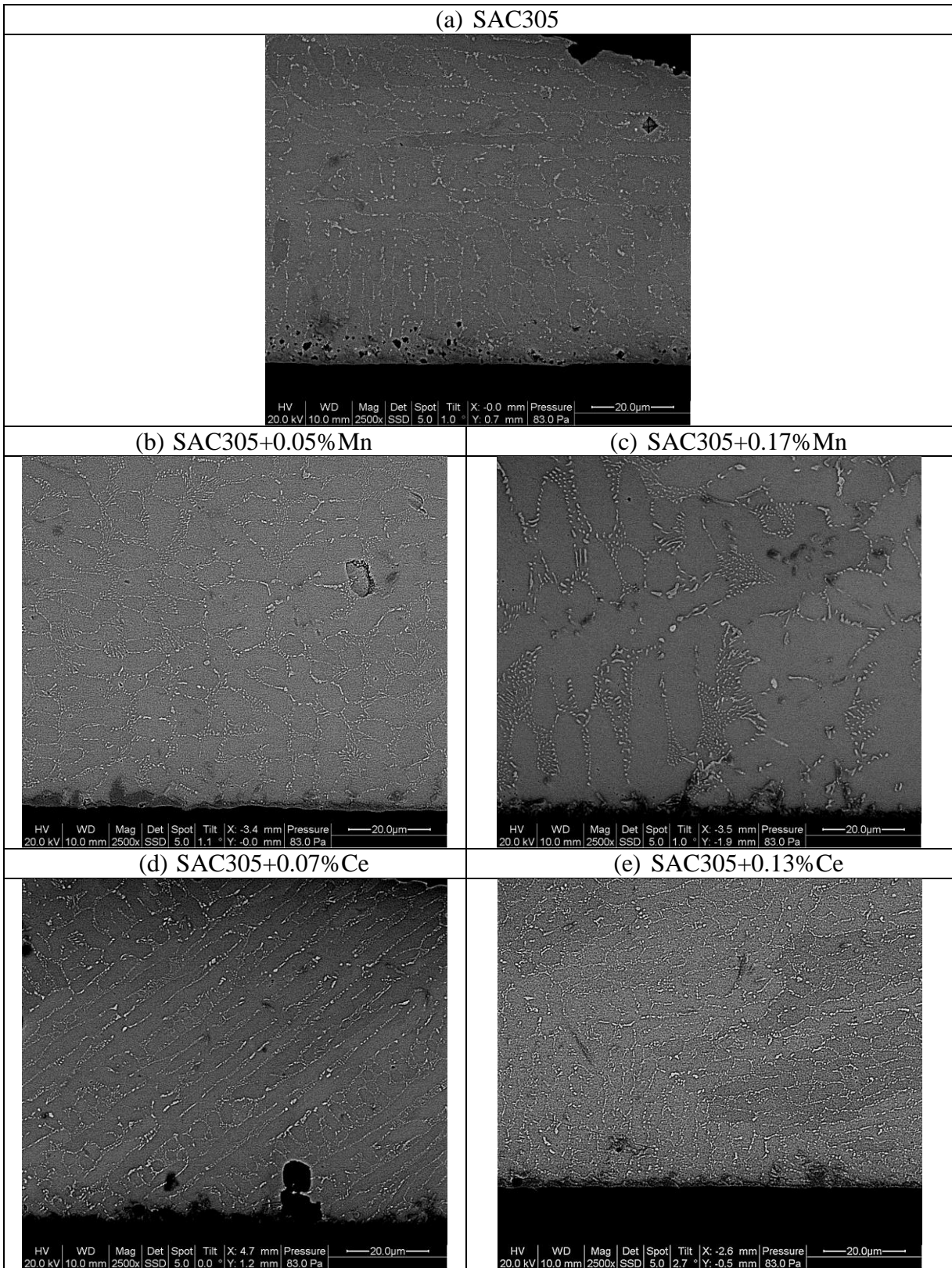


Figure 7-4: ESEM Image at 2500x Magnification of Various Solders in QFN32 Package: (a) SAC305, (b) Low Mn, (c) High Mn, (d) Low Ce, (e) High Ce

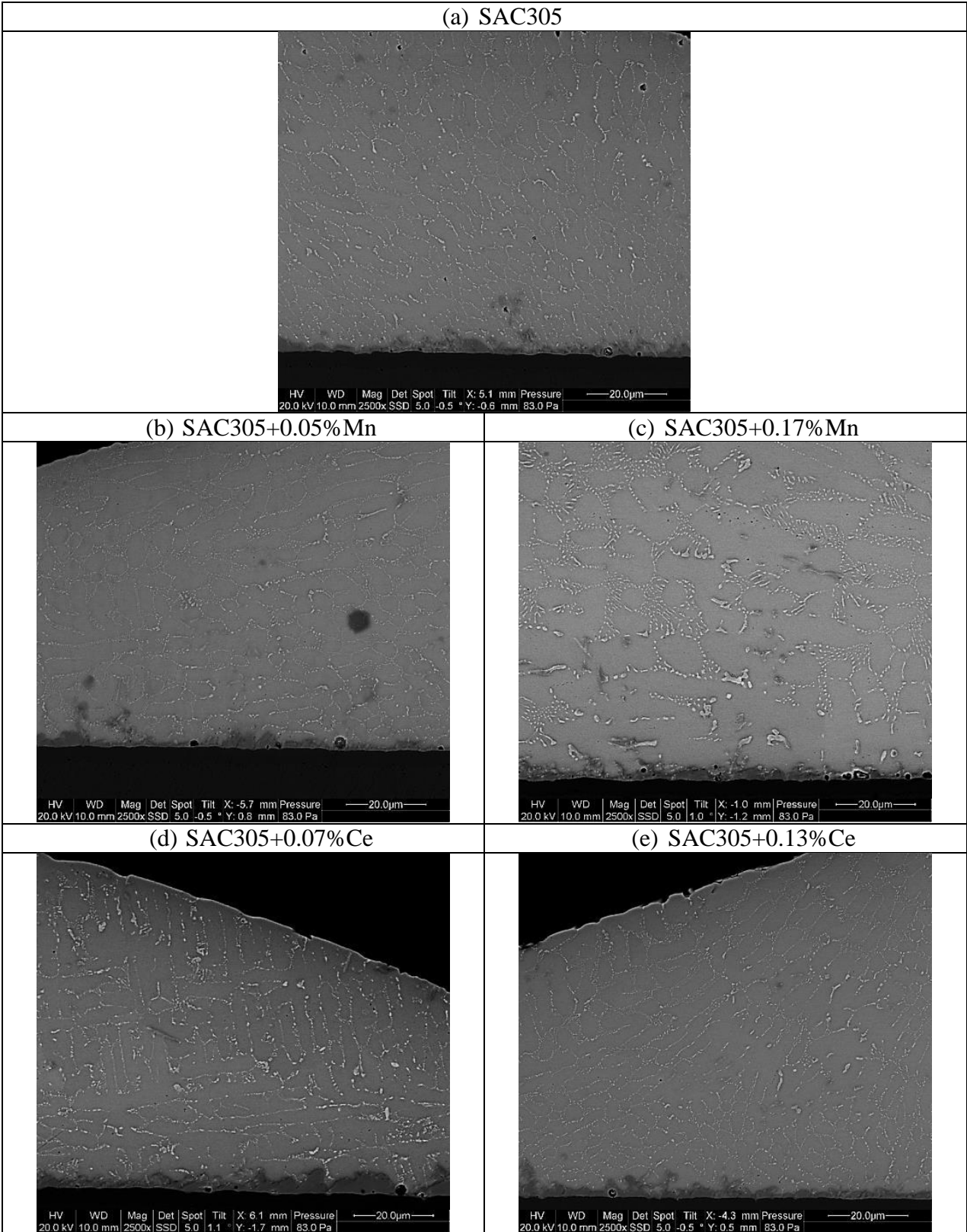
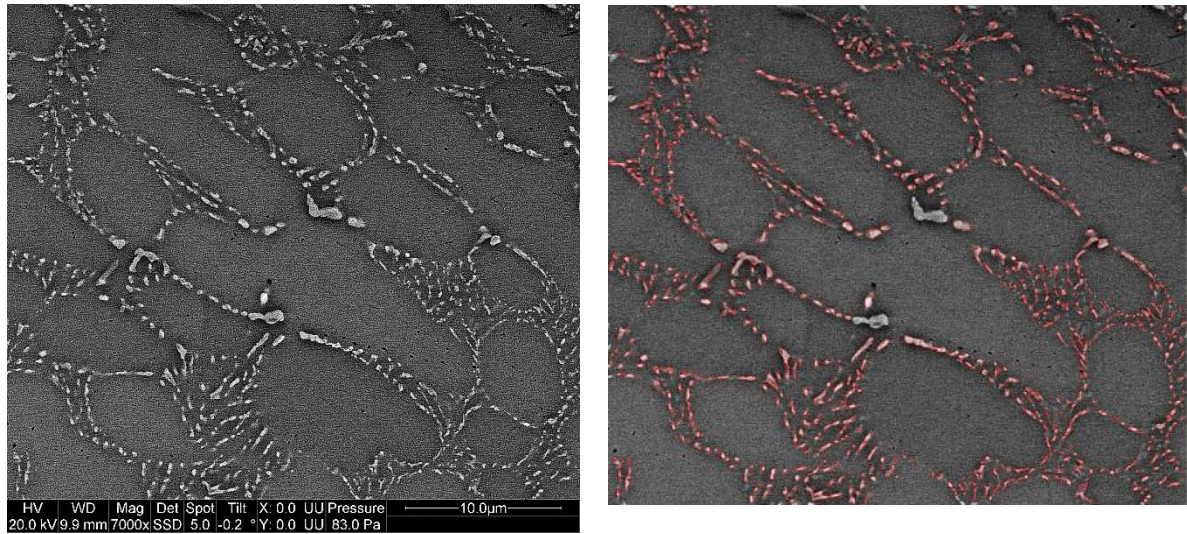


Figure 7-5: ESEM Image at 2500x Magnification of Various Solders in QFN44 Package (a) SAC305, (b) Low Mn, (c) High Mn, (d) Low Ce, (e) High Ce



In order to measure various attributes of microstructure, ESEM images were retaken at higher magnification (7000x) and image processing techniques were performed to extract microstructure attributes. Image processing software, Image-Pro Plus, was used to calculate size of  $\text{Ag}_3\text{Sn}$  IMC particles, number of  $\beta$ -tin dendrites/lobes, area fraction of eutectic region and area fraction of  $\beta$ -tin dendrites.

In order to calculate size of  $\text{Ag}_3\text{Sn}$  IMC particles, length along major axis and width along minor axis of  $\text{Ag}_3\text{Sn}$  IMC particles were measured. First step in Image Pro-Plus software was calibrating an image from the scale bar given at the bottom of the ESEM image. After performing spatial scale calibration, brightness and contrast were adjusted to have the  $\text{Ag}_3\text{Sn}$  IMC particles stand out. For the next step, scale bar at the bottom on an image was removed and gray scale thresholding was performed. Gray scale thresholding selects all the particles of a given brightness within an image. However, the selection criteria of gray scale thresholding should be such that no  $\text{Cu}_6\text{Sn}_5$  IMC particles (darker than  $\text{Ag}_3\text{Sn}$  IMC) and  $\text{AuSn}_4$  IMC particles (brighter than  $\text{Ag}_3\text{Sn}$  IMC) get selected. Figure 7-6 shows an example of this process where Figure 7-6 (a) shows ESEM image of solder at 7000x magnification; whereas Figure 7-6 (b) shows selected  $\text{Ag}_3\text{Sn}$  IMC particles in the solder bulk. After performing gray scale thresholding, length along major axis and width along minor axis were measured to calculate average size of  $\text{Ag}_3\text{Sn}$  IMC particles.

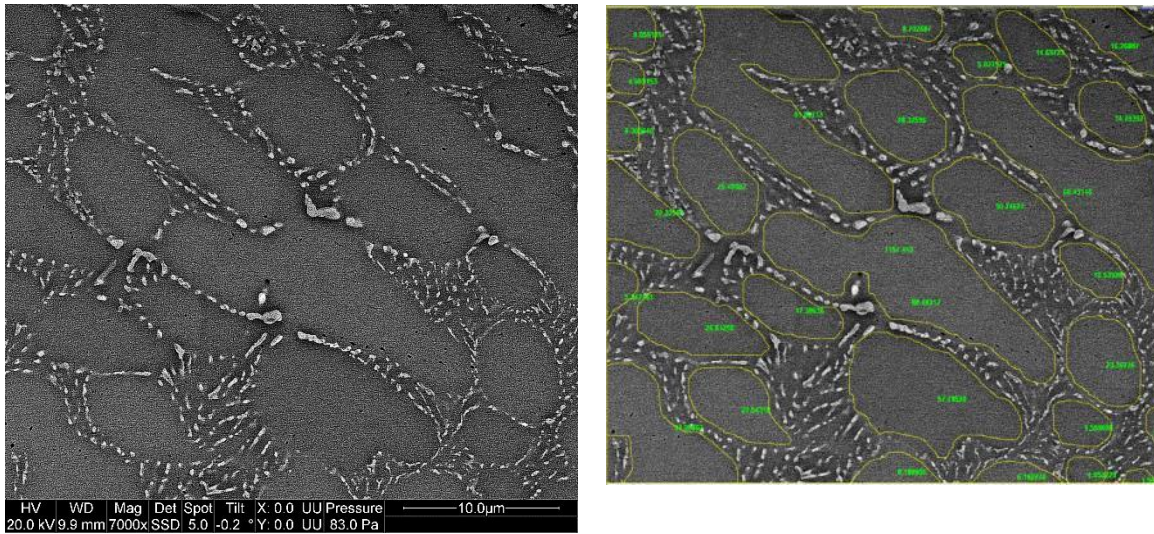


(a)

(b)

Figure 7-6: (a) ESEM Image of Solder at 7000x Magnification (b) Selected Ag-Sn IMC Particles in the Solder Bulk

In order to calculate the remaining attributes of solder microstructure, such as number of  $\beta$ -tin dendrites/lobes, area fraction of eutectic region and area fraction of  $\beta$ -tin dendrites, a region representing the size of  $\beta$ -tin lobes was manually drawn, as shown in Figure 7-7 (b). The manually drawn  $\beta$ -tin lobes are highlighted in yellow color; whereas their respective area value is shown in green color. By measuring the area of each  $\beta$ -tin dendrites within an image, the area fraction of eutectic region and the area fraction of  $\beta$ -tin dendrites were also calculated. In addition numbers of  $\beta$ -tin dendrites/lobes were also calculated from this measurement.



(a)

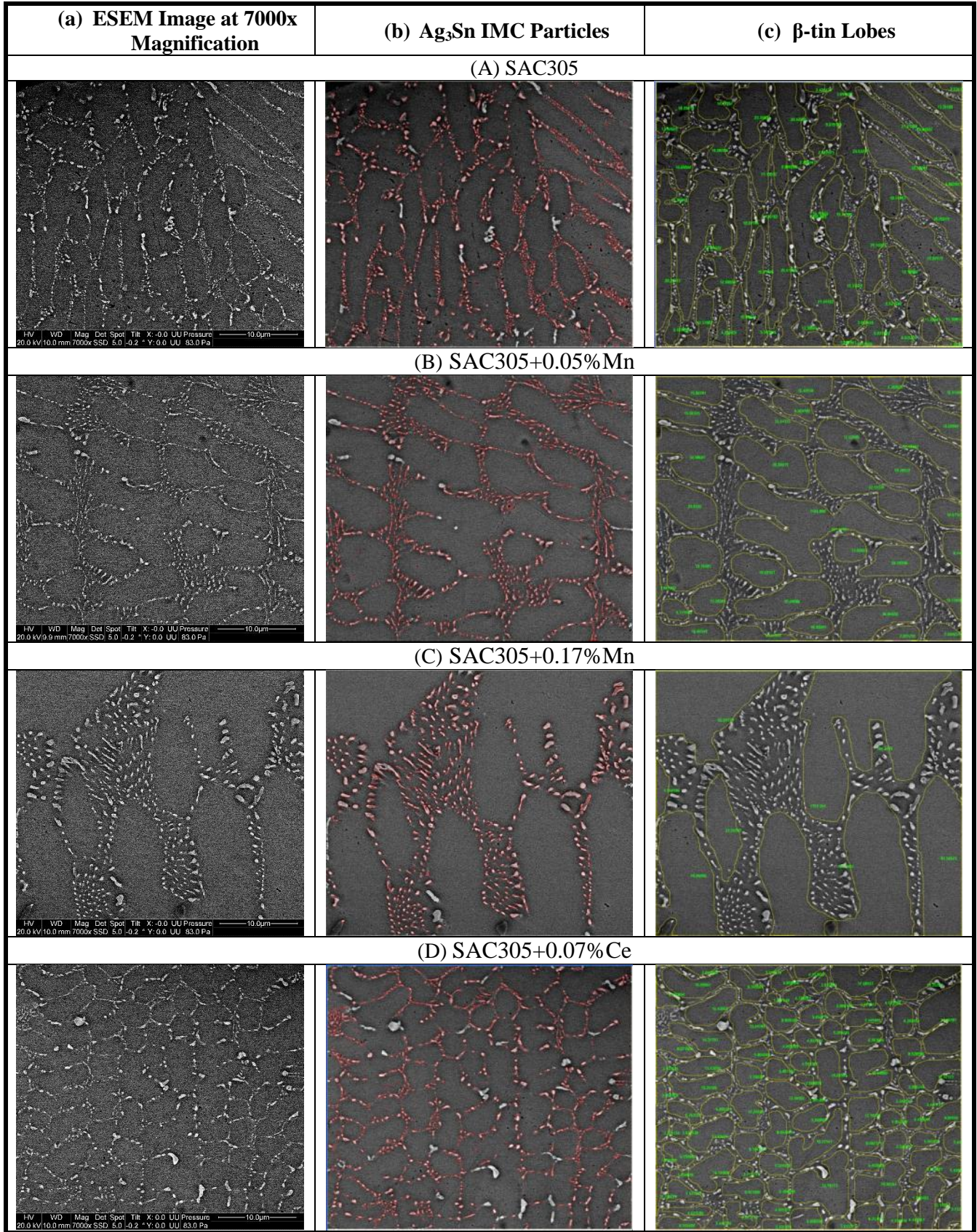
(b)

Figure 7-7: (a) ESEM Image of Solder at 7000x Magnification (b) Selected Region for  $\beta$ -tin Dendrites

Figure 7-8 shows an example of microstructure in one unit representative area (URA) for all five solders. Column (a) in Figure 7-8 shows ESEM image at 7000x magnification, column (b) shows detected  $\text{Ag}_3\text{Sn}$  IMC particles, and column (c) shows selected  $\beta$ -tin lobes for all five solders.

For calculating size of  $\text{Ag}_3\text{Sn}$  IMC particles, number of  $\beta$ -tin dendrites/lobes, area fraction of eutectic region and area fraction of  $\beta$ -tin dendrites for all five solders, four URAs were considered for analysis from different locations on the solder joint. The calculated attribute values from four URAs by image processing were averaged and plotted in bar charts which are presented next.







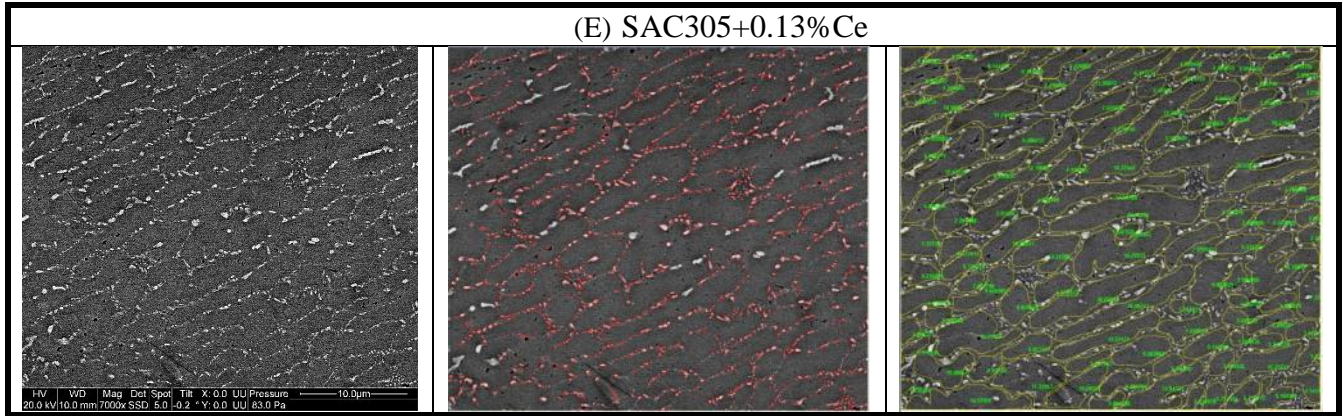


Figure 7-8: Column (a) ESEM Image at 7000x Magnification, Column (b) Detected Ag<sub>3</sub>Sn IMC Particles, and Column (c) Selected β-tin Lobes: (A) SAC305, (B) Low Mn, (C) High Mn, (D) Low Ce, (E) High Ce

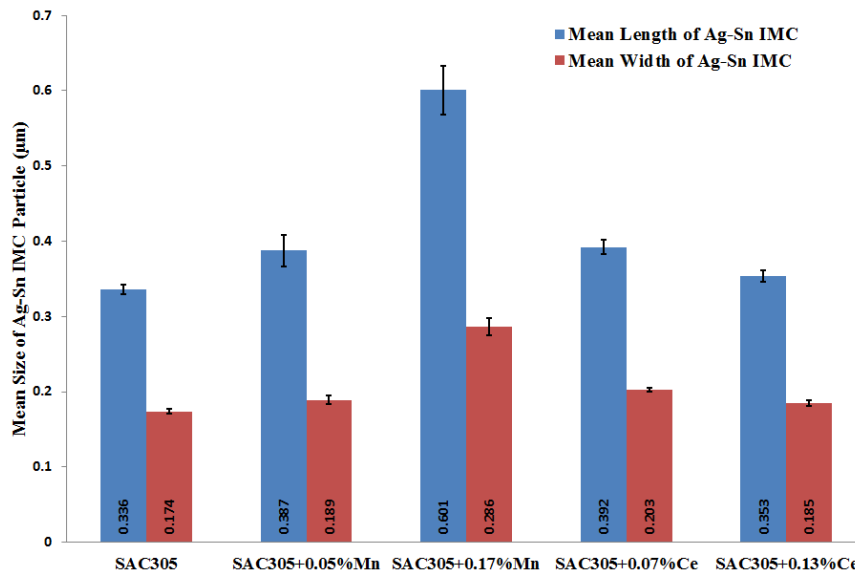


Figure 7-9: Mean Length and Width of Ag-Sn IMC Particles for Solders

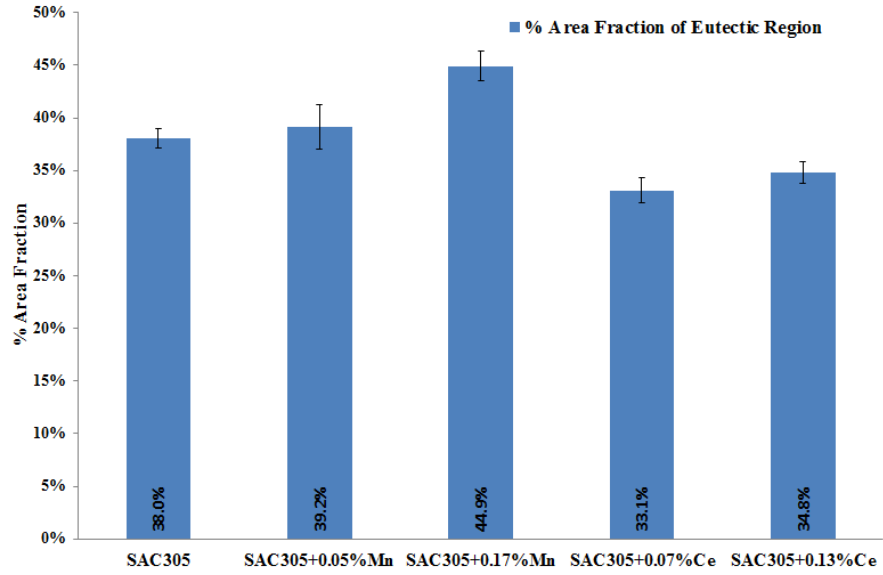


Figure 7-10: Area Fraction of Eutectic Region

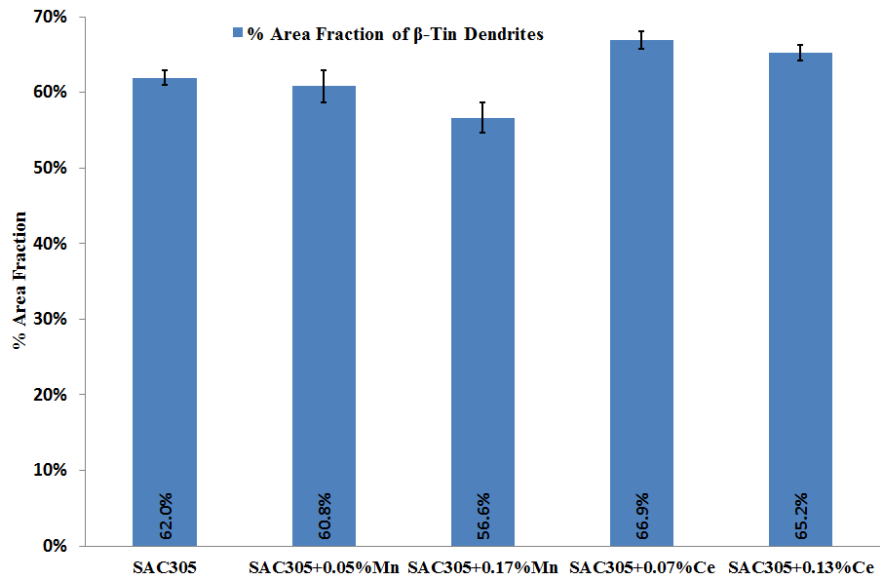


Figure 7-11: Area Fraction of  $\beta$ -tin Dendrites

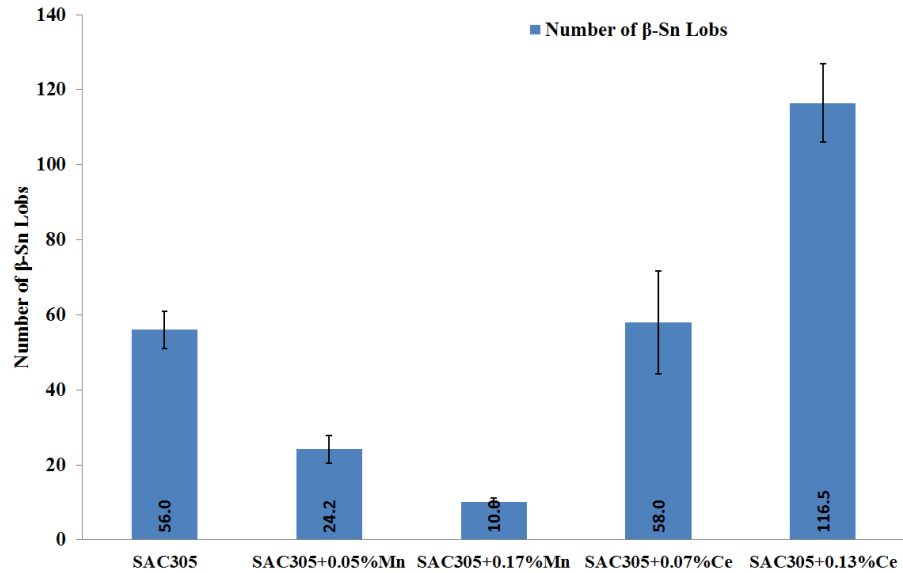


Figure 7-12: Number of  $\beta$ -tin dendrites/Lobes

Table 7-2 shows %change in microstructure attributes of modified SAC305 solders compared to SAC305. Looking at the change in the size (length and width) of  $Ag_3Sn$  IMC particles, High Mn solder showed significant increase; whereas, High Ce showed smallest increase in the size of  $Ag_3Sn$  IMC particles. Looking at the change in %area fraction of eutectic region, High Mn showed highest increase; whereas, Low Ce and High Ce showed reduction in %area fraction of eutectic region compare to SAC305. Comparing %change in number of  $\beta$ -tin dendrites/lobes, High Ce showed highest increase; whereas, both Low Mn and High Mn showed considerable reduction in number of  $\beta$ -tin dendrites/lobes compare to SAC305.

Table 7-2: % Change in Microstructure Attributes of Modified SAC305 Solders Compared to SAC305

| Solders        | Mean Length of Ag <sub>3</sub> Sn | Mean Width of Ag <sub>3</sub> Sn | %Area Fraction of Eutectic Region | %Area Fraction of $\beta$ -Tin Dendrites | Number of $\beta$ -Tin Dendrites /Lobes |
|----------------|-----------------------------------|----------------------------------|-----------------------------------|--|---|
| SAC305         | -                                 | -                                | -                                 | -  | -                                       |
| SAC305+0.05%Mn | 15%                               | 9%                               | 3%                                | -2%                                      | -57%                                    |
| SAC305+0.17%Mn | 79%                               | 64%                              | 18%                               | -9%                                      | -82%                                    |
| SAC305+0.07%Ce | 17%                               | 17%                              | -13%                              | 8%                                       | 4%                                      |
| SAC305+0.13%Ce | 5%                                | 6%                               | -8%                               | 5%                                       | 108%                                    |

## 7.2.Mechanical Properties of Solders

Mechanical properties of solders were characterized using nanoindentation equipment, (i.e., Agilent G200 nano-indenter). The measured mechanical properties of solders include elastic modulus and hardness. A continuous stiffness measurement (CSM) technique was used for the measurement. Parameters used during the indentation were measurement window = 200-300 nm, surface approach velocity = 10 nm/s, depth limit 300 nm, strain rate target  $0.05s^{-1}$ , harmonic displacement target = 2 nm, frequency target 45 Hz.

It is important to note that elastic modulus and hardness measured from an indent strongly depend on its location. Since solder is a composite material made-up of  $\beta$ -tin dendrites and various IMC particles, depending on the location of indentation, measurement values may vary. Thus, in order to minimize measurement uncertainty, 30 measurements were performed for each solder sample. Figure 7-13 shows a few examples of indentations on the solder sample.



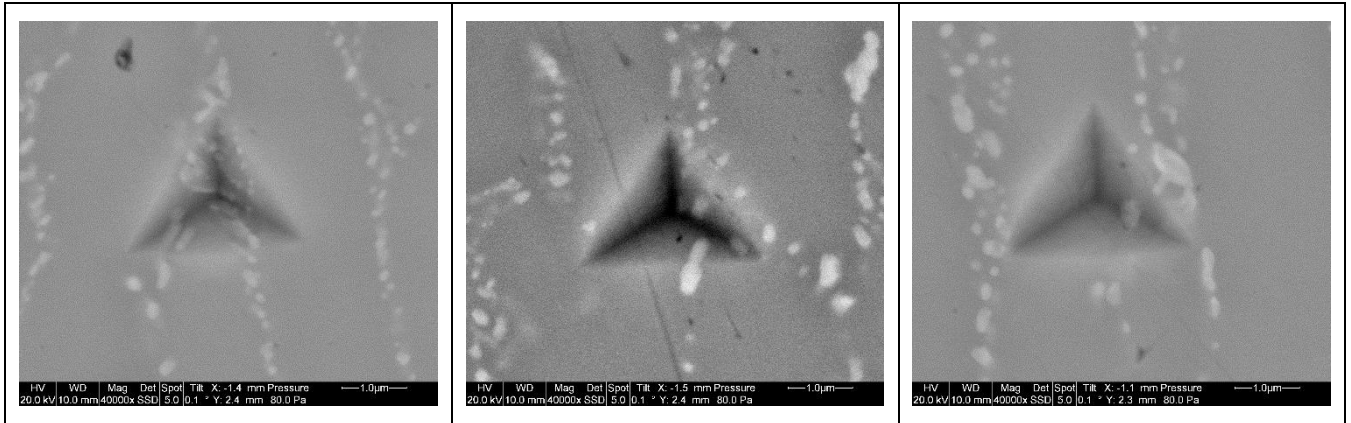


Figure 7-13: Example of Indentations in Solder Bulk

Figure 7-14 plots the average elastic modulus of solders as measured by nanoindentation test. It appears that addition of Mn dopant reduces the elastic modulus of SAC305 solder. Increase in Mn dopant concentration further reduces elastic modulus. Such an observation has been previously reported in literature by Lin et al. [77] [80]. In this study, the reduction in elastic modulus by Mn dopant could be due to microstructural changes as Mn doped solders features large  $\beta$ -tin dendrites and a coarser and less-packed eutectic region. Reduction in the elastic modulus of solder helps to improve drop/shock performance as the compliant solder bulk can absorb more energy during deformation and thus transfers less stress to the interfaces. Unlike the Mn dopant addition, it appears that the addition of Ce dopant has no observable effect on elastic modulus of solder.

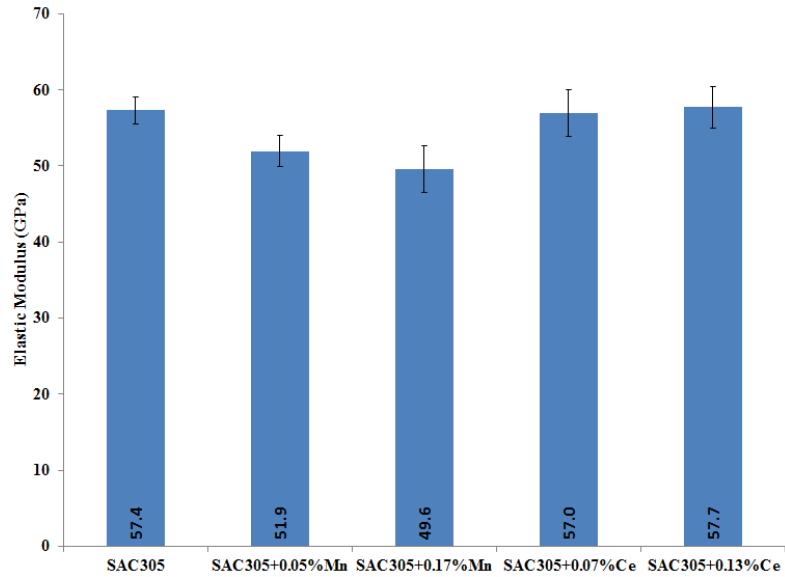


Figure 7-14: Elastic Modulus of Various Solders

Figure 7-14 presents the average hardness of all five solders as measured by nanoindentation testing. Large scattering in the data was observed for all five solders. It is due to variation in hardness measurement from different locations in the solder bulk. It appears that addition of Mn and Ce dopant has no observable effect of the hardness of the base solder (SAC305). Similar observations have been previously reported in literature by Liu and Lee [71] [70].

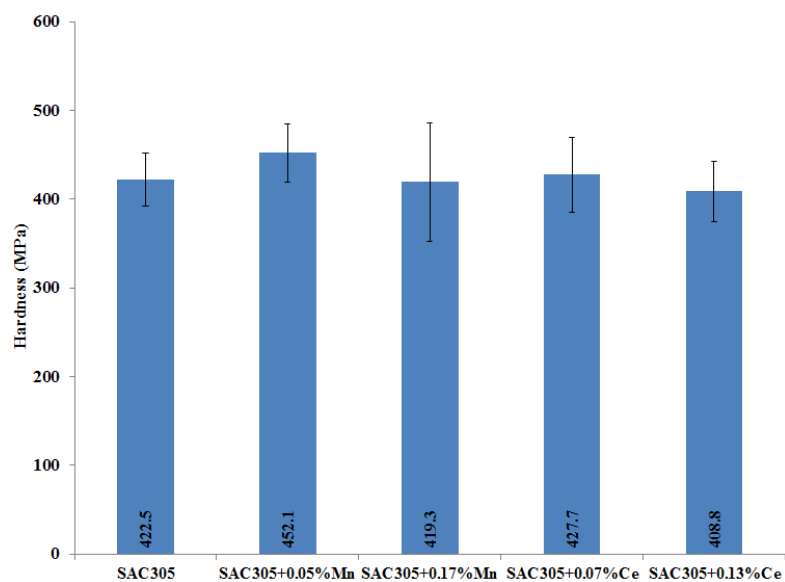


Figure 7-15: Hardness of Various Solders

## **8. Interfacial Intermetallic Growth during Isothermal Aging at 185°C and 200°C on QFN44 and QFN32 Packages**

This chapter discusses the growth of interfacial IMCs on QFN44 and QFN32 packages observed during isothermal aging at 185°C and 200°C up to 1000 hours. In addition to measurement of the interfacial intermetallic layer thickness, analysis of voiding observed during aging at the interface between the  $\text{Cu}_6\text{Sn}_5$  IMC layer and the solder bulk is also presented. The results of these aging tests help to understand the reliability of selected solders subjected to the mechanical shock testing, as discussed in chapter 10.

Both QFN44 and QFN32 packages feature a large pad underneath the package called the “Central Pad,” which provides extra rigidity to the package and also assists in heat transfer when soldered to the board. To test the worst case condition, the central pads of the QFN44 and QFN32 packages were not soldered to the PCB board, thus permitting the solder interconnects of the QFNs to experience higher stresses. Both QFN44 and QFN32 also feature dummy die to simulate the effect of real die of functional QFNs. ESEM images of QFN44 and QFN32 packages after reflow are shown in Figure 8-1.

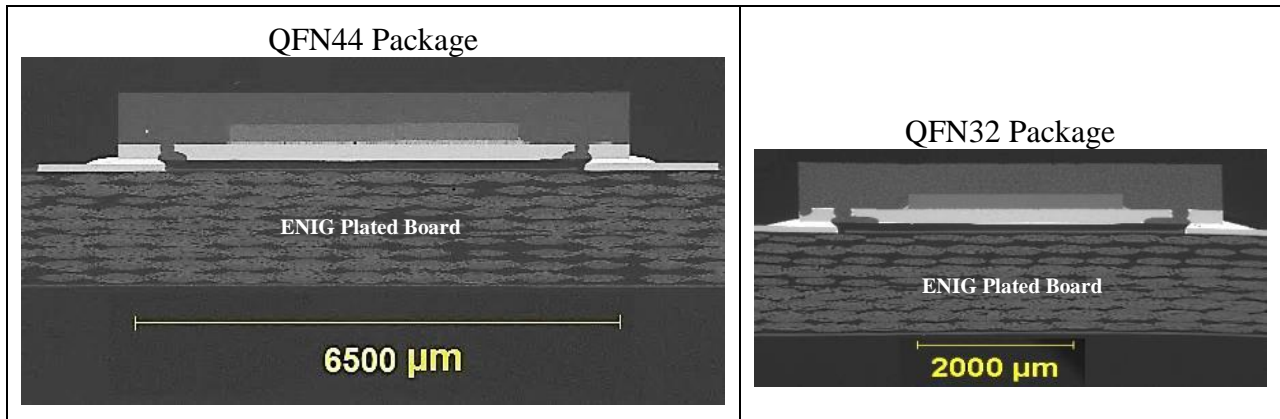


Figure 8-1: An ESEM Image of QFN44 and QFN32 after Reflow

### 8.1. Interfacial Intermetallic Formation during Reflow on QFN Packages

QFN44 and QFN32 packages have peripheral copper interconnect pads plated with matte tin finish. QFNs were soldered to ENIG-plated board. A left and a right solder joint of QFN44 after reflow are shown in Figure 8-2. During reflow, the matte tin finish dissolved in solder, allowing direct access to the copper pad. This resulted in direct interaction between tin (from solder) and copper pad, which formed  $\text{Cu}_6\text{Sn}_5$  interfacial intermetallic layer at the component side. The average thickness of the  $\text{Cu}_6\text{Sn}_5$  interfacial IMC layer after reflow was found to be around 4 to 5 microns.

On the board side, copper traces were plated with ENIG finish. During reflow, the gold on the ENIG finish dissolved in solder, allowing direct access between nickel from ENIG and tin from solder. With copper diffusing from the component pad to the board side, the interfacial intermetallic layer at the board side was found to be  $(\text{Cu},\text{Ni})_6\text{Sn}_5$ . The average thickness of the  $(\text{Cu},\text{Ni})_6\text{Sn}_5$  interfacial IMC layer after reflow was around 2 to 3 microns. Both interfacial intermetallic layers formed on a

QFN package are shown in Figure 8-3. In addition to interfacial IMCs, bulk IMCs, such as  $\text{Ag}_3\text{Sn}$  and  $\text{Cu}_6\text{Sn}_5$ , were also formed during reflow, as shown in Figure 8-3.

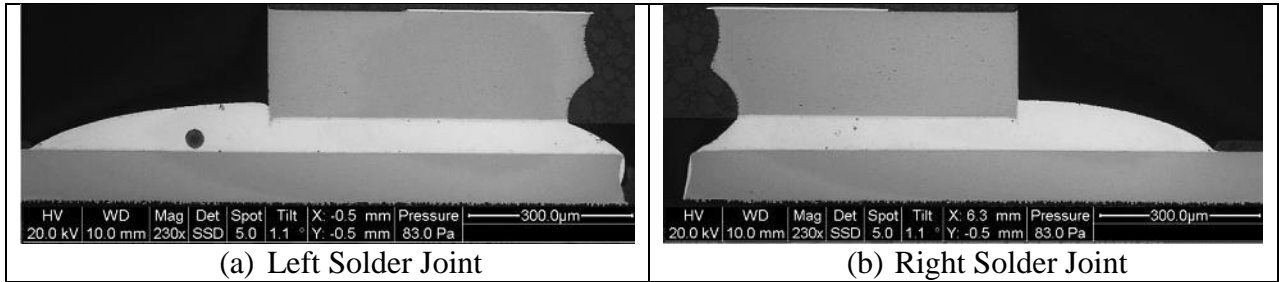


Figure 8-2: Left and Right Solder Joint of QFN44

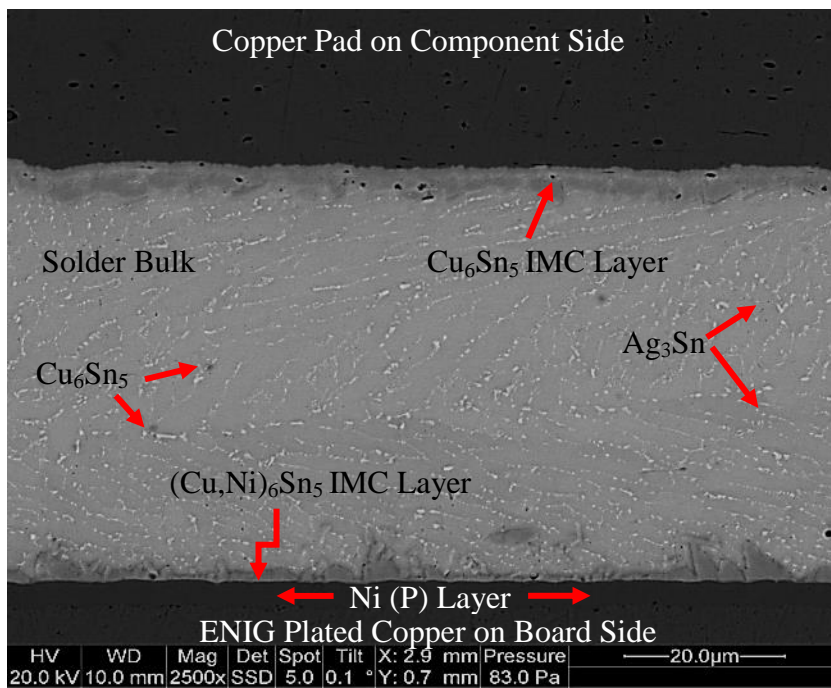


Figure 8-3: Interfacial IMC Formation on QFN Package during Reflow (SAC305 – Time=0)

## 8.2. Effect of Isothermal Aging on QFN Package

In this study, isothermal aging was conducted at 185°C and 200°C up to 1000 hours. The aged QFN samples were removed and analyzed at various time intervals including 0, 100, 200, 400, 600, and 1000 hours. During isothermal aging, two different phenomena were observed. One was the growth of interfacial IMCs, and the other was void creation and coalescence at the interface.

### **8.2.1. The Growth of Interfacial Intermetallic Layers during Isothermal Aging**

It is well known that interfacial intermetallic growth during isothermal aging is a diffusion-controlled mechanism dependent on time and temperature. During isothermal aging, significant growth was observed for  $\text{Cu}_6\text{Sn}_5$  IMC layer after just 100 hours of temperature exposure at both 185°C and 200°C aging conditions. During further analysis, a second interfacial IMC layer,  $\text{Cu}_3\text{Sn}$  was also found between  $\text{Cu}_6\text{Sn}_5$  and the copper pad on the component side. Formation of this layer has been previously observed in the literature. The interfacial IMC layer on the board side,  $(\text{Cu,Ni})_6\text{Sn}_5$ , also thickens during aging; however, the growth of the  $(\text{Cu,Ni})_6\text{Sn}_5$  layer was much slower than that of the  $\text{Cu}_6\text{Sn}_5$  layer observed on the component side. Bulk IMCs ( $\text{Ag}_3\text{Sn}$  and  $\text{Cu}_6\text{Sn}_5$ ) also coalesced and increased in their size with aging.

### **8.2.2. Void Creation and Coalescence at the Interface during Isothermal Aging**

Two types of voids were found near the component side interfaces that were not present before aging or after reflow.

One type of void which was sub-micron in size (called micro-voids) was found at the interface between the  $\text{Cu}_3\text{Sn}$  layer and the copper pad on the component side as shown in Figure 8-4. This type of void has been previously reported in the literature as being present at the interface between Cu-Sn IMC and copper pad during high temperature exposure for extended periods [96][97][61]. These voids are known as a Kirkendall voids, and they form due to the unbalanced interdiffusion of tin and

copper at the interface. Cu has a higher diffusivity in Sn than Sn does in Cu. Thus, during migration, vacancies created by Cu atoms are not filled by Sn atoms, and eventually these vacancies coalesce and form micro-voids at the interface or within the  $\text{Cu}_3\text{Sn}$  IMC layer [61].

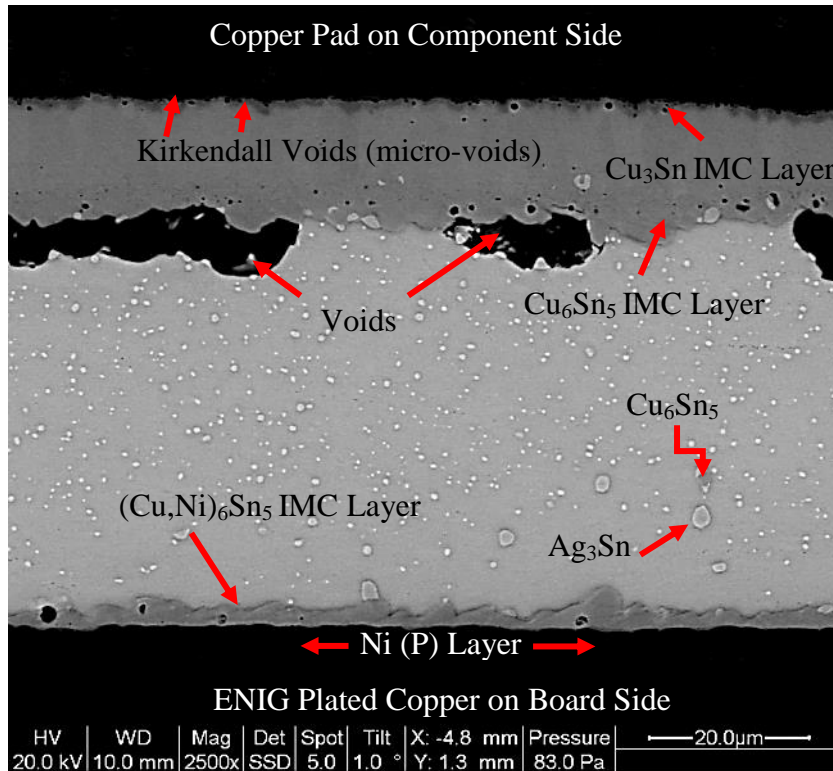


Figure 8-4: Interfacial IMC Growth and Void Creation during Isothermal Aging (SAC305 - 185°C/100 hours)

The second type of void was found at the interface between the  $\text{Cu}_6\text{Sn}_5$  IMC layer and the solder bulk, and is also shown in Figure 8-4. These voids were quite large and significantly reduced the contact area between the  $\text{Cu}_6\text{Sn}_5$  interfacial IMC and bulk solder. This type of void has not been previously reported in the literature. These voids could not be classified as champagne voids or planar micro-voids because they were bigger than the reported size of champagne voids and they were neither related to galvanic corrosion during immersion plating of silver metal nor formed during the

reflow process [97]. During high temperature aging, these voids form at multiple interfacial locations; enlarge during subsequent aging; and eventually coalesce with neighboring voids to form even bigger voids at the  $\text{Cu}_6\text{Sn}_5$  IMC layer/solder bulk interface as shown in Figure 8-5.

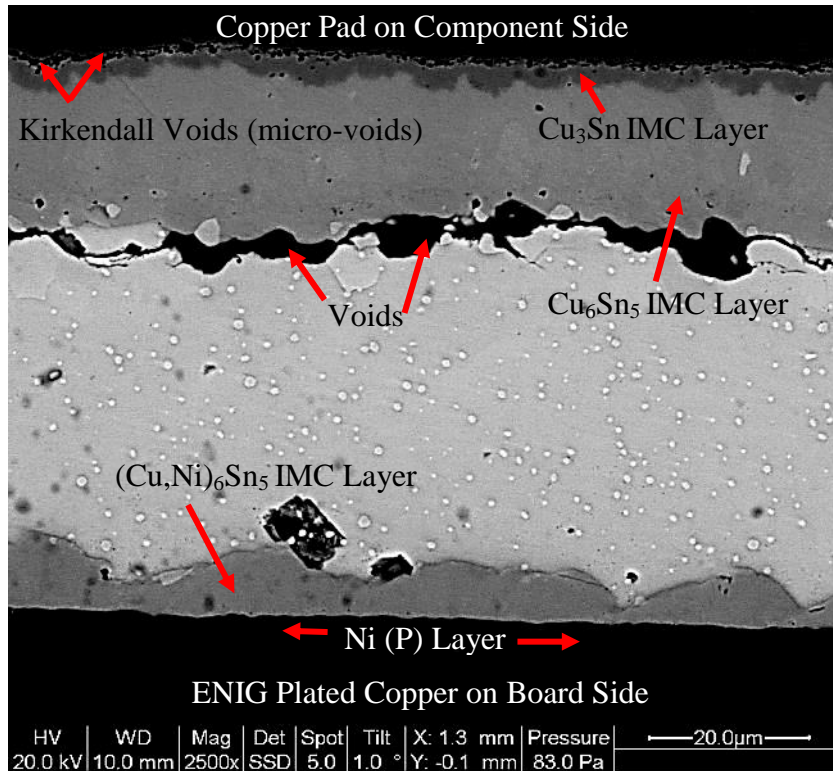


Figure 8-5: Interfacial IMC Growth and Void Coalescing during further Isothermal Aging (SAC305 - 185°C/600 hours)

The mechanism of such void formation is unknown. It is believed that high diffusion rates during high temperature aging are related to void formation. A detailed study is recommended to further understand the mechanism of such void formation; however, it is beyond the scope of this study. Both types of voids discussed earlier can have detrimental effects on the long-term reliability of solder joints, especially in mechanical shock/drop loading. The effects these voids have on the long-term reliability of solder joints have not been well studied.



By looking at Figure 8-3, Figure 8-4, and Figure 8-5, it can be seen that the  $\text{Cu}_6\text{Sn}_5$  interfacial IMC layer had faster growth compared to the  $\text{Cu}_3\text{Sn}$  and  $(\text{Cu},\text{Ni})_6\text{Sn}_5$  layers during high temperature aging. This combined with its inherent brittleness relative to  $(\text{Cu},\text{Ni})_6\text{Sn}_5$  makes the  $\text{Cu}_6\text{Sn}_5$  IMC layer the most critical for solder reliability, and thus it is the one whose interfacial IMC thickness is measured for QFN44 and QFN32 packages. In order to measure average thickness of the  $\text{Cu}_6\text{Sn}_5$  IMC layer, ESEM images at 2500x magnification were taken at various locations covering the horizontal  $\text{Cu}_6\text{Sn}_5$  IMC layer formed underneath the copper pad on the component side as shown in Figure 8-6 (a). Image processing software, XTDocument was used to calculate the total area of  $\text{Cu}_6\text{Sn}_5$  IMC layer and the horizontal distance from each ESEM image at 2500x magnification as shown in Figure 8-6 (b). An average thickness of the  $\text{Cu}_6\text{Sn}_5$  IMC layer for each ESEM image was calculated by dividing the IMC total area by the horizontal distance. Then, the average  $\text{Cu}_6\text{Sn}_5$  IMC layer thickness for a sample was calculated by averaging the calculated result for each ESEM image.

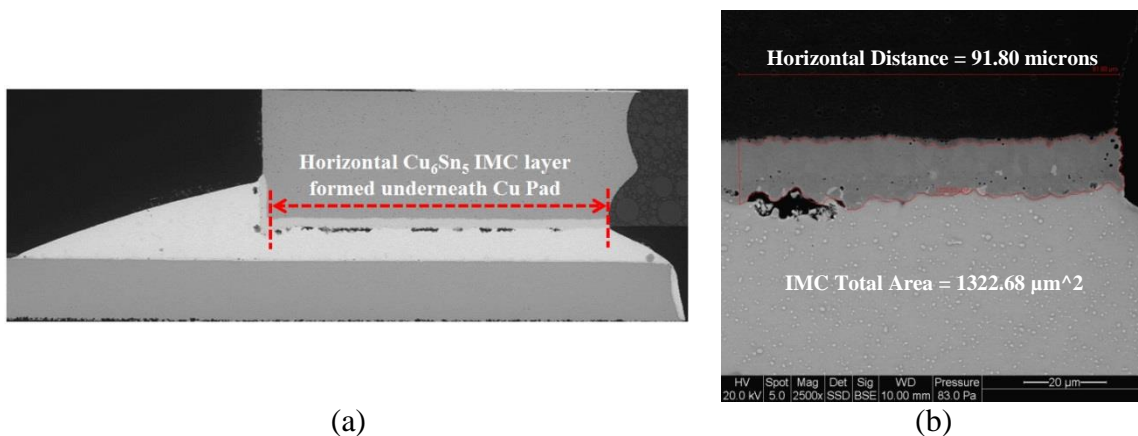


Figure 8-6  $\text{Cu}_6\text{Sn}_5$  IMC Layer Thickness Measurement (a) Length of the Horizontal  $\text{Cu}_6\text{Sn}_5$  IMC Layer used for Measurement (b) ESEM Image at 2500x Magnification for Average  $\text{Cu}_6\text{Sn}_5$  IMC Layer Thickness Measurement.

In addition to  $\text{Cu}_6\text{Sn}_5$  IMC thickness measurement, void measurement was also performed to calculate the %voiding (% contact length reduction due to voiding) at the  $\text{Cu}_6\text{Sn}_5$  IMC layer/solder bulk interface. Using Image-J image processing software, the total contact length before and after voiding was calculated. An example of %voiding calculation is shown in Figure 8-7.

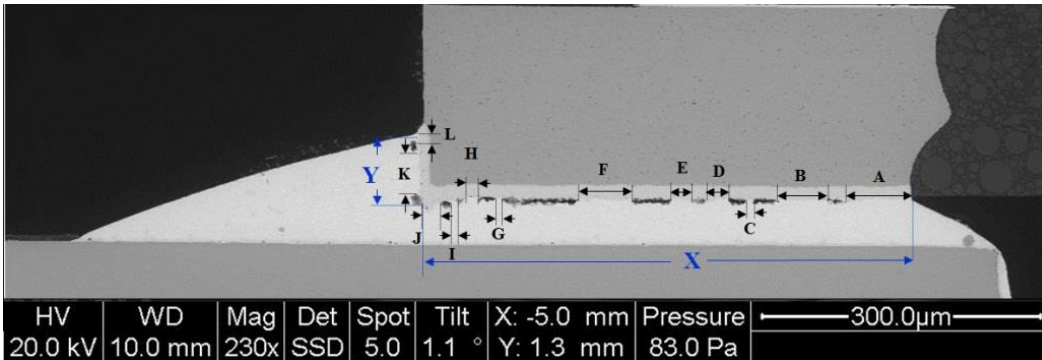


Figure 8-7: ESEM Image of Solder Joint Indicating Length Measurement Marks for %voiding Calculation.

After the contact length measurement before and after voiding, %voiding was calculating using following equation:

$$\%Voiding = \left( \frac{[X + Y] - [A + \dots + L]}{[X + Y]} \right) * 100$$

For both aging test measurement parameters (i.e.  $\text{Cu}_6\text{Sn}_5$  IMC layer thickness and %voiding), multiple readings were measured covering the whole solder joint on the left and right sides of QFN44 and QFN32 packages.

The next few sections provide the detailed information on the  $\text{Cu}_6\text{Sn}_5$  interfacial IMC growth and %voiding for QFN44 and QFN32 under 185°C and 200°C isothermal aging at 0, 100, 200, 400, 600, and 1000 hour intervals.

### 8.3.QFN44 - Cu<sub>6</sub>Sn<sub>5</sub> IMC Growth and %Voiding during 185°C

#### Aging

The average thickness of the Cu<sub>6</sub>Sn<sub>5</sub> IMC layer for each solder with aging time at 185°C are summarized in Figure 8-8. Also, the results of %voiding at the interface between the Cu<sub>6</sub>Sn<sub>5</sub> IMC layer and the solder bulk during 185°C aging are summarized in Figure 8-9. The error bar shown in both Figure 8-8 and Figure 8-9 indicate the standard deviation of measurements.

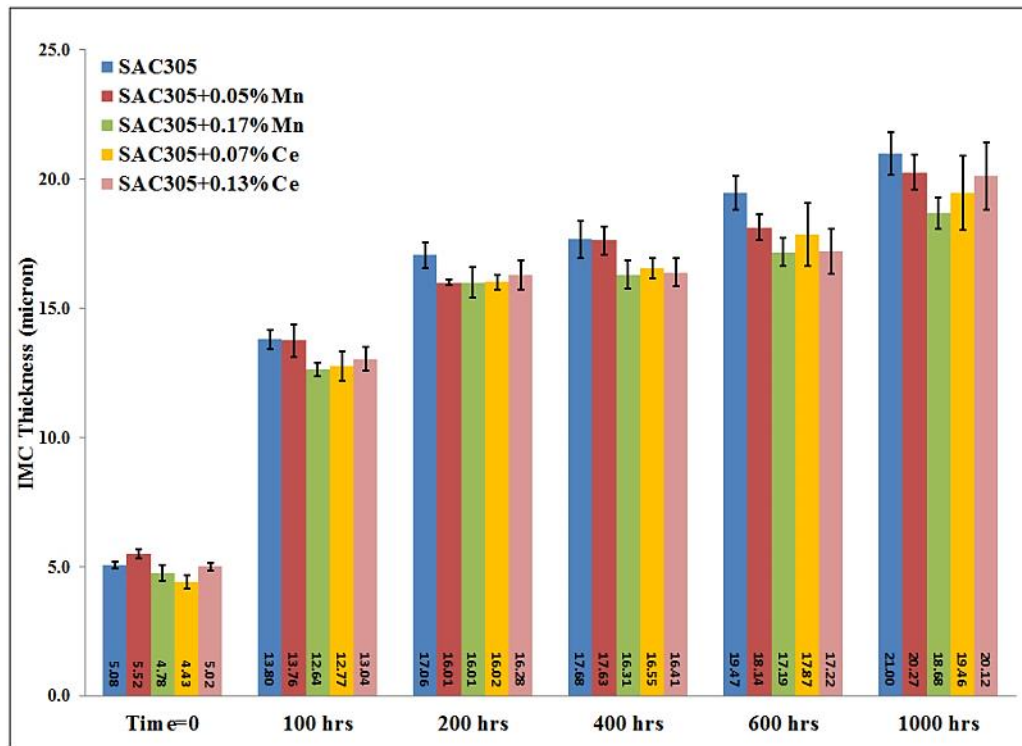


Figure 8-8: QFN44 - Cu<sub>6</sub>Sn<sub>5</sub> IMC Layer Growth Summary during 185°C Aging

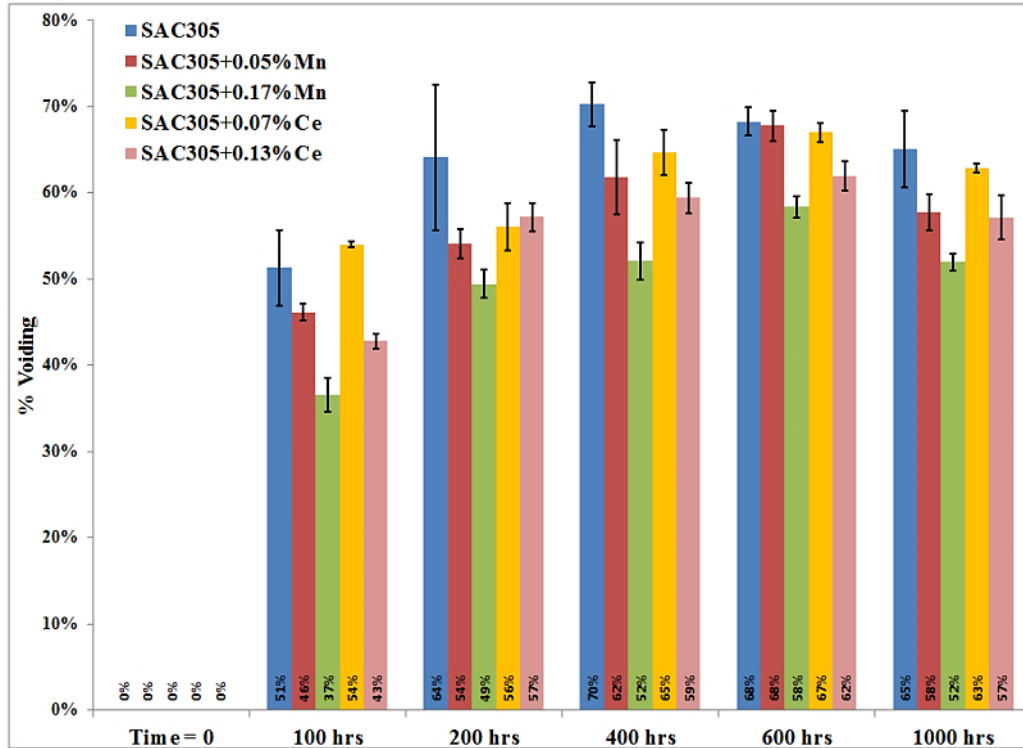


Figure 8-9: QFN44 - %Voiding Measurements during 185°C Aging

It can be seen from Figure 8-8 that after 100 hours of aging at 185°C, there was a significant increase in the thickness of the  $\text{Cu}_6\text{Sn}_5$  IMC layer was observed for all solders. During subsequent aging after 100 hours, the  $\text{Cu}_6\text{Sn}_5$  IMC layer had steady growth. It is also clear that all modified SAC305 solders were effective in suppressing the growth of the  $\text{Cu}_6\text{Sn}_5$  IMC layer during 185°C aging. High Mn suppressed the growth most effectively and resulted in the thinnest  $\text{Cu}_6\text{Sn}_5$  IMC layer. After 1000 hours of aging at 185°C, High Mn showed a 12% reduction in  $\text{Cu}_6\text{Sn}_5$  IMC layer thickness compared to that found in SAC305. Low Mn initially formed the thickest  $\text{Cu}_6\text{Sn}_5$  IMC layer; however, it suppressed the growth of the  $\text{Cu}_6\text{Sn}_5$  IMC layer during subsequent aging. Overall, SAC305 solder showed the thickest  $\text{Cu}_6\text{Sn}_5$  IMC layer at each time interval during 185°C aging.

In Figure 8-9, it can be seen that substantial voiding (reduction in contact length) was observed after 100 hours of aging at 185°C for all solders. Except for the 100 hour interval for Low Ce, all modified SAC305 solders were effective in reducing voiding at the interface between the  $\text{Cu}_6\text{Sn}_5$  IMC layer and solder bulk during 185°C aging. High Mn was the most effective solder to form fewer voids, as evident at each time interval during 185°C aging. Compared to SAC305, High Mn formed 15% to 29% lesser voids during 185°C aging. In general, High Ce is the second most effective solder after High Mn to form fewer voids. Compared to SAC305, High Ce formed 9% to 17% lesser voids. Overall, SAC305 solder showed the highest voiding at each time interval during 185°C aging.

In order to further evaluate interfacial IMCs, bulk IMCs and voiding during 185°C aging, ESEM images at 2500x magnification for all solders after reflow, after 100 hours/185°C aging, and after 1000 hours/185°C aging are used for the discussion present below.

Figure 8-10 shows a SAC305 solder joint. After reflow, the bulk microstructure contained fine  $\text{Ag}_3\text{Sn}$  particles,  $\text{Cu}_6\text{Sn}_5$  particles and  $\beta$ -tin dendrites. Upon aging, both  $\text{Ag}_3\text{Sn}$  and  $\text{Cu}_6\text{Sn}_5$  particles coalesced and coarsened. After 1000 hours of aging, large  $\text{Ag}_3\text{Sn}$  particles could be seen in the solder bulk. A few coarsened  $\text{Ag}_3\text{Sn}$  particles also migrated to the surface of both the component and the board side interfacial IMCs. Evidence of  $\text{Ag}_3\text{Sn}$  particles within the  $\text{Cu}_6\text{Sn}_5$  interfacial IMC layer could also be seen during aging. Kirkendall voids found after 100 hours of aging resulted in a crack during subsequent aging between the  $\text{Cu}_3\text{Sn}$  IMC layer and the component pad as shown in Figure 8-10 (c). The interfacial IMC on the board side

also changed from acicular (needle-like) after reflow to laminar during 100 hours of aging. After 1000 hours of aging, the board side interfacial IMC changed to a scallop morphology. As discussed earlier, significant growth in the  $\text{Cu}_6\text{Sn}_5$  IMC layer and void formation could be seen during 185°C aging.

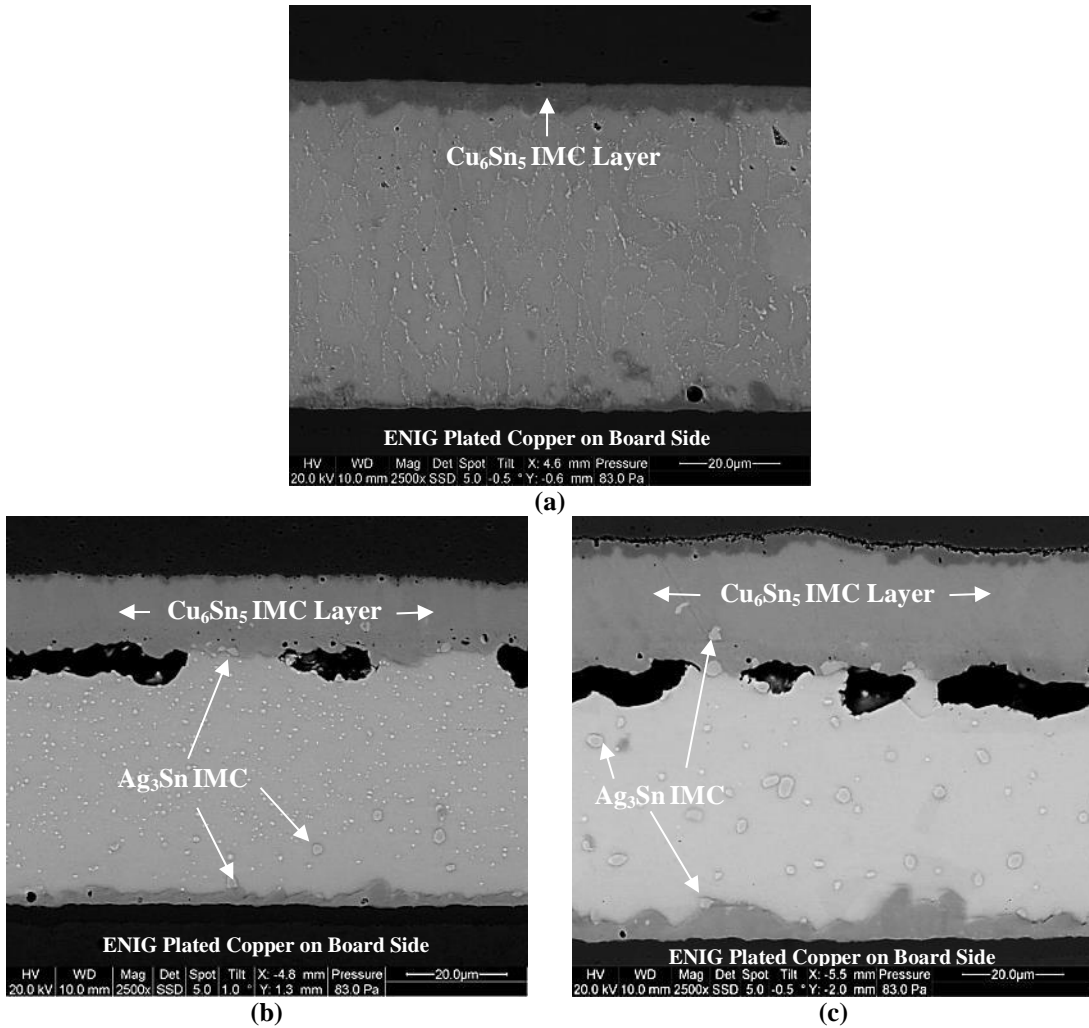


Figure 8-10: QFN44 - SAC305 Solder Joint (a) After Reflow, (b) After 100 hours/185°C Aging, (c) After 1000 hours/185°C Aging

Figure 8-11 shows a SAC305+0.05%Mn solder joint. After reflow, fine  $\text{Ag}_3\text{Sn}$  and  $\text{Cu}_6\text{Sn}_5$  particles formed in the solder bulk. However, the average size of the  $\text{Ag}_3\text{Sn}$  particles after reflow was larger than that found in SAC305 solder. In addition, the size of the  $\text{Ag}_3\text{Sn}$ -Sn eutectic region after reflow was also bigger than that found in

SAC305 solder. A crack passing through the  $\text{Cu}_3\text{Sn}$  interfacial IMC layer on the component side, and the scallop type interfacial IMC on the board side, were also evident after 1000 hours of aging. The bulk IMCs ( $\text{Ag}_3\text{Sn}$  and  $\text{Cu}_6\text{Sn}_5$ ) were also coarsened after 1000 hours of aging. The growth of  $\text{Cu}_6\text{Sn}_5$  IMC layer was lesser in Low Mn solder compared to that of SAC305.

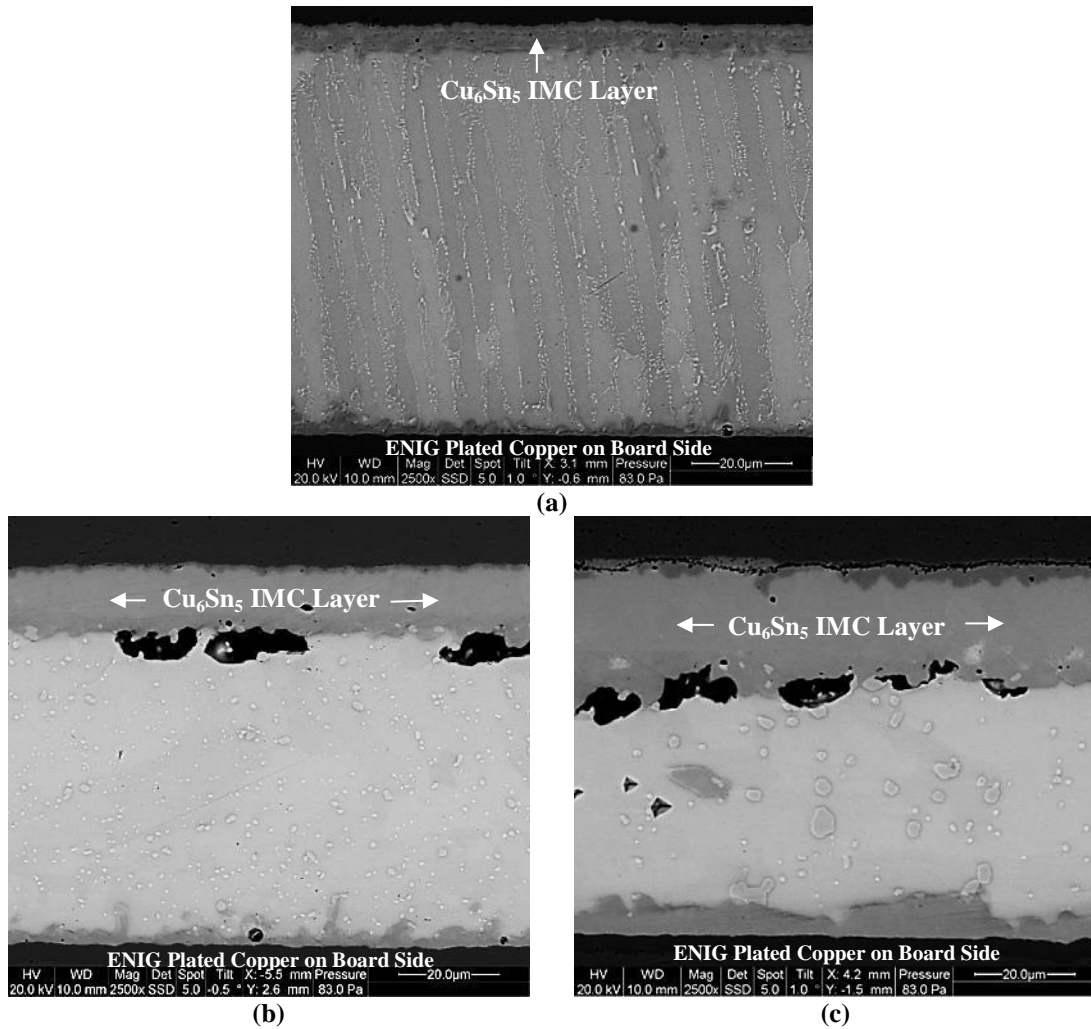


Figure 8-11: QFN44 - SAC305+0.05%Mn Solder Joint (a) After Reflow, (b) After 100 hours/185°C Aging, (c) After 1000 hours/185°C Aging

Figure 8-12 shows a SAC305+0.17%Mn solder joint. With higher concentrations of Mn, the average sizes of the  $\text{Ag}_3\text{Sn}$  particles and the  $\text{Ag}_3\text{Sn}$ -Sn eutectic region in solder bulk after reflow were much larger than in the SAC305 and

SAC305+0.05%Mn solders. However, after 1000 hours of aging, many small and only a few large  $\text{Ag}_3\text{Sn}$  coarsened particles could be seen in Figure 8-12 (c). This indicates that SAC305+0.17%Mn solder suppresses the growth of bulk IMCs during aging. The interfacial IMC layer on the board side remains planar without forming scallops during aging. In addition, a few small cracks along with Kirkendall voids have been observed in the  $\text{Cu}_3\text{Sn}$  interfacial IMC layer after 1000 hours of aging. Overall, High Mn showed thinner  $\text{Cu}_6\text{Sn}_5$  IMC layer, less coarsened bulk IMCs and reduced interfacial voiding compared to SAC305 during 185°C aging.

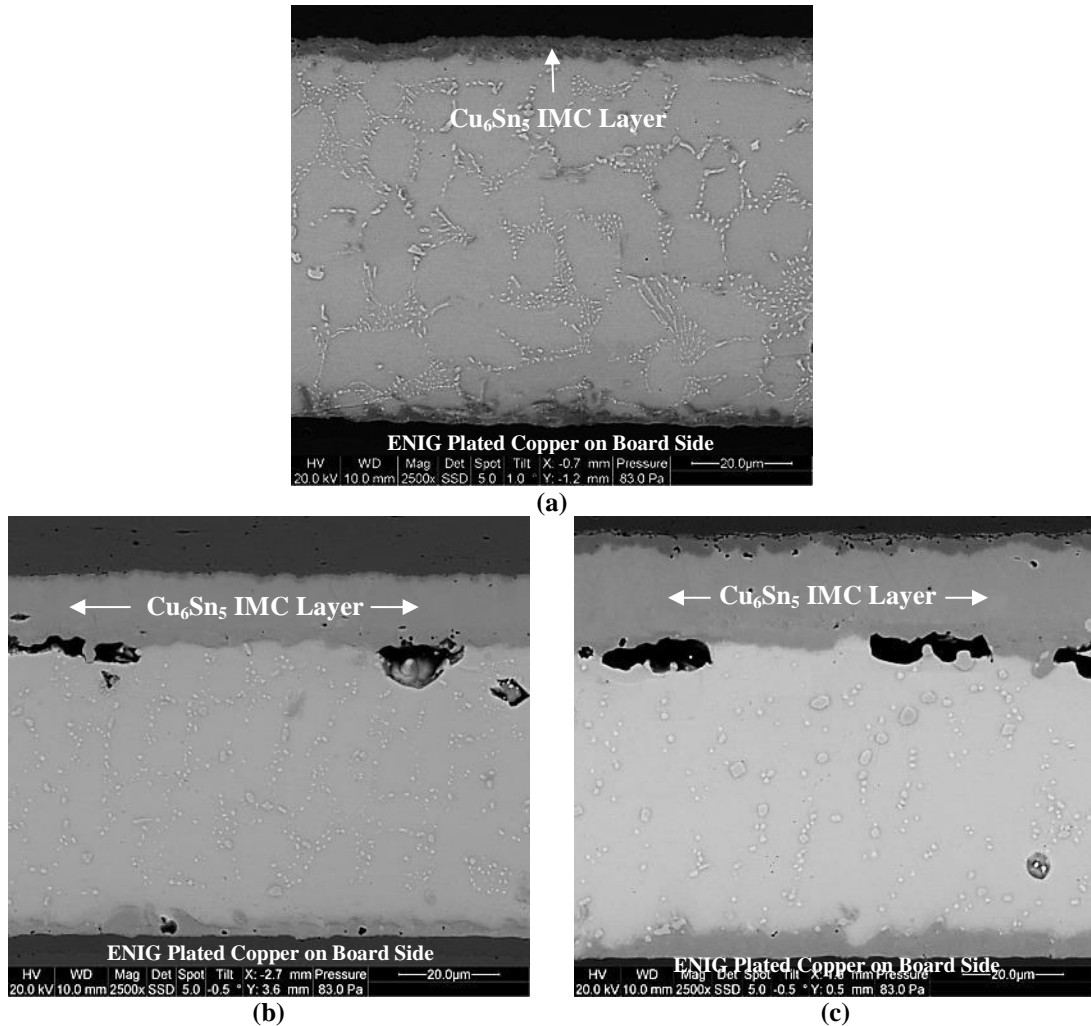


Figure 8-12: QFN44 - SAC305+0.17%Mn Solder Joint (a) After Reflow, (b) After 100 hours/185°C Aging, (c) After 1000 hours/185°C Aging



Figure 8-13 shows a SAC305+0.07%Ce solder joint. After reflow, the microstructure of the solder bulk was found to be similar to SAC305. After 1000 hours of aging, the size of coarsened  $\text{Ag}_3\text{Sn}$  particles was smaller than that for SAC305. Thus, SAC305+0.07%Ce solder suppressed the growth of both bulk IMCs during aging. The interfacial IMC on the board side exhibited a scallop-type morphology after 1000 hours of aging. In addition, a crack was also observed passing through the  $\text{Cu}_3\text{Sn}$  interfacial IMC layer on the component side, as shown in Figure 8-13 (c).

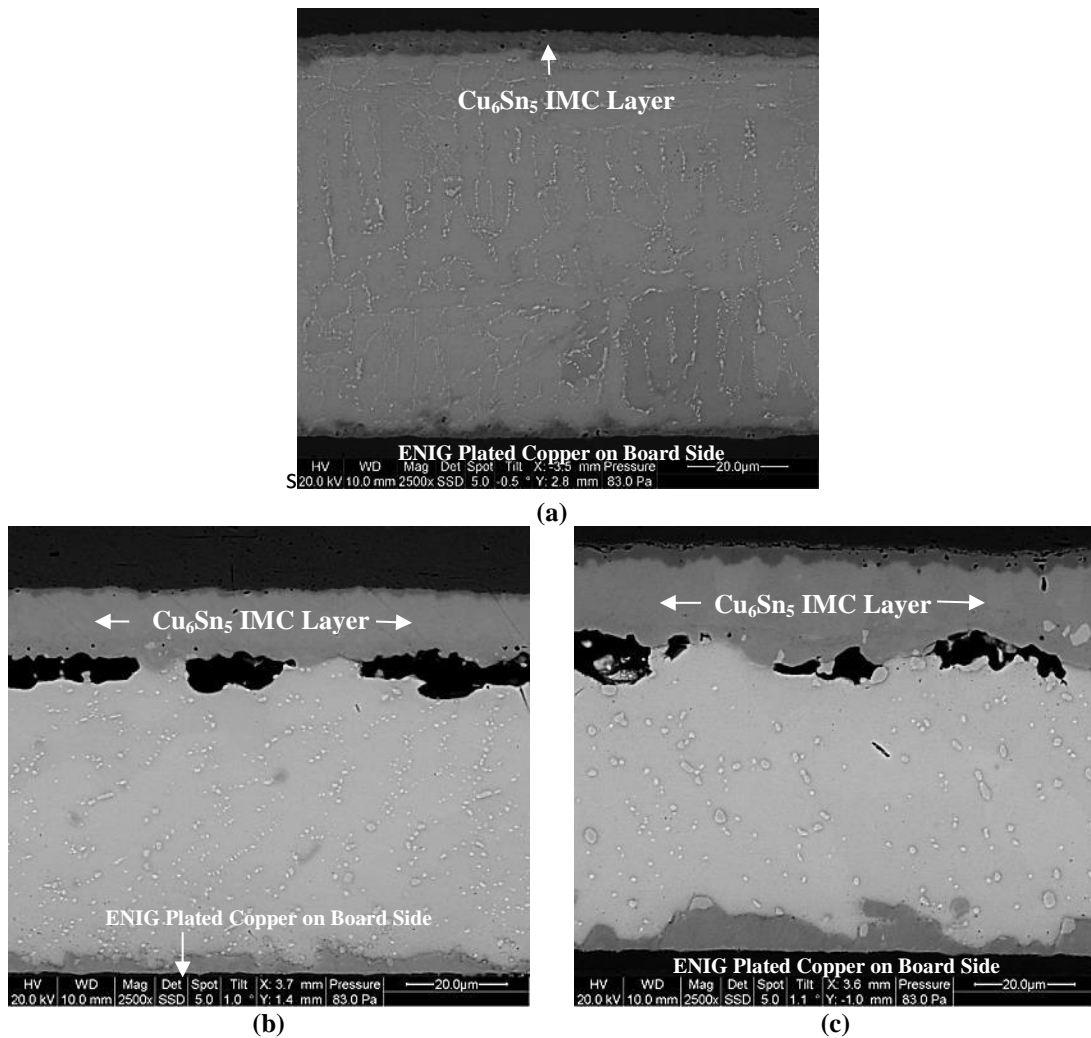


Figure 8-13: QFN44 - SAC305+0.07%Ce Solder Joint (a) After Reflow, (b) After 100 hours/185°C Aging, (c) After 1000 hours/185°C Aging

Figure 8-14 shows a SAC305+0.13%Ce solder joint. After reflow, more  $\beta$ -Sn dendrites with a smaller size were observed in the solder bulk compared to SAC305. Upon aging, the size of the resultant  $\text{Ag}_3\text{Sn}$  particles after 1000 hours of aging was smaller than for SAC305 solder. This suggests that SAC305+0.13%Ce solder minimize the growth of bulk IMC during aging. Also, the morphology of the interfacial IMC layer on the board size changed from acicular (i.e. needle-like) (after reflow) to lamellar (after 100 hours/185°C aging) to scallop-shaped (after 1000 hours/185°C aging).

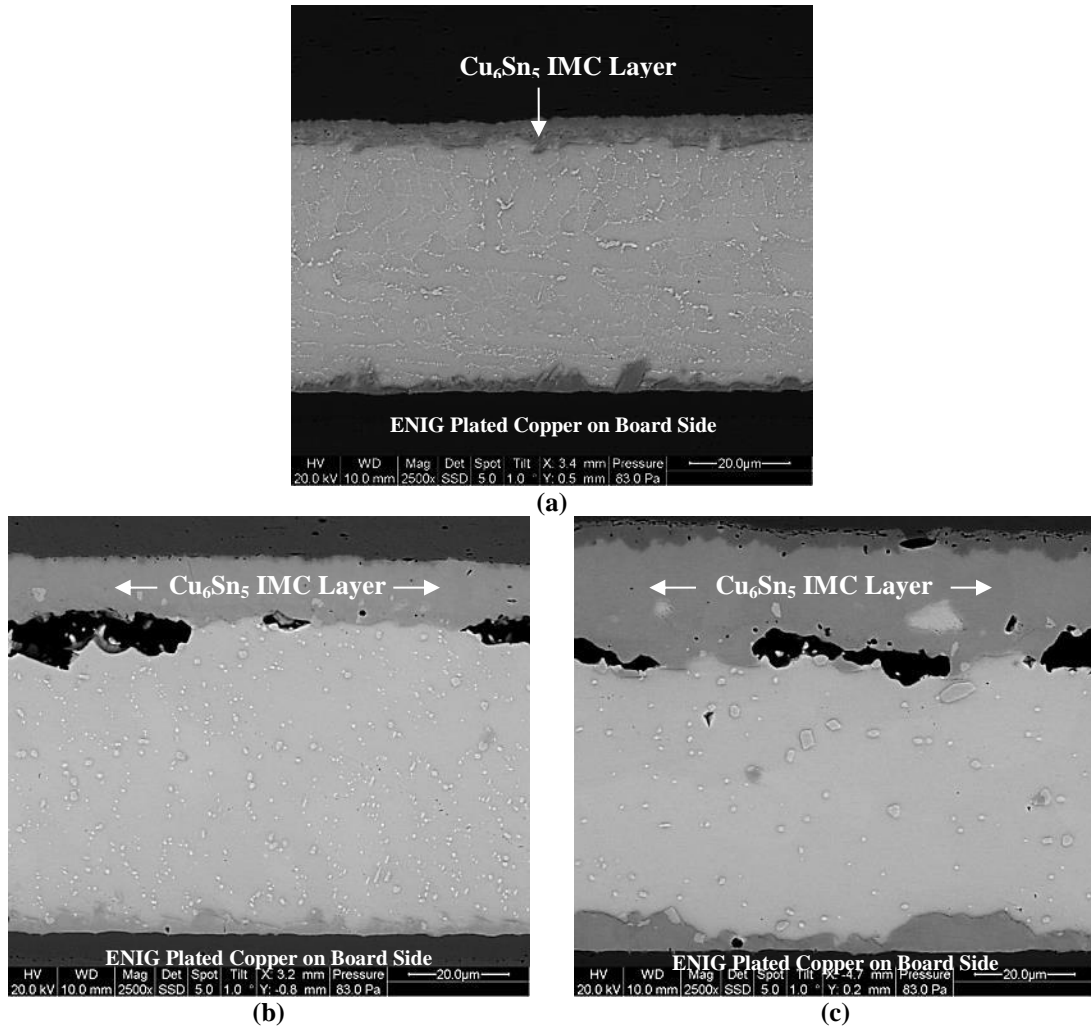


Figure 8-14: QFN44 - SAC305+0.13%Ce Solder Joint (a) After Reflow, (b) After 100 hours/185°C Aging, (c) After 1000 hours/185°C Aging

## 8.4.QFN44 - Cu<sub>6</sub>Sn<sub>5</sub> IMC Growth and %Voiding during 200°C

### Aging

The average thickness of the Cu<sub>6</sub>Sn<sub>5</sub> IMC layer for each solder during 200°C aging are summarized in Figure 8-15. The error bar shown in Figure 8-15 indicates the standard deviation of measurements.

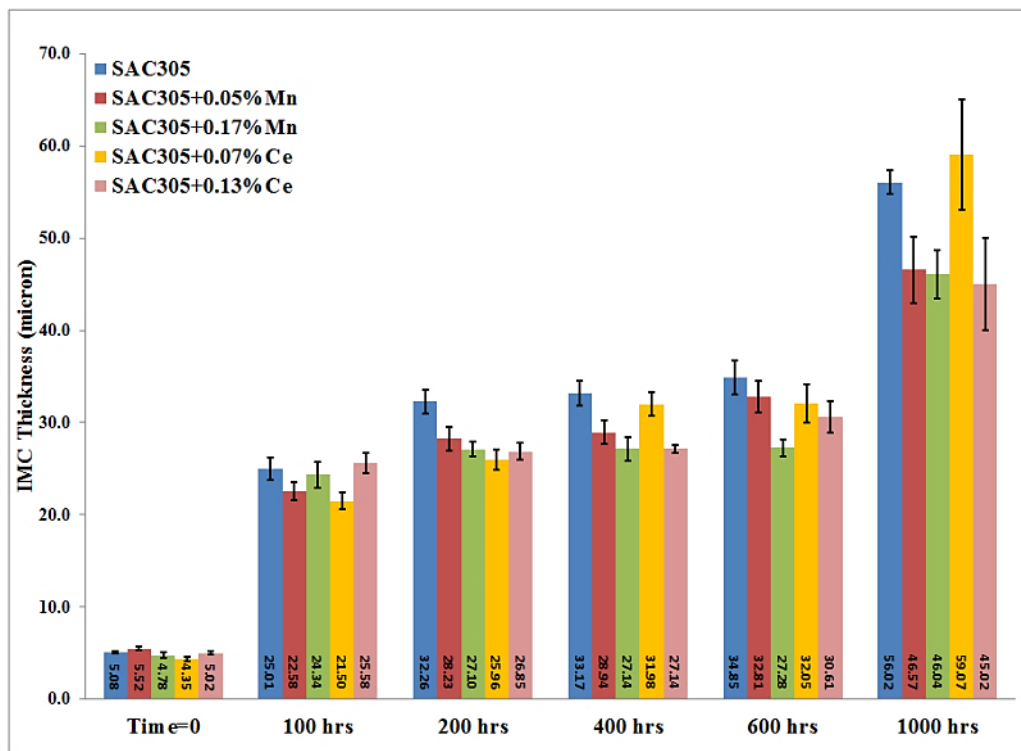


Figure 8-15: QFN44 - Cu<sub>6</sub>Sn<sub>5</sub> IMC Growth Summary during 200°C Aging

It can be seen from Figure 8-15 that except for the Low Ce/1000 hour interval, all modified SAC305 solders effectively suppressed the growth of Cu<sub>6</sub>Sn<sub>5</sub> IMC during 200°C aging. After 1000 hours of aging at 200°C, it was found that Low Mn, High Mn and High Ce showed 17%, 18%, and 20% reduction in the growth of Cu<sub>6</sub>Sn<sub>5</sub> IMC layer, respectively, than that of SAC305.

From Figure 8-15, two interesting findings can be observed in the growth pattern for the  $\text{Cu}_6\text{Sn}_5$  IMC for all solders during 200°C aging. First, there was a sudden growth of the  $\text{Cu}_6\text{Sn}_5$  IMC layer after just 100 hours of aging at 200°C. And second, an additional sudden growth of the  $\text{Cu}_6\text{Sn}_5$  IMC layer was observed after 1000 hours of aging at 200°C.

The first sudden growth after 100 hours was due to high diffusivity between the tin (from the solder) and the copper (from the component pad) leading to thick  $\text{Cu}_6\text{Sn}_5$  IMC layer at the component side during 200°C aging. From Figure 8-15, it is apparent that  $\text{Cu}_6\text{Sn}_5$  IMC thickness jumped from ~5 microns (after reflow) to ~24 microns within 100 hours of aging at 200°C. It is also important to note that the  $\text{Cu}_6\text{Sn}_5$  IMC layer thickness after 100 hours at 200°C aging was much higher than that observed after 1000 hours of aging at 185°C. Thus, a 15°C increase in the aging temperature from 185°C to 200°C can cause a significant increase in the  $\text{Cu}_6\text{Sn}_5$  IMC layer thickness in a short period of time.

During subsequent aging after 100 hours at 200°C, the thickness of  $\text{Cu}_6\text{Sn}_5$  IMC grows steadily up to 600 hours for all solders, as shown in Figure 8-15. An additional sudden growth of the  $\text{Cu}_6\text{Sn}_5$  interfacial IMC has been observed after 1000 hours. Such a rapid increase in the thickness of  $\text{Cu}_6\text{Sn}_5$  IMC observed after 1000 hours was quite unexpected. Further analyses revealed that such an unexpected increase in the growth of  $\text{Cu}_6\text{Sn}_5$  IMC layer was due to the consumption of the Ni layer from the ENIG finish on the board side.

In order to explain Ni layer consumption phenomenon, an SAC305 solder joint sample was used as an example. Figure 8-16 shows a SAC305 solder joint in a

QFN44 package at time intervals of 0, 100, 200, 400, 600, and 1000 hours under 200°C aging.

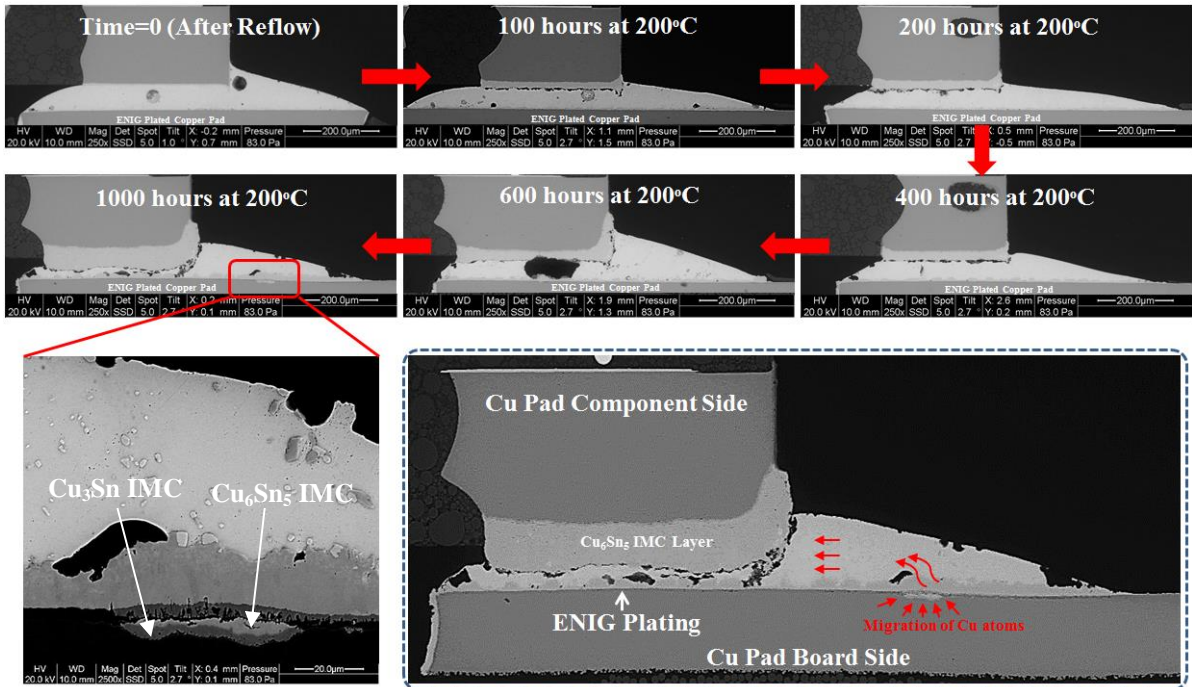


Figure 8-16: Ni layer consumption phenomenon in QFN44 package, a demonstration using SAC305 solder joint at various time intervals under 200°C aging.

As shown in Figure 8-16, the  $\text{Cu}_6\text{Sn}_5$  IMC layer grew steadily from 100 to 600 hours aging at 200°C during which the Ni layer on the board side seemed unaffected. The Ni layer in ENIG plating for board finish acts as a diffusion barrier layer to prevent the consumption of Cu pad on the board side. If the Ni layer is consumed, no barrier layer exists between the copper pad and the board side interfacial IMC. Due to lack of the barrier layer, copper atoms from the board side start migrating toward the  $\text{Cu}_6\text{Sn}_5$  IMC layer on the component side. With copper atoms migrating from the board side and tin atoms present from the solder bulk, the reaction between the tin and the copper continues and eventually forms an even thicker  $\text{Cu}_6\text{Sn}_5$  IMC layer as observed after 1000 hours of aging at 200°C. The magnified view of consumed Ni layer in

SAC305 solder joint after 1000 hours of aging at 200°C is shown in Figure 8-16. In addition to copper atoms migration from board side to component side, tin atoms from solder bulk also start reacting with copper pad on the board side and form two additional IMCs such as  $\text{Cu}_6\text{Sn}_5$  and  $\text{Cu}_3\text{Sn}$ .

Similar findings have been also observed for a resistor package, which is discussed in detail in chapter 9. It is important to note that even though the Ni layer breaks after 1000 hours, Low Mn, High Mn, and High Ce solders still suppress the growth of  $\text{Cu}_6\text{Sn}_5$  IMC layer, as shown in Figure 8-15. High Mn solder almost stabilized the growth of the  $\text{Cu}_6\text{Sn}_5$  IMC layer between 200 and 600 hours. At 1000 hours of aging, Low Mn, High Mn, and High Ce solders resulted in much lower thickness of  $\text{Cu}_6\text{Sn}_5$  interfacial IMCs compared to SAC305; and Low Ce showed the thickest  $\text{Cu}_6\text{Sn}_5$  IMC at 1000 hours aging at 200°C.

The results of % voiding at the interface between the  $\text{Cu}_6\text{Sn}_5$  IMC layer and the solder bulk during 200°C aging are summarized in Figure 8-17. The error bar shown in Figure 8-17 indicates the standard deviation of measurements.

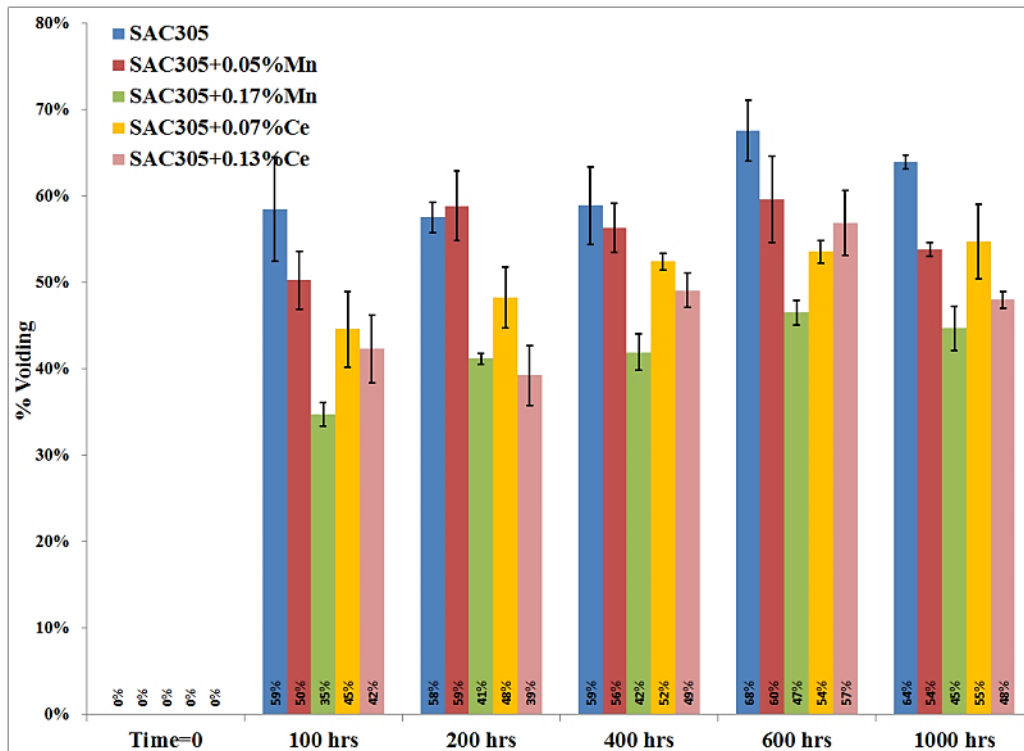


Figure 8-17: QFN44 - %Voiding Measurements during 200°C Aging

It can be seen from Figure 8-17 that substantial voiding (reduction in contact length) was observed after 100 hours of aging at 200°C. Except for Low Mn solder at the 200 hour interval, all modified SAC305 solders were effective at reducing voiding at the interface between the  $\text{Cu}_6\text{Sn}_5$  IMC layer and the solder bulk during 200°C aging. In general, High Mn solder is the most effective solder for forming the fewest voids. Compared to SAC305, High Mn formed 29% to 41% less voids. High Ce is the second most effective in reducing voiding with 16% to 32% less voids than SAC305 during 1000 hours of aging at 200°C. Except for High Ce at 200 hours, High Mn resulted in the thinnest  $\text{Cu}_6\text{Sn}_5$  IMC layer during aging. SAC305 solder showed the highest voiding at each time interval except for 200 hours during 200°C aging.

In addition to the  $\text{Cu}_6\text{Sn}_5$  IMC layer thickness and %voiding, the evolution of interfacial IMCs is also important. ESEM images at 2500x magnification for all

solders after 100 hours/200°C aging and after 1000 hours/200°C aging are used in the discussion below.

Figure 8-18 shows a SAC305 solder joint. During 100 hours of aging at 200°C, both  $\text{Ag}_3\text{Sn}$  and  $\text{Cu}_6\text{Sn}_5$  particles were coarsened. Migration of few  $\text{Ag}_3\text{Sn}$  particles near the IMC surface and within the  $\text{Cu}_6\text{Sn}_5$  IMC layer can also be seen in Figure 8-18 (a). In addition, a scallop shaped board side IMC layer was also visible after 100 hours of aging at 200°C. Evidence of thick  $\text{Cu}_6\text{Sn}_5$  IMC layer,  $\text{Cu}_3\text{Sn}$  IMC layer and voids can be also seen Figure 8-18 (a).

After 1000 hours of aging, a large  $\text{Cu}_6\text{Sn}_5$  IMC layer was observed, as shown in Figure 8-18 (b). The solder bulk was completely consumed at the expense of the sudden growth of the  $\text{Cu}_6\text{Sn}_5$  IMC layer. The consumption of bulk solder was so aggressive that it reached close to the board side interfacial IMC layer and resulted in large voids between two interfacial IMCs. Large  $\text{Ag}_3\text{Sn}$  particles were also visible within the  $\text{Cu}_6\text{Sn}_5$  IMC layer. In addition, a crack was also observed within the  $\text{Cu}_6\text{Sn}_5$  IMC layer. Thickness of the  $\text{Cu}_3\text{Sn}$  IMC layer was also increased during aging from 100 to 1000 hours. The board side interfacial IMC showed large scallops after 1000 hours of aging at 200°C.



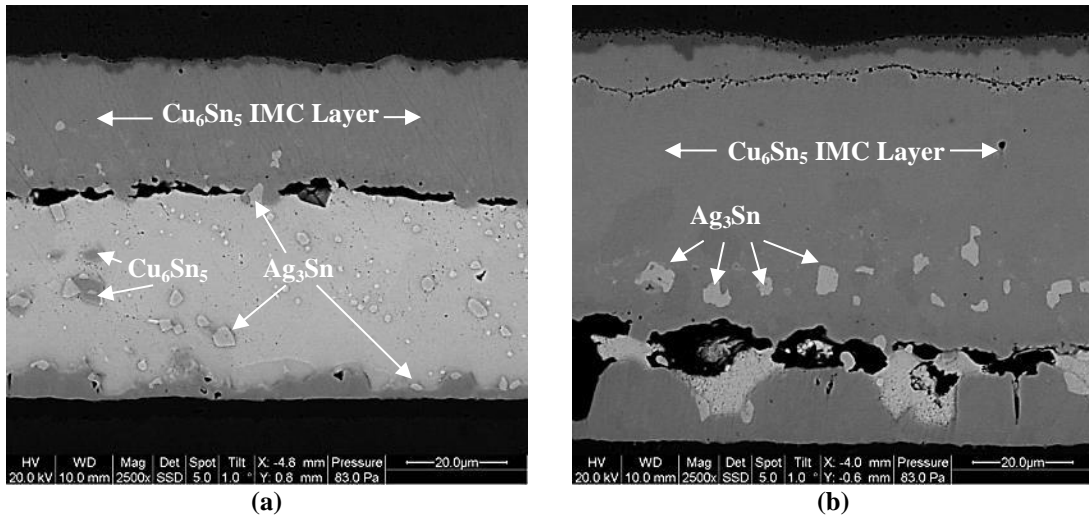


Figure 8-18: QFN44 - SAC305 Solder Joint (a) After 100 hours/200°C Aging, (b) After 1000 hours/200°C Aging

Figure 8-19 shows a SAC305+0.05%Mn solder joint. During 100 hours of aging, both the  $\text{Ag}_3\text{Sn}$  and  $\text{Cu}_6\text{Sn}_5$  particles coarsened; however, the size of the larger  $\text{Ag}_3\text{Sn}$  and  $\text{Cu}_6\text{Sn}_5$  particles observed in the Low Mn solder was smaller than that of SAC305. The board side interfacial IMC showed laminar type morphology after 100 hours of aging. Figure 8-19 (b) shows many intermittent cracks passing through the  $\text{Cu}_3\text{Sn}$  IMC and the interface between the  $\text{Cu}_6\text{Sn}_5$  and  $\text{Cu}_3\text{Sn}$  IMC layers. The presence of large  $\text{Ag}_3\text{Sn}$  particles and concentrated tin within  $\text{Cu}_6\text{Sn}_5$  IMC layer after 1000 hours of aging can be also seen in Figure 8-19 (b). It is important to note that the thickness of the  $\text{Cu}_6\text{Sn}_5$  IMC layer observed in Low Mn solder was much smaller than that of SAC305.

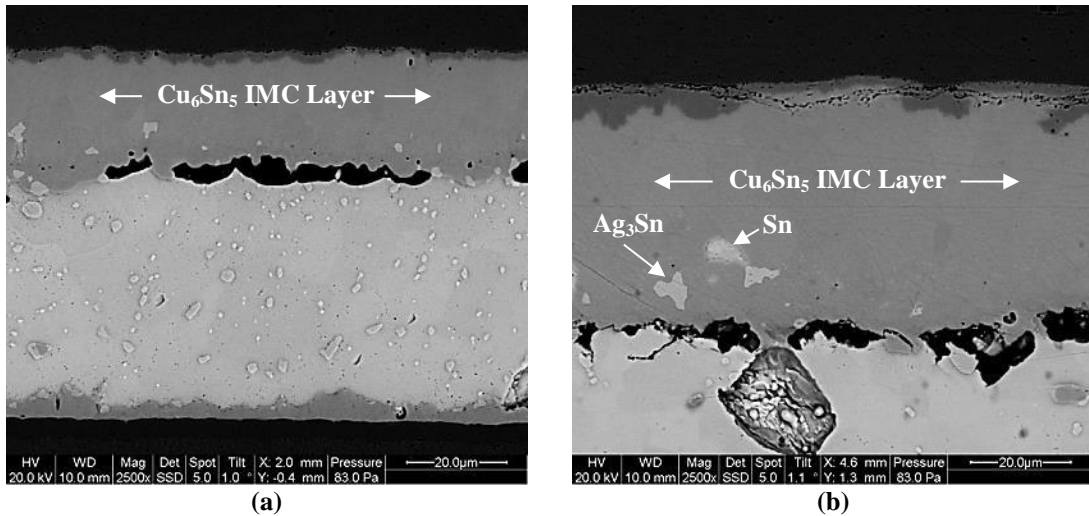


Figure 8-19: QFN44 - SAC305+0.05%Mn Solder Joint (a) After 100 hours/200°C Aging, (b) After 1000 hours/200°C Aging

Figure 8-20 shows a SAC305+0.17%Mn solder joint. Within 100 hours of aging, less coarsening of  $\text{Ag}_3\text{Sn}$  and  $\text{Cu}_6\text{Sn}_5$  particles was observed in the bulk solder, as shown in Figure 8-20 (a). This indicates that High Mn solder is effective in reducing the growth of bulk IMCs during 200°C aging. The interfacial IMC on the board side showed a laminar-type morphology. After 1000 hours of aging, small intermittent cracks within the  $\text{Cu}_6\text{Sn}_5$  IMC layer were observed. The presence of large  $\text{Ag}_3\text{Sn}$  particles and concentrated tin within the  $\text{Cu}_6\text{Sn}_5$  IMC layer after 1000 hours of aging can be also seen from Figure 8-20 (b). Both Figure 8-20 (a) and Figure 8-20 (b) clearly show that the thickness of the  $\text{Cu}_6\text{Sn}_5$  IMC layer and interfacial voids observed in High Mn solder were much smaller than that of SAC305.

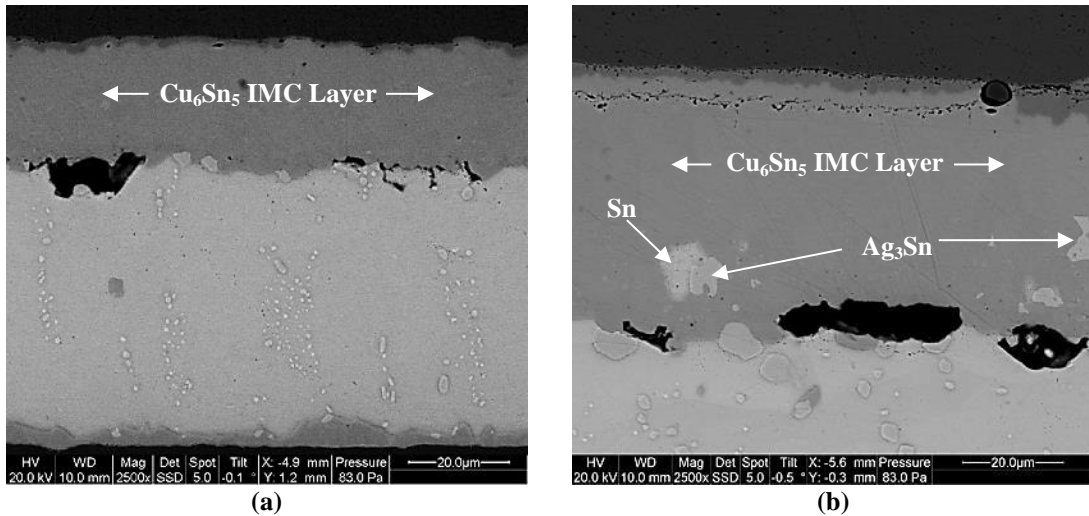


Figure 8-20: QFN44 - SAC305+0.17%Mn Solder Joint (a) After 100 hours/200°C Aging, (b) After 1000 hours/200°C Aging

Figure 8-21 shows a SAC305+0.07%Ce solder joint. After 100 hours of aging, a thicker board side interfacial IMC in Low Ce than that of SA305 was observed. In addition, coarsening of the  $Ag_3Sn$  particles in the solder bulk and their migration to the  $Cu_6Sn_5$  IMC layer can be seen in Figure 8-21 (a). After 1000 hours of aging, the thickest  $Cu_6Sn_5$  IMC layer in Low Ce solder was observed. Many small intermittent cracks at several locations within the  $Cu_6Sn_5$  IMC layer can be seen in Figure 8-21 (b). In addition, a crack passing through the interface between the  $Cu_3Sn$  IMC layer and the copper pad can be also seen in Figure 8-21 (b).

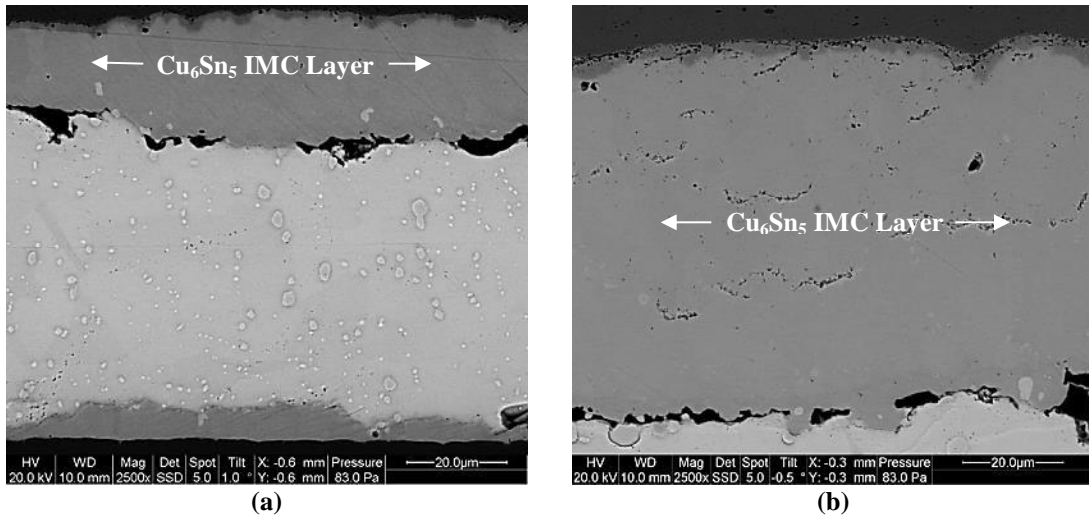
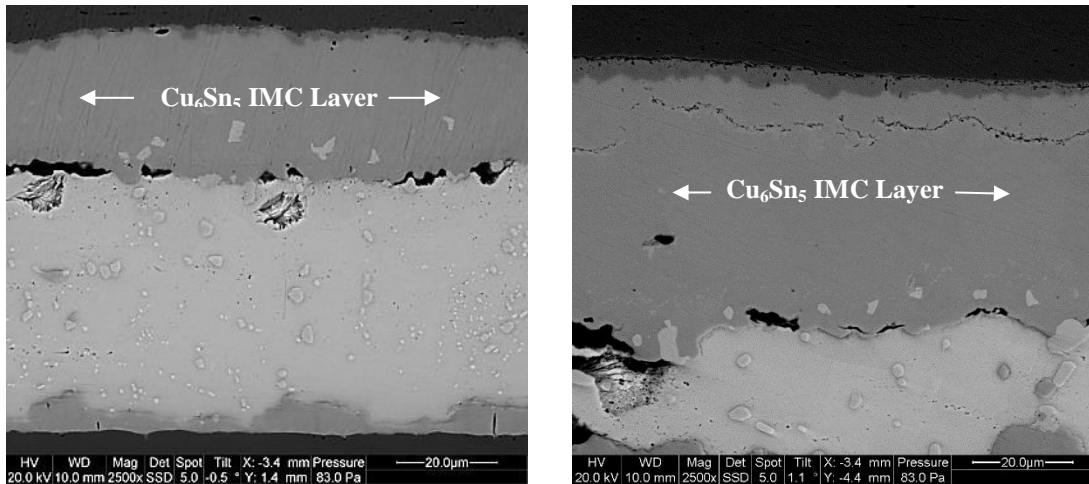


Figure 8-21: QFN44 - SAC305+0.07%Ce Solder Joint (a) After 100 hours/200°C Aging, (b) After 1000 hours/200°C Aging

Figure 8-22 shows a SAC305+0.13%Ce solder joint. Along with a few large  $Ag_3Sn$  particles, many smaller  $Ag_3Sn$  particles after 100 hours of aging can be seen in Figure 8-22 (a). The migration of a few large  $Ag_3Sn$  particles near the surface and within the  $Cu_6Sn_5$  IMC layer can also be found. After 1000 hours of aging, a crack at the interface between the  $Cu_3Sn$  IMC layer and the copper pad was found. Also, intermittent cracks within the  $Cu_6Sn_5$  IMC layer can be also seen in Figure 8-22 (b). It is important to note that the thickness of the  $Cu_6Sn_5$  IMC layer in High Ce solder was much smaller than that of SAC305.



(a) (b)  
 Figure 8-22: QFN44 - SAC305+0.13%Ce Solder Joint (a) After 100 hours/200°C Aging, (b) After 1000 hours/200°C Aging

In addition to QFN44 packages, QFN32 packages were also analyzed during isothermal aging at 185°C and 200°C up to 1000 hours. The aging result summary of the QFN32 package is discussed next.

### 8.5.QFN32 - $\text{Cu}_6\text{Sn}_5$ IMC Growth and %Voiding during 185°C Aging

The average thickness of the  $\text{Cu}_6\text{Sn}_5$  interfacial IMC layer during 185°C aging (up to 1000 hours) observed in QFN32 package for all five solders are summarized in Figure 8-23. The results for % voiding at the interface between the  $\text{Cu}_6\text{Sn}_5$  IMC layer and the solder bulk observed in QFN32 package during 185°C aging are summarized in Figure 8-24. The error bar shown in both Figure 8-23 and Figure 8-24 indicates the standard deviation of measurements.

The results observed in QFN44 and QFN32 packages are quite similar. Thus, only key points from QFN32 study are highlighted in this section. ESEM images at 2500x

magnification for all solders observed in QFN32 package after reflow, after 100 hours/185°C aging, and after 1000 hours/185°C aging are shown in Appendix-B.

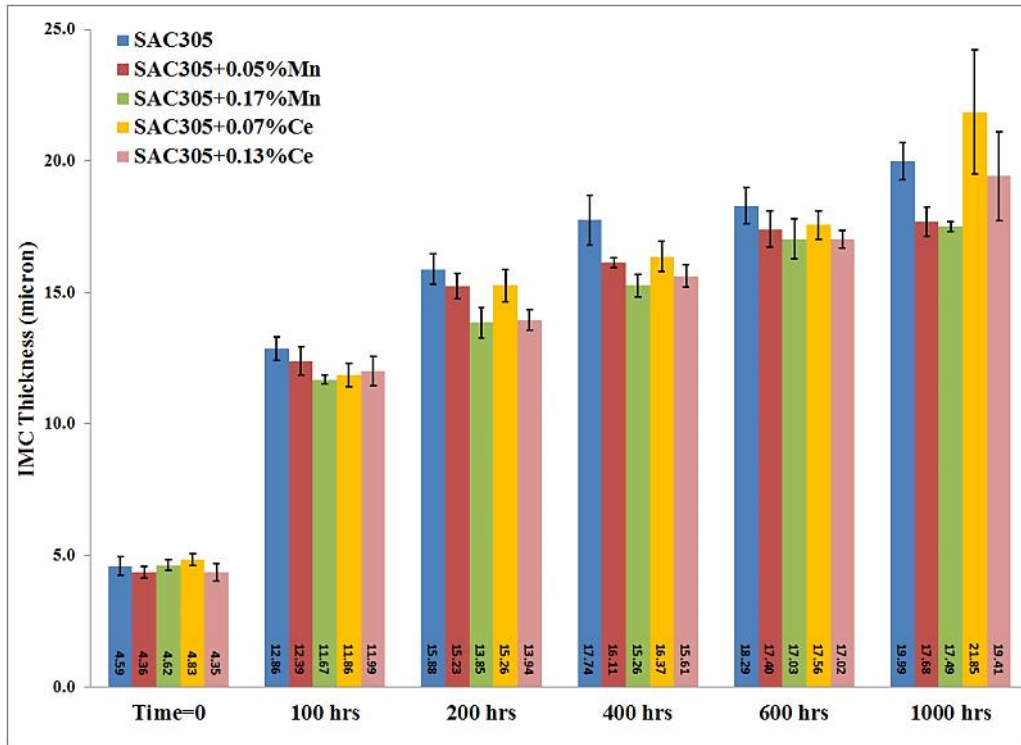


Figure 8-23: QFN32 -  $\text{Cu}_6\text{Sn}_5$  IMC Growth Summary during 185°C Aging

It is important to note that the average thickness of the  $\text{Cu}_6\text{Sn}_5$  IMC layer for all solders found in QFN32 was a little lower than that of QFN44. This is believed to be due to the smaller copper pad size of QFN32. From Figure 8-23, it can be concluded that except for the Low Ce/1000 hour interval, all modified SAC305 solders were effective in suppressing the growth of  $\text{Cu}_6\text{Sn}_5$  IMC layer during 185°C. High Mn solder was the most effective in reducing the growth and resulted in the thinnest  $\text{Cu}_6\text{Sn}_5$  IMC layer during aging. After 1000 hours of aging at 185°C, High Mn showed 14% lower  $\text{Cu}_6\text{Sn}_5$  IMC layer thickness than that of SAC305. Low Ce solder does not appear to be effective at suppressing the  $\text{Cu}_6\text{Sn}_5$  IMC layer growth during

extensive aging (up to 1000 hours) at 185°C. Overall, SAC305 solder formed the thickest  $\text{Cu}_6\text{Sn}_5$  IMC layer during aging.

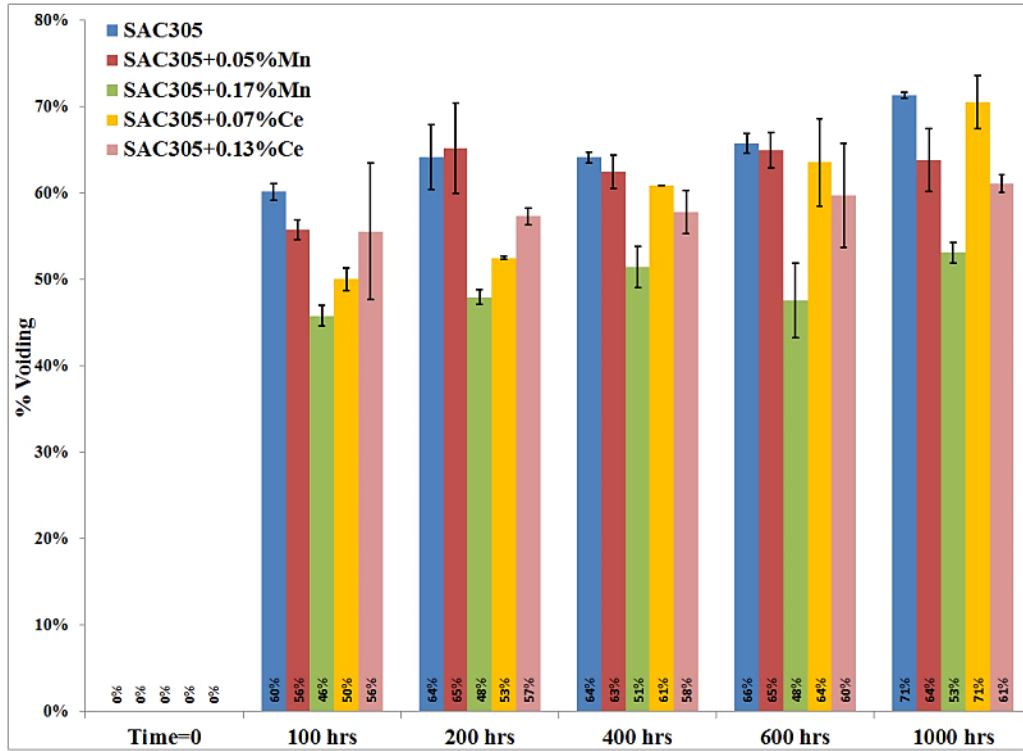


Figure 8-24: QFN32 - % Voiding Measurements during 185°C Aging

Comparing solder performance by % voiding measurement from Figure 8-24, it can be seen that substantial voiding (reduction in contact length) was observed after 100 hours of aging at 185°C for all solders. Except for the Low Mn/200 hour and Low Ce/1000 hour intervals, all modified SAC305 solders reduced voiding at the interface between the  $\text{Cu}_6\text{Sn}_5$  IMC layer and the solder bulk during 185°C aging relative to SAC305. High Mn was the most effective solder in forming the fewest voids as evident at each time interval during 185°C aging. Compared to SAC305, High Mn formed 20% to 28% less voids. In general, High Ce was the second most effective solder after High Mn in terms of forming fewer voids. Compared to SAC305, High

Ce formed 8% to 14% fewer voids. Overall, SAC305 solder showed the highest voiding during 185°C aging.

## **8.6.QFN32 - $\text{Cu}_6\text{Sn}_5$ IMC Growth and %Voiding during 200°C Aging**

The average thicknesses of the  $\text{Cu}_6\text{Sn}_5$  IMC layers during 200°C aging up to 1000 hours observed in QFN32 packages for each solder are summarized in Figure 8-25. The results for %voiding at the interface between the  $\text{Cu}_6\text{Sn}_5$  IMC layer and the solder bulk observed for the QFN32 package during 200°C aging are summarized in Figure 8-27. The error bars shown in both Figure 8-25 and Figure 8-27 indicate the standard deviation of measurements. ESEM images at 2500x magnification for all solders observed in QFN32 package after 100 hours/200°C aging, and after 1000 hours/200°C aging are shown in Appendix-B.



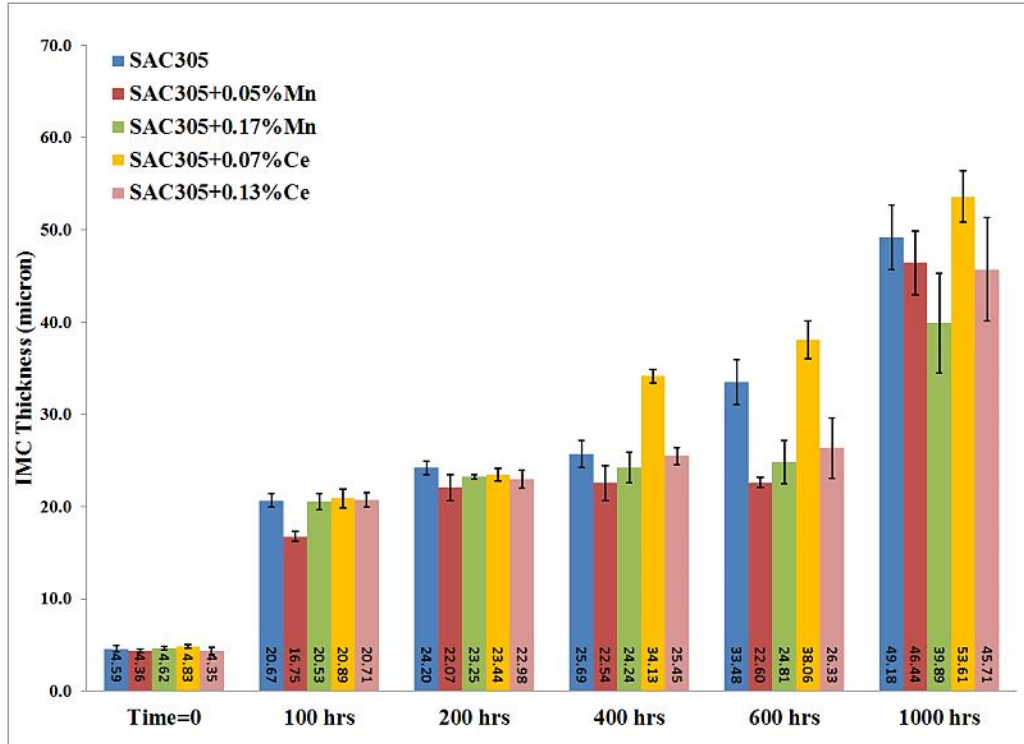
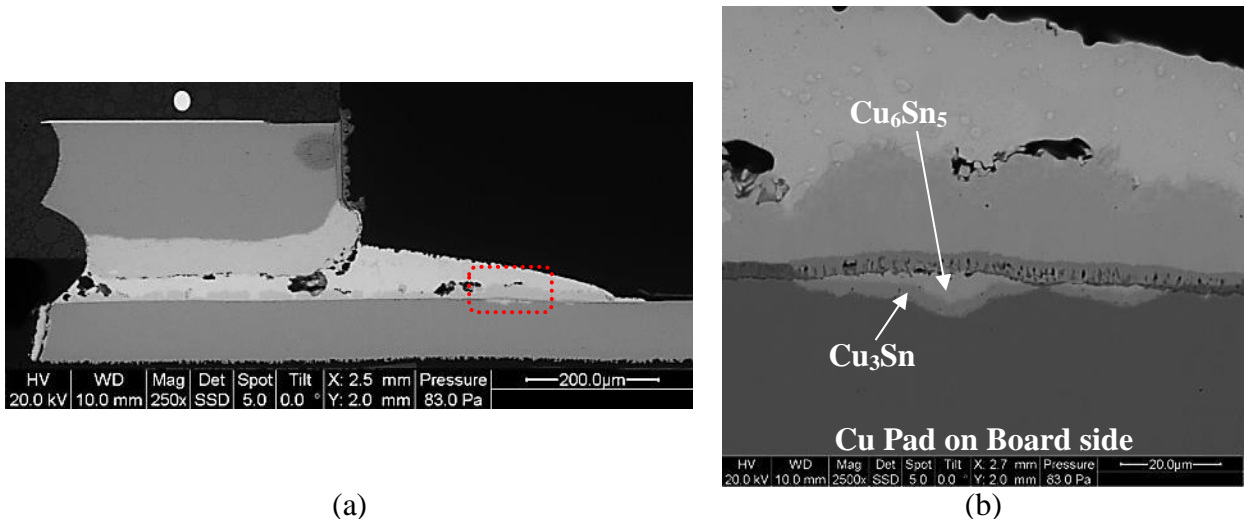


Figure 8-25: QFN32 -  $\text{Cu}_6\text{Sn}_5$  IMC Growth Summary during 200°C Aging

It is important to note that average thickness of the  $\text{Cu}_6\text{Sn}_5$  IMC layer for all solders found for QFN32 was lower than that observed for QFN44 for the same condition. This is believed to be due to the smaller pad size of QFN32. Similar to QFN44, a sudden growth in the  $\text{Cu}_6\text{Sn}_5$  IMC layer thickness was also observed in QFN32 after 100 hours of aging at 200°C. For Low Ce solder, a second sudden growth of the  $\text{Cu}_6\text{Sn}_5$  IMC layer was observed after 400 hours of aging. Upon subsequent aging, the  $\text{Cu}_6\text{Sn}_5$  IMC layer further grew during 600 hours and growth again accelerated that formed the thickest  $\text{Cu}_6\text{Sn}_5$  IMC layer observed after 1000 hours of aging at 200°C. These sudden growths at 400, 600, and 1000 hours aging were believed to be related to consumption of the Ni barrier layer, as discussed previously in the section 8.4. Evident of a consumed Ni layer for Low Ce solder after 1000 hours of aging at 200°C

is shown in Figure 8-26 (b). The formation of  $\text{Cu}_6\text{Sn}_5$  and  $\text{Cu}_3\text{Sn}$  IMCs can also be seen on the board side in Figure 8-26 (b).



(a) SAC305+0.07%Ce Solder Joint after 1000 hours of Aging at 200°C,  
 (b) Magnified View of Consumed Ni Layer

From Figure 8-25, it can be seen that for SAC305, the Ni layer was partially consumed at 600 hours, and complete consumption occurred during subsequent aging, which resulted in a very thick  $\text{Cu}_6\text{Sn}_5$  IMC layer observed after 1000 hours of aging at 200°C. Low Mn, High Mn, and High Ce solders also exhibited sudden growth; however, the average thicknesses of  $\text{Cu}_6\text{Sn}_5$  IMC layers for these solders were smaller than for SAC305. High Mn solder was the most effective in suppressing the growth of the  $\text{Cu}_6\text{Sn}_5$  IMC layer. After 1000 hours of aging at 200°C, High Mn showed a 19% reduction in the  $\text{Cu}_6\text{Sn}_5$  IMC layer compared to that of SAC305.

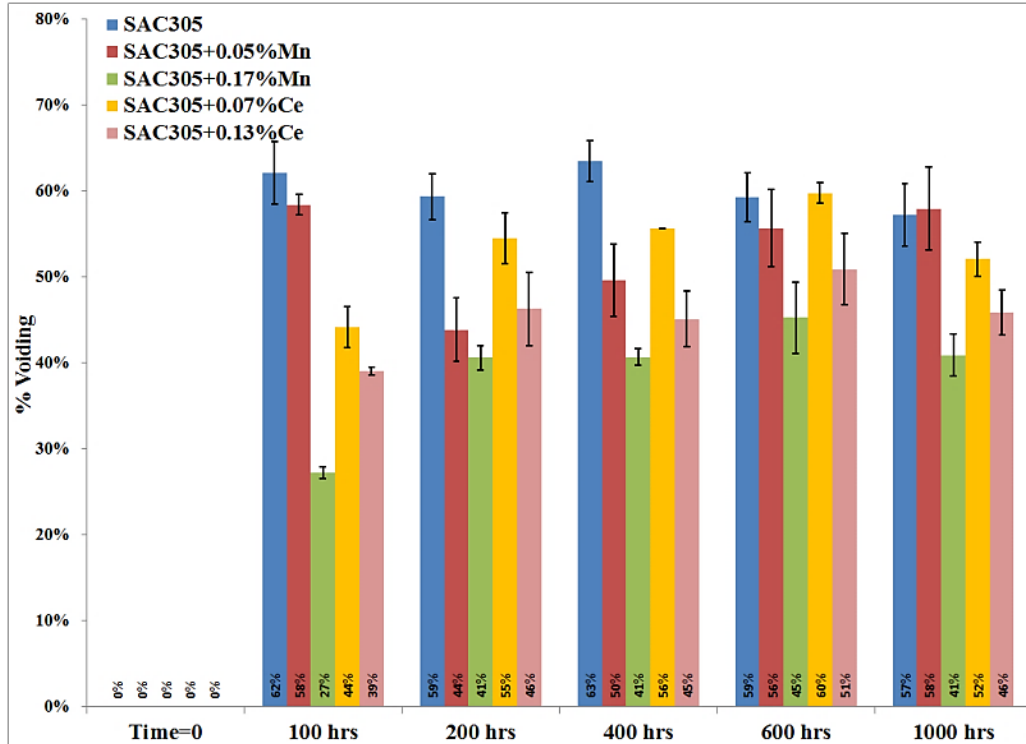


Figure 8-27: QFN32 - %Voiding Measurements during 200°C Aging

Comparing solder performance by % voiding measurement from Figure 8-27, it can be seen that substantial voiding (reduction in contact length) was observed after 100 hours of aging at 200°C for all solders. Except for the Low Ce/600 hour interval and the Low Mn/1000 hour interval, all modified SAC305 solders performed better than SAC305 at reducing voiding. High Mn was the most effective solder in forming the fewest voids as evident at each time interval during aging. Compared to SAC305, High Mn formed 24% to 56% less voids. In addition, High Ce was the second most effective in reducing voiding. Compared to SAC305, High Ce formed 14% to 37% less voids. In general SAC305 solder showed the highest voiding during 200°C aging.

## 8.7. Conclusions

This study was conducted to examine the aging effect on five selected solders at two different temperatures (viz. 185°C and 200°C) by analyzing two different sizes of QFN (viz. QFN44 and QFN32). This study has resulted many in important findings as summarized below.

- A sudden growth in the thickness of  $\text{Cu}_6\text{Sn}_5$  IMC layer was observed after just 100 hours of aging at 185°C and 200°C for all selected solders in QFN44 and QFN32 packages.
- Overall, all modified SAC305 solders were effective in suppressing the growth of  $\text{Cu}_6\text{Sn}_5$  interfacial IMC during 185°C aging.
- Except Low Ce solder, remaining modified SAC305 solders were also effective in suppressing the growth of  $\text{Cu}_6\text{Sn}_5$  interfacial IMC during 200°C aging.
- High Mn solder was the most effective solder in retarding the growth of  $\text{Cu}_6\text{Sn}_5$  interfacial IMC during both 185°C and 200°C aging conditions.
- After 1000 hours of aging at 200°C, a sudden increase in the thickness of  $\text{Cu}_6\text{Sn}_5$  IMC layer was observed for all solders in the QFN44 package. It was found that this unexpected growth was related to consumption of the Ni layer which allows direct path for copper atoms to migration from the board side to the component side to further increase the thickness of the  $\text{Cu}_6\text{Sn}_5$  IMC layer on the component side. In addition, QFN32 package examined under 200°C aging also revealed Ni layer consumption; however, SAC305 and Low Ce

solders showed the Ni layer consumption around 400 or 600 hours of aging at 200°C which resulted the thickest  $\text{Cu}_6\text{Sn}_5$  interfacial IMC. Once the Ni layer was consumed, two additional IMCs, such as  $\text{Cu}_6\text{Sn}_5$  and  $\text{Cu}_3\text{Sn}$ , were found of the board side.

- A sudden increase in voids or reduction in contact length IMC was observed after just 100 hours of aging at 185°C and 200°C for all selected solders in QFN44 and QFN32 packages.
- High Mn showed the lowest %voiding, and SAC305 showed the highest %voiding during aging at 185°C and 200°C in QFN44 and QFN32 packages.
- SAC305 and High Mn show direct correlation between the  $\text{Cu}_6\text{Sn}_5$  IMC layer growth and the void growth. For other solders, no such direct correlation was observed.

## **9. Interfacial Intermetallic Formation and Growth during Isothermal Aging at 185°C and 200°C on R2512 Package**

This chapter discusses the growth of interfacial IMCs on a R2512 package observed during isothermal aging at 185°C and 200°C up to 1000 hours. The interfacial IMC thickness measurement was conducted on both the component side and the board side interfacial IMCs of R2512 package. This study was conducted to understand the growth of interfacial IMCs on R2512 during 185°C and 200°C aging that can affect the reliability of R2512 package when subjected to the mechanical shock testing after exposing to thermal aging, as discussed in the chapter 10.

A R2512 package consists of an alumina ( $\text{Al}_2\text{O}_3$ ) substrate with leads or terminations coated with electroplated nickel. These nickel leads are again plated with matte tin finish. A left and a right side solder joint of R2512 after reflow are shown in Figure 9-1. When a R2512 package is soldered to the ENIG-plated board, during reflow, electroplated nickel on the component side and electroless nickel on the board side react with solder bulk and form  $\text{Ni}_3\text{Sn}_4$  IMC on the component side and  $(\text{Ni,Cu})_3\text{Sn}_4$  IMC on the board side, as shown in Figure 9-2 (a). In addition to interfacial IMCs, IMCs within the solder bulk were also found. These bulk IMCs were  $\text{Cu}_6\text{Sn}_5$ ,  $\text{Ag}_3\text{Sn}$ , and  $\text{AuSn}_4$ , as shown in Figure 9-2 (b). During subsequent aging at 185°C and 200°C up to 1000 hours, both IMCs at the interface and within the solder bulk grow with time and temperature. In this study, emphasis is placed on the interfacial IMCs because exposure to high temperature can lead to significant growth in the interfacial IMCs, and they can become primary failure sites during mechanical shock loading.

The detailed information on the growth of interfacial IMCs on the component and board side of R2512 package at 185°C and 200°C up to 1000 hours is discussed next.

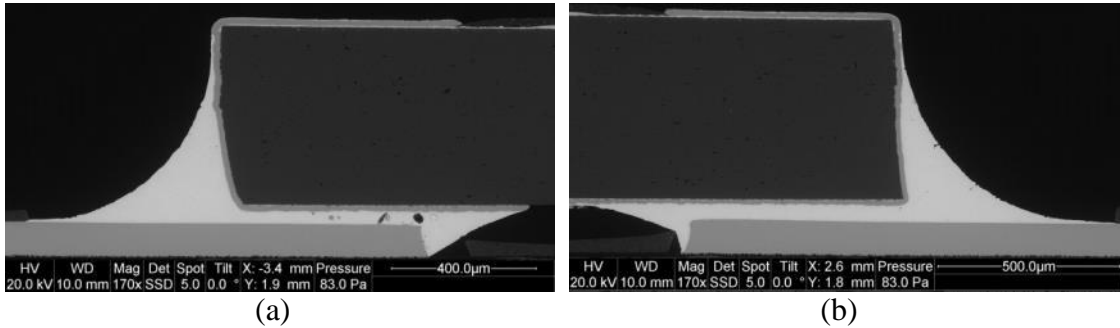


Figure 9-1: A Left and a Right Solder Joint of R2512 after Reflow (SAC305 – Time=0)

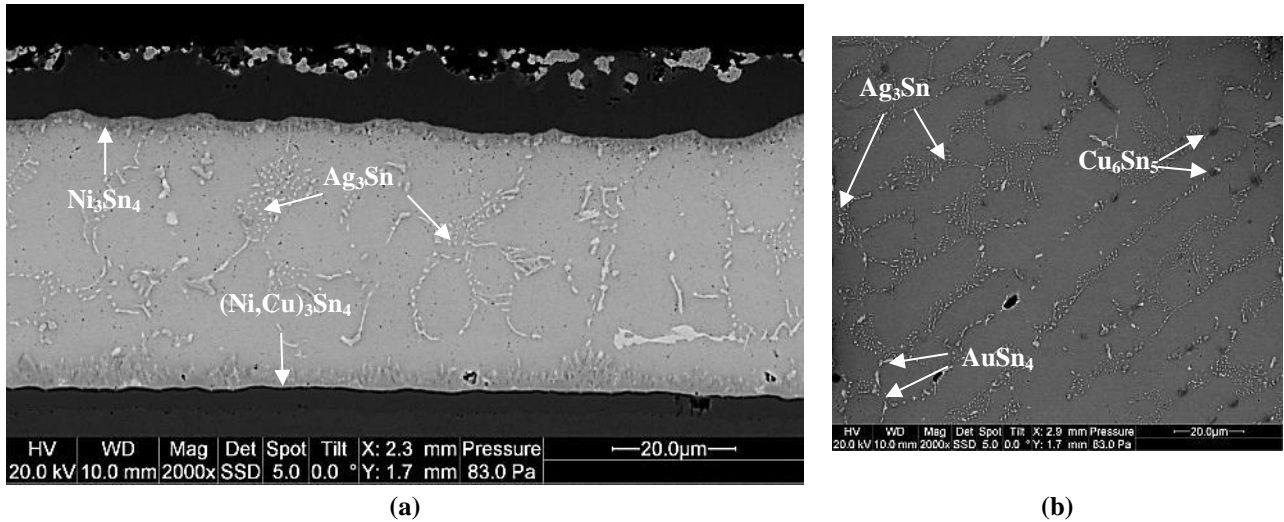


Figure 9-2: (a) Interfacial IMCs (b) bulk IMCs formation after Reflow on R2512 Package (SAC305 – Time=0)

In order to measure average thickness of interfacial IMCs on R2512 package, ESEM images at 2000x magnification were taken at various locations covering the entire IMC layer region on the component and board side. Figure 9-3 shows regions of interfacial IMC on the component and board side that were used for IMC layer thickness measurement. Image processing software, Image-J was used to calculate the total area of IMC layer and the horizontal distance from each ESEM image. An average thickness of the IMC layer for each ESEM image was calculated by dividing

the IMC total area by the horizontal distance. Then, the sample average IMC layer thickness was calculated by averaging the calculated result for each ESEM image.

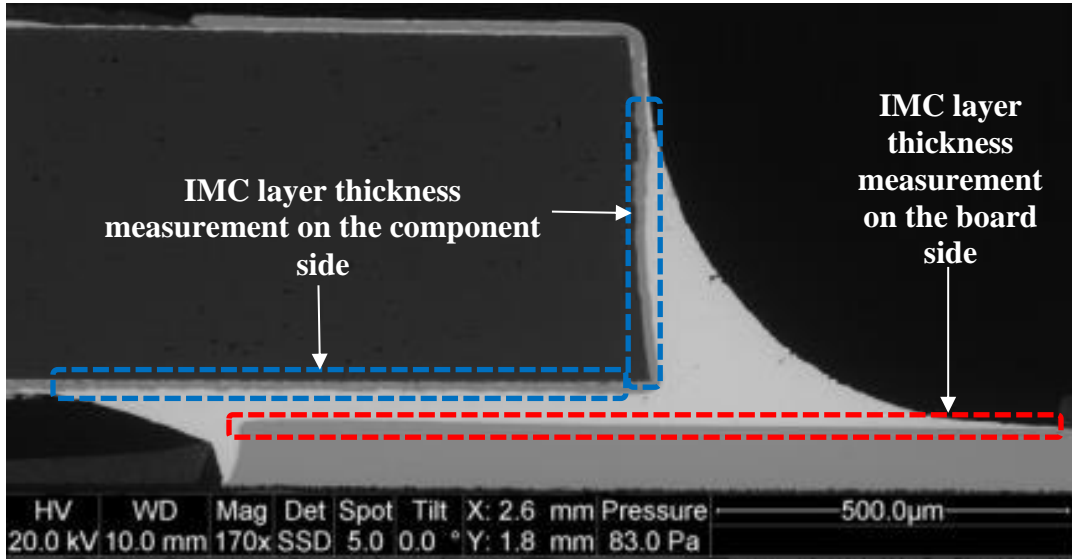


Figure 9-3: Regions of IMC Layer on the Component and Board Side for Calculating Interfacial IMC Layer Thickness

The next few sections provide the detailed information on IMC layer growth on the component and the board side of R2512 package under 185°C and 200°C isothermal aging at 0, 100, 200, 400, 600, and 1000 hour intervals.

### **9.1.R2512 – Interfacial IMC Growth on the Component and the Board side during 185°C Aging**

Figure 9-4 and Figure 9-5 show the growth summary of interfacial IMC on the component side and the board side, respectively, during 185°C aging up to 1000 hours.



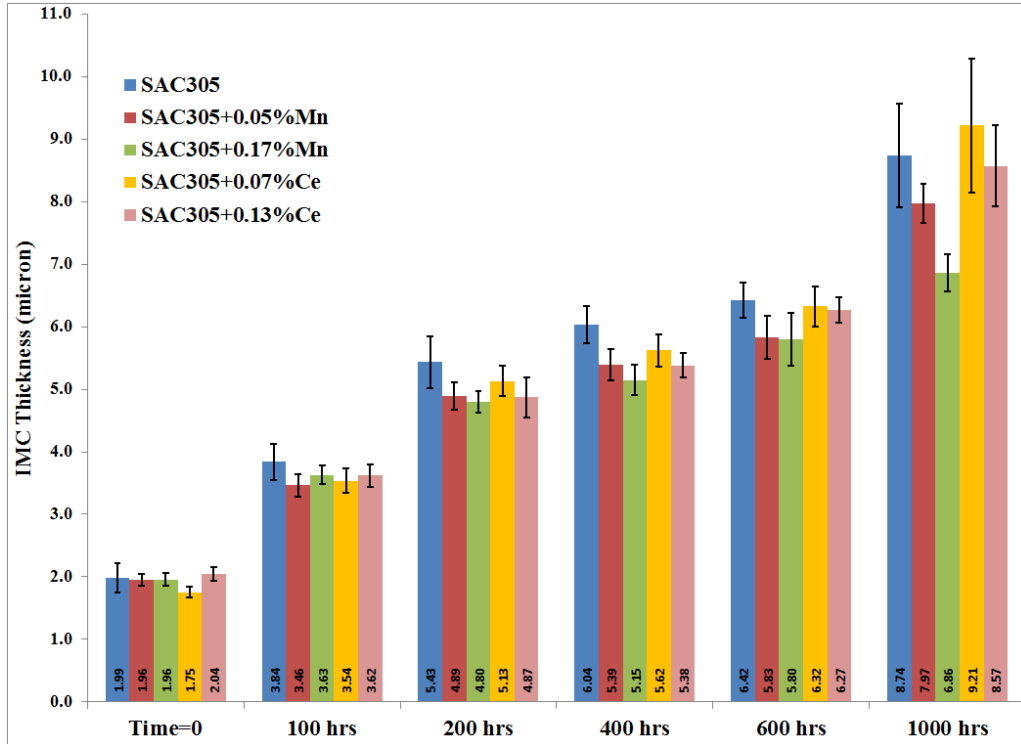


Figure 9-4: R2512 - Component Side  $\text{Ni}_3\text{Sn}_4$  Interfacial IMC Growth Summary during 185°C Aging

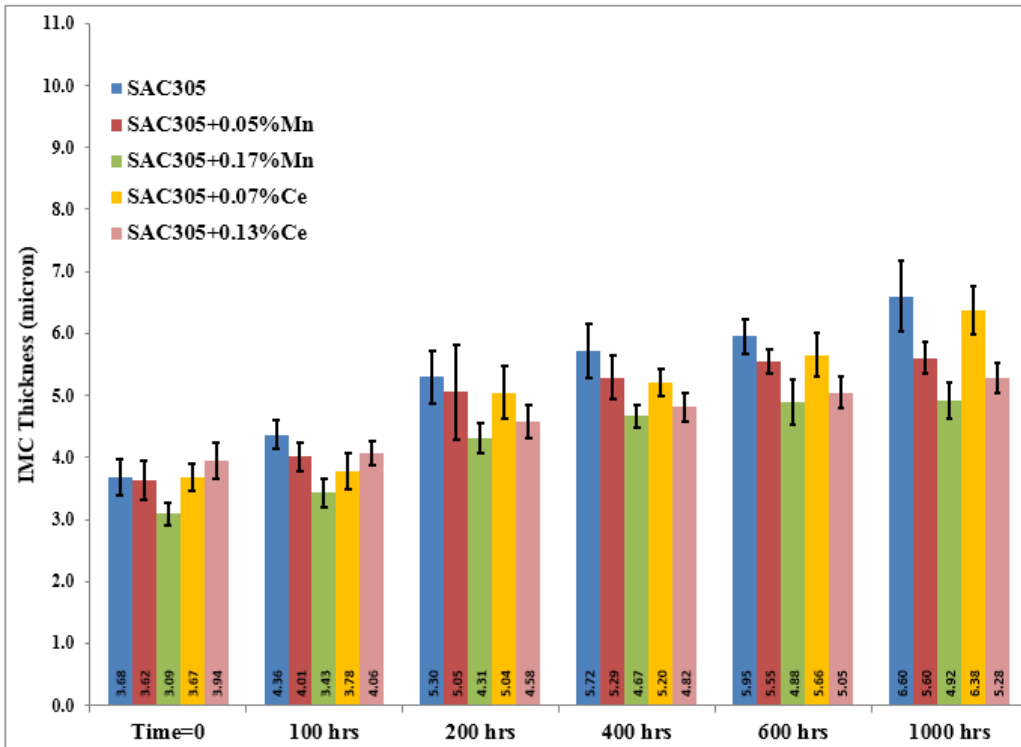


Figure 9-5: R2512 – Board Side  $(\text{Ni,Cu})_3\text{Sn}_4$  Interfacial IMC Growth Summary during 185°C Aging

From Figure 9-4, it can be concluded that all modified SAC305 solders were effective in suppressing the growth of the  $\text{Ni}_3\text{Sn}_4$  interfacial IMC on the component side. High Mn solder was the most effective in suppressing the growth, and resulted in the thinnest  $\text{Ni}_3\text{Sn}_4$  IMC layer during 185°C aging. After 1000 hours of aging at 185°C, High Mn achieved a 22% reduction in the growth of  $\text{Ni}_3\text{Sn}_4$  IMC layer compared to that of SAC305. Low Ce solder seems less effective during extended aging hours especially after 1000 hours. Overall, SAC305 solder showed the thickest  $\text{Ni}_3\text{Sn}_4$  IMC layer during 185°C aging, except Low Ce/1000 hour interval.

By comparing the growth of board side  $(\text{Ni,Cu})_3\text{Sn}_4$  interfacial IMC from Figure 9-5, it can be concluded that all modified SAC305 solders were also effective in suppressing the growth of  $(\text{Ni,Cu})_3\text{Sn}_4$  IMC layer. High Mn solder was the most effective in suppressing the growth, and resulted in the thinnest  $(\text{Ni,Cu})_3\text{Sn}_4$  IMC layer on the board side during 185°C aging. After 1000 hours of aging at 185°C, High Mn achieved a 26% reduction in the growth of  $(\text{Ni,Cu})_3\text{Sn}_4$  IMC layer compared to that of SAC305. High Ce initially formed thick  $(\text{Ni,Cu})_3\text{Sn}_4$  IMC layer after reflow; however, during subsequent aging, High Ce was effective in suppressing the IMC layer growth, and turned out to be the second most effective after High Mn solder. Overall, SAC305 solder showed the thickest  $(\text{Ni,Cu})_3\text{Sn}_4$  IMC layer on the board side at all intervals during 185°C aging.

It is important to note that, after reflow, the  $\text{Ni}_3\text{Sn}_4$  IMC layer on the component side for all solders was initially thinner than the  $(\text{Ni,Cu})_3\text{Sn}_4$  IMC layer on the board side. During aging, both these IMCs continued to grow and resulted thicker IMC layer; however, after some period of aging, it was found that the growth rate of the  $\text{Ni}_3\text{Sn}_4$

IMC layer was faster than the growth rate of  $(\text{Ni,Cu})_3\text{Sn}_4$  IMC layer. Figure 9-4 and Figure 9-5 show that after 200 hours of aging at  $185^\circ\text{C}$ , the thickness of  $\text{Ni}_3\text{Sn}_4$  IMC surpassed the thickness of  $(\text{Ni,Cu})_3\text{Sn}_4$  IMC layer, and resulted higher thickness in  $\text{Ni}_3\text{Sn}_4$  IMC layer during subsequent aging at  $185^\circ\text{C}$ .

In order to further discuss the growth of interfacial and bulk IMCs during  $185^\circ\text{C}$  aging, ESEM images for all five solders at 2000x magnification after reflow and after 1000 hours/ $185^\circ\text{C}$  aging (solder interfaces and solder bulk) are shown next.

Figure 9-6 shows a SAC305 solder joint. After reflow, both  $\text{Ni}_3\text{Sn}_4$  and  $(\text{Ni,Cu})_3\text{Sn}_4$  interfacial IMCs were acicular (needle-like), as shown in Figure 9-6 (a). During aging both IMCs grew and become laminar (planar-type) after 1000 hours of aging, as shown in Figure 9-6 (b). Due to aggressive polishing, both side interfacial IMC layers were found to be partially shattered. Ni barrier layer on the board side was also found to be partially consumed after 1000 aging, as shown in Figure 9-6 (b). Figure 9-6 (a) also shows bulk IMCs that includes fine particles of  $\text{Ag}_3\text{Sn}$  and  $\text{AuSn}_4$  IMCs. During aging, both these particles also coarsened. Figure 9-6 (c) shows solder bulk IMCs after 1000 hours of aging at  $185^\circ\text{C}$ . Clearly, significant coarsening and enlargement can be seen in both  $\text{Ag}_3\text{Sn}$  and  $\text{AuSn}_4$  IMCs. After 1000 hours of aging, these particles were found to be migrated to the surface of interfacial IMC layers, as shown in Figure 9-6 (b). The migration of coarsened bulk IMC particles to the interfacial IMCs can also be seen in Figure 9-6 (b).

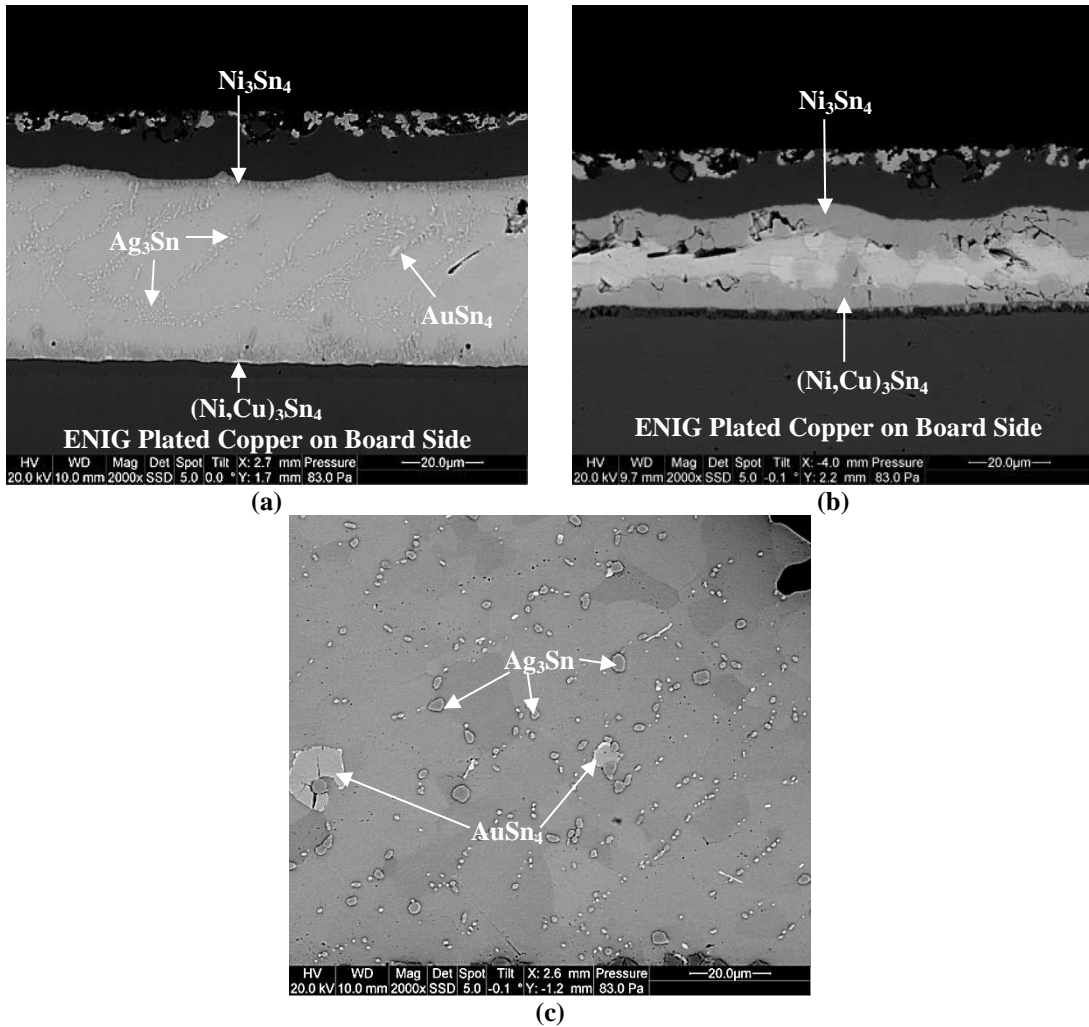


Figure 9-6: R2512 - SAC305 Solder Joint (a) After Reflow, (b) Solder Interfaces after 1000 hours/185°C Aging, (c) Solder Bulk after 1000 hours/185°C Aging

Figure 9-7 shows a SAC305+0.05%Mn solder joint. From Figure 9-7 (a), it can be seen that  $Ni_3Sn_4$  IMC layer is acicular type; whereas,  $(Ni,Cu)_3Sn_4$  IMC layer is planar type. In addition, after reflow,  $(Ni,Cu)_3Sn_4$  IMC layer is also found to be thicker than the  $Ni_3Sn_4$  IMC layer. Interfacial IMCs grow during aging but slower than SAC305 solder, as shown in Figure 9-7 (b). After 1000 hours of aging, both  $Ag_3Sn$  and  $AuSn_4$  IMCs were found to be much smaller than those observed in SAC305. This shows that Low Mn solder is also effective to minimize coarsening of bulk IMCs during 185°C aging.

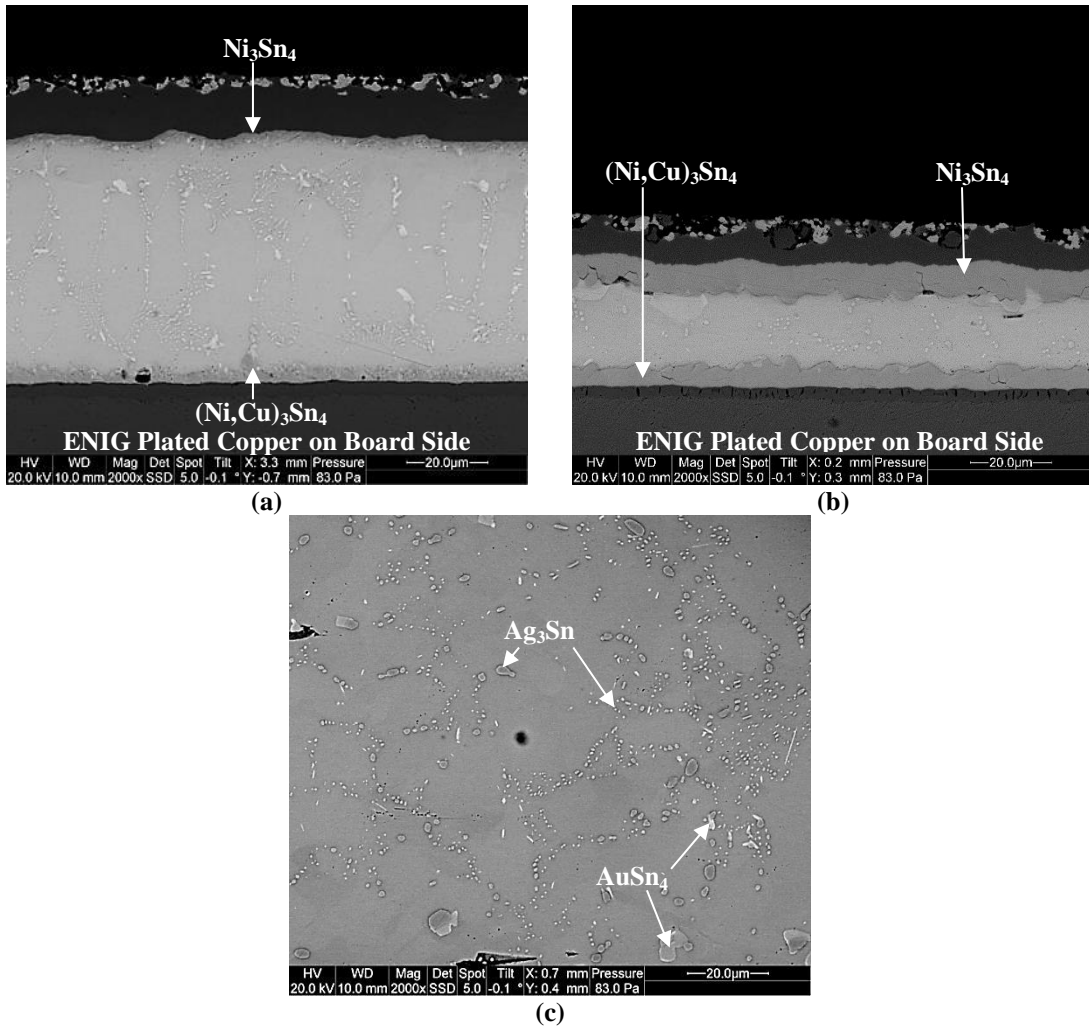


Figure 9-7: R2512 - SAC305+0.05%Mn Solder Joint (a) After Reflow, (b) Solder Interfaces after 1000 hours/185°C Aging, (c) Solder Bulk after 1000 hours/185°C Aging

Figure 9-8 shows a SAC305+0.17%Mn solder joint. Figure 9-8 (a) shows that both  $Ni_3Sn_4$  and  $(Ni,Cu)_3Sn_4$  IMC layers are laminar type. After 1000 hours of aging at 185°C, both interfacial IMC layers showed sluggish growth and resulted in the thinnest IMC layers. In addition to reduction in growth in the interfacial IMCs, bulk IMCs were also found to coarsen less. Both Figure 9-8 (b) and Figure 9-8 (c) show many small  $Ag_3Sn$  and  $AuSn_4$  IMC particles distributed in the solder bulk. Thus, High Mn solder effectively reduces the growth of both interfacial and bulk IMCs during 185°C aging.

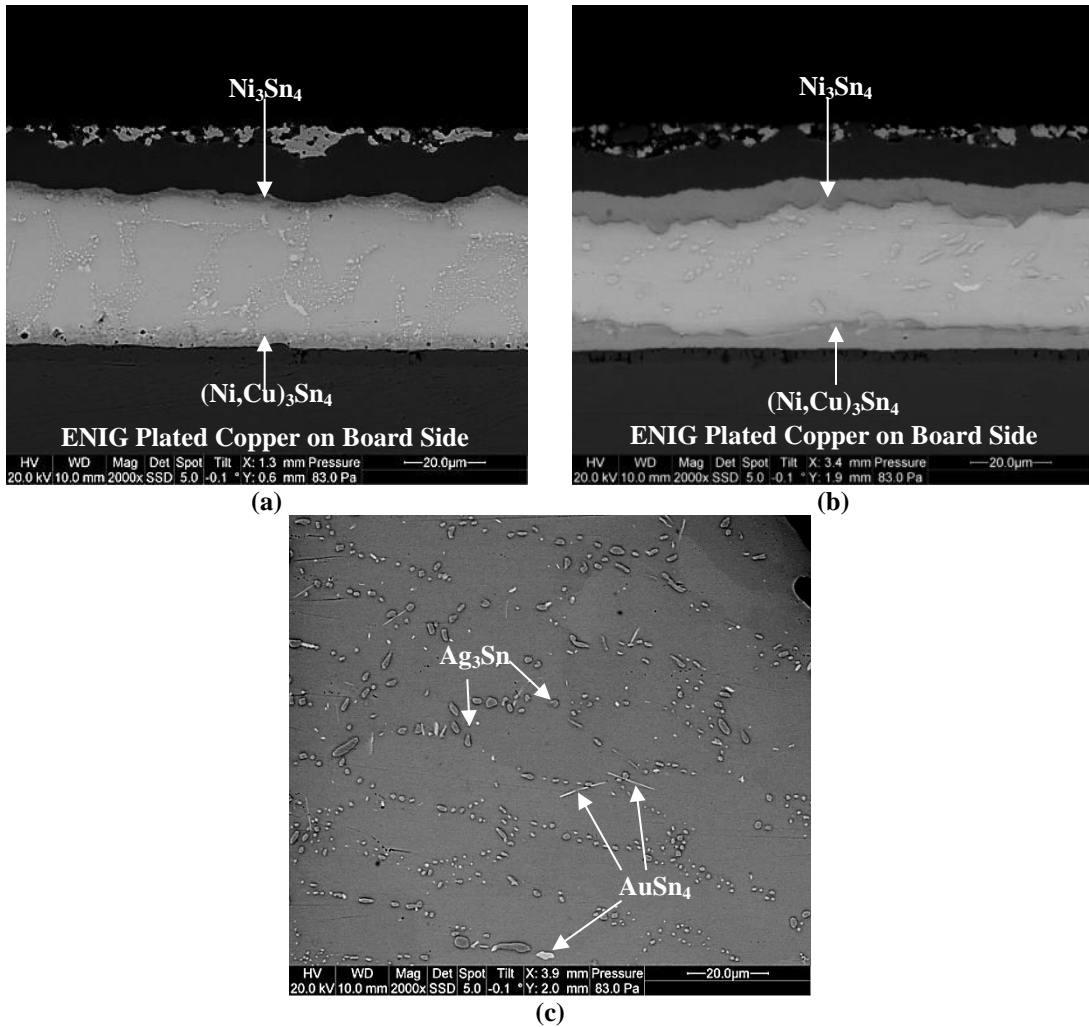


Figure 9-8: R2512 - SAC305+0.17%Mn Solder Joint (a) After Reflow, (b) Solder Interfaces after 1000 hours/185°C Aging, (c) Solder Bulk after 1000 hours/185°C Aging

Figure 9-9 shows a SAC305+0.07%Ce solder joint. Figure 9-9 (a) shows acicular type interfacial IMCs on both the component and the board side. After 1000 hours of aging, considerable growth in the  $\text{Ni}_3\text{Sn}_4$  IMC layer was observed compared to the  $(\text{Ni,Cu})_3\text{Sn}_4$  IMC layer. Due to aggressive polishing, both side interfacial IMC layers were found to be shattered, as shown in Figure 9-9 (b). Many large coarsened IMC particles of  $\text{Ag}_3\text{Sn}$  and  $\text{AuSn}_4$  can also be seen in Figure 9-9 (c).

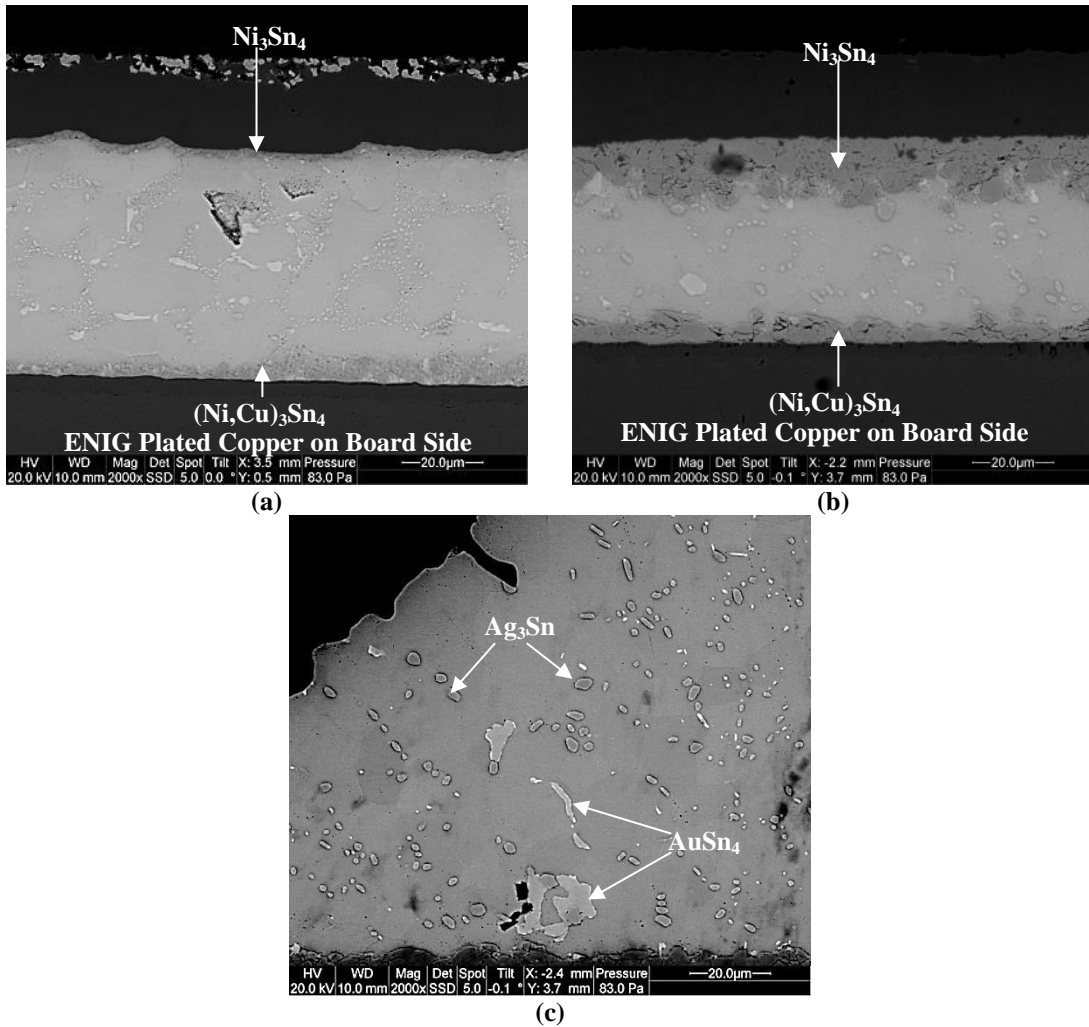


Figure 9-9: R2512 - SAC305+0.07%Ce Solder Joint (a) After Reflow, (b) Solder Interfaces after 1000 hours/185°C Aging, (c) Solder Bulk after 1000 hours/185°C Aging

Figure 9-10 shows a SAC305+0.13%Ce solder joint. After 1000 hours of aging, both  $\text{Ni}_3\text{Sn}_4$  and  $(\text{Ni,Cu})_3\text{Sn}_4$  IMC layers were found to be much thinner than those of SAC305, as shown in Figure 9-10 (b). Both layers were found to be laminar type. Both Figure 9-10 (b) and Figure 9-10 (c) show many small  $\text{Ag}_3\text{Sn}$  IMC particles distributed in the solder bulk. In addition, both Figure 9-10 (b) and Figure 9-10 (c) also show many smaller and few larger particles of  $\text{AuSn}_4$ . Thus, it can be concluded that High Ce is more effective in suppressing the growth of both side interfacial IMCs and  $\text{Ag}_3\text{Sn}$  bulk IMC particles, and less effective in suppressing the growth of  $\text{AuSn}_4$ .

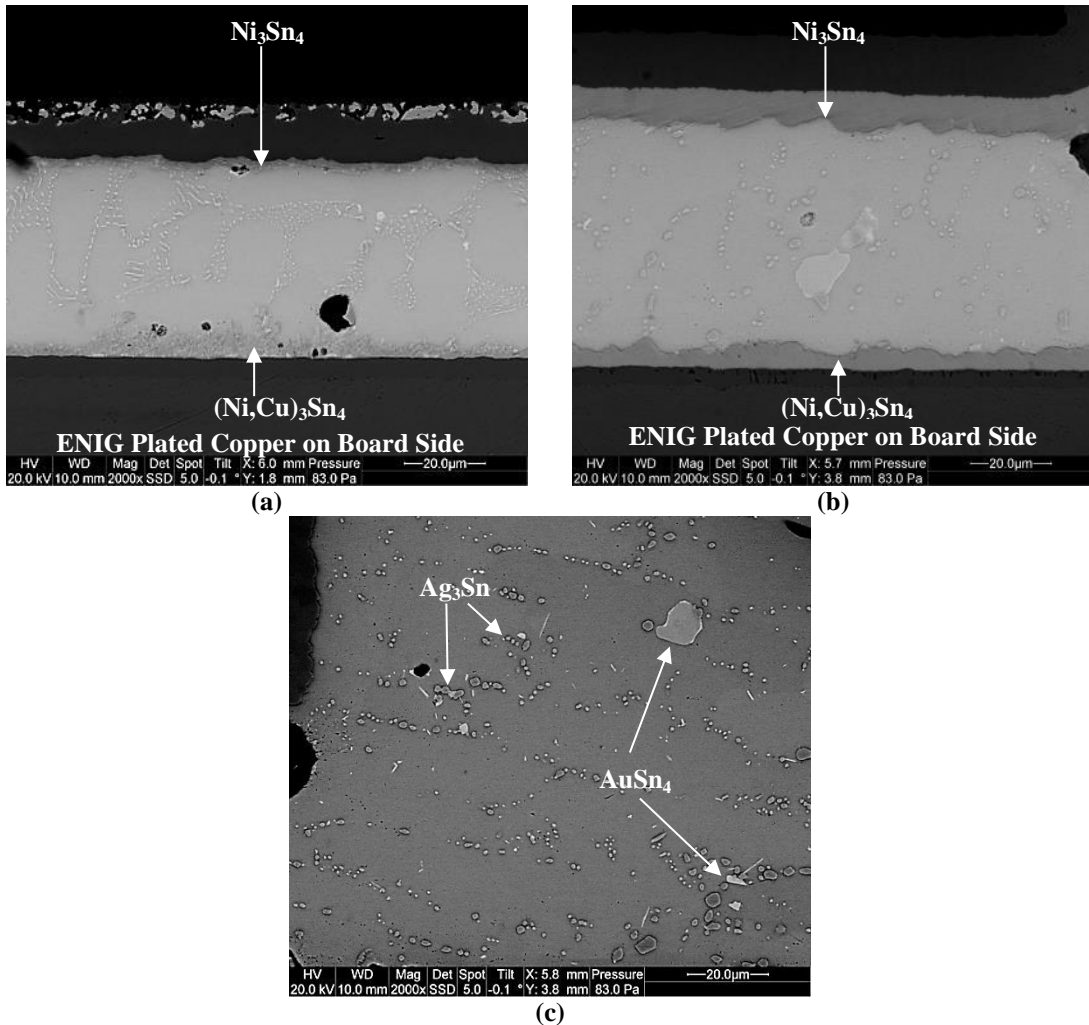


Figure 9-10: R2512 - SAC305+0.13%Ce Solder Joint (a) After Reflow, (b) Solder Interfaces after 1000 hours/185°C Aging, (c) Solder Bulk after 1000 hours/185°C Aging

## 9.2.R2512 – Interfacial IMC Growth on Component and Board side during 200°C Aging

Figure 9-11 shows the growth summary of  $Ni_3Sn_4$  interfacial IMCs on the component side during 200°C aging. It can be concluded that in general all modified SAC305 solders were effective to suppress the growth of  $Ni_3Sn_4$  interfacial IMC on component side. Overall, High Mn solder was the most effective to suppress the growth and



resulted in the thinnest  $\text{Ni}_3\text{Sn}_4$  IMC layer during 200°C aging. In general, SAC305 solder had the thickest  $\text{Ni}_3\text{Sn}_4$  IMC layer on component side during 200°C aging.

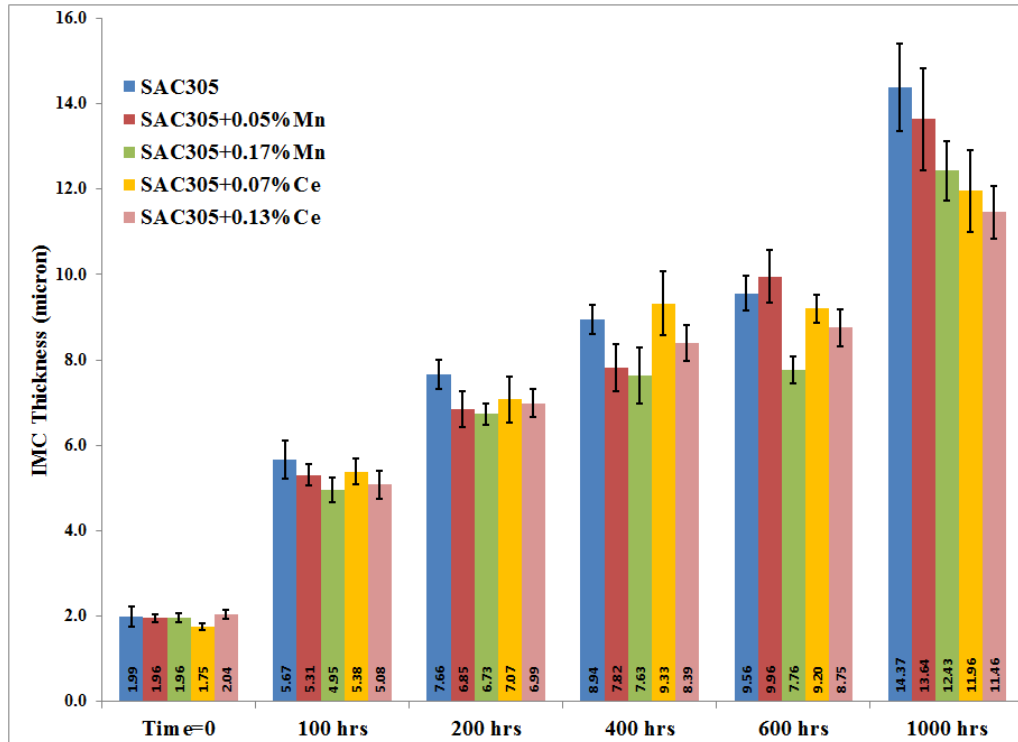


Figure 9-11: R2512 - Component Side  $\text{Ni}_3\text{Sn}_4$  Interfacial IMC Growth Summary during 200°C Aging

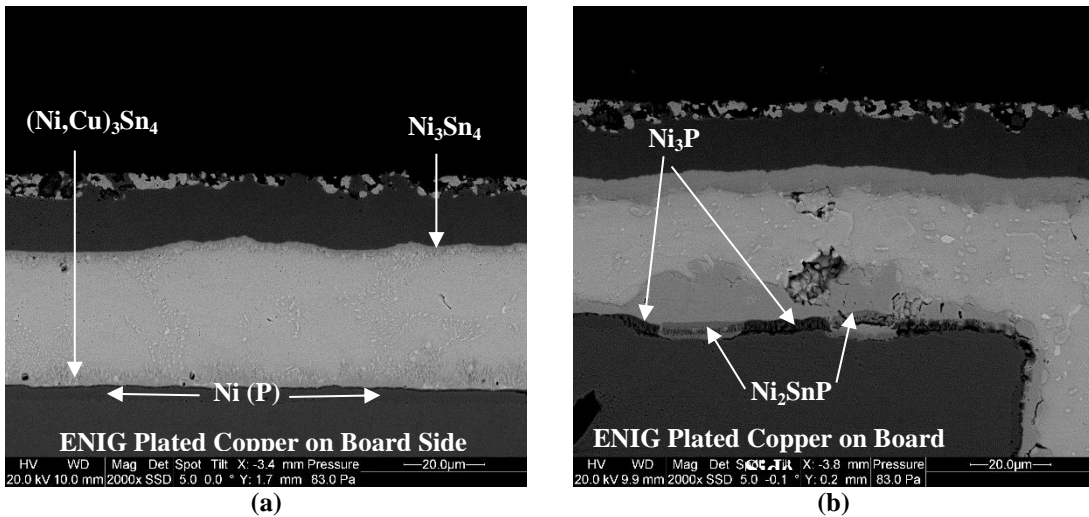
During interfacial IMC measurement analysis on the board side for 200°C aging, a strange phenomenon was observed. The interfacial IMC growth on the board side for all solders except High Mn was quite unexpected. All solders except High Mn showed very rapid growth on the board side IMC after 100 hours aging, and this unexpected trend continued during the aging at 200°C. Upon further analysis, it was found that this strange phenomenon was related to the Ni layer consumption which resulted in very thick interfacial IMC layer on the board side. First this phenomenon is discussed in detail, and then the board side IMC layer thickness measurements for all solders are presented.

### 9.2.1. Evolution of Ni Layer Consumption during 200°C Aging

SAC305 solder joint is used for a reference to explain the evolution of Ni layer consumption on the board side during 200°C aging. ESEM image of SAC305 solder joint at six different aging time intervals including (a) after reflow, (b) after 100 hour, (c) after 200 hour, (d) after 400 hour, (e) after 600 hour, and (d) after 1000 hour exposure to 200°C are shown in Figure 9-12. After reflow condition as shown in Figure 9-12 (a), a uniform Ni layer was found between the copper pad on the board side and  $(\text{Ni,Cu})_3\text{Sn}_4$  IMC layer as shown in Figure 9-12 (a). Ni layer also contains phosphorus used during electroless Ni layer deposition as a part of ENIG plating process. This Ni layer works as a diffusion barrier layer to prevent the solder interaction with the copper pad on the board side. However, during aging, phosphorus reacts with the Ni layer and forms a  $\text{Ni}_3\text{P}$  dark layer which contains many small vertical voids after just 100 hours of exposure at 200°C, as shown in Figure 9-12 (b). This dark layer ( $\text{Ni}_3\text{P}$ ) is also called the reaction layer, and it forms at the cost of Ni layer consumption. As aging continues, the reaction layer further transforms into  $\text{Ni}_2\text{SnP}$  layer by completely consuming the Ni barrier layer, as shown in Figure 9-12 (b). Once  $\text{Ni}_2\text{SnP}$  layer is formed, no barrier layer exists. Thus reaction between Sn atoms (present in the solder) and Cu atoms (present at the copper pad) starts occurring that forms two additional IMC layers,  $\text{Cu}_3\text{Sn}$  and  $\text{Cu}_6\text{Sn}_5$ , between the copper pad and  $\text{Ni}_2\text{SnP}$  layer, as shown in Figure 9-12 (a). It is important to note that Ni layer consumption phenomenon is not uniform throughout the copper pad on the board side. It starts randomly at multiple locations during the initial phase of aging, and eventually forms four IMC layers within a small pocket during subsequent aging.

These pockets are visible in Figure 9-12 (b), Figure 9-12 (c), Figure 9-12 (d), and Figure 9-12 (f). These small pockets eventually combine and form thick layers on the board side, as shown in Figure 9-12 (f). The magnified view of Figure 9-12 (f) is shown in Figure 9-13. The presence of Kirkendall voids can also be seen between  $\text{Cu}_3\text{Sn}$  and Cu pad on the board side in Figure 9-13.

EDS (Energy dispersive spectroscopy) point analysis was performed to find the composition of four intermetallic layers found after 1000 hours of aging at 200°C. Before Ni layer consumption, it was found that the interfacial IMC on the board side was  $(\text{Ni,Cu})_3\text{Sn}_4$ . After the Ni layer was consumed, Cu atoms started migrating towards the  $(\text{Ni,Cu})_3\text{Sn}_4$  IMC layer (top layer) changing the layer composition from  $(\text{Ni,Cu})_3\text{Sn}_4$  to  $(\text{Cu,Ni})_6\text{Sn}_5$ , as shown in Figure 9-13.



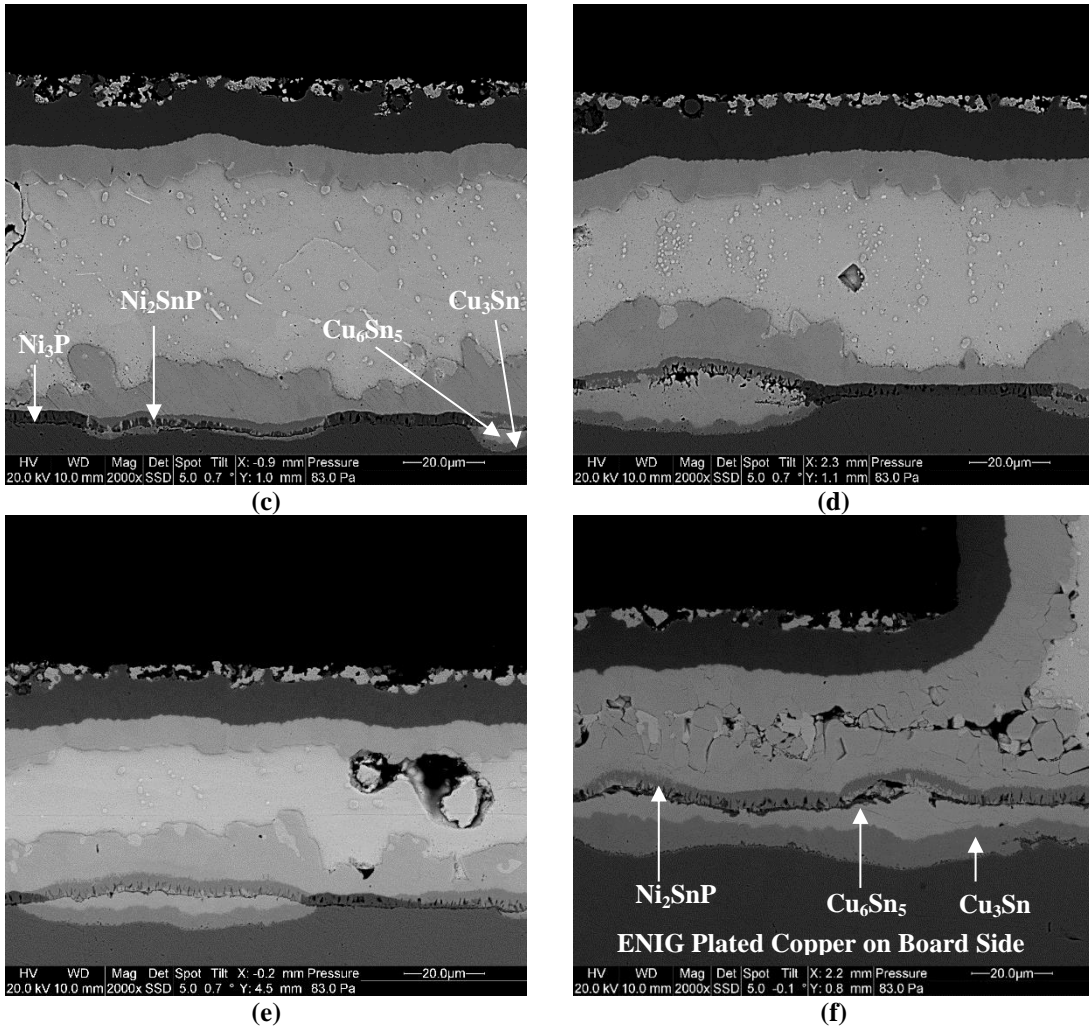


Figure 9-12: R2512 - Board side Interfacial IMC evolution for SAC305 Solder joint, (a) After Reflow, (b) After 100 hours/200°C Aging, (c) After 200 hours/200°C Aging, (d) After 400 hours/200°C Aging, (e) After 600 hours/200°C Aging, (f) After 1000 hours/200°C Aging

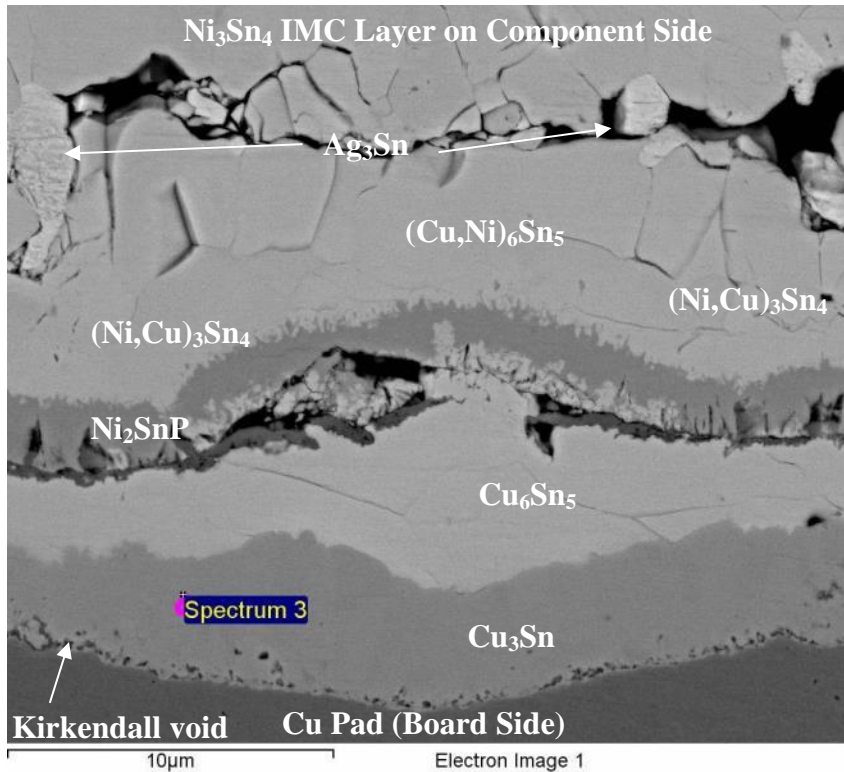


Figure 9-13: R2512- EDS Point Analysis on Board Side IMC Layers (SAC305 Solder, 1000 hours/ 200°C Aging)

### 9.2.2. Board Side Interfacial IMC Thickness Measurement

Due to the non-uniform formation of four layers at different locations on the board side during 200°C aging, it was difficult to measure the average thickness of any individual layer formed on the board side. In order to keep consistency with the component side  $\text{Ni}_3\text{Sn}_4$  IMC layer thickness measurement, it was decided to measure the thickness of only the top layer for all solders during 200°C aging. It is important to note that the composition of the top layer on the board side can vary from location to location as confirmed from EDS analysis. Thus, for simplicity, this top layer is referred as Ni-Cu-Sn layer.

Figure 9-14 shows the growth summary of Ni-Cu-Sn interfacial IMC layer on the board side during 200°C aging. The asterisk for Low Ce solder is used to indicate that

even though Ni-Cu-Sn interfacial IMC layer thickness was found to be smaller for Low Ce than that of SAC305 solder, severe Ni layer consumption was observed for Low Ce solder. More detail is provided for Low Ce solder with ESEM images in a later part of this section. From Figure 9-14, it can be concluded that High Mn solder was the most effective solder to suppress the thickness of board side IMC layer. In addition, it was also found that High Mn did not show any sign of Ni layer consumption, and thus it did not form four different IMC layers on the board side. Low Mn solder was the second most effective to suppress the growth of Ni-Cu-Sn interfacial IMC layer. In general, SAC305 and Low Ce formed the thickest Ni-Cu-Sn interfacial IMC layer during 200°C aging.

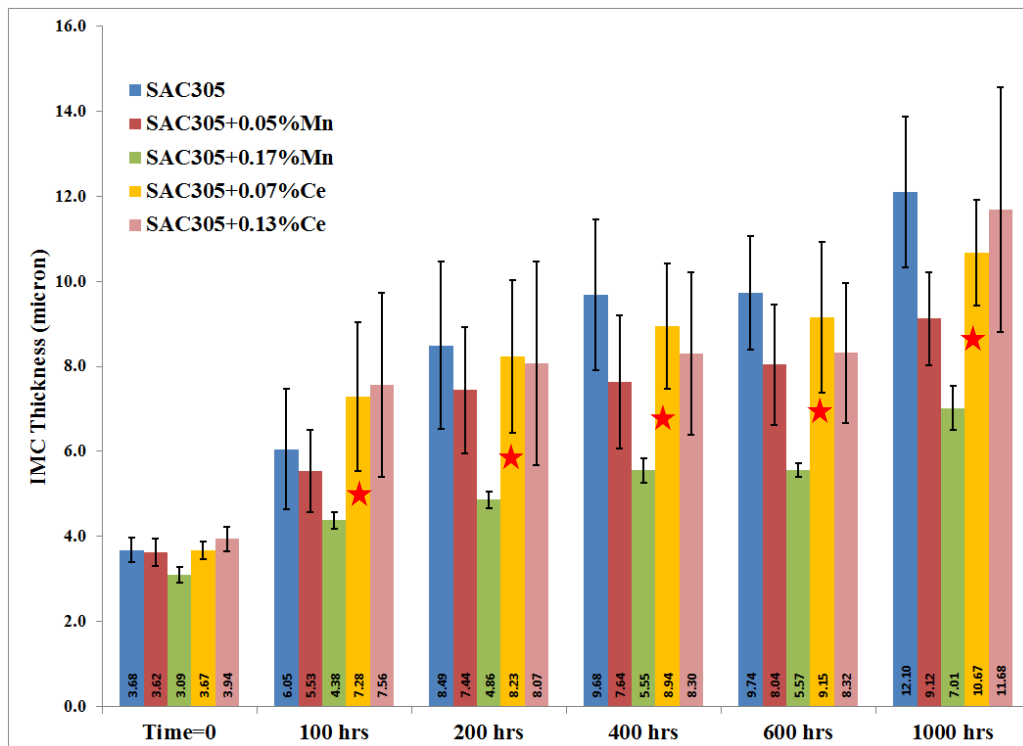


Figure 9-14: R2512 – Board Side Ni-Cu-Sn Interfacial IMC Growth Summary during 200°C Aging

In order to further discuss the effect of Ni layer consumption on the IMC growth during 200°C aging, ESEM image of both component and board side IMC at 2000x

magnification after 100 hours and 1000 hours aging for all solders is shown next. In addition, ESEM image of whole left and right solder joint of R2512 at 170x magnification aged after 1000 hours at 200°C for all solders is also shown.

Figure 9-15 shows a SAC305 solder joint after 100 hours and 1000 hours aging at 200°C. Figure 9-16 shows the left and the right side of SAC305 solder joint after 1000 hours aging at 200°C. Initiation and complete consumption of Ni layer after 100 hours can be seen from Figure 9-15 (a). Upon further aging, Ni layer consumption starts occurring at various locations and eventually merges to form four layers on the board side which can be seen after 1000 hours of aging, as shown in Figure 9-15 (b). The severity of these layers is so high that it completely consumed tin within the solder underneath the resistor package, as shown in Figure 9-15 (b). At few locations underneath the package, voids can also be seen due to tin migration from the solder to the board side to form  $\text{Cu}_3\text{Sn}$  and  $\text{Cu}_6\text{Sn}_5$  IMCs near the copper pad on the board side. Figure 9-16 shows ESEM image of the left and the right side of solder joint of R2512 package after 1000 hours of aging at 200°C. Both Figure 9-16 (a) and Figure 9-16 (b) show many pockets on the board side indicating the evidence of Ni layer consumption.

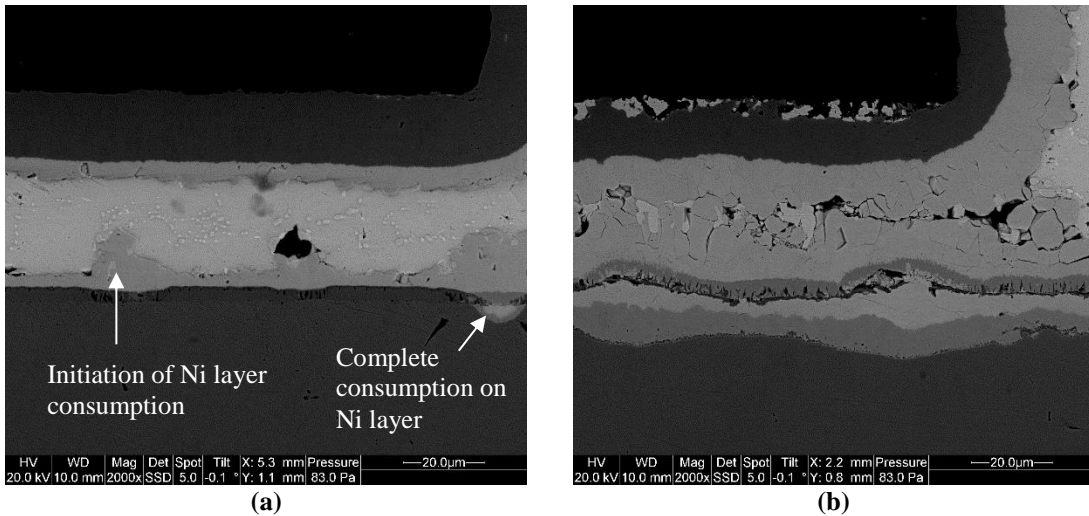


Figure 9-15: R2512 - SAC305 Solder Joint (a) After 100 hours/200°C Aging, (b) After 1000 hours/200°C Aging

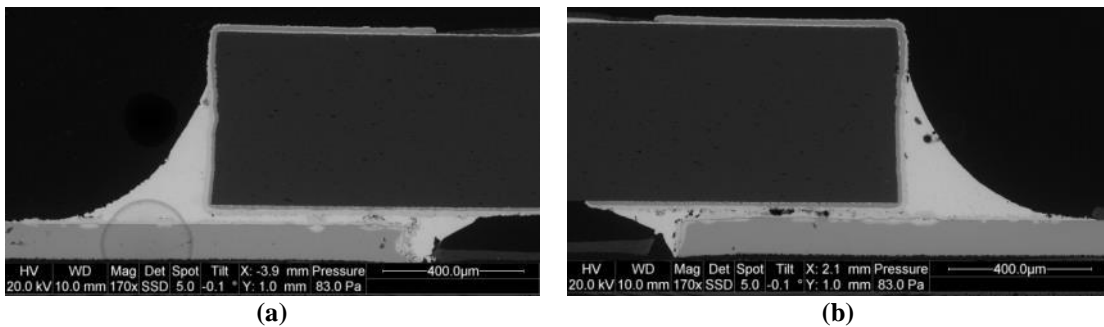


Figure 9-16: R2512 – SAC305 (a) Left Solder Joint (b) Right Solder Joint after 1000 hours/200°C Aging

Figure 9-17 shows a SAC305+0.05%Mn solder joint after 100 hours and 1000 hours aging at 200°C. Figure 9-18 shows left and right side of SAC305+0.05%Mn solder joint after 1000 hours aging at 200°C. After 100 hours of aging, complete consumption of Ni layer can be seen from Figure 9-17 (a). The initiation of  $\text{Cu}_6\text{Sn}_5$  IMC formation between copper pad and  $\text{Ni}_2\text{SnP}$  layer can also be seen in Figure 9-17 (a). After 1000 hours of aging, few evidence of four layers formation can be seen from Figure 9-17 (b). The formation of four layers due to Ni layer consumption had created many voids underneath the package on both the left and the right side of the solder joint after 1000 hours of aging, as shown in Figure 9-18 (a) and Figure 9-18



(b). It is also important to note that only few pockets can be seen on the board side in Figure 9-18 (a) and Figure 9-18 (b) indicating less consumption of Ni layer after 1000 hours of aging at 200°C.

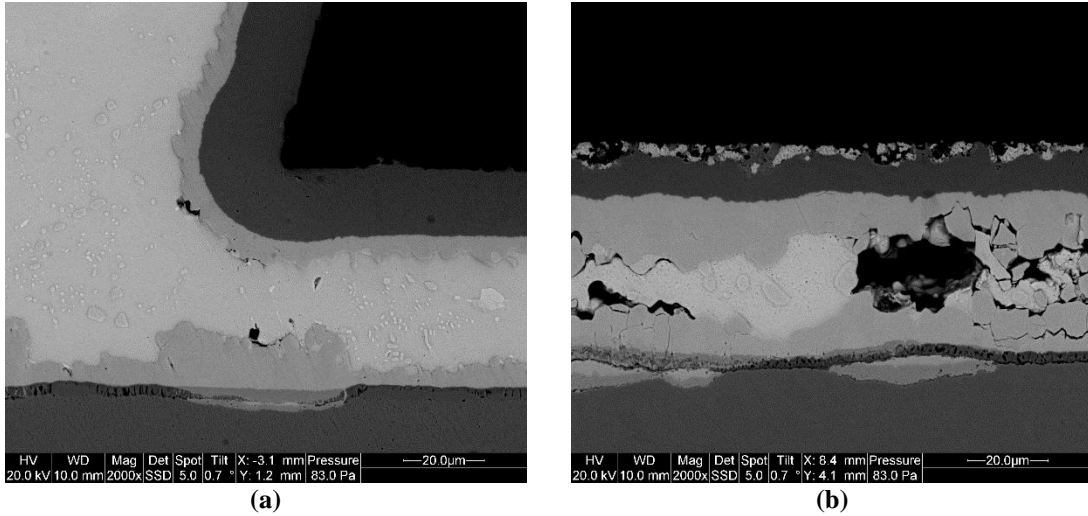


Figure 9-17: R2512 - SAC305+0.05% Mn Solder Joint (a) After 100 hours/200°C Aging, (b) After 1000 hours/200°C Aging

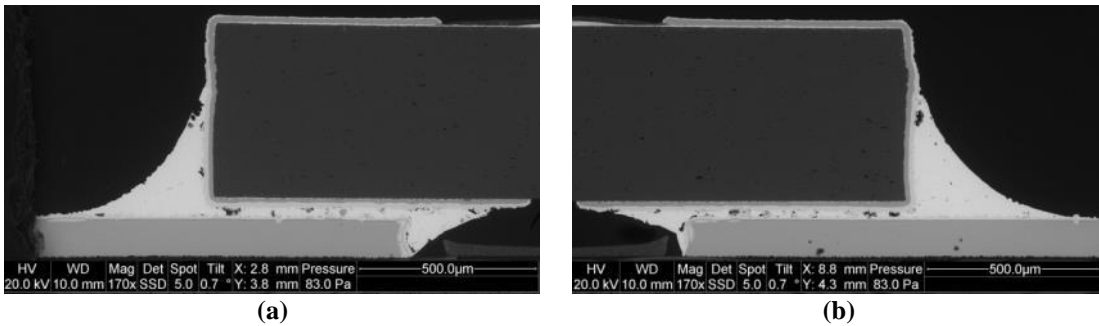


Figure 9-18: R2512 – SAC305+0.05%Mn (a) Left Solder Joint (b) Right Solder Joint after 1000 hours/200°C Aging

Figure 9-19 shows a SAC305+0.17%Mn solder joint after 100 hours and 1000 hours aging at 200°C. Figure 9-20 shows the left and the right side of SAC305+0.17%Mn solder joint after 1000 hours aging at 200°C. After 100 hours of aging, Ni layer remains unaffected, as shown in Figure 9-19 (a).  $\text{Ni}_3\text{Sn}_4$  IMC layer on the component side and  $(\text{Ni,Cu})_3\text{Sn}_4$  IMC layer on the board side remain laminar (planar-type). Many fine  $\text{Ag}_3\text{Sn}$  particles and a few large  $\text{AuSn}_4$  IMCs can also be seen in the solder bulk

in Figure 9-19 (a). After 1000 hours of aging, Ni layer still remains unaffected. Both component and board side interfacial IMCs were coarsened due to aging. Partial cracking of both interfacial IMCs can be found. This was due to an aggressive grinding and polishing. The component side interfacial IMC was found to be thicker than the board side interfacial IMC. Looking at the complete solder joint on the left and the right side from Figure 9-20 (a) and Figure 9-20 (b), no evidence of Ni layer consumption can be found after 1000 hours of aging at 200°C. Two voids can be seen in Figure 9-20 (b); however, these voids were process related and formed during reflow.

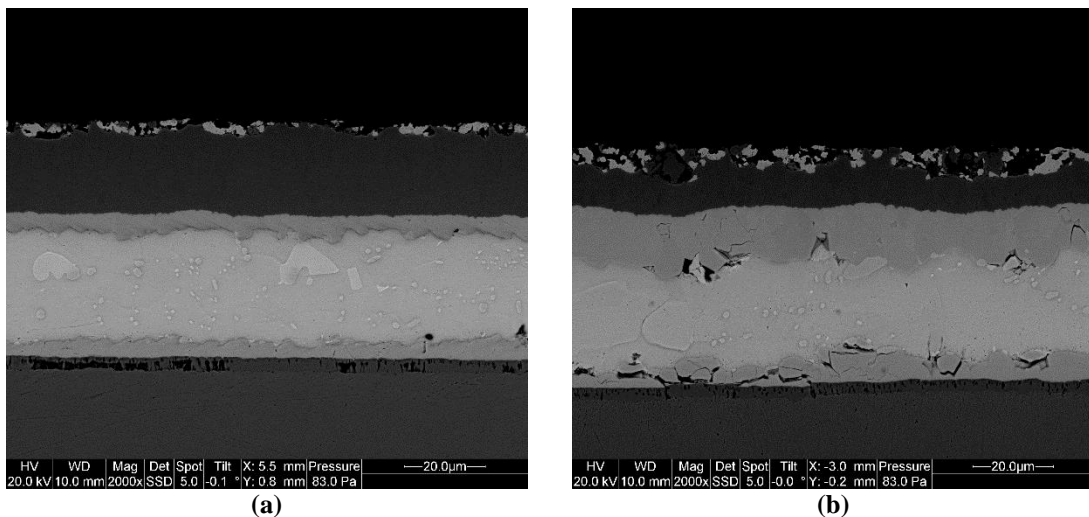


Figure 9-19: R2512 - SAC305+0.17%Mn Solder Joint (a) After 100 hours/200°C Aging, (b) After 1000 hours/200°C Aging

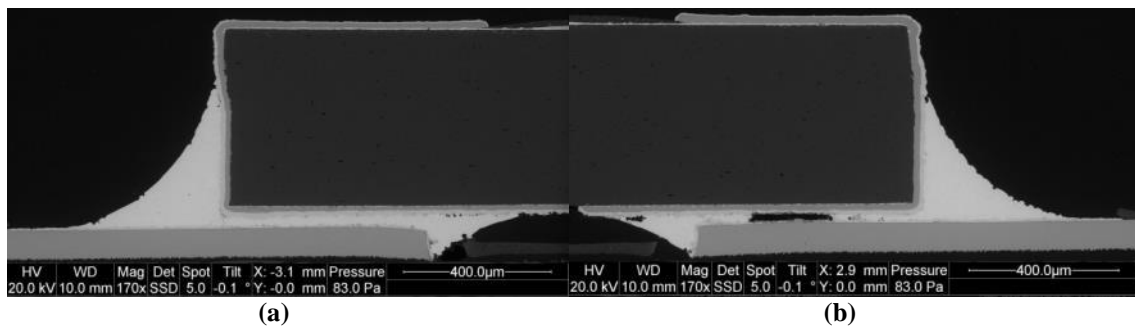


Figure 9-20: R2512 – SAC305+0.17%Mn (a) Left Solder Joint (b) Right Solder Joint after 1000 hours/200°C Aging

Figure 9-21 shows a SAC305+0.07%Ce solder joint after 100 hours and 1000 hours aging at 200°C. Figure 9-22 shows the left and the right side of SAC305+0.07%Ce solder joint after 1000 hours aging at 200°C. After 100 hours of aging, complete consumption of Ni layer at two locations can be found from Figure 9-21 (a). A void in the solder bulk on the surface of top layer can be also found in Figure 9-21 (a). Upon further aging, Ni layer consumption starts occurring at various locations and eventually these locations merge together and form layers which can be seen after 1000 hours of aging from Figure 9-21 (b). The severity of these layers is so high that it consumed most of the tin within the solder bulk and formed big voids at multiple locations, as shown in Figure 9-21 (b), Figure 9-22 (a), and Figure 9-22 (b). Low Ce solder was found to be severely affected due to Ni layer consumption compared to other solders during 200°C aging. The formation of multiple IMC layers and voids can significantly affect the reliability of a solder joint especially in mechanical drop/shock condition.

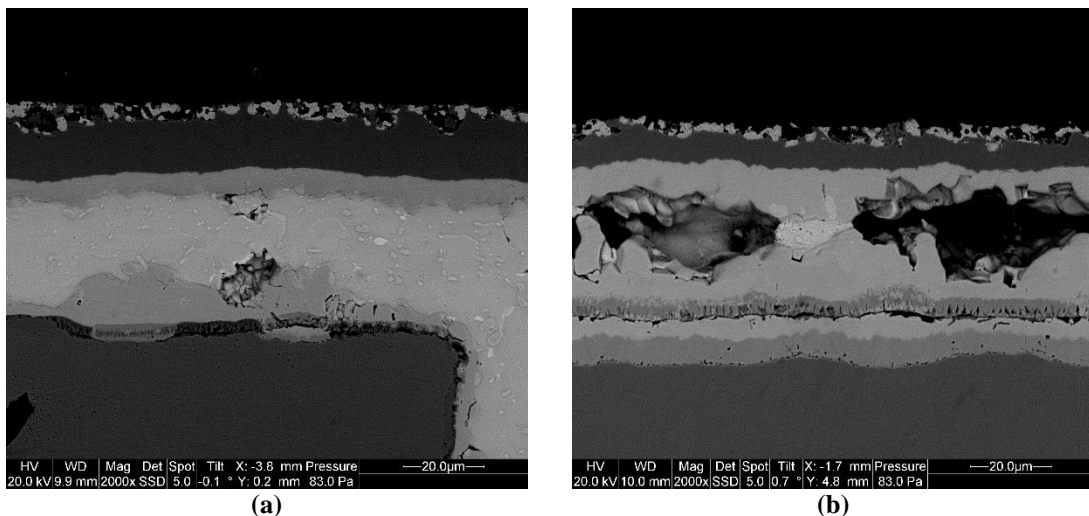


Figure 9-21: R2512 - SAC305+0.07%Ce Solder Joint (a) After 100 hours/200°C Aging, (b) After 1000 hours/200°C Aging

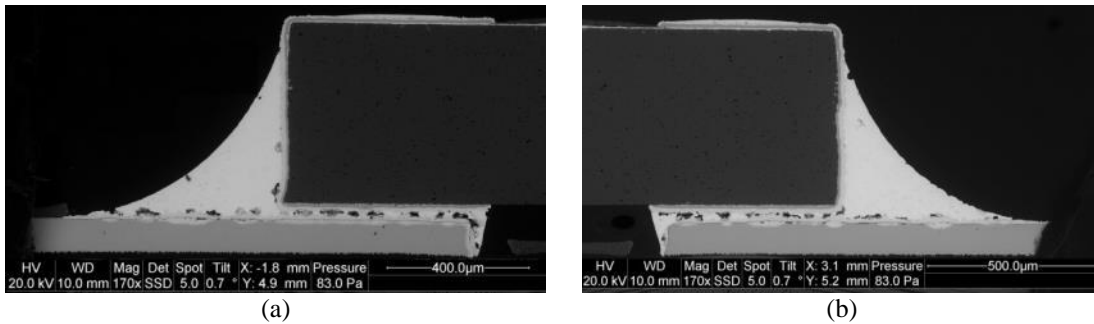


Figure 9-22: R2512 – SAC305+0.07%Ce (a) Left Solder Joint (b) Right Solder Joint after 1000 hours/200°C Aging

Figure 9-23 shows a SAC305+0.13%Ce solder joint after 100 hours and 1000 hours aging at 200°C. Figure 9-24 shows the left and the right side of SAC305+0.13%Ce solder joint after 1000 hours aging at 200°C. After 100 hours of aging, the Ni layer was found to be consumed, as shown in Figure 9-23 (a). Upon further aging, consumption of Ni layer started and formed four IMC layers at the board side. After 1000 hours of aging, the growth of IMCs at the location on the board side is shown in Figure 9-23 (b). It was found to be significant that the board side IMC formed a big scallop that merged with the component side interfacial IMC, as shown in Figure 9-23 (b). A formation of big void can also be seen Figure 9-23 (b). Looking at the complete solder joint on the left and the right side after 1000 hours of aging at 200°C from Figure 9-24 (a) and Figure 9-24 (b), it can be concluded that severity of Ni layer consumption in High Ce solder was lower than Low Ce solder as fewer locations on High Ce solder joint were found with Ni layer consumption. Presence of voids can also be seen in Figure 9-24 (a) and Figure 9-24 (b).

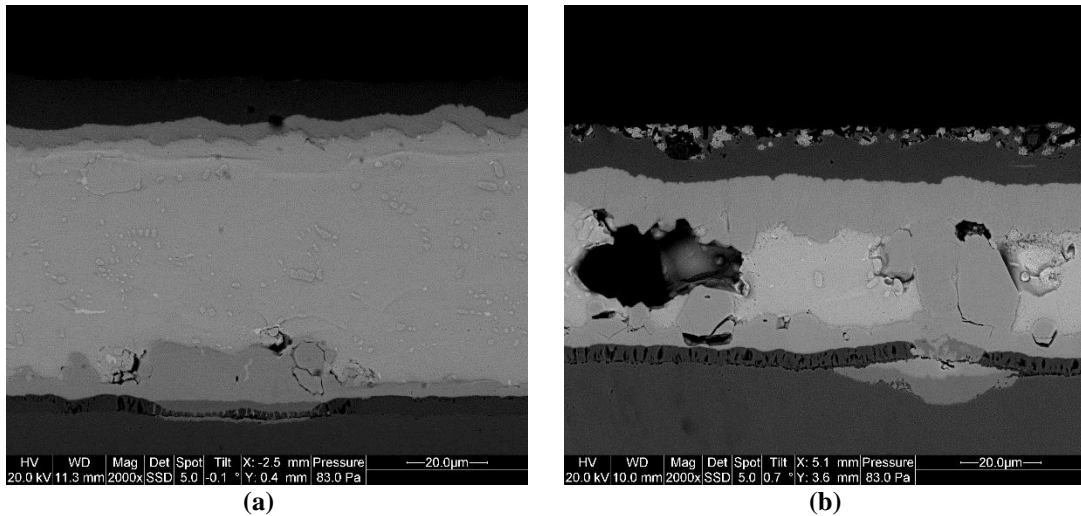


Figure 9-23: R2512 - SAC305+0.13%Ce Solder Joint (a) After 100 hours/200°C Aging, (b) After 1000 hours/200°C Aging

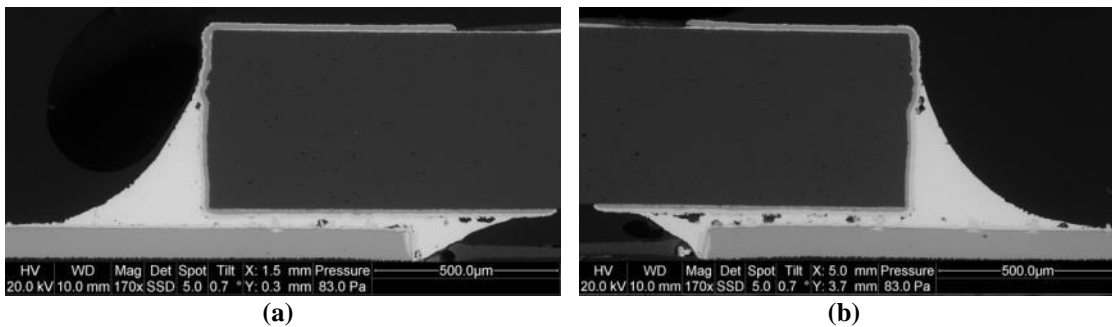


Figure 9-24: R2512 – SAC305+0.13%Ce (a) Left Solder Joint (b) Right Solder Joint after 1000 hours/200°C Aging

Based on the finding from 200°C aging test, it can be concluded that High Mn solder turned out to be an exceptionally good solder to prevent Ni layer consumption and suppress the growth of interfacial IMCs even up to 1000 hours of aging at 200°C. In order to further investigate the mechanism of such extraordinary behavior, High Mn solder was further analyzed with two elemental analysis techniques namely EDS (Energy Dispersive X-ray Spectroscopy) and WDS (Wavelength Dispersive X-ray Spectroscopy). The results of EDS and WDS analysis are discussed in the next section.

### **9.3.EDS and WDS Analysis on High Mn Solder Sample**

The first technique used for elemental analysis was EDS. Two types of analyses were performed using EDS technique. The first type of analysis was point scan analysis and the other type of analysis was line-scan analysis. Due to small concentration of Mn dopant (0.17% by weight) in High Mn solder, more accurate analysis was also performed using WDS technique. WDS technique has higher detection sensitivity especially for trace elements.

For both elemental analysis techniques, High Mn solder sample that was aged for 1000 hours at 200°C was used for the analysis. The results from both EDS and WDS techniques are discussed next.

#### **9.3.1. EDS Analysis Result**

Due to the lower resolution of EDS technique to detect a smaller concentration, numerous attempts had been made to detect Mn dopant in High Mn solder sample. After several attempts, it was found that the high concentration of Mn atoms was present at the interface between the Ni(P) layer and the  $(\text{Ni,Cu})_3\text{Sn}_4$  interfacial IMC layer on the board side. Results of point analysis and line-scan analysis using EDS technique are discussed next.

##### **9.3.1.1. Point Scan Analysis**

Figure 9-25 (a) shows the location of 10 points used for point scan analysis on High Mn solder sample. The first eight points were located at the interface between the Ni (P) layer and the  $(\text{Ni,Cu})_3\text{Sn}_4$  interfacial IMC layer indicated by X1 to X8, as shown

in Figure 9-25 (a). X9 was located within  $(\text{Ni,Cu})_3\text{Sn}_4$  interfacial IMC layer; whereas, X10 was located within Ni(P) layer. Figure 9-25 (b) shows the elemental spectrum for the location X3. Three peaks of Mn element can be found in Figure 9-25 (b). The first peak was near 1 keV, and two additional peaks were near 6 keV. The measured concentrations of Mn by weight% for all 10 points are summarized in Figure 9-25 (c). All eight points measured at the interface between the Ni(P) layer and the  $(\text{Ni,Cu})_3\text{Sn}_4$  interfacial IMC layer show the presence of Mn atoms with concentration varying from 0.38 to 1.74 weight%. No Mn was found at X9 and X10 locations. In order to further confirm the presence of Mn element at the interface where Mn was detected by point scan analysis, a line-scan analysis was further carried out using EDS technique at the same interface.

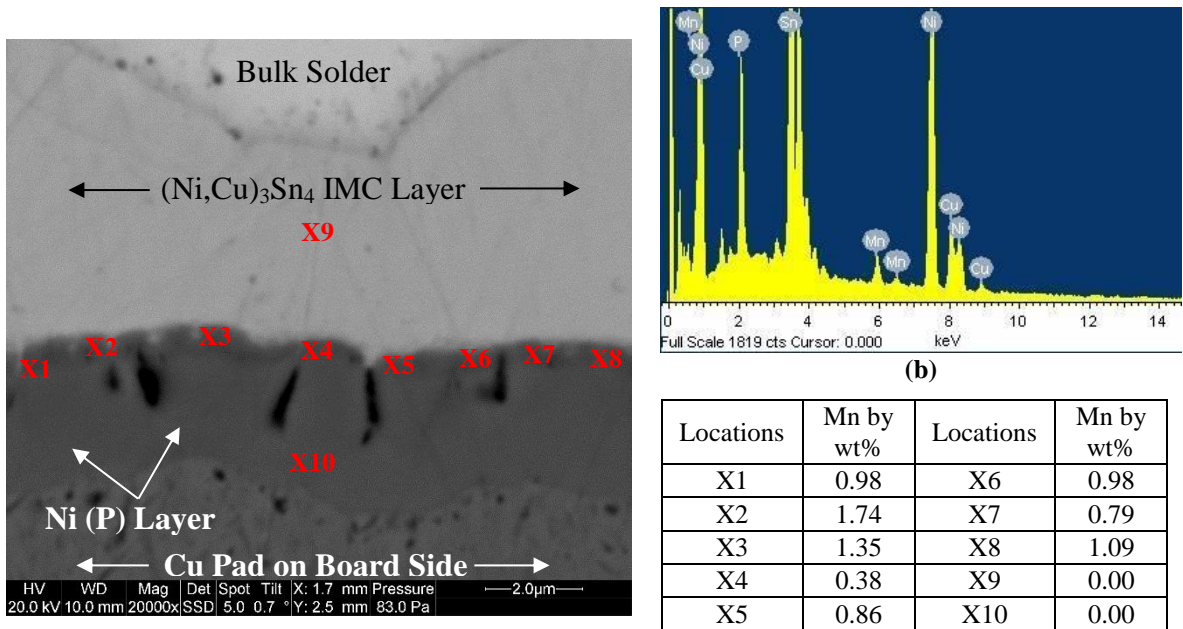


Figure 9-25: R2512 – (a) Locations of Point Scan Analysis, (b) Elemental Spectrum of X3 Location (c) Measurement of Mn Dopant by Weight% (High Mn Solder after 1000 hours/200°C Aging)

### 9.3.1.2. Line Scan Analysis

Figure 9-26 shows ESEM image of High Mn solder at 5000x magnification. The location for the line-scan analysis and reference line is shown in Figure 9-26. It is important to note that scan line passes through the bulk solder,  $\text{Ag}_3\text{Sn}$  bulk IMC particles,  $(\text{Ni,Cu})_3\text{Sn}_4$  interfacial IMC, Ni(P) layer, and the copper pad on the board side. Reference line was located at the interface between  $(\text{Ni,Cu})_3\text{Sn}_4$  interfacial IMC layer and the bulk solder. Due to the lower sensitivity of EDS technique to detecting small concentrations, a line scan analysis measurement was performed continuously for 4 hours to get higher counts to differentiate noise signal from raw signal. The qualitative representations of different elements found along the line scan with their elemental plots are shown in Figure 9-27. The elemental plot of Mn can be seen in Figure 9-27 (b). The measured counts for Mn element were less than other elements due to its smaller concentration in High Mn Solder. Though the counts are few, the presence of high concentration of Mn atoms can be seen at the interface between Ni(P) layer and  $(\text{Ni,Cu})_3\text{Sn}_4$  interfacial IMC layer from Figure 9-27 (b). The magnified view of the elemental plot of Mn is shown in Figure 9-28. This finding confirms the presence of high concentration of Mn atoms as previously found during the point scan analysis from the measurement at X1 to X8 locations.



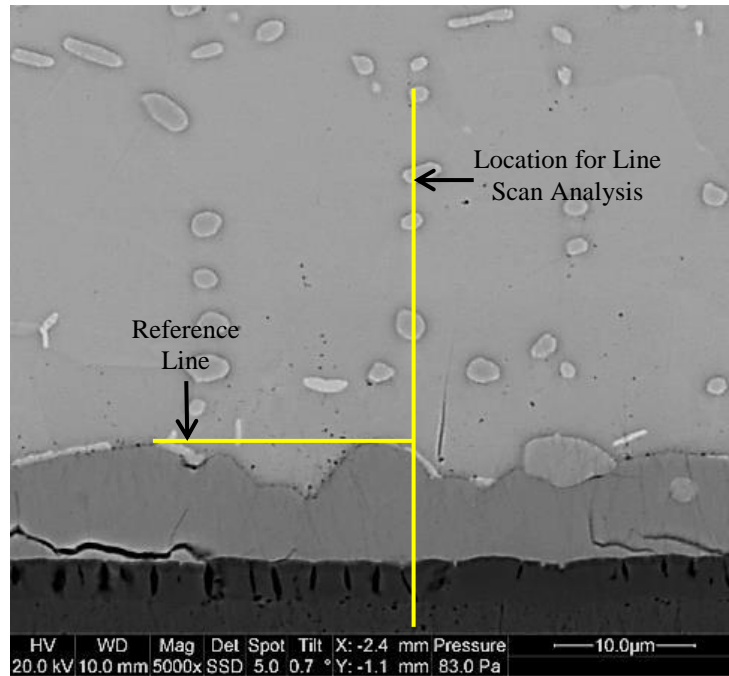


Figure 9-26: R2512 - Location of Line Scan Analysis and Reference Line for EDS Technique (High Mn Solder after 1000 hours/200°C aging)

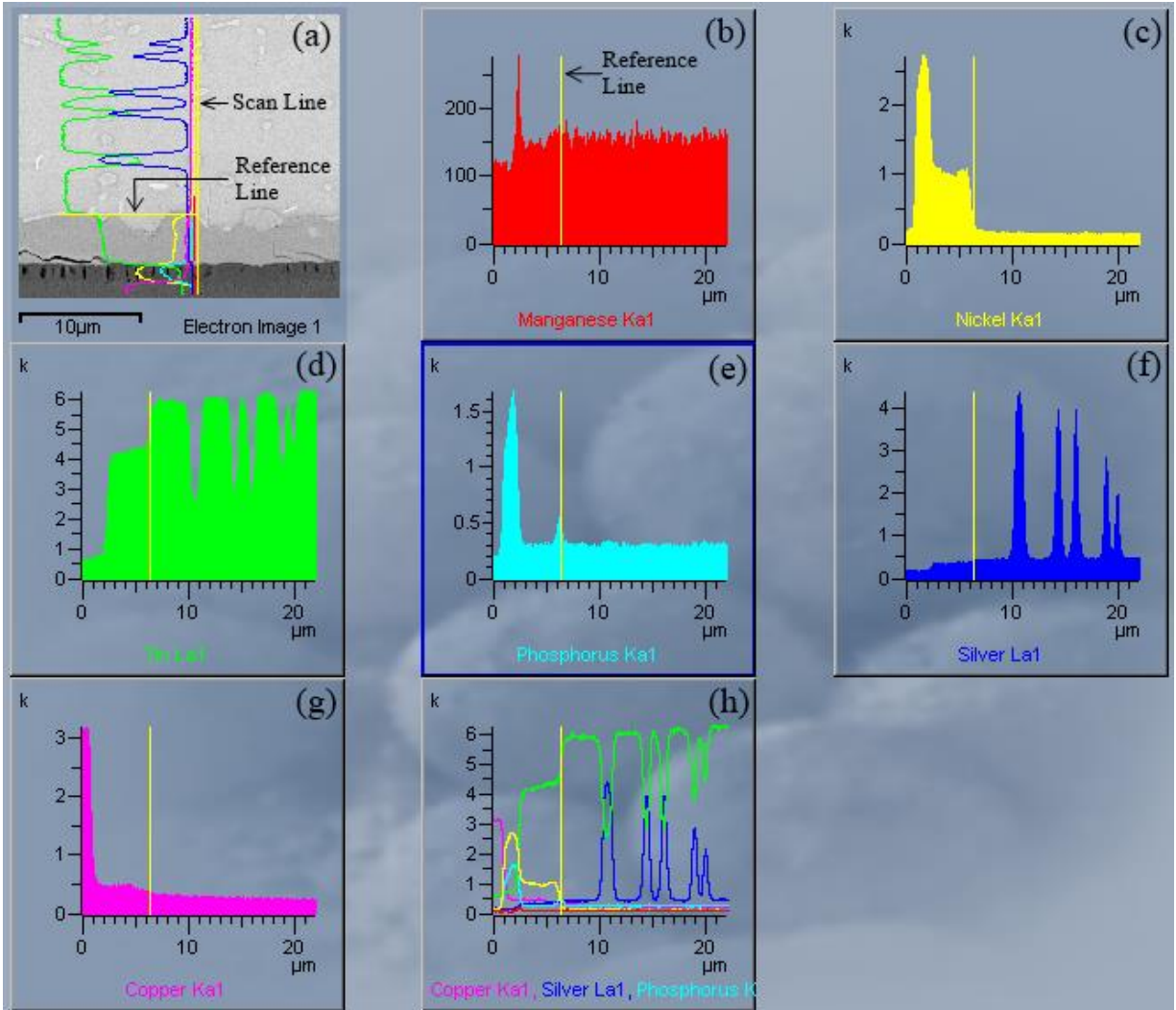


Figure 9-27: R2512 - EDS Line Scan Measurement Results (a) Compiled Elemental Plot with Line Scan and Reference Line (b) Elemental Plot of Mn (c) Elemental Plot of Ni (d) Elemental Plot of Sn (e) Elemental Plot of P (f) Elemental Plot of Ag (g) Elemental Plot of Cu (h) Combined Elemental Plot of All Elements (High Mn Solder after 1000 hours/200°C Aging)

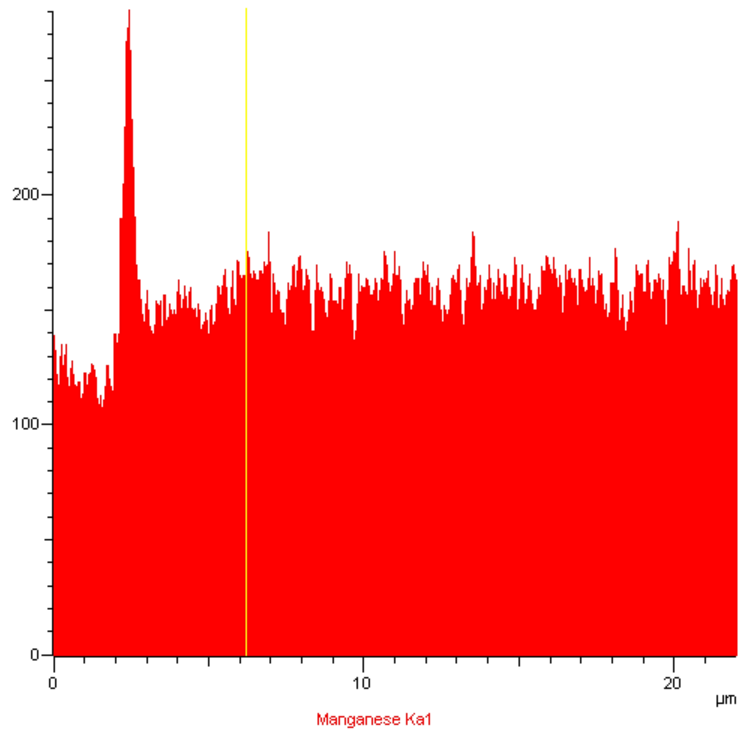


Figure 9-28: R2512 - Elemental Plot of Mn during EDS Line Scan Analysis (High Mn Solder after 1000 hours/200°C Aging)

### 9.3.2. WDS Analysis Result

High Mn solder sample was further analyzed with WDS technique that has higher detection sensitivity especially for trace elements. A line scan analysis was again performed using WDS technique. The location for line scan is shown in Figure 9-29. It is important to note that line scan passes through the bulk solder,  $\text{Ag}_3\text{Sn}$  bulk IMC at the surface of  $(\text{Ni,Cu})_3\text{Sn}_4$  interfacial IMC,  $(\text{Ni,Cu})_3\text{Sn}_4$  interfacial IMC, Ni(P) layer, and the copper pad on the board side. The qualitative representation of different elements found along the line during WDS analysis is shown in Figure 9-30. Looking at Mn plot from Figure 9-30, a clear peak for Mn can be seen at the interface between Ni(P) layer and  $(\text{Ni,Cu})_3\text{Sn}_4$  interfacial IMC layer. The magnified view of Mn elemental plot with the raw data and refined data signal are shown in Figure 9-31.

Figure 9-30 and Figure 9-31 confirms results from EDS technique by accurately showing presence of high concentration of Mn atoms at interface between Ni(P) layer and  $(\text{Ni,Cu})_3\text{Sn}_4$  interfacial IMC layer.

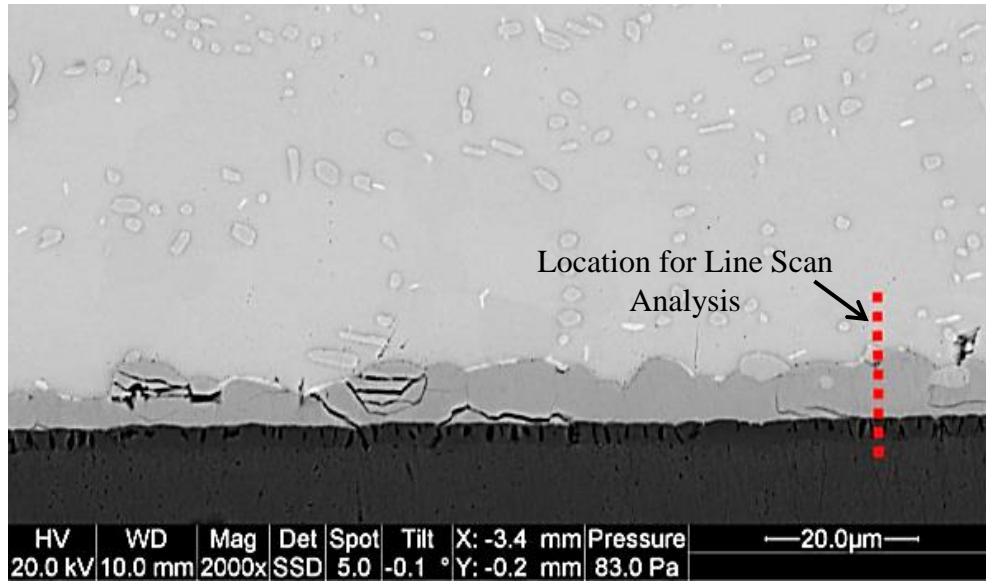


Figure 9-29: R2512 - Location of Line Scan Analysis for WDS Technique (High Mn Solder after 1000 hours/200°C aging)

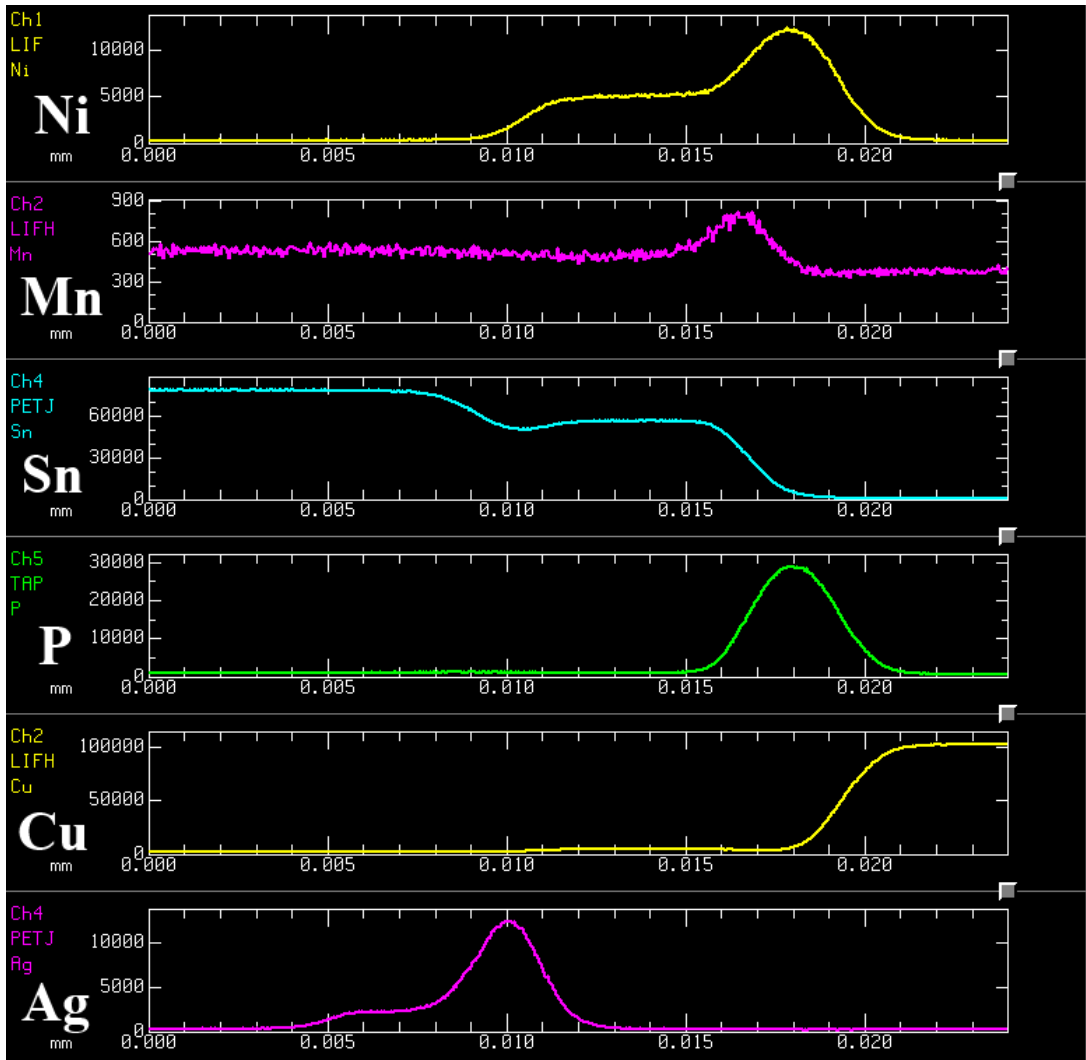


Figure 9-30: R2512 - WDS Line Scan Measurement Results. Elements are ordered as follow Ni, Mn, Sn, P, Cu and Ag (High Mn Solder after 1000 hours/200°C aging)

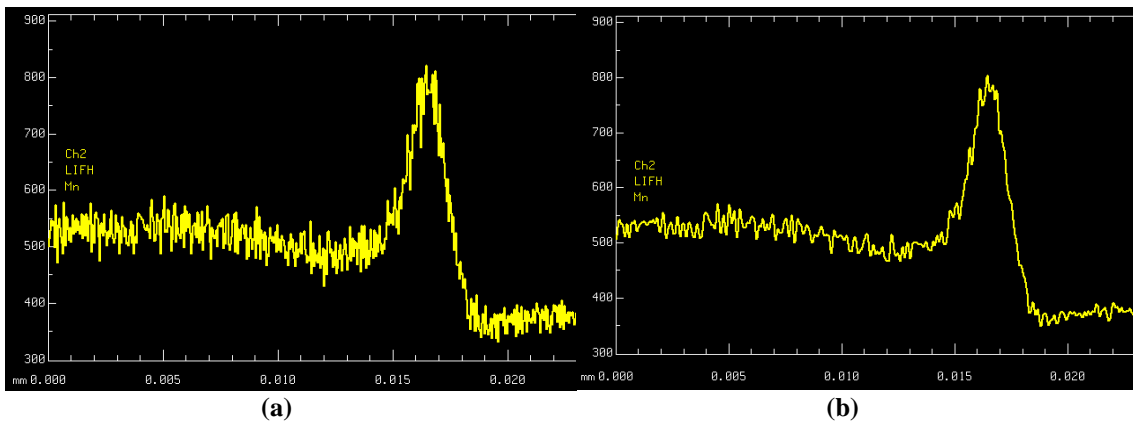


Figure 9-31: R2512 - Elemental Plot of Mn during WDS Line Scan Analysis (a) Raw Signal (b) Refined Signal (High Mn Solder after 1000 hours/200°C Aging)

All three different analysis performed using EDS and WDS techniques confirm the presence of high concentration of Mn at the interface between Ni(P) layer and  $(\text{Ni,Cu})_3\text{Sn}_4$  interfacial IMC layer. This indicates that migration of Mn atoms at the interface is the reason for stopping Ni layer consumption during 200°C aging. It is believed that the presence of high concentration of Mn atoms at the interface works as a diffusion barrier. This high concentration of Mn atoms does not allow Sn atoms migrating from the solder bulk through  $(\text{Ni,Cu})_3\text{Sn}_4$  IMC layer to react with the Ni(P) layer. Thus, formation of  $\text{Ni}_2\text{SnP}$  IMC layer can be prevented and the integrity of Ni(P) layer can be maintained during high temperature thermal aging. In addition, a high concentration of Mn atoms at the interface also minimizes the migration of Ni atoms from Ni(P) layer to the  $(\text{Ni,Cu})_3\text{Sn}_4$  interfacial IMC layer which suppresses the growth of  $(\text{Ni,Cu})_3\text{Sn}_4$  interfacial IMC layer during high temperature thermal aging.

Overall, the presence of high concentrations of Mn at the interface between Ni(P) layer and  $(\text{Ni,Cu})_3\text{Sn}_4$  interfacial IMC layer maintains Ni layer stability and also reduces the growth of  $(\text{Ni,Cu})_3\text{Sn}_4$  interfacial IMC layer during 200°C aging.

#### **9.4. Conclusions**

This study was conducted to examine the aging effect on five selected solders at two different temperatures (viz. 185°C and 200°C) by analyzing Ni plated R2512 package mounted on ENIG-plated board. This study has resulted many important findings as summarized below.

- All modified SAC305 solders were effective to suppress the growth of both the component side and the board side interfacial IMC during 185°C aging.

Low Ce was found to be less effective in suppressing the growth of interfacial IMCs during extended period of aging at 185°C.

- High Mn solder was the most effective to suppress interfacial IMC growth and resulted in the thinnest interfacial IMC on both the component and the board side during 185°C aging.
- In general, SAC305 solder showed the thickest interfacial IMC on both the component and the board side during 185°C aging.
- During 200°C aging, all solders except High Mn showed an unexpected growth of interfacial IMC on the board side. Further analysis found that this unexpected growth was related to Ni layer consumption on the board side. This phenomenon was observed after just 100 hours of aging at 200°C. During subsequent aging, four different IMC layers were found at the board side at for all solders except High Mn solder.
- During 200°C aging, High Mn solder outperformed by preventing Ni layer consumption even after 1000 hours of aging at 200°C. High Mn solder also very effective in suppressing the growth of  $(\text{Ni,Cu})_3\text{Sn}_4$  interfacial IMC layer on the board side during 200°C aging.
- SAC305 and Low Ce solders showed severe degradation of Ni layer consumption compared to other solders under 200°C aging.
- Based on elemental analysis using EDS and WDS techniques, it was confirmed that Mn atoms migrated at the interface between Ni(P) layer and  $(\text{Ni,Cu})_3\text{Sn}_4$  interfacial IMC layer during aging. It is believed that presence of

high concentration of Mn at the interface between Ni(P) layer and  $(\text{Ni,Cu})_3\text{Sn}_4$  interfacial IMC layer prevents the consumption of Ni layer and maintain its stability. In addition, the high concentration of Mn atoms also reduces the growth of  $(\text{Ni,Cu})_3\text{Sn}_4$  interfacial IMC layer during 200°C aging.



## 10. Mechanical Shock Reliability Test

This chapter discusses the impact of isothermal aging on the mechanical shock reliability of selected solders. Mechanical shock reliability of lead-free solders has been a concern for electronic industries because, more than a decade after introducing lead-free solders into the market, a direct replacement to SnPb solder for mechanical shock durability is still missing. This problem creates a big fear especially when lead-free solders are being used for high temperature applications where electronics are also subjected to mechanical drop/shock loading. Interfacial IMC formation within a solder joint is governed by thermally activated diffusion process. At high temperatures, high diffusion rate leads to formation of thick interfacial IMCs. The formation of various interfacial IMCs on QFN44, QFN32, and R2512 package types under 185°C and 200°C aging has been thoroughly investigated, as discussed previously in chapter 8 and 9.

The interfacial IMCs of solder play an important role in mechanical shock loading as they are usually found to be the primary failure sites. Therefore, it is important to correlate the growth of interfacial IMCs to the mechanical shock reliability. From the literature, it was found that the effect of high temperature isothermal aging on the mechanical shock reliability of lead-free solder has not been thoroughly investigated.

This study investigates the impact of high temperature isothermal aging on the mechanical shock reliability of selected solders. High temperature isothermal aging was performed at 185°C and 200°C up to 1000 hours. A set of test boards were removed after 400 and 1000 hours of aging at both temperatures (185°C and 200°C)

for mechanical shock testing. Two boards per solder at each time and temperature interval (i.e., 40 boards total for five solders) were isothermally aged and then tested under mechanical shocks. It was decided to subject these boards to 100,000 mechanical shocks with a shock pulse of 500G with 1.3 millisecond duration. For a baseline, un-aged test boards (time=0 or 0 hour of aging) were also tested under mechanical shocks. Without any aging, un-aged test boards were expected to last longer than aged test boards under mechanical shocks. Thus, un-aged boards were subjected to 600,000 mechanical shocks. For the baseline test, two boards per solder for five solders making 10 test boards total were tested for 600,000 mechanical shocks. The testing outline discussed above is summarized in Figure 10-1.

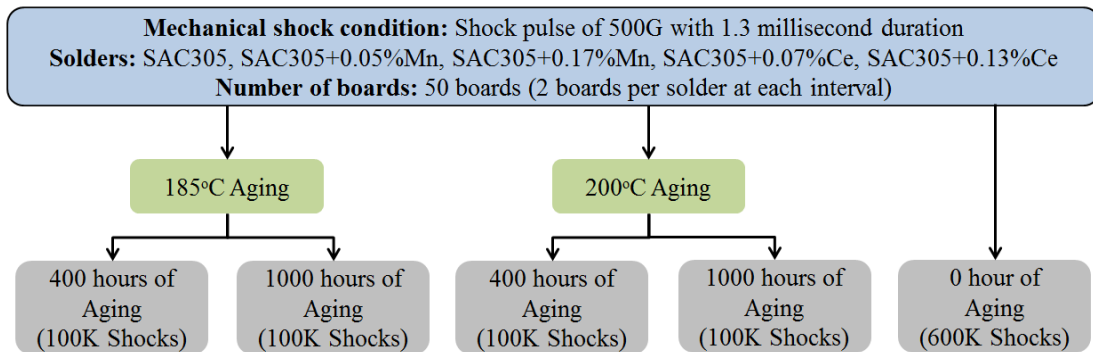


Figure 10-1: Mechanical Shock Testing Outline

A test board features five different package types including QFN44, QFN32, QFP256, R2512 and R2010. Each test board comprises two QFP256, four QFN44, four QFN32, eight R2512, and eight R2010 package types. Due to the dissimilar construction of selected package types, time-to-failure for each package type under mechanical shocks can also vary. In order to keep the comparison straightforward for selected solders, mechanical shock test results of each package type with pre-aging are grouped together and presented in the following sequence: QFN44, QFN32,

QFP256, R2512 and R2010. The test result of all package types from un-aged test boards are combined together, and test data are presented in tabulated form.

### **10.1. QFN44 - Mechanical Shock Test Results after Thermal Aging at 185°C and 200°C**

Two test boards for each solder comprise a total of eight QFN44 samples per solder. All eight QFN44 samples for all five solders failed during 100,000 mechanical shocks. The obtained QFN44 cycles to failure data from mechanical shock test were plotted using Weibull two-parameter distribution.

Figure 10-2 shows Weibull plot for QFN44 after 400 hours of aging at 185°C. The extracted Weibull parameters from Weibull analysis are shown in Table 10-1. In addition to Weibull shape parameter (Weibull slope), Weibull scale parameter (characteristic life) and Rho (goodness of fit), Table 10-1 also includes cycles to 1% failure, cycles to first failure and cycles to 50% failure. The similar value of Weibull slope obtained for all solders indicates that solders failed by the same failure mechanism. Mechanical shock reliability of High Mn and High Ce solders is quite distinguishable from the rest of the solders. To perform reliability comparison of selected solders, characteristic life (Weibull scale parameter) was used as a matrix to rank solder performance. Based on characteristic life value, the mechanical shock reliability of selected solders can be ranked in the following order:

High Mn > High Ce > Low Mn > Low Ce > SAC305

All modified SAC305 solders exhibited better mechanical shock reliability than SAC305 after 400 hours of aging at 185°C. High Mn solder showed around 8.0 times

better performance than SAC305. Also, High Ce solder showed around 3.8 times better performance than SAC305. Low Mn and Low Ce solders were less effective compared to High Mn and High Ce; however, they showed improved performance of around 1.7 and 1.3 times than SAC305, respectively. In order to determine statistically significant difference in the performance of modified SAC305 solders compared to SAC305, Kruskal-Wallis test was performed. Table 10-2 shows p-value from Kruskal-Wallis test for all modified SAC305 solders in comparison to SAC305. P-value < 0.05 shows statistical significant difference between two groups. From Table 10-2, it can be concluded that High Mn and High Ce show a statistically significant difference with SAC305; whereas, no statistically significant difference exists for Low Mn and Low Ce with SAC305.

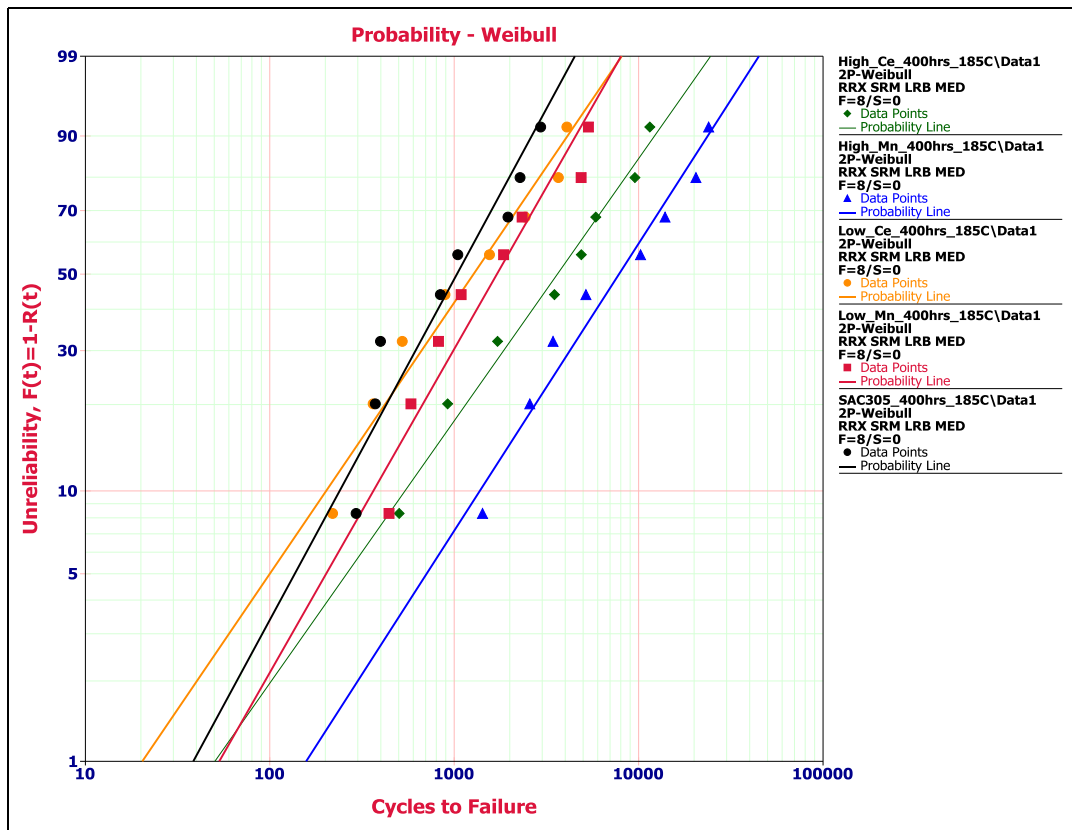


Figure 10-2: QFN44 Weibull Plot - 400 hours of Aging at 185°C

Table 10-1: Weibull Parameters for QFN44 - 400 hours of Aging at 185°C

|  | SAC305 | Low Mn | High Mn | Low Ce | High Ce |
|--|--------|--------|---------|--------|---------|
| $\beta$ (Weibull Slope)                    | 1.29   | 1.22   | 1.08    | 1.02   | 0.99    |
| Cycles to 1% Failure                       | 38     | 53     | 158     | 20     | 50      |
| Cycles to First Failure                    | 295    | 445    | 1430    | 220    | 505     |
| Cycles to 50% Failure                      | 1034   | 1705   | 7825    | 1273   | 3628    |
| $\eta$ (Characteristic Life) 63.2% Failure | 1376   | 2301   | 10972   | 1821   | 5253    |
| Improvement in $\eta$ (times)              | -      | 1.7    | 8.0     | 1.3    | 3.8     |
| Rho (Goodness of fit)                      | 0.95   | 0.96   | 0.98    | 0.98   | 0.99    |

Table 10-2: Kruskal-Wallis Test - QFN44 (400 hours of Aging at 185°C)

| p-value for SAC305-X solders from Kruskal-Wallis test in comparison to SAC305 |         |  |
|---|---------|--|
| Solders   | p-value | Does statistical significant difference exist? |
| Low Mn  | 0.294   | No   |
| High Mn   | 0.003   | Yes  |
| Low Ce  | 0.674   | No   |
| High Ce   | 0.036   | Yes  |

Figure 10-3 shows Weibull plot for QFN44 after 1000 hours aging at 185°C. The extracted Weibull parameters are shown in Table 10-3. Based on characteristic life value, the mechanical shock reliability of selected solders can be ranked in the following order:

$$\text{High Mn} > \text{High Ce} > \text{Low Mn} > \text{SAC305} = \text{Low Ce}$$

Except Low Ce solder, all other modified SAC305 solders exhibited better mechanical shock reliability than SAC305 after 1000 hours aging at 185°C. High Mn solder showed around 8.2 times better performance than SAC305. High Ce and Low Mn solders showed around 3.0 and 2.1 times better performance than SAC305, respectively. Low Ce and SAC305 solders exhibited similar mechanical shock performance. Table 10-4 shows p-value from Kruskal-Wallis test for all modified SAC305 solders in comparison to SAC305. P-value < 0.05 shows statistically significant difference between two groups. From Table 10-4, it can be concluded that

High Mn and High Ce show a statistically significant difference with SAC305; whereas, no statistically significant difference exists for Low Mn and Low Ce with SAC305.

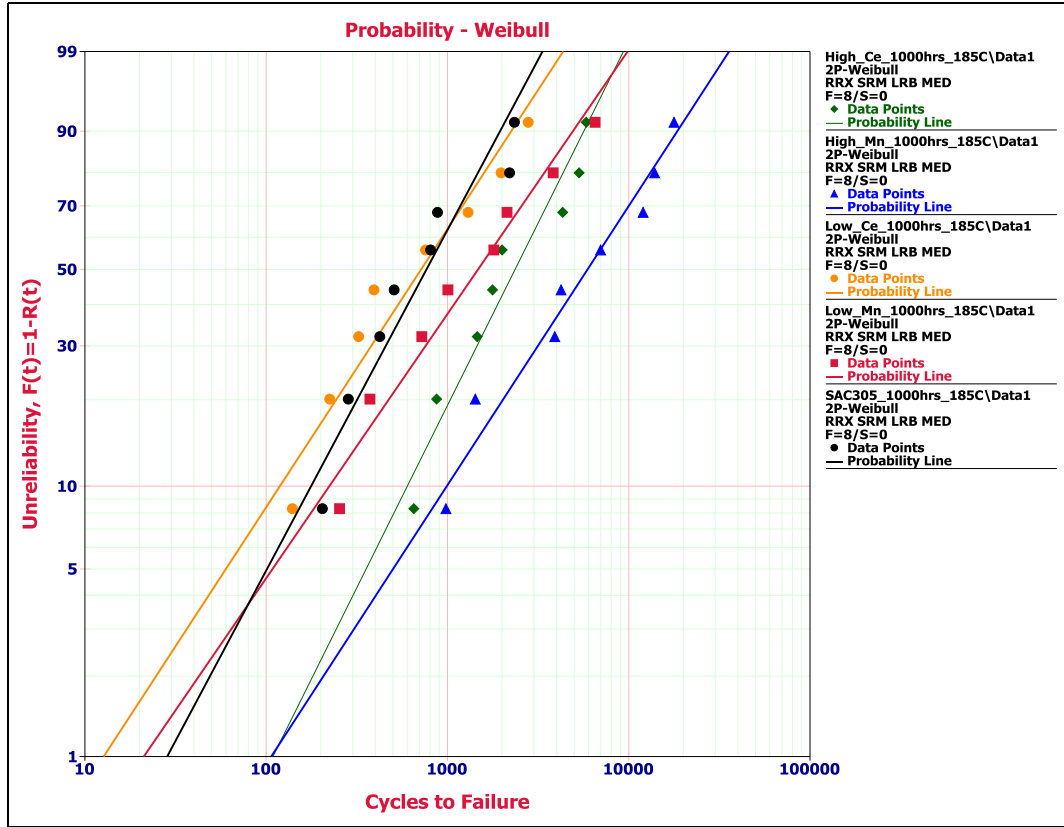


Figure 10-3: QFN44 Weibull Plot - 1000 hours of Aging at 185°C

Table 10-3: Weibull Parameters for QFN44 - 1000 hours of Aging at 185°C

|  | SAC305 | Low Mn | High Mn | Low Ce | High Ce |
|--|--------|--------|---------|--------|---------|
| $\beta$ (Weibull Slope)                    | 1.29   | 1.00   | 1.05    | 1.05   | 1.38    |
| Cycles to 1% Failure                       | 28     | 21     | 107     | 13     | 109     |
| Cycles to First Failure                    | 205    | 255    | 985     | 140    | 655     |
| Cycles to 50% Failure                      | 766    | 1476   | 5929    | 716    | 2361    |
| $\eta$ (Characteristic Life) 63.2% Failure | 1019   | 2131   | 8396    | 1015   | 3082    |
| Improvement in $\eta$ (times)              | -      | 2.1    | 8.2     | 1.0    | 3.0     |
| Rho (Goodness of fit)                      | 0.96   | 0.98   | 0.98    | 0.97   | 0.97    |

Table 10-4: Kruskal-Wallis Test - QFN44 (1000 hours of Aging at 185°C)

| p-value for SAC305-X solders from Kruskal-Wallis test in comparison to SAC305 |         |  |
|---|---------|--|
| Solders   | p-value | Does statistical significant difference exist? |
| Low Mn  | 0.345   | No   |
| High Mn   | 0.003   | Yes  |
| Low Ce  | 0.753   | No   |
| High Ce   | 0.046   | Yes  |

Figure 10-4 shows Weibull plot for QFN44 after 400 hours aging at 200°C. The extracted Weibull parameters are shown in Table 10-5. Based on characteristic life value, the mechanical shock reliability of selected solders can be ranked in the following order:

$$\text{High Mn} > \text{High Ce} > \text{Low Mn} > \text{Low Ce} > \text{SAC305}$$

All modified SAC305 solders exhibited better mechanical shock reliability than SAC305 after 400 hours of aging at 200°C. High Mn solder showed around 5.7 times better performance than SAC305. Also, High Ce solder showed around 3.1 times better performance than SAC305. Low Mn and Low Ce solders were less effective than High Mn and High Ce; however, they showed improved performance of around 1.6 and 1.3 times than SAC305, respectively.

Table 10-6 shows p-value from Kruskal-Wallis test for all modified SAC305 solders in comparison to SAC305. P-value < 0.05 shows statistically significant difference between two groups. From Table 10-6, it can be concluded that High Mn and High Ce show statistically significant difference with SAC305; whereas, no statistically significant difference exists for Low Mn and Low Ce with SAC305.

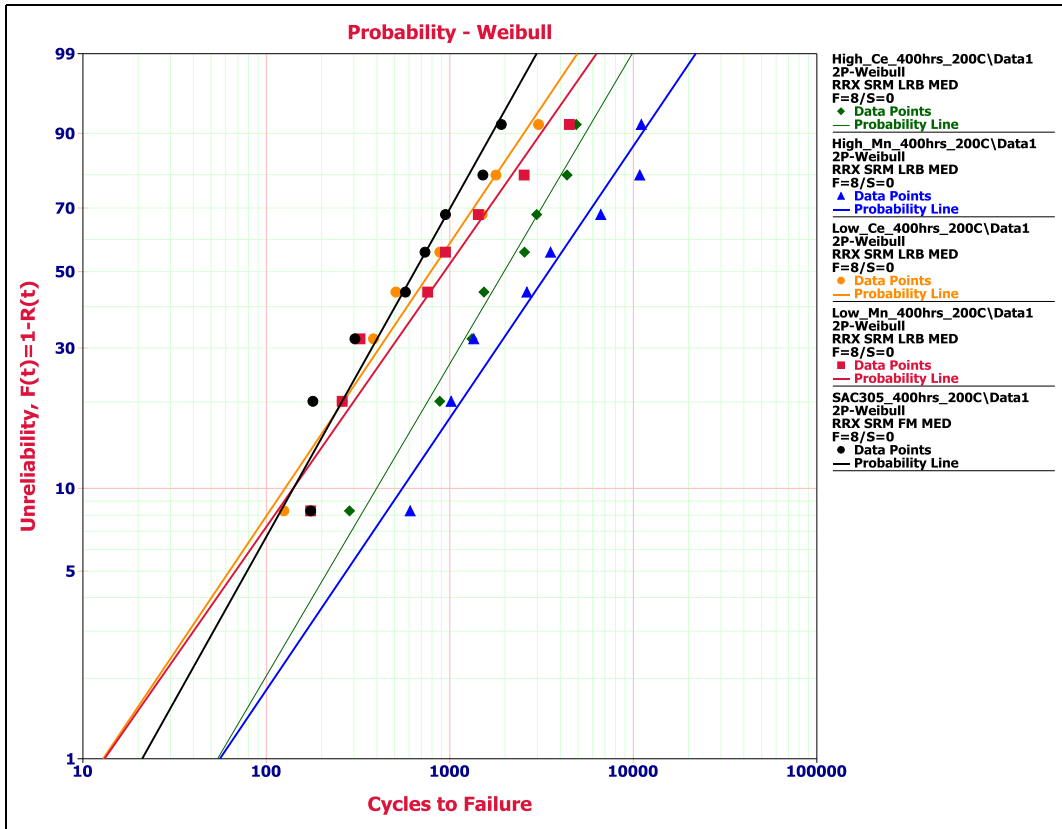


Figure 10-4: QFN44 Weibull Plot - 400 hours of Aging at 200°C

Table 10-5: Weibull Parameters for QFN44 - 400 hours of Aging at 200°C

|  | SAC305 | Low Mn | High Mn | Low Ce | High Ce |
|--|--------|--------|---------|--------|---------|
| $\beta$ (Weibull Slope)                    | 1.24   | 0.99   | 1.03    | 1.04   | 1.18    |
| Cycles to 1% Failure                       | 21     | 13     | 56      | 13     | 54      |
| Cycles to First Failure                    | 175    | 175    | 610     | 125    | 285     |
| Cycles to 50% Failure                      | 643    | 935    | 3454    | 787    | 1975    |
| $\eta$ (Characteristic Life) 63.2% Failure | 865    | 1352   | 4937    | 1124   | 2696    |
| Improvement in $\eta$ (times)              | -      | 1.6    | 5.7     | 1.3    | 3.1     |
| Rho (Goodness of fit)                      | 0.97   | 0.97   | 0.98    | 0.99   | 0.99    |

Table 10-6: Kruskal-Wallis Test - QFN44 (400 hours of Aging at 200°C)

| p-value for SAC305-X solders from Kruskal-Wallis test in comparison to SAC305 |         |  |
|---|---------|--|
| Solders   | p-value | Does statistical significant difference exist? |
| Low Mn  | 0.528   | No   |
| High Mn   | 0.012   | Yes  |
| Low Ce  | 0.834   | No   |
| High Ce   | 0.036   | Yes  |



Figure 10-5 shows Weibull plot for QFN44 after 400 hours aging at 200°C. The extracted Weibull parameters are shown in Table 10-7. Based on characteristic life value, the mechanical shock reliability of selected solders can be ranked in the following order:

High Mn > High Ce > Low Mn > SAC305 > Low Ce

Except Low Ce solder, all other modified SAC305 solders exhibited better mechanical shock reliability than SAC305 after 1000 hours aging at 200°C. High Mn solder showed around 3.6 times better performance than SAC305. High Ce and Low Mn solders showed around 3.0 and 1.7 times better performance than SAC305 respectively. Low Ce exhibited poor mechanical shock performance than SAC305.

Table 10-8 shows p-value from Kruskal-Wallis test for all modified SAC305 solders in comparison to SAC305. P-value < 0.05 shows statistically significant difference between two groups. From Table 10-8, it can be concluded that High Mn and High Ce show statistically significant difference with SAC305; whereas, no statistically significant difference exists for Low Mn and Low Ce with SAC305.

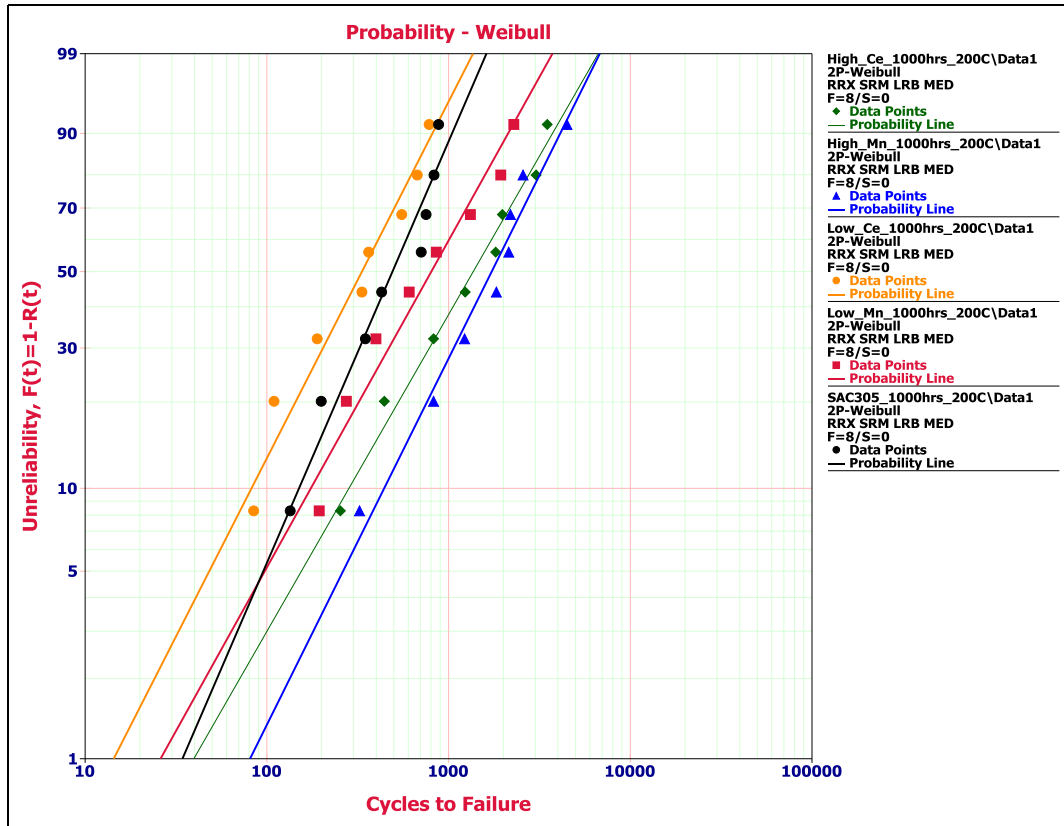


Figure 10-5: QFN44 Weibull Plot - 1000 hours of Aging at 200°C

Table 10-7: Weibull Parameters for QFN44 - 1000 hours of Aging at 200°C

|  | SAC305 | Low Mn | High Mn | Low Ce | High Ce |
|--|--------|--------|---------|--------|---------|
| $\beta$ (Weibull Slope)                    | 1.59   | 1.23   | 1.38    | 1.35   | 1.20    |
| Cycles to 1% Failure                       | 34     | 26     | 81      | 14     | 40      |
| Cycles to First Failure                    | 135    | 195    | 320     | 85     | 255     |
| Cycles to 50% Failure                      | 491    | 804    | 1727    | 334    | 1367    |
| $\eta$ (Characteristic Life) 63.2% Failure | 619    | 1082   | 2252    | 438    | 1857    |
| Improvement in $\eta$ (times)              | -      | 1.7    | 3.6     | 0.7    | 3.0     |
| Rho (Goodness of fit)                      | 0.98   | 0.98   | 0.98    | 0.98   | 0.99    |

Table 10-8: Kruskal-Wallis Test - QFN44 (1000 hours of Aging at 200°C)

| p-value for SAC305-X solders from Kruskal-Wallis test in comparison to SAC305 |         |  |
|---|---------|--|
| Solders   | p-value | Does statistical significant difference exist? |
| Low Mn  | 0.345   | No   |
| High Mn   | 0.012   | Yes  |
| Low Ce  | 0.208   | No   |
| High Ce   | 0.036   | Yes  |

### **10.1.1. Discussion on QFN44 Mechanical Shock Test Results**

The characteristic life data obtained from Weibull analysis for all solders after 400 and 1000 hours of aging at 185°C and 200°C are compiled together as shown in Figure 10-6. Due to large variation in characteristic life of solders, Y axis of Figure 10-6 uses a logarithmic scale. From Figure 10-6, it can be seen that as the aging time and temperature increase, reduction in the characteristic life of solders is quite evident. Thus, it can be concluded that high temperature aging substantially reduces the mechanical shock reliability of solders. High Mn solder outperformed at all intervals during mechanical shock test. It showed performance improvement of 8.2 to 3.6 times to SAC305 during mechanical shock testing. High Ce solder was found to be the second most effective solder with performance improvement of 3.8 to 3.0 times to SAC305. The difference in the performance of High Mn and High Ce solders is reduced at higher temperature aging. Low Mn solder also exhibited higher mechanical shock reliability with improved performance of 2.0 to 1.6 times to SAC305. Low Ce solder performed slightly better than SAC305 to mechanical shocks after 400 hours of aging at 185°C and 200°C with performance improvement of around 1.3 times; however, an extended aging exposure seems to cause more damage to Low Ce solder which resulted lower mechanical shock reliability than SAC305 after 1000 hours of aging at 185°C and 200°C. In general, all modified SAC305 solders except Low Ce solder performed better than SAC305 to mechanical shocks after 400 and 1000 hours of aging at 185°C and 200°C. Characteristic life comparison between all modified SAC305 solders and SAC305 is shown in Table 10-9.

Table 10-9: QFN44 - Characteristic Life Comparison

| Solders | Characteristic Life Improvement Compared to SAC305 |                  |
|---------|--|------------------|
|         | 185°C Aging  | 200°C Aging      |
| Low Mn  | 8.2 to 8.0 times                                   | 5.7 to 3.6 times |
| High Mn | 3.8 to 3.0 times                                   | 3.1 to 3.0 times |
| Low Ce  | 2.0 to 1.7 times                                   | 1.7 to 1.6 times |
| High Ce | 1.3 to 1.0 times                                   | 1.3 to 0.7 times |

The improved performance of modified SAC305 solders can be due to the reduction in the growth of  $\text{Cu}_6\text{Sn}_5$  interfacial IMC and less voiding observed during aging analysis, as discussed previously in chapter 8. In order to correlate the mechanical shock reliability to  $\text{Cu}_6\text{Sn}_5$  interfacial IMC and interfacial voiding, previously presented results of  $\text{Cu}_6\text{Sn}_5$  interfacial IMC growth and %voiding for all solders after 400 and 1000 hours of aging at 185°C and 200°C are summarized, as shown in Figure 10-7 and Figure 10-8, respectively. By carefully comparing results from Figure 10-6, Figure 10-7, and Figure 10-8, it can be concluded that there seems to be a correlation of mechanical shock reliability of solder with  $\text{Cu}_6\text{Sn}_5$  interfacial IMC and interfacial voiding. For example, High Mn solder showed, in general, the thinnest  $\text{Cu}_6\text{Sn}_5$  interfacial IMC and lowest interfacial voiding which resulted in the highest mechanical shock reliability. In contrast, similar correlation can be seen for SAC305 for its poor mechanical shock performance. In addition, it also appears that interfacial voiding has much more influence on mechanical shock reliability of solder compared to  $\text{Cu}_6\text{Sn}_5$  interfacial IMC. For Low Ce solder, thicker  $\text{Cu}_6\text{Sn}_5$  interfacial IMC after 1000 hours of aging at 200°C seems be the reason for lower mechanical shock reliability.

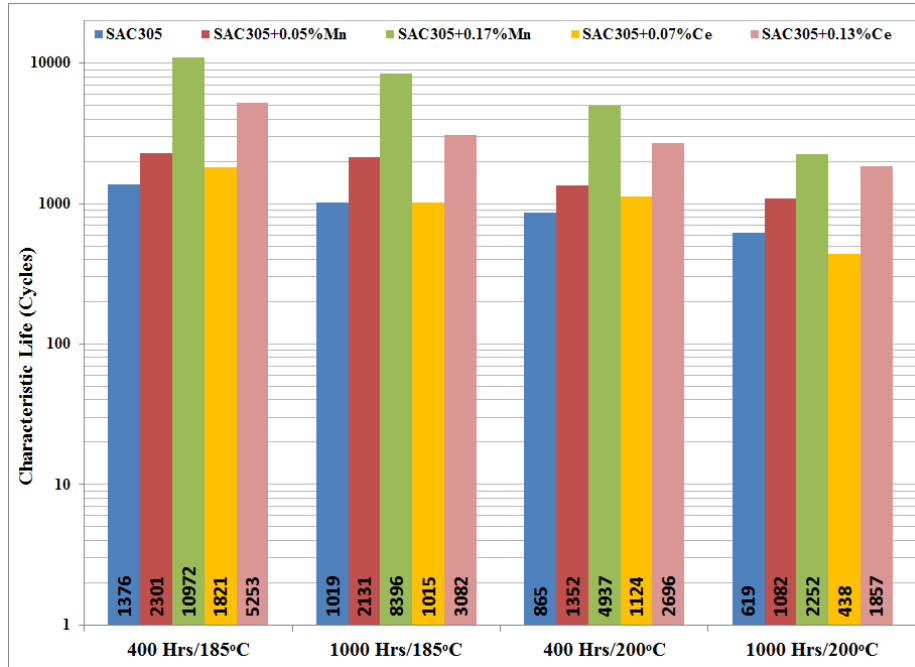


Figure 10-6: QFN44 - Characteristic Life after 400 and 1000 hours of Aging at 185°C and 200°C

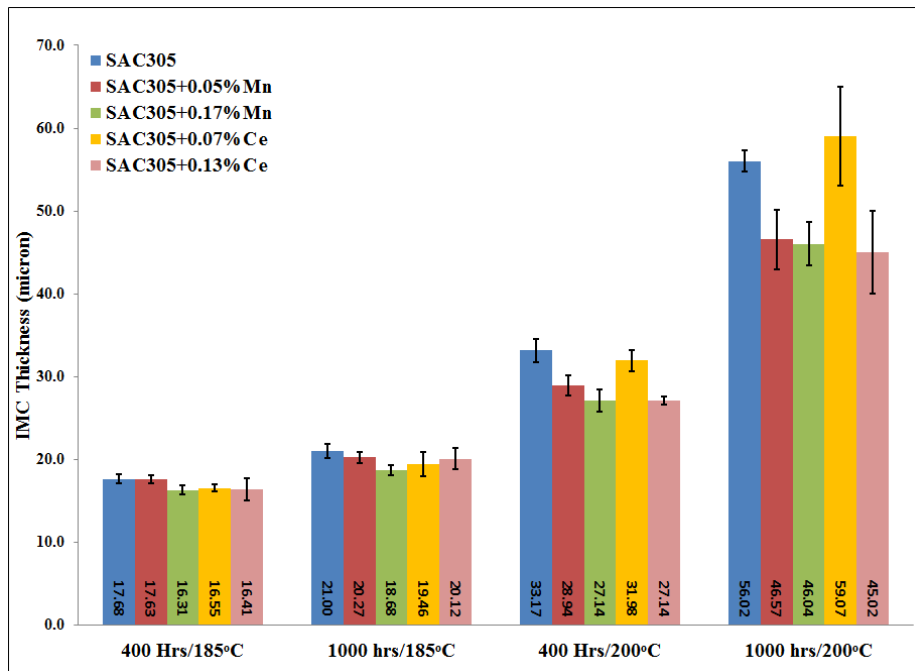


Figure 10-7: QFN44 – Cu<sub>6</sub>Sn<sub>5</sub> IMC Thickness after 400 and 1000 hours of Aging at 185°C and 200°C

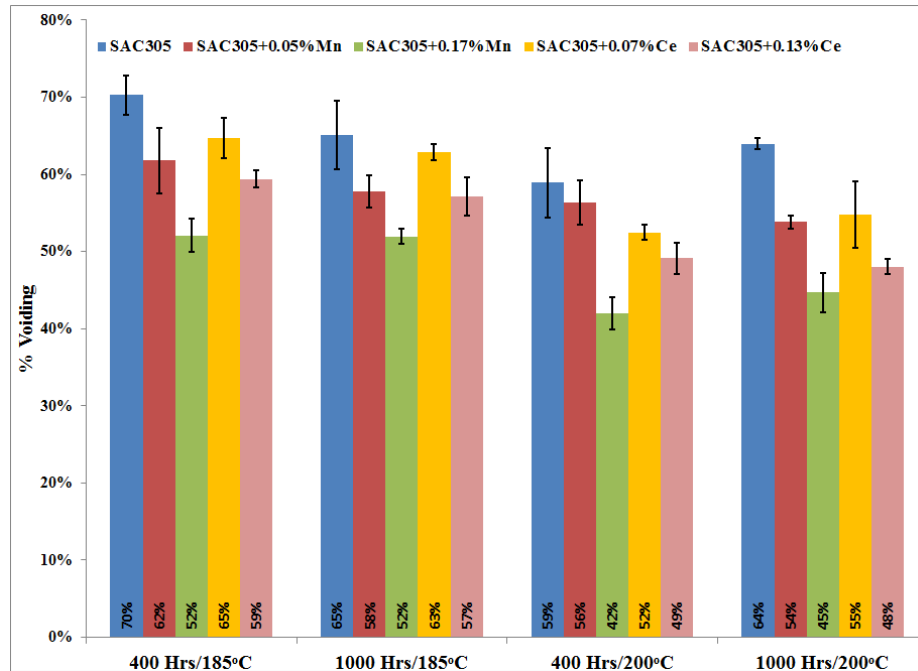


Figure 10-8: QFN44 – % Voiding after 400 and 1000 hours of Aging at 185°C and 200°C

## 10.2. QFN32 - Mechanical Shock Test Results after Thermal Aging at 185°C and 200°C

Similar to QFN44, there were a total of eight QFN32 samples on two test boards for each solder. All eight QFN32 samples failed during 100,000 mechanical shocks. The obtained QFN32 cycles to failure data from mechanical shock test were plotted using Weibull two-parameter distribution and reliability comparison were made.

Figure 10-9 shows Weibull plot for QFN32 after 400 hours aging at 185°C. The extracted Weibull parameters from Weibull analysis are shown in Table 10-10. To perform reliability comparison of selected solders, characteristic life (Weibull scale parameter) was used as a matrix to rank solder performance. Based on characteristic life value, the mechanical shock reliability of selected solders can be ranked in the following order:

High Mn > High Ce > Low Mn > Low Ce  $\geq$  SAC305

All modified SAC305 solders exhibited better mechanical shock reliability than SAC305 after 400 hours of aging at 185°C. High Mn solder showed around 7.0 times better performance than SAC305. Also, High Ce solder showed around 3.6 times better performance than SAC305. Low Mn and Low Ce solders were less effective than High Mn and High Ce; however, they showed improved performance of around 1.5 and 1.1 times than SAC305, respectively. In order to determine if there was a statistically significant difference in the reliability of modified SAC305 solders compared to SAC305, Kruskal-Wallis test was performed.

Table 10-11 shows p-value from Kruskal-Wallis test for all modified SAC305 solders in comparison to SAC305. P-value < 0.05 shows statistically significant difference between two groups. From

Table 10-11, it can be concluded that High Mn and High Ce show a statistically significant difference with SAC305; whereas, no statistically significant difference exists for Low Mn and Low Ce with SAC305.

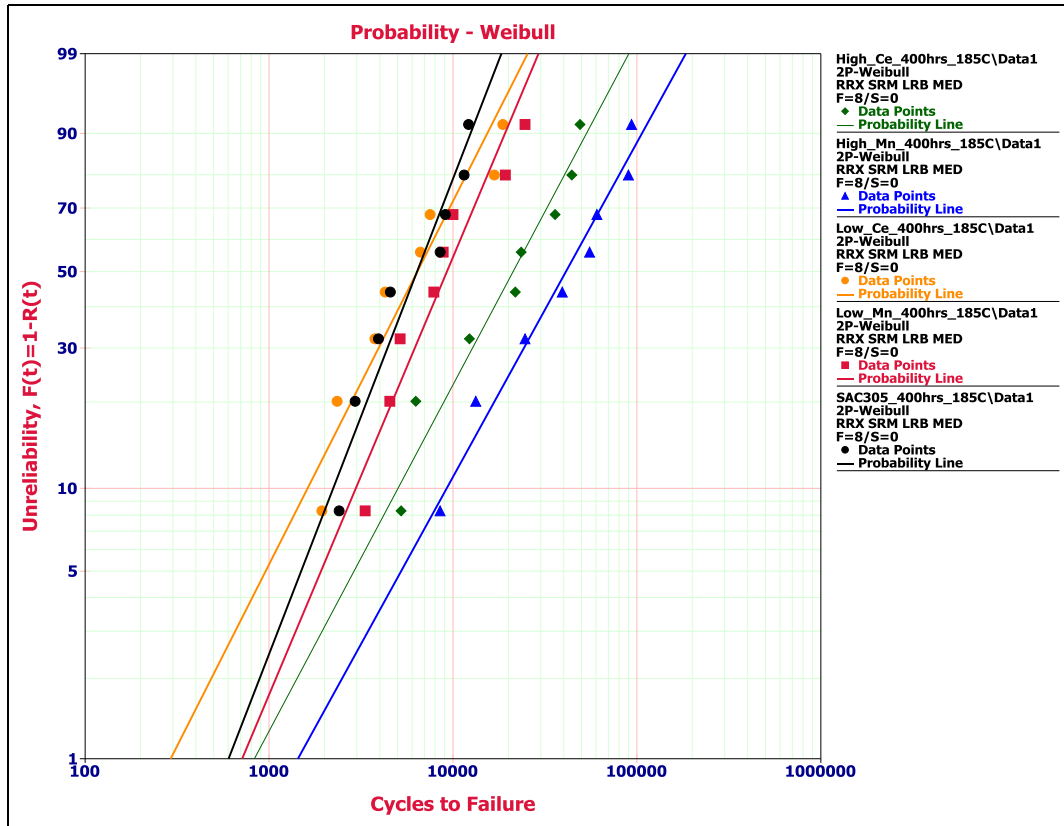


Figure 10-9: QFN32 Weibull Plot - 400 hours of Aging at 185°C

Table 10-10: Weibull Parameters for QFN32 - 400 hours of Aging at 185°C

|  | SAC305 | Low Mn | High Mn | Low Ce | High Ce |
|--|--------|--------|---------|--------|---------|
| $\beta$ (Weibull Slope)                    | 1.79   | 1.65   | 1.26    | 1.37   | 1.31    |
| Cycles to 1% Failure                       | 603    | 714    | 1435    | 292    | 833     |
| Cycles to First Failure                    | 2415   | 3310   | 8545    | 1940   | 5235    |
| Cycles to 50% Failure                      | 6381   | 9272   | 41124   | 6400   | 21232   |
| $\eta$ (Characteristic Life) 63.2% Failure | 7827   | 11575  | 54985   | 8361   | 28104   |
| Improvement in $\eta$ (times)              | -      | 1.5    | 7.0     | 1.1    | 3.6     |
| Rho (Goodness of fit)                      | 0.96   | 0.96   | 0.99    | 0.96   | 0.98    |

Table 10-11: Kruskal-Wallis Test – QFN32 (400 hours of Aging at 185°C)

| p-value for SAC305-X solders from Kruskal-Wallis test in comparison to SAC305 |         |  |
|---|---------|--|
| Solders   | p-value | Does statistical significant difference exist? |
| Low Mn  | 0.401   | No   |
| High Mn   | 0.003   | Yes  |
| Low Ce  | 0.753   | No   |
| High Ce   | 0.012   | Yes  |



Figure 10-10 shows Weibull plot for QFN32 after 1000 hours aging at 185°C. The extracted Weibull parameters from Weibull analysis are shown in Table 10-12. Based on characteristic life value, the mechanical shock reliability of selected solders can be ranked in the following order:

High Mn > High Ce > Low Mn > SAC305 > Low Ce

Except Low Ce solder, all other modified SAC305 solders exhibited better mechanical shock reliability than SAC305 after 1000 hours aging at 185°C. High Mn solder showed around 5.4 times better performance than SAC305. High Ce and Low Mn solders showed around 2.5 and 1.7 times better performance than SAC305 respectively. Low Ce exhibited poorer mechanical shock performance than SAC305. Table 10-13 shows p-value from Kruskal-Wallis test for all modified SAC305 solders in comparison to SAC305. P-value < 0.05 shows statistically significant difference between two groups. From Table 10-13, it can be concluded that High Mn shows statistically significant difference with SAC305; whereas, no statistically significant difference exists for Low Mn, Low Ce, and High Ce with SAC305.

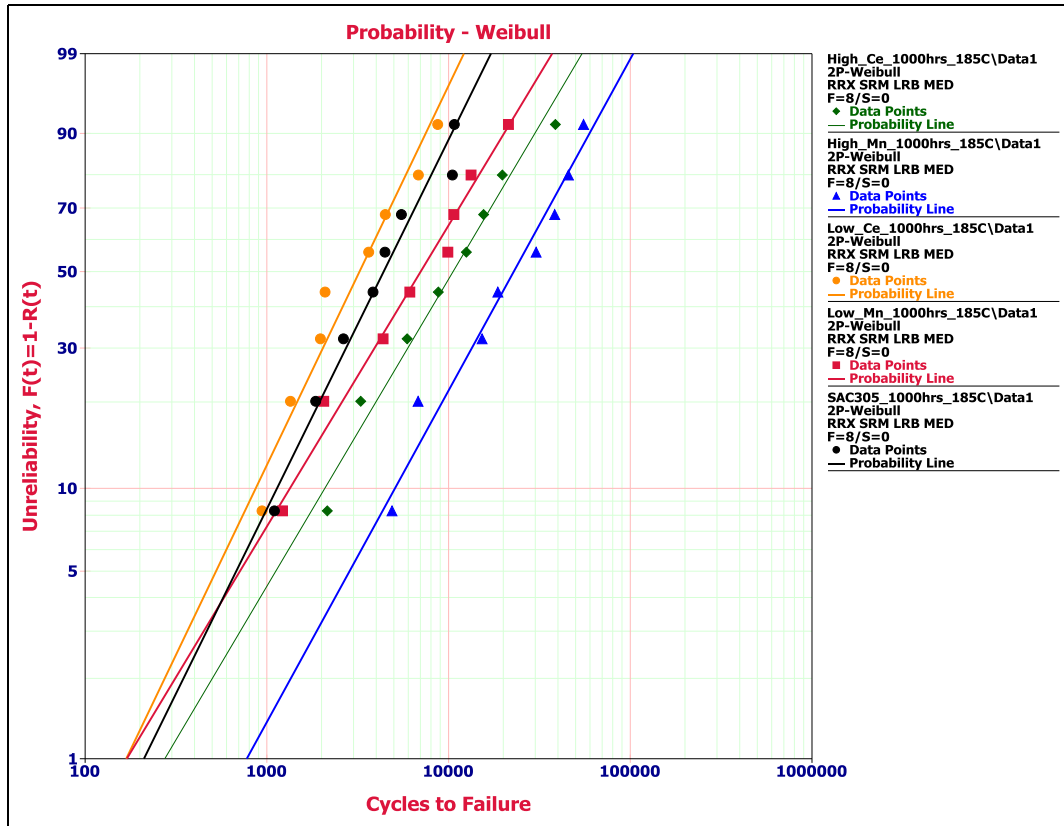


Figure 10-10: QFN32 Weibull Plot - 1000 hours of Aging at 185°C

Table 10-12: Weibull Parameters for QFN32 - 1000 hours of Aging at 185°C

|  | SAC305 | Low Mn | High Mn | Low Ce | High Ce |
|--|--------|--------|---------|--------|---------|
| $\beta$ (Weibull Slope)                    | 1.39   | 1.14   | 1.25    | 1.43   | 1.16    |
| Cycles to 1% Failure                       | 211    | 170    | 776     | 168    | 275     |
| Cycles to First Failure                    | 1105   | 1225   | 4905    | 945    | 2160    |
| Cycles to 50% Failure                      | 4395   | 7023   | 22852   | 3236   | 10589   |
| $\eta$ (Characteristic Life) 63.2% Failure | 5718   | 9694   | 30629   | 4197   | 14527   |
| Improvement in $\eta$ (times)              | -      | 1.7    | 5.4     | 0.7    | 2.5     |
| Rho (Goodness of fit)                      | 0.99   | 0.99   | 0.98    | 0.98   | 0.99    |

Table 10-13: Kruskal-Wallis Test – QFN32 (1000 hours of Aging at 185°C)

| p-value for SAC305-X solders from Kruskal-Wallis test in comparison to SAC305 |         |  |
|---|---------|--|
| Solders   | p-value | Does statistical significant difference exist? |
| Low Mn  | 0.294   | No   |
| High Mn   | 0.005   | Yes  |
| Low Ce  | 0.462   | No   |
| High Ce   | 0.074   | No   |

Figure 10-11 shows Weibull plot for QFN32 after 400 hours aging at 200°C. The extracted Weibull parameters from Weibull analysis are shown in Table 10-14. Based on characteristic life value, the mechanical shock reliability of selected solders can be ranked in the following order:

High Mn > High Ce > Low Mn > SAC305 > Low Ce

Except Low Ce solder, all other modified SAC305 solders exhibited better mechanical shock reliability than SAC305 after 400 hours aging at 200°C. High Mn solder showed around 6.3 times better performance than SAC305. High Ce and Low Mn solders showed around 2.9 and 1.5 times better performance than SAC305, respectively. Low Ce exhibited poorer mechanical shock performance than SAC305.

Table 10-15 shows p-value from Kruskal-Wallis test for all modified SAC305 solders in comparison to SAC305. P-value < 0.05 shows statistically significant difference between two groups. From

Table 10-15, it can be concluded that High Mn and High Ce show statistically significant difference with SAC305; whereas, no statistically significant difference exists for Low Mn and Low Ce with SAC305.

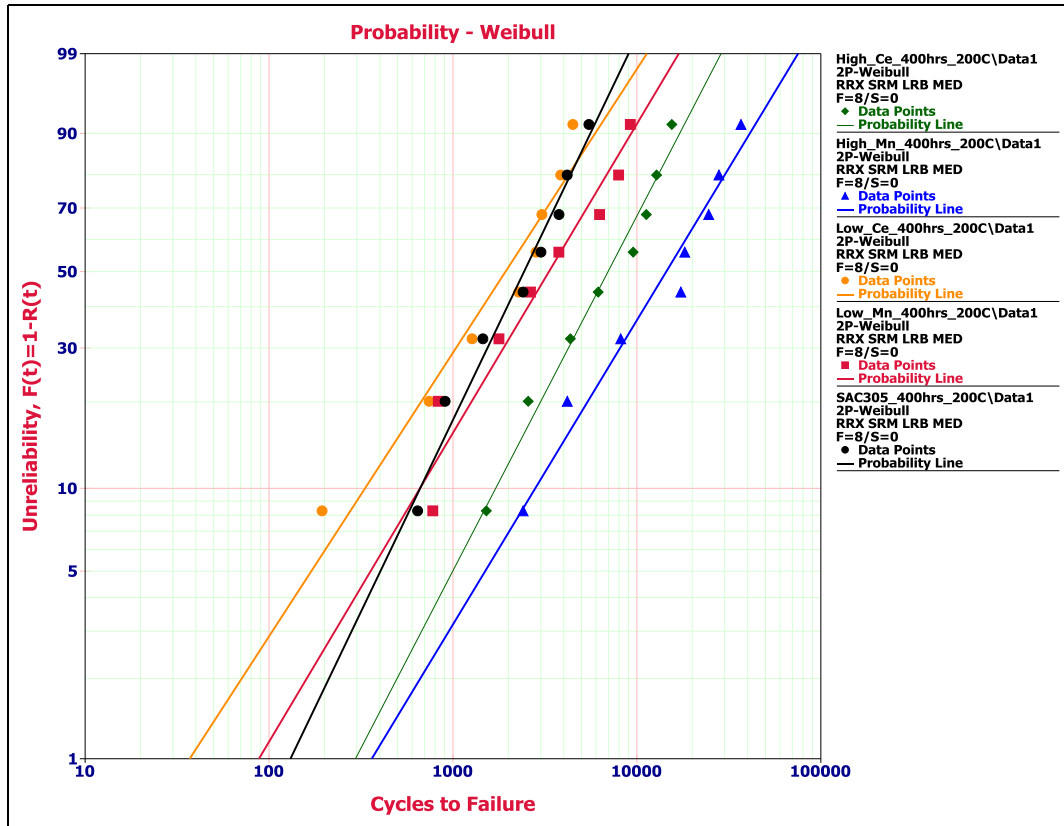


Figure 10-11: QFN32 Weibull Plot - 400 hours of Aging at 200°C

Table 10-14: Weibull Parameters for QFN32 - 400 hours of Aging at 200°C

|  | SAC305 | Low Mn | High Mn | Low Ce | High Ce |
|--|--------|--------|---------|--------|---------|
| $\beta$ (Weibull Slope)                    | 1.45   | 1.17   | 1.15    | 1.07   | 1.34    |
| Cycles to 1% Failure                       | 131    | 88     | 362     | 37     | 295     |
| Cycles to First Failure                    | 645    | 780    | 2415    | 195    | 1525    |
| Cycles to 50% Failure                      | 2436   | 3326   | 14452   | 1932   | 6969    |
| $\eta$ (Characteristic Life) 63.2% Failure | 3138   | 4555   | 19886   | 2721   | 9164    |
| Improvement in $\eta$ (times)              | -      | 1.5    | 6.3     | 0.9    | 2.9     |
| Rho (Goodness of fit)                      | 0.99   | 0.97   | 0.98    | 0.97   | 0.99    |

Table 10-15: Kruskal-Wallis Test – QFN32 (400 hours of Aging at 200°C)

| p-value for SAC305-X solders from Kruskal-Wallis test in comparison to SAC305 |         |  |
|---|---------|--|
| Solders   | p-value | Does statistical significant difference exist? |
| Low Mn  | 0.529   | No   |
| High Mn   | 0.005   | Yes  |
| Low Ce  | 0.674   | No   |
| High Ce   | 0.021   | Yes  |

Figure 10-12 shows Weibull plot for QFN32 after 1000 hours aging at 200°C. The extracted Weibull parameters from Weibull analysis are shown in Table 10-16. Based on characteristic life value, the mechanical shock reliability of selected solders can be ranked in the following order:

High Mn > High Ce > SAC305 > Low Ce > Low Mn

Only High Mn and High Ce solders exhibited better mechanical shock reliability than SAC305. High Mn solder showed around 4.7 times better performance than SAC305. High Ce solders showed around 2.3 better performances than SAC305. Low Mn and Low Ce solders exhibited poorer mechanical shock performance than SAC305.

Table 10-17 shows p-value from Kruskal-Wallis test for all modified SAC305 solders in comparison to SAC305. P-value < 0.05 shows statistically significant difference between two groups. From

Table 10-17, it can be concluded that High Mn shows statistically significant difference with SAC305; whereas, no statistically significant difference exists for Low Mn, Low Ce, and High Ce with SAC305.

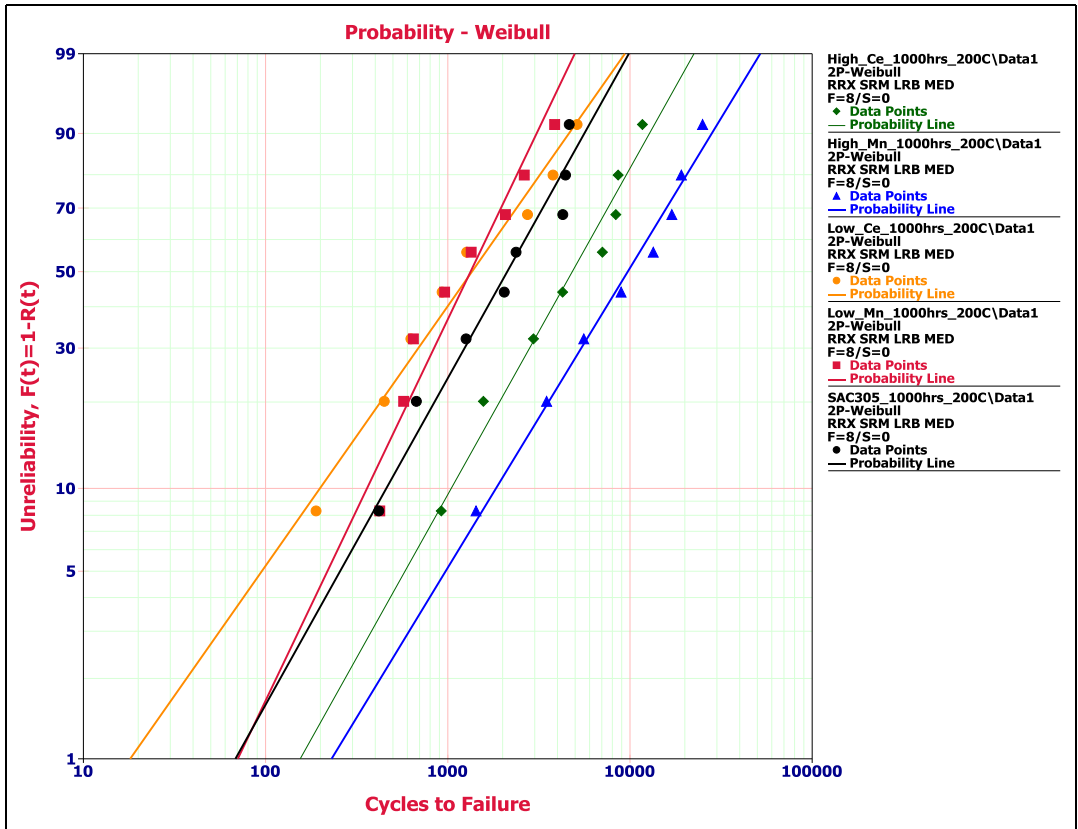


Figure 10-12: QFN32 Weibull Plot - 1000 hours of Aging at 200°C

Table 10-16: Weibull Parameters for QFN32 - 1000 hours of Aging at 200°C

|  | SAC305 | Low Mn | High Mn | Low Ce | High Ce |
|--|--------|--------|---------|--------|---------|
| $\beta$ (Weibull Slope)                    | 1.23   | 1.44   | 1.13    | 0.98   | 1.23    |
| Cycles to 1% Failure                       | 68     | 70     | 230     | 18     | 155     |
| Cycles to First Failure                    | 420    | 425    | 1435    | 190    | 925     |
| Cycles to 50% Failure                      | 2120   | 1334   | 9725    | 1358   | 4824    |
| $\eta$ (Characteristic Life) 63.2% Failure | 2854   | 1722   | 13446   | 1974   | 6497    |
| Improvement in $\eta$ (times)              | -      | 0.6    | 4.7     | 0.7    | 2.3     |
| Rho (Goodness of fit)                      | 0.98   | 0.97   | 0.99    | 0.99   | 0.99    |

Table 10-17: Kruskal-Wallis Test – QFN32 (1000 hours of Aging at 200°C)

| p-value for SAC305-X solders from Kruskal-Wallis test in comparison to SAC305 |         |  |
|---|---------|--|
| Solders   | p-value | Does statistical significant difference exist? |
| Low Mn  | 0.294   | No   |
| High Mn   | 0.012   | Yes  |
| Low Ce  | 0.462   | No   |
| High Ce   | 0.115   | No   |

### **10.2.1. Discussion on QFN32 Mechanical Shock Test Results**

For QFN32, the characteristic life data obtained from Weibull analysis for all solders after 400 and 1000 hours of aging at 185°C and 200°C are compiled, as shown in Figure 10-13. Due to large variation in characteristic life of solders, Y axis of Figure 10-13 uses logarithmic scale. From Figure 10-13, it can be noticed that with time and temperature increase, reduction in the characteristic life of solders under mechanical shock testing is quite evident. This finding is similar to QFN44, as discussed previously. Thus, it can be concluded that high temperature aging substantially reduces the mechanical shock reliability of selected solders.

High Mn solder outperformed and resulted in the highest mechanical shock reliability at all intervals. It showed performance improvement of 7.0 to 4.7 times to SAC305 during mechanical shock testing. High Ce solder was found to be the second most effective solder with performance improvement of 3.6 to 2.3 times to SAC305. Low Mn solder seems to perform well during 185°C aging and resulted in performance improvement of 1.7 to 1.5 times SAC305; however, its mechanical shock reliability is reduced especially after 1000 hours of aging at 200°C. Low Ce solder performed comparable to SAC305 after 400 hours of aging at 185°C; however, with an extended aging exposure at 185°C and further increase in aging temperature to 200°C, Low Ce solder resulted in the lowest mechanical shock reliability with respect to SAC305.

In general, High Mn and High Ce solders performed far better than SAC305 solder after 400 and 1000 hours of aging at 185°C and 200°C. Low Mn solder performed better than SAC305 at 185°C aging; however, it performs either equivalent or lower than SAC305 at 200°C aging. Low Ce exhibited lower mechanical shock reliability

than SAC305 during 200°C aging. Characteristic life comparison between all modified SAC305 solders and SAC305 is shown in Table 10-18.

Table 10-18: QFN32 - Characteristic Life Comparison

| Solders        | Characteristic Life Improvement Compared to SAC305 |                  |
|----------------|--|------------------|
|                | 185°C Aging  | 200°C Aging      |
| SAC305+0.17%Mn | 7.0 to 5.4 times                                   | 6.3 to 4.7 times |
| SAC305+0.13%Ce | 3.6 to 2.5 times                                   | 2.9 to 2.3 times |
| SAC305+0.05%Mn | 1.7 to 1.5 times                                   | 1.5 to 0.6 times |
| SAC305+0.07%Ce | 1.1 to 0.7 times                                   | 0.9 to 0.7 times |

In order to correlate the mechanical shock reliability to  $\text{Cu}_6\text{Sn}_5$  interfacial IMC and interfacial voiding, the results of  $\text{Cu}_6\text{Sn}_5$  interfacial IMC growth and %voiding measured from QFN32 for all solders after 400 and 1000 hours of aging at 185°C and 200°C are summarized as shown in Figure 10-14 and Figure 10-15, respectively. By carefully comparing the results from Figure 10-13, Figure 10-14, and Figure 10-15, similar to QFN44, a correlation of mechanical shock reliability with  $\text{Cu}_6\text{Sn}_5$  interfacial IMC and interfacial voiding can be found. For example, High Mn and High Ce solders showed thinner  $\text{Cu}_6\text{Sn}_5$  interfacial IMC and lower interfacial voiding resulted higher mechanical shock reliability. For Low Mn solder, higher voiding was observed after 1000 hours aging at 200°C which might be the reason for lower mechanical shock reliability. For Low Ce solder, excessive thickness of  $\text{Cu}_6\text{Sn}_5$  interfacial IMC at 185°C and 200°C aging seems like the reason for poor reliability in mechanical shock.



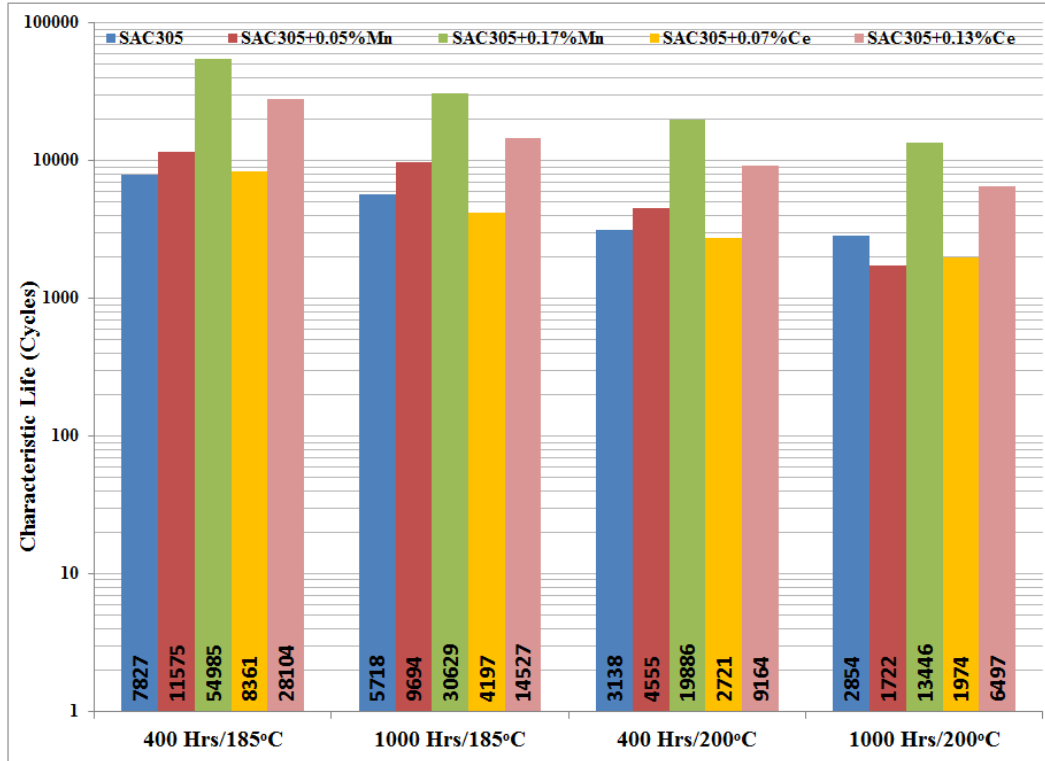


Figure 10-13: QFN32 - Characteristic Life after 400 and 1000 hours of Aging at 185°C and 200°C

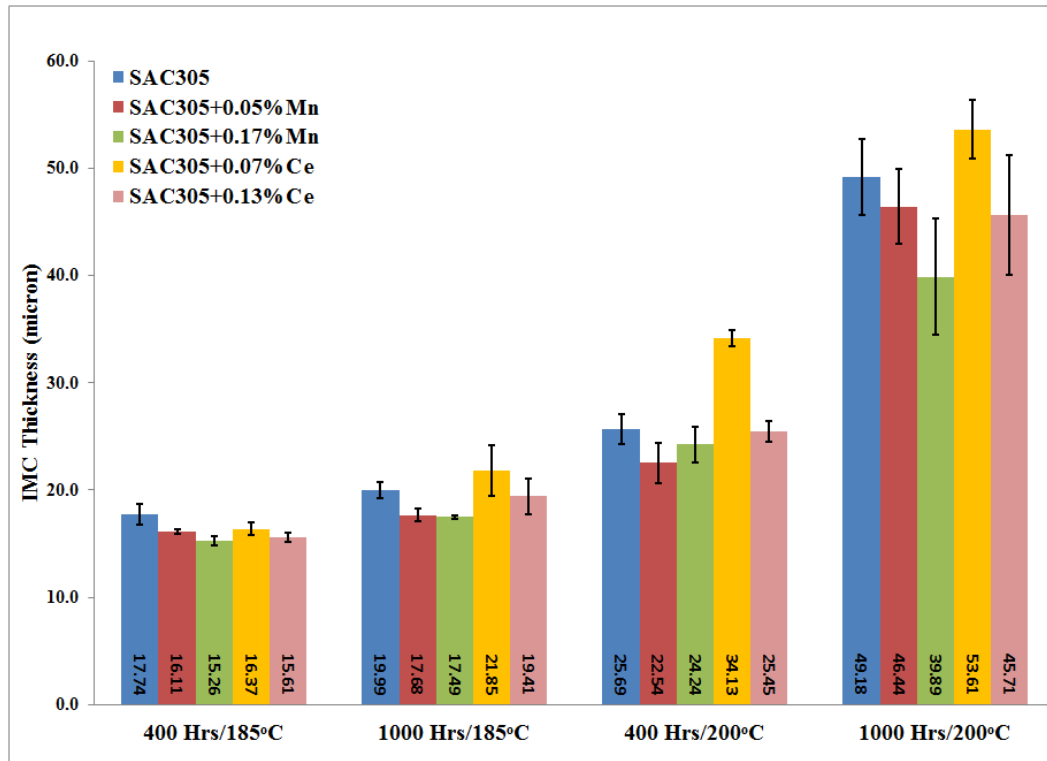


Figure 10-14: QFN32 – Cu<sub>6</sub>Sn<sub>5</sub> IMC Thickness after 400 and 1000 hours of Aging at 185°C and 200°C

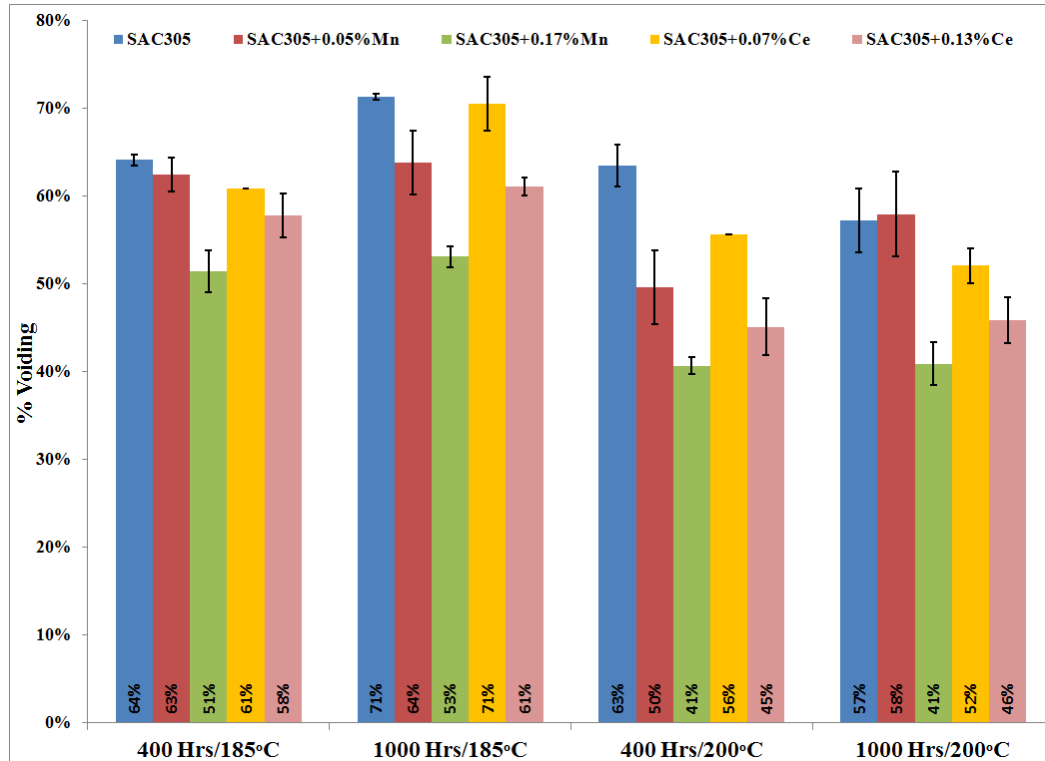


Figure 10-15: QFN32 – % voiding after 400 and 1000 hours of Aging at 185°C and 200°C

### 10.3. QFP256 - Mechanical Shock Test Results after Thermal Aging at 185°C and 200°C

A total of four QFP256 samples were tested on two boards for each solder after 400 and 1000 hours of aging at 185°C and 200°C. All four QFP256 samples failed during 100,000 mechanical shocks. Due to a sample size of only four, rather than comparing solder performance through Weibull two-parameter distribution, it was decided to bin the number of failed packages into four different mechanical shock ranges based on their cycles-to-failure data. Table 10-19 shows all four QFP256 samples for all five solders at each time and temperature interval segregated into four mechanical shock ranges. It is important to note that mechanical shock range intervals were determined such that four QFPs can be binned into intervals so that easy comparison can be made

between solders. Due to wide variation in time-to-failure for QFPs among various aging time and temperature conditions, the selected interval values of mechanical shock ranges are also different.

From Table 10-19, solder performance comparison can be made by ranking each solder. Based on the lifetime of QFP256 samples, all selected solders can be ranked in the following orders at various aging time and temperature intervals tested.

For 400 hours aging at 185°C, solder ranking is:

High Mn > High Ce > SAC305 > Low Mn > Low Ce

For 1000 hours aging at 185°C, solder ranking is:

High Mn > High Ce > Low Mn > Low Ce > SAC305

For 400 hours aging at 200°C, solder ranking is:

High Mn > High Ce = Low Mn > SAC305 > Low Ce

For 1000 hours aging at 200°C, solder ranking is:

High Mn > High Ce > Low Mn > SAC305 = Low Ce

It appears that High Mn and High Ce solders performed better than the remaining three solders. High Mn and High Ce solders maintained their first and second performance ranking, respectively, as previously seen with QFN44 and QFN32 package types. For the most part, Low Mn solder performed better than SAC305 solder. SAC305 and Low Ce solders showed poor mechanical shock reliability. Due to lack of information on interfacial IMC growth and interfacial %voiding data during thermal aging for QFP256, a correlation between mechanical shock and interfacial

IMC and void cannot be confirmed. However, the lead material and lead finish of QFP256 were same as QFN44 and QFN32 package types, thus a similar correlation can be expected for QFP256 as observed for QFN44 and QFN32.

Table 10-19: QFP256 - Mechanical Shock Test Result Summary after 400 and 1000 hours of Aging at 185°C and 200°C

| Time/<br>Temperature<br>Interval | Mechanical<br>Shock<br>Range | # of QFP256 Failure |        |         |        |         |
|----------------------------------|------------------------------|---------------------|--------|---------|--------|---------|
|                                  |                              | SAC305              | Low Mn | High Mn | Low Ce | High Ce |
| 400 Hrs<br>/185°C                | 1 - 10000                    | 1                   | 2      | 0       | 2      | 1       |
|                                  | 10001 - 25000                | 1                   | 1      | 1       | 2      | 0       |
|                                  | 25001 - 50000                | 2                   | 1      | 1       | -      | 2       |
|                                  | 50001 - 100000               | -                   | -      | 2       | -      | 1       |
| 1000 Hrs<br>/185°C               | 1 - 2000                     | 1                   | 0      | 0       | 0      | 0       |
|                                  | 2001 - 10000                 | 2                   | 2      | 1       | 3      | 2       |
|                                  | 10001 - 25000                | 1                   | 2      | 2       | 1      | 1       |
|                                  | 25001 - 100000               | -                   | -      | 1       | -      | 1       |
| 400 Hrs<br>/200°C                | 1 - 1000                     | 1                   | 0      | 0       | 1      | 0       |
|                                  | 1001 - 5000                  | 3                   | 2      | 1       | 2      | 2       |
|                                  | 5001 - 15000                 | -                   | 2      | 2       | 1      | 2       |
|                                  | 15001 - 100000               | -                   | -      | 1       | -      | -       |
| 1000 Hrs<br>/200°C               | 1 - 500                      | 1                   | 0      | 0       | 1      | 0       |
|                                  | 501 - 2000                   | 2                   | 3      | 1       | 2      | 3       |
|                                  | 2001 - 3500                  | 1                   | 1      | 2       | 1      | 0       |
|                                  | 3501 - 100000                | -                   | -      | 1       | -      | 1       |

#### 10.4. R2512 and R2010 - Mechanical Shock Test Results after Thermal Aging at 185°C and 200°C

Two test boards for each solder comprise total 16 samples of R2512 and R2010 package types. During 100,000 mechanical shocks, only few R2512 and R2010 failed. Due to the limited number of failed samples, solder comparison were made by comparing number of failed samples during 100,000 mechanical shocks.

**10.4.1. R2512 Mechanical Shock Test Results after Thermal Aging at 185°C and 200°C**

Out of 16 R2512 samples tested, only a few R2512 failed during 100,000 mechanical shocks at each aging time and temperature interval, as shown Table 10-20. Green label indicates no failure, blue label indicates 1 to 2 failures; whereas, red label indicates 4 to 6 failures. High Mn solder had no failures at any aging intervals in mechanical shocks. Low Mn and High Ce solders performed well with no failures except after 1000 hours aging at 200°C. Low Mn solder resulted lesser failure than High Ce solder. High Ce solder exhibited sudden increased failure after 1000 hours of aging at 200°C. Failure analysis is required to find the causes of such unexpected behavior of High Ce solder. Both Low Ce and SAC305 solders showed gradual increase in failure during mechanical shock with increase of aging time and temperatures. SAC305 had the highest number of package failures compared to other solders. Based on the total number of R2512 failure, all solders can be ranked in the following orders:

High Mn > Low Mn > High Ce > Low Ce > SAC305

Table 10-20:R2512 - Mechanical Shock Test Result Summary after 400 and 1000 hours of Aging at 185°C and 200°C

| <b>Time/<br/>Temperature<br/>Interval</b> | <b>SAC305</b> | <b>Low Mn</b> | <b>High Mn</b> | <b>Low Ce</b> | <b>High Ce</b> |
|---|---------------|---------------|----------------|---------------|----------------|
| 400<br>Hrs/185°C                          | 0/16          | 0/16          | 0/16           | 0/16          | 0/16           |
| 1000<br>Hrs/185°C                         | 1/16          | 0/16          | 0/16           | 1/16          | 0/16           |
| 400<br>Hrs/200°C                          | 2/16          | 0/16          | 0/16           | 1/16          | 0/16           |
| 1000<br>Hrs/200°C                         | 6/16          | 2/16          | 0/16           | 4/16          | 5/16           |

In order to find the correlation between package failure and interfacial IMCs for R2512, both the board and the component side interfacial IMC thickness measured for R2512 for all solders after 400 and 1000 hours of aging at 185°C and 200°C are summarized, as shown in Figure 10-16 and Figure 10-17, respectively. It is important to note that the board side interfacial IMC thickness measurement at 400 and 1000 hours shows large variation due to four IMC layers growth as a result of Ni layer consumption discussed previously in chapter 9. By carefully comparing results from Table 10-20, Figure 10-16 and Figure 10-17, there seems to be a correlation between R2512 failure and interfacial IMCs. More specifically, for R2512 samples aged at 185°C, it appears that R2512 failure is correlated to both the board and the component side interfacial IMCs since the solder that showed higher IMC growth also resulted in an increased number of R2512 failures during mechanical shock testing. For R2512 aged at 200°C, Ni layer consumption occurred on the board side for all solders except High Mn resulting in significant variation in the board side interfacial IMC thickness among five solders. It can be seen that R2512 failure trend follows the board side IMC growth trend quite well compared to the component side IMC growth trend. Thus, it can be concluded that for R2512 exposed to 200°C aging, the board side interfacial IMC growth plays an important role in solder interconnect reliability.

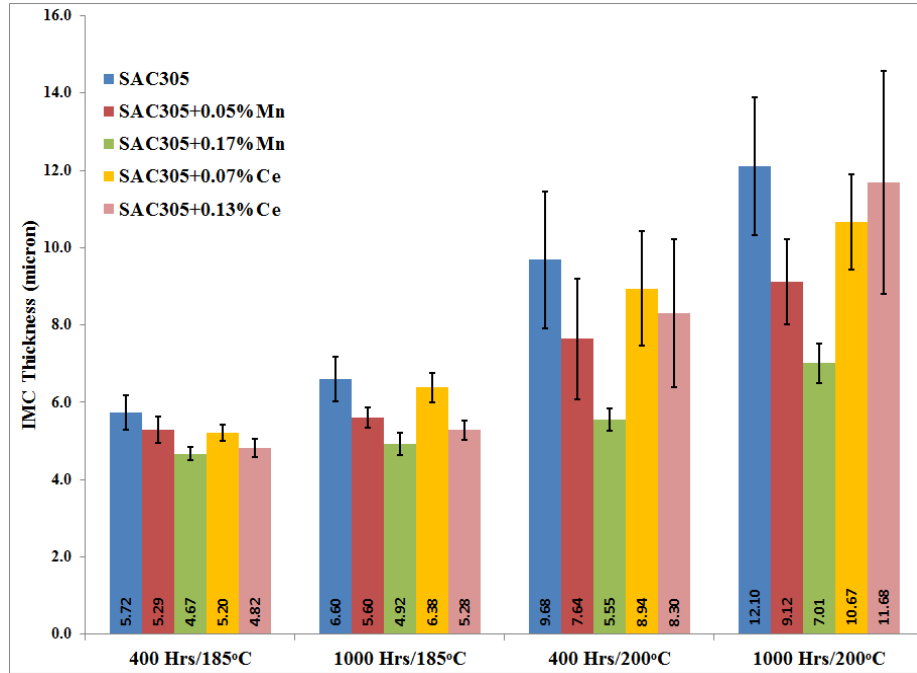


Figure 10-16: R2512 – Ni-Cu-Sn Board Side Interfacial IMC Thickness after 400 and 1000 hours of Aging at 185°C and 200°C

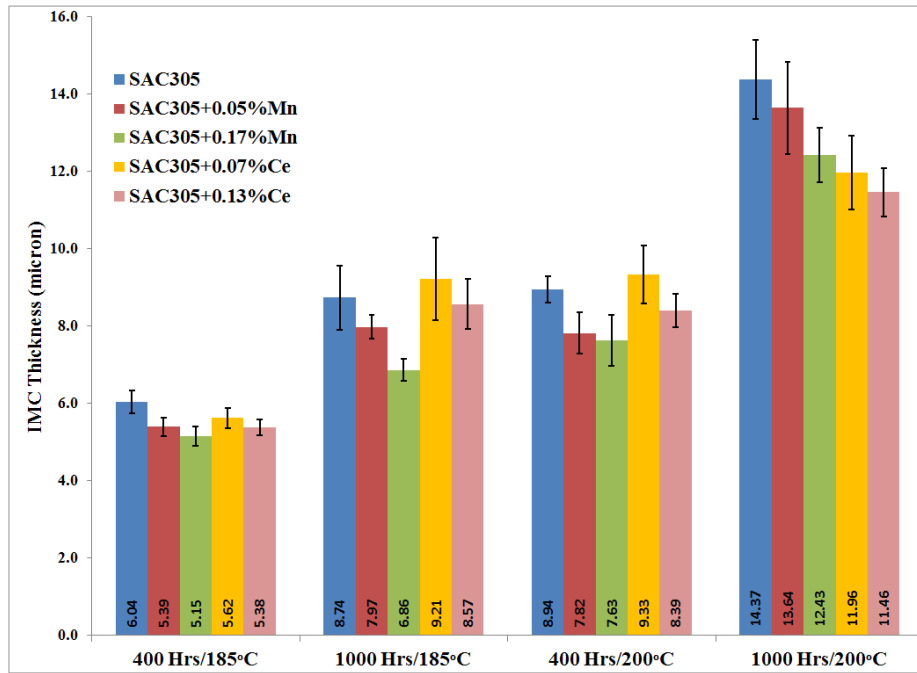


Figure 10-17: R2512 – (Ni,Cu)<sub>3</sub>Sn<sub>4</sub> Component Side Interfacial IMC Thickness after 400 and 1000 hours of Aging at 185°C and 200°C

**10.4.2. R2010 Mechanical Shock Test Results after Thermal Aging at 185°C and 200°C**

Similar to R2512, out of 16 R2010 samples tested, only a few R2010 failed during 100,000 mechanical shocks at aging time and temperature intervals as shown Table 10-21. Green label indicates no failure, blue label indicates 1 to 2 failures; whereas, red label indicates 4 to 6 failures. High Mn solder outperformed having no failure in mechanical shocks at any aging intervals. High Ce solder performed well with no failure except 1000 hours aging at 200°C. Low Mn solder performed well at 185°C aging; however, its performance slightly degraded at 200°C aging. Both Low Ce and SAC305 solders showed a gradual increase in failure during mechanical shock with increase of aging time and temperatures. SAC305 had the highest number of failures compared to other solders. Based on the total number of R2010 failure, all solders can be ranked in the following orders:

$$\text{High Mn} > \text{High Ce} \geq \text{Low Mn} > \text{Low Ce} > \text{SAC305}$$

Table 10-21: R2010 - Mechanical Shock Test Result Summary after 400 and 1000 hours of Aging at 185°C and 200°C

| <b>Time/<br/>Temperature<br/>Interval</b> | <b>SAC305</b> | <b>Low Mn</b> | <b>High Mn</b> | <b>Low Ce</b> | <b>High Ce</b> |
|---|---------------|---------------|----------------|---------------|----------------|
| 400 Hrs/185°C                             | 0/16          | 0/16          | 0/16           | 0/16          | 0/16           |
| 1000 Hrs/185°C                            | 1/16          | 0/16          | 0/16           | 1/16          | 0/16           |
| 400 Hrs/200°C                             | 2/16          | 1/16          | 0/16           | 2/16          | 0/16           |
| 1000 Hrs/200°C                            | 5/16          | 1/16          | 0/16           | 2/16          | 2/16           |

Due to lack of the board and the component side interfacial IMC growth data during thermal aging for R2010, a correlation between mechanical shock and interfacial IMC



cannot be established. However, R2512 and R2010 packages were identical except package size, thus a similar correlation can be expected for R2010, as observed for R2512.

### **10.5. Time=0 Test Boards - Mechanical Shock Test Results**

For a baseline, Time=0 (un-aged) test boards were also tested under mechanical shocks. Without any aging, Time=0 test boards were expected to last longer than thermally aged test boards under mechanical shocks. Thus, Time=0 boards were subjected to 600,000 mechanical shocks. For a baseline test, a total of 10 test boards (two boards per solder for five solders) were tested for 600,000 mechanical shocks. For each solder, the two test boards featured eight QFN44 samples, eight QFN32 samples, four QFP256 samples, sixteen R2512 samples and sixteen R2010 samples.

Even after 600,000 mechanical shocks, it was found that only a few components failed. The large package types such as QFP256 and QFN44 failed much earlier than small package types such as QFN32, R2512 and R2010. The failure summary of various package types during 600,000 mechanical shocks is presented in Table 10-22. Based on cycles to failure detail for all package types, an additional summary of cycles to failure for all package types within first 100,000 mechanical shocks is also presented, as shown in Table 10-23. Green label indicates no failure, blue label indicates 1 to 3 failures; whereas, red label indicates 4 or more failures.

Table 10-22: Failure Summary of various Package Types (Time=0) during 600,000 Mechanical Shocks

| Packages | SAC305 | Low Mn | High Mn | Low Ce | High Ce |
|----------|--------|--------|---------|--------|---------|
| QFN44    | 5/8    | 2/8    | 1/8     | 3/8    | 2/8     |
| QFN32    | 1/8    | 0/8    | 0/8     | 1/8    | 0/8     |
| QFP256   | 4/4    | 4/4    | 4/4     | 4/4    | 4/4     |
| R2512    | 3/16   | 0/16   | 0/16    | 0/16   | 0/16    |
| R2010    | 4/16   | 2/16   | 0/16    | 2/16   | 0/16    |

Table 10-23: Failure of various Package Types (Time=0) during 100,000 Mechanical Shocks

| Packages | SAC305 | Low Mn | High Mn | Low Ce | High Ce |
|----------|--------|--------|---------|--------|---------|
| QFN44    | 1/8    | 0/8    | 0/8     | 1/8    | 0/8     |
| QFN32    | 0/8    | 0/8    | 0/8     | 0/8    | 0/8     |
| QFP256   | 4/4    | 3/4    | 2/4     | 3/4    | 3/4     |
| R2512    | 0/16   | 0/16   | 0/16    | 0/16   | 0/16    |
| R2010    | 0/16   | 0/16   | 0/16    | 0/16   | 0/16    |

Based on the test results presented in Table 10-22 and Table 10-23, it can be seen that the QFP256 package failed much earlier than other package types during mechanical shock testing. This was unexpected because QFP256 features gullwing leads that add compliance to the package. During thermal fatigue (thermal cycling), gullwing leads help to reduce stress and strain to solder joint and thus improve thermal fatigue reliability. However, based on the finding from mechanical shock test, it can be concluded that the heavy mass of QFP256 adversely affects the solder joint reliability under mechanical shocks. By comparing package failure from Table 10-22 and Table 10-23, all solders can be ranked in the following orders:

High Mn > High Ce > Low Mn > Low Ce > SAC305

To find a correlation between interfacial IMC and package failure detail from Time=0 mechanical shock test, the interfacial IMC thickness measurement after reflow for QFN44, QFN32 and R2512 are extracted and presented, as shown in Figure 10-18. By carefully comparing the results from Table 10-22, Table 10-23 and Figure 10-18, it can be concluded that no correlation exists between interfacial IMC and package failure for as-reflowed package types. Thus, interfacial IMC formed after reflow is not responsible for solder interconnect failure during mechanical shock test. In such situation, mechanical properties of bulk solder, number of  $\beta$ -tin grains, size and distribution of bulk IMCs play an important role for solder failure under mechanical shock stress conditions.

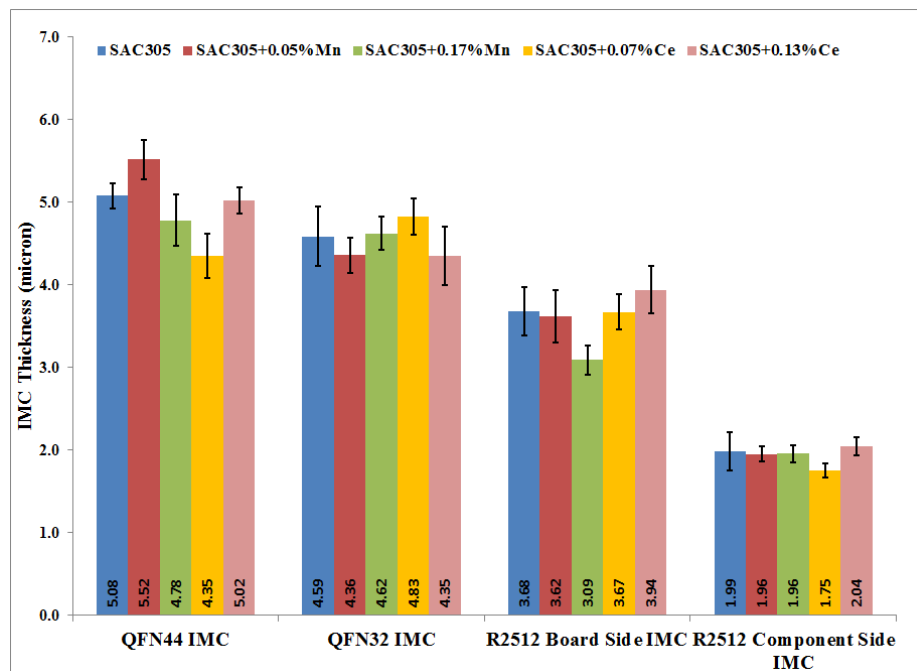


Figure 10-18: Interfacial IMC Thickness Measurement after Reflow of QFN44  $\text{Cu}_6\text{Sn}_5$  IMC on Component Side, QFN32  $\text{Cu}_6\text{Sn}_5$  IMC on Component Side, R2512  $(\text{Ni,Cu})_3\text{Sn}_4$  IMC on Board Side, R2512  $(\text{Ni,Cu})_3\text{Sn}_4$  IMC on Component Side

## 10.6. Failure Analysis

The objective of failure analysis was to determine the differences in the failure mode due to different solder composition. The components that failed during mechanical shock test but were still attached to the board after completion of mechanical shock testing were further analyzed. After performing electrical probing and optical inspection on failed components, these components were carefully removed from the board, cold mounted, cross-sectioned, and further analyzed under an ESEM.

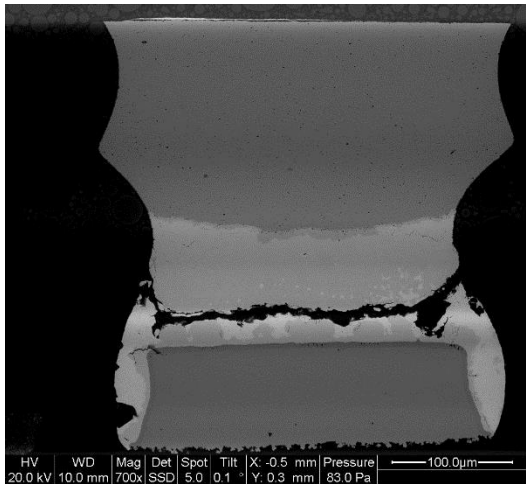
Two package types were selected for failure analysis. One was the QFN44 package and the other was the R2512 package. The failure analysis detail of both package types for all five solders is discussed next.

### 10.6.1. SAC305 Solder

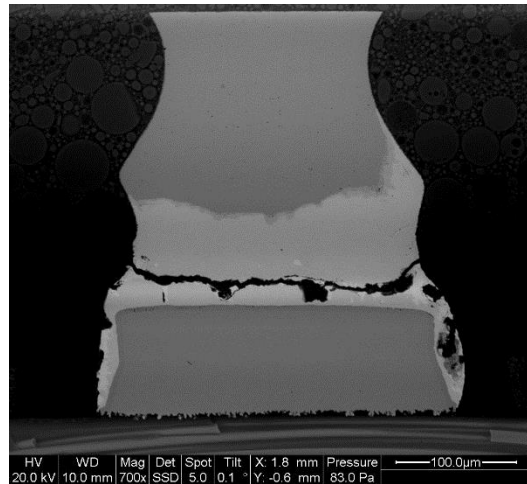
Figure 10-19 shows failed SAC305 solder joints in QFN44 and R2512 packages. Figure 10-19 (a) and Figure 10-19 (b) show failed QFN44 in mechanical shock after 1000 hours of aging at 200°C. Both failed solder joints confirm that failure occurred at the interface between  $\text{Cu}_6\text{Sn}_5$  interfacial IMC and the bulk solder. This type of failure mode was consistent for all failed SAC305 solder joint in QFNs. The voids developed during high temperature thermal aging at the interface between  $\text{Cu}_6\text{Sn}_5$  interfacial IMC and the bulk solder reduced the interfacial strength. During mechanical shock, a crack developed at high stress concentration region. This crack propagated through a weak interface connecting interfacial voids and caused complete separation between the component side interfacial IMC and the bulk solder.

This finding confirms the lower mechanical shock reliability of SAC305 solder observed in QFNs after high temperature aging exposure.

For R2512 package, a failed SAC305 solder joint is shown Figure 10-19 (c). The failure mode for R2512 package was crack propagation at the board side interface region. Figure 10-19 (c) shows four IMC layers on the board side after 1000 hours of aging at 200°C. The magnified view is also shown in Figure 10-19 (d). As discussed previously, the four layer phenomenon was related to Ni layer consumption during 200°C aging. The development of four layers on the board side caused substantial reduction in the interfacial strength. During mechanical shock, a crack can easily initiate at any weak point on this layer and quickly propagate through the interface to cause complete separation of component from the board. This confirms a large number of R2512 package failures for SAC305 solder in mechanical shock testing. This finding also confirms that four IMC layers developed during 200°C aging causes considerable reduction in mechanical shock reliability of solder joint.



(a)



(b)

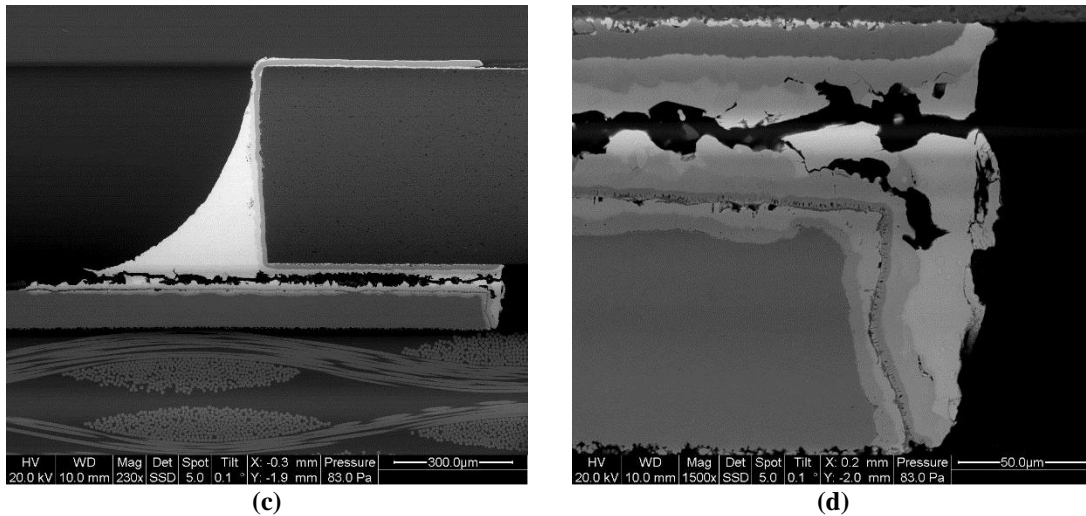


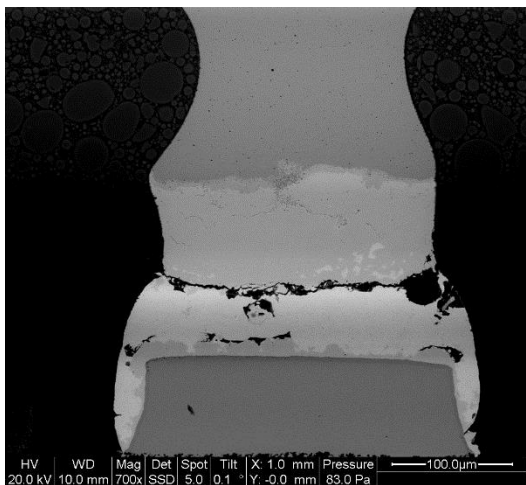
Figure 10-19: SAC305 Solder Failure during Mechanical Shock Test (a) QFN44 – 1000 hours/200°C Aging (b) Additional QFN44 - 1000 hours/200°C Aging (c) R2512 - 1000 hours/200°C Aging (d) Magnified view of R2512 Crack

### 10.6.2. Low Mn Solder

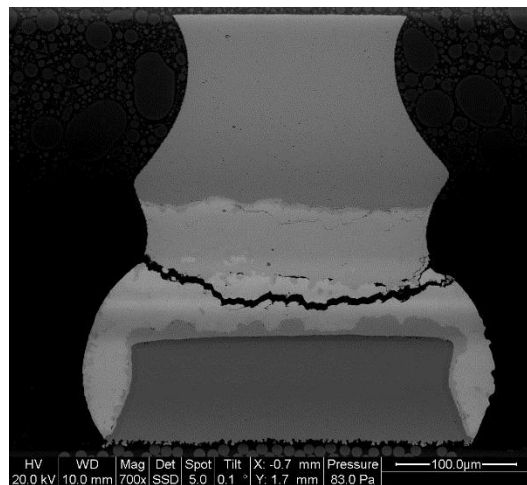
Figure 10-20 shows failed SAC305+0.05%Mn solder joints in QFN44 and R2512 packages. Figure 10-20 (a) and Figure 10-20 (b) show the solder joint of failed QFN44 in mechanical shock after 1000 hours of aging at 200°C. During failure analysis, an interesting finding was observed for Low Mn solder. Two types of failure modes were found for Low Mn solder in QFN44 package. The first one was pure interfacial failure as shown in Figure 10-20 (a). This failure mode was similar to as observed in SAC305 solder. Second type of failure mode was mixed mode where a crack propagated through the interface and solder bulk. The failure caused by mixed mode is shown in Figure 10-20 (b). For Low Mn solder, only a few solder joints showed the mixed type of failure mode. Most of the solder joints failed by pure interfacial failure. It is important to note that mixed mode failure indicates a stronger interface. A crack takes a longer time to propagate for mixed mode compared to pure interfacial mode and thus the solder joint can last longer. The evidence of mixed

mode failure in addition to pure interfacial failure confirms better performance of Low Mn solder in mechanical shock testing compared to SAC305 solder.

The failed R2512 Low Mn solder joint is shown Figure 10-20 (c). The magnified view of the crack in R2512 can be seen from Figure 10-20 (d). Low Mn solder joint showed a few spots of Ni layer consumption. Four IMCs can be seen within each spot; however, these spots did not merge and form layers. A crack was initiated underneath the package, propagated through the board side interface until it reached to Ni termination bend in vertical direction. Due to higher resistance to continued crack propagation through the interface region, the crack propagated vertically following component side interfacial IMC and eventually cracked through solder bulk, causing complete separation. This type of crack propagation usually takes a longer time to cause a failure compared to crack propagation in severely consumed Ni layer as previously observed in SAC305 solder joint. This is believed be the reason for lower resistor package failure for Low Mn solder in mechanical shock testing compared to SAC305 solder.



(a)



(b)

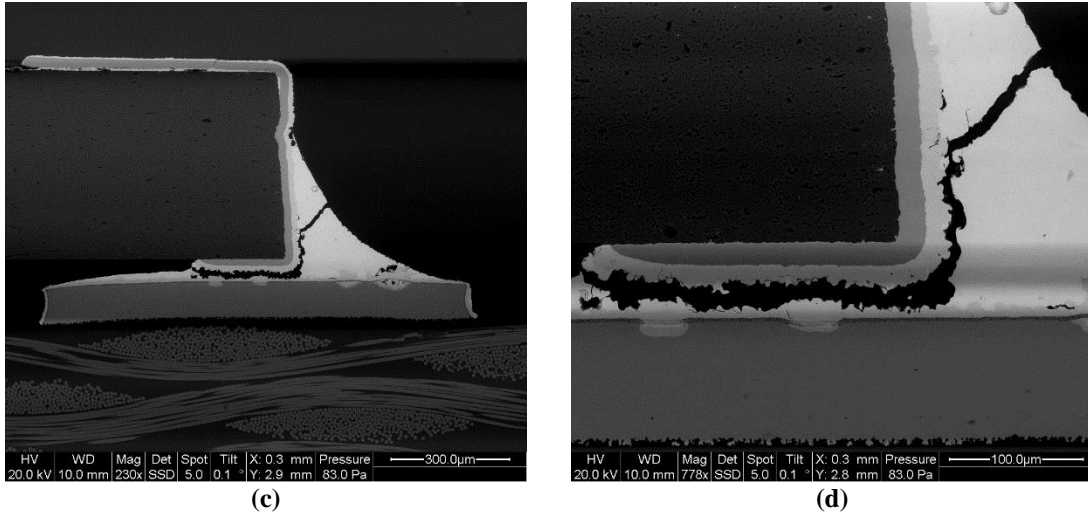


Figure 10-20: SAC305+0.05%Mn Solder Failure during Mechanical Shock Test (a) QFN44 – 1000 hours/200°C Aging (b) Additional QFN44 - 1000 hours/200°C Aging (c) R2512 - 1000 hours/200°C Aging (d) Magnified view of R2512 Crack

### 10.6.3. High Mn Solder

None of the resistor packages failed for High Mn solder during mechanical shock testing. Thus only failed QFNs underwent failure analysis. Figure 10-21 shows a failed High Mn solder joint in QFN44 package after 1000 hours of aging at 200°C. Failure analysis revealed a quite interesting crack path pattern for High Mn solder. It was found that High Mn solder showed a more mixed type of failure mode compared to a pure interfacial type. Further analysis revealed that solder failed by mixed mode, with a crack generally initiated at the end of component side  $\text{Cu}_6\text{Sn}_5$  interfacial IMC. After crack initiated at the interface, crack propagated through solder bulk as shown in both Figure 10-21 (a) and Figure 10-21 (b). This kind of failure still falls under mixed mode, however, it utilized mostly solder bulk for crack propagation. This shows that the interface between  $\text{Cu}_6\text{Sn}_5$  interfacial IMC and solder bulk is strong enough to prevent crack propagation through the solder interface. Such behavior is an unusual case compared to other solders where cracks partially or fully propagate



through the solder interface. Presence of fewer interfacial voids with thinner  $\text{Cu}_6\text{Sn}_5$  interfacial IMC are believed to be the reason for the type of failure observed in High Mn solder. Due to a stronger solder interface on the component side, High Mn solder outperformed and showed much higher mechanical shock reliability compare to other solders.

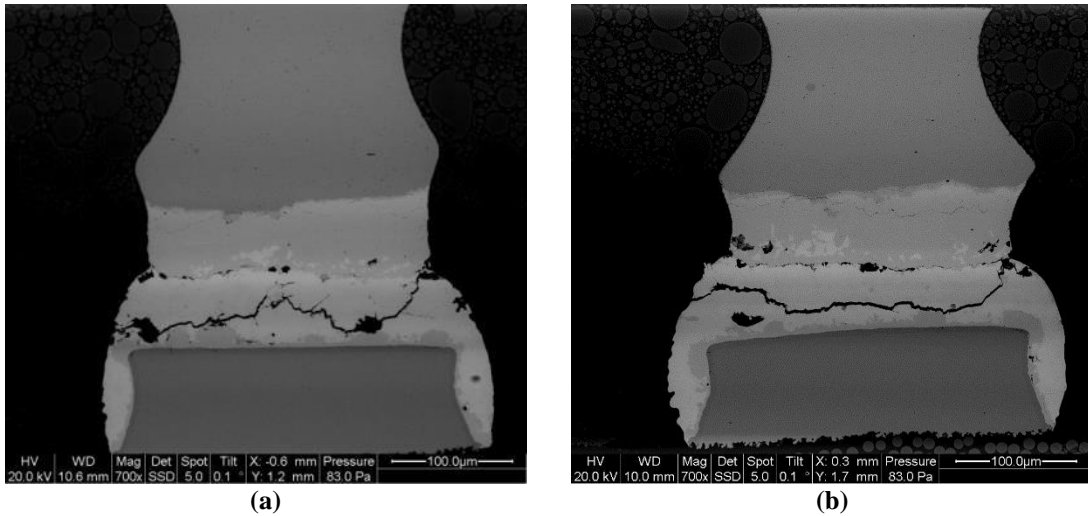


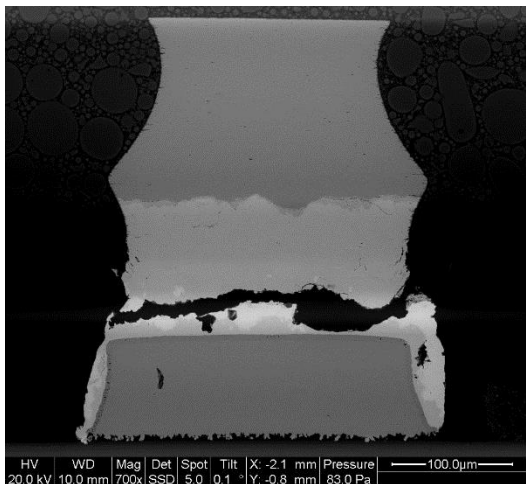
Figure 10-21: SAC305+0.17%Mn Solder Failure during Mechanical Shock Test (a) QFN44 – 1000 hours/200°C Aging (b) Additional QFN44 - 1000 hours/200°C Aging

#### 10.6.4. Low Ce Solder

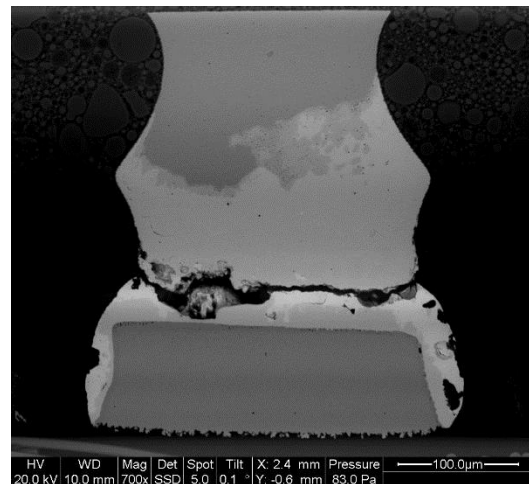
Figure 10-22 shows the failure of SAC305+0.07%Ce solder joints in QFN44 and R2512 packages. Figure 10-22 (a) and Figure 10-22 (b) show the solder joint of failed QFN44 in mechanical shock after 1000 hours of aging at 200°C. Both failed QFN44 solder joints confirm that failure occurred at the interface between  $\text{Cu}_6\text{Sn}_5$  interfacial IMC and bulk solder. Huge growth in  $\text{Cu}_6\text{Sn}_5$  interfacial IMC can be also seen in Figure 10-22 (b), along with excessive voids formed at the interface during high temperature aging which reduced interfacial strength even further. With presence of large interfacial voids and thicker  $\text{Cu}_6\text{Sn}_5$  interfacial IMC, Low Ce solder joint failed at the solder interface during mechanical shock testing. This result confirms lower

mechanical shock reliability of Low Ce solder observed in QFNs after high temperature aging exposure.

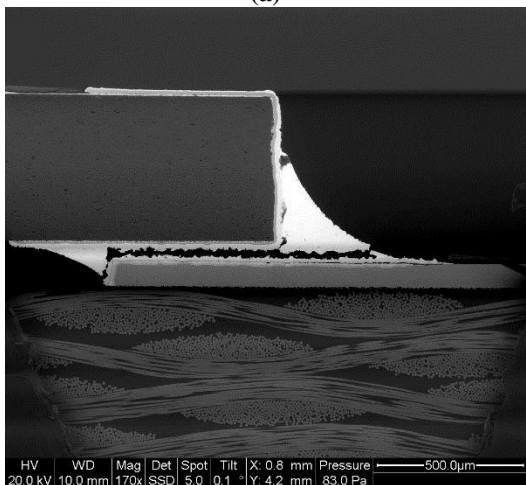
The failed R2512 Low Ce solder joint is shown Figure 10-22 (c). The failure mode for R2512 package was crack propagation at the board side interface region. Figure 10-22 (c) also shows four IMC layers on the board side after 1000 hours of aging at 200°C. The magnified view is also shown in Figure 10-22 (d). The failure observed in Low Ce solder is identical to the failure previously observed in SAC305 solder joint. This confirms higher R2512 package failure for Low Ce solder during mechanical shock testing after 200°C aging.



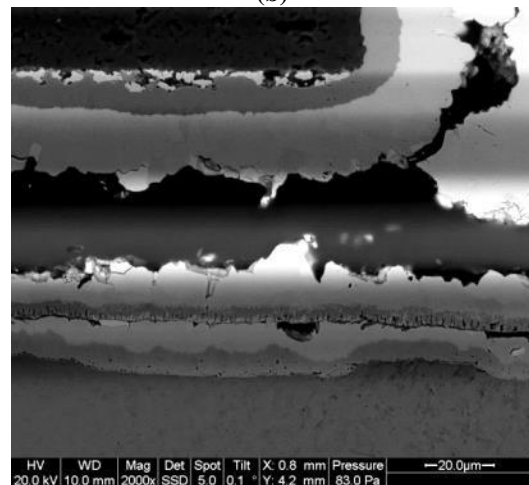
(a)



(b)



(c)



(d)

Figure 10-22: SAC305+0.07%Ce Solder Failure during Mechanical Shock Test (a) QFN44 – 1000 hours/200°C Aging (b) Additional QFN44 - 1000 hours/200°C Aging (c) R2512 - 1000 hours/200°C Aging (d) Magnified view of R2512 Crack

### **10.6.5. High Ce Solder**

Figure 10-23 shows the failure of SAC305+0.13%Ce solder joints in QFN44 and R2512 packages. Figure 10-23 (a) and Figure 10-23 (b) show the solder joint of failed QFN44 during mechanical shock after 1000 hours of aging at 200°C. Failure analysis revealed that High Ce solder showed two types of failure mode as previously observed in Low Mn and High Mn solders. More mixed mode type failures were observed in High Ce solder as shown in Figure 10-23 (a) and Figure 10-23 (b). The evidence of more mixed mode type failure confirms better performance of High Ce solder in mechanical shock testing.

The failed R2512 High Ce solder joint is shown Figure 10-23 (c). The failure mode for R2512 package was crack propagation at the board side interface region. The magnified view of the crack in R2512 is shown in Figure 10-23 (d). Both Figure 10-23 (c) and Figure 10-23 (d) show four IMC layers on the board side after 1000 hours of aging at 200°C. The failure observed in High Ce solder is identical to the failure previously observed in SAC305 and Low Ce solders. This confirms higher R2512 package failure for High Ce solder during mechanical shock testing after 200°C aging.

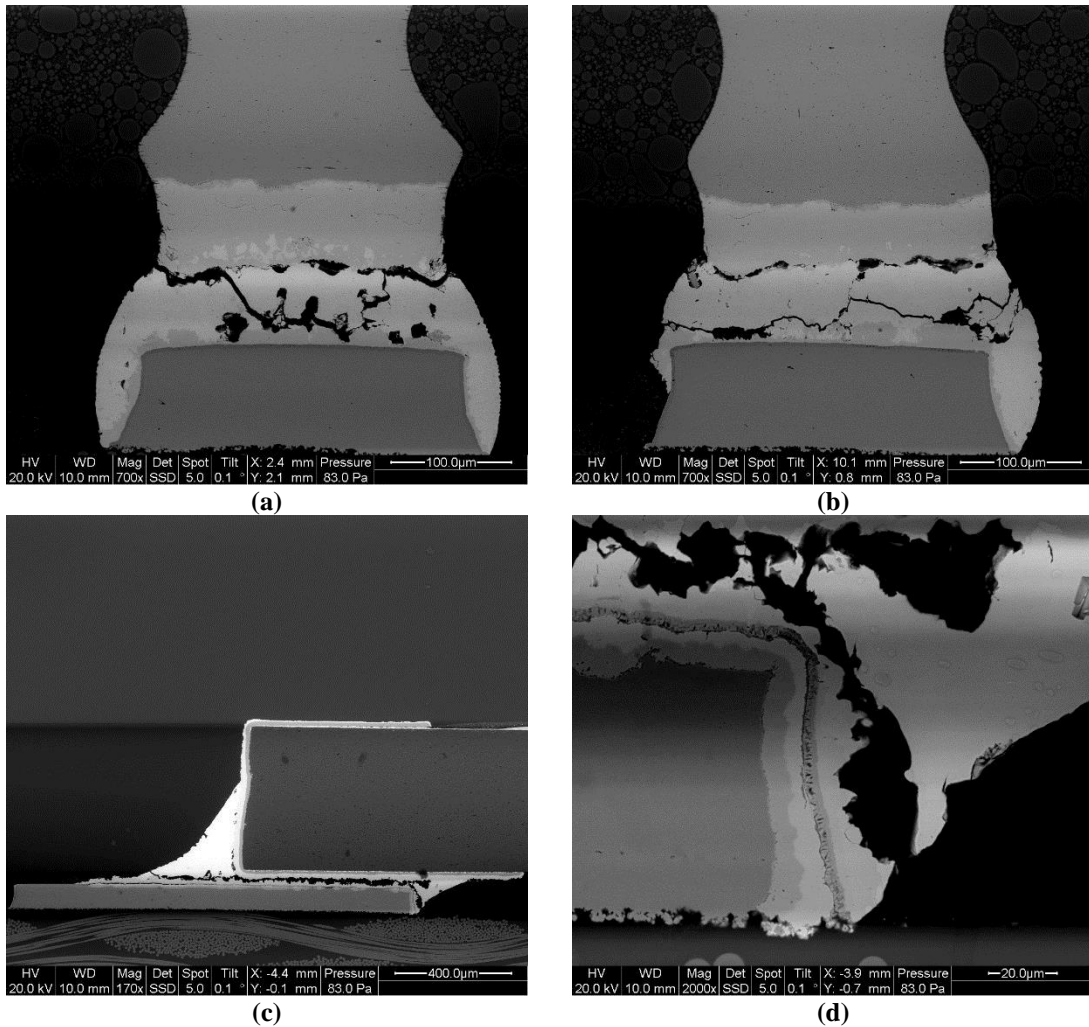


Figure 10-23: SAC305+0.13%Ce Solder Failure during Mechanical Shock Test (a) QFN44 – 1000 hours/200°C Aging (b) Additional QFN44 - 1000 hours/200°C Aging (c) R2512 - 1000 hours/200°C Aging (d) Magnified view of R2512 Crack

## 10.7. Conclusions

Many findings were obtained from the mechanical shock reliability test performed on thermally aged and un-aged test boards. These findings are summarized as below:

- This study shows that mechanical shock reliability of solders is significantly reduced after high temperature aging exposure. It was confirmed that a reduction in mechanical shock reliability of solder joint was due to either

growth in interfacial IMCs or combination of interfacial IMC growth and voids at the interface.

- For QFN package without any barrier layer on the component side, interfacial voids formed during high temperature aging play significant role for mechanical shock reliability reduction.
- In general, it was found that solder that effectively suppresses the growth of interfacial IMC and voids exhibited superior mechanical shock reliability.
- High Mn solder had the highest reliability in all mechanical shock tests on thermally aged test boards.
- High Ce solder was found to be the second most effective solder for QFN44 and QFN32 packages. However, for R2512 package, High Ce showed Ni layer consumption that reduced solder joint reliability under mechanical shock testing.
- For the most part, Low Mn solder performed better than SAC305 and Low Ce solders.
- Overall, Low Ce and SAC305 solders showed poor solder joint reliability under mechanical shock testing.
- Failure analysis confirms that the improved mechanical shock reliability observed for High Mn, High Ce and Low Mn solders were related to the stronger solder interface. During failure analysis, all thee solders indicated an additional mixed mode type of failure mode.

- For un-aged test boards, it was found that package failure was not related to interfacial IMC thickness. This indicates that various other factors including mechanical properties of bulk solder, number of  $\beta$ -tin grains, size and distribution of bulk IMCs play an important role for mechanical shock reliability of as-reflowed solder interconnects.

## 11. Contributions

This dissertation resulted in multiple contributions which are summarized below:

### **Performance assessment study of MEMS gyroscope:**

- A comprehensive test methodology has been developed to understand the performance limit of MEMS gyroscopes under elevated temperature conditions that includes characterization of commercially available MEMS gyroscopes in high temperature environments.
- An analytical model which incorporates the effects of multiple temperature dependent factors on MEMS gyroscope performance was developed. The accuracy of this model was confirmed by experiments. The model enables the identification of dominating temperature dependent variables and their effect in high temperature environments.

### **Shock durability evaluation study of SAC305 and SAC305-X solders:**

- A systematic high temperature thermal aging analysis of Mn doped SAC305 solders on copper (QFN44 and QFN32) and nickel (R2512) leaded components at 185°C and 200°C showed that addition of 0.05%Mn and 0.17%Mn in SAC305 effectively reduces the growth of interfacial IMCs for QFN32, QFN44, and R2512 during high temperature aging.
- A systematic high temperature thermal aging analysis of Ce doped SAC305 solders on copper (QFN44 and QFN32) and nickel (R2512) leaded components at 185°C and 200°C revealed that addition of 0.13%Ce in

SAC305 effectively reduces the growth of interfacial IMCs from QFN32 and QFN44 during high temperature aging.

- A detailed mechanical shock reliability assessment of SAC305 and SAC305-X (where X refers to 0.05%Mn, 0.17%Mn, 0.07%Ce and 0.13%Ce) on test boards as-reflowed and thermally aged at 185°C and 200°C showed that microalloy addition of selected dopants at the prescribed concentrations improve the shock duration of SAC305. More specifically, addition of 0.17%Mn and 0.13%Ce in SAC305 indicated significant improvement in shock durability of SAC305.
- The mechanism was determined by which a 0.17% concentration of Mn dopant in SAC305 solder suppresses Ni layer consumption in ENIG-plated board, and thus allows the Ni layer to maintain its diffusion barrier capability under prolonged exposure to high temperature environment at 200°C.
- A unique type of void was found at the interface between  $\text{Cu}_6\text{Sn}_5$  interfacial IMC and the solder bulk that developed during high temperature aging at 185°C and 200°C, and its effect on SAC305 and SAC305-X solder joint reliability under mechanical shock loading was determined.
- A correlation was established between high temperature aging effects (interfacial IMC growth, and void formation and coalescence) and mechanical shock reliability of SAC305 and SAC305-X solders showing that interfacial IMC growth and especially void formation/coalescence during high temperature aging significantly reduces shock reliability of solder joints.



## Appendix-A

Appendix-A shows the result of Unit-B and Unit-C. These both the units were used to understand the short term effects of an elevated temperature on the MEMS vibratory gyroscope. The baseline test results of stationary and rotary conditions are summarized in table; while, thermal test results are shown graphically.

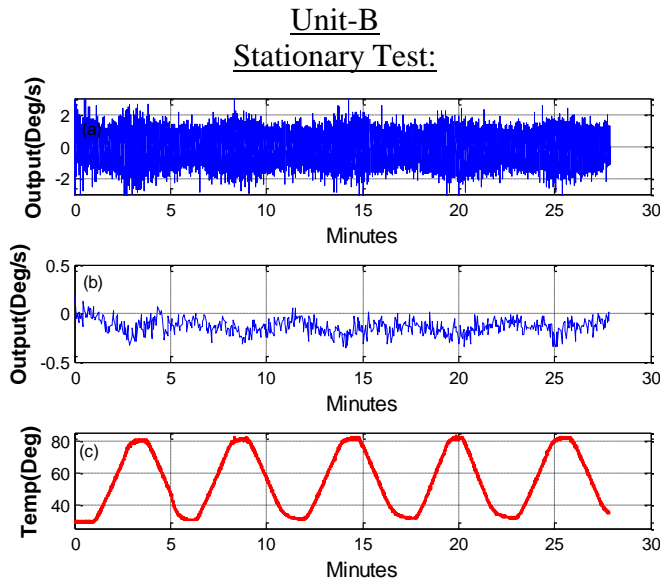


Figure 0-1: (a) Stationary thermal test results from 25°C to 85°C; (b) Mean of angular rate data with window size = 100; (c) Thermal cycles from 25°C to 85°C.

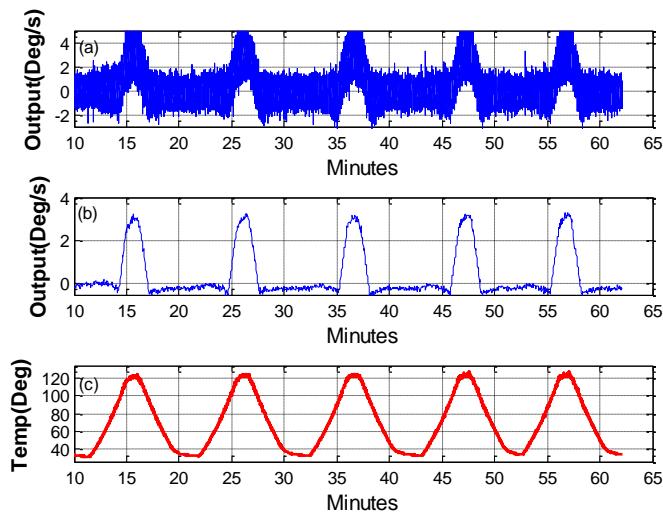


Figure 0-2: (a) Stationary thermal test results from 25°C to 125°C; (b) Mean of angular rate data with window size = 100; (c) Thermal cycles from 25°C to 125°C.

| Cycles       | Temperature Dependent Bias (°/s) |
|--------------|----------------------------------|
| First cycle  | 3.20                             |
| Second cycle | 3.25                             |
| Third cycle  | 3.25                             |
| Fourth cycle | 3.30                             |
| Fifth cycle  | 3.30                             |
| Avg.         | 3.26                             |

Table 0-1: Temperature dependent bias values of five stationary thermal cycles from 25°C to 125°C.

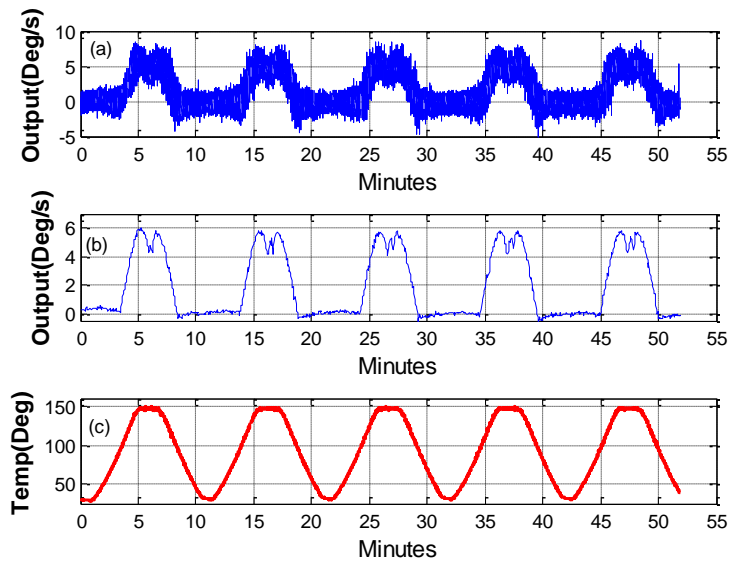


Figure 0-3: (a) Stationary thermal test results from 25°C to 150°C; (b) Mean of angular rate data with window size = 100; (c) Thermal cycles from 25°C to 150°C.

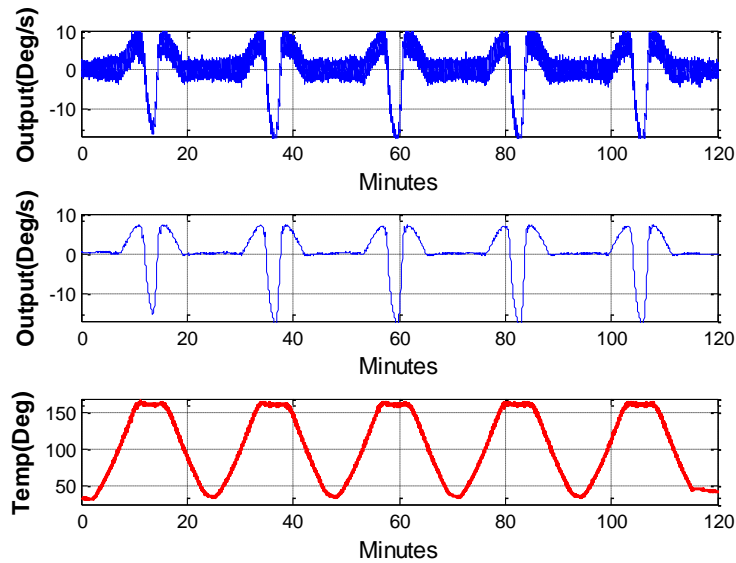


Figure 0-4: (a) Stationary thermal test results from 25°C to 175°C; (b) Mean of angular rate data with window size = 100; (c) Thermal cycles from 25°C to 175°C.

| No | Tests                           | Mean (°/s) | Standard Deviation (°/s) |
|----|---------------------------------|------------|--------------------------|
| 1  | First stationary baseline test  | 0.01       | 0.43                     |
| 2  | Second stationary baseline test | 0.02       | 0.49                     |
| 3  | Third stationary baseline test  | 0.01       | 0.45                     |
| 4  | Fourth stationary baseline test | -0.01      | 0.44                     |
| 5  | Fifth stationary baseline test  | 0.02       | 0.43                     |

Table 0-2: Mean and Standard Deviation of Stationary Baseline Test

**Rotary Test:**

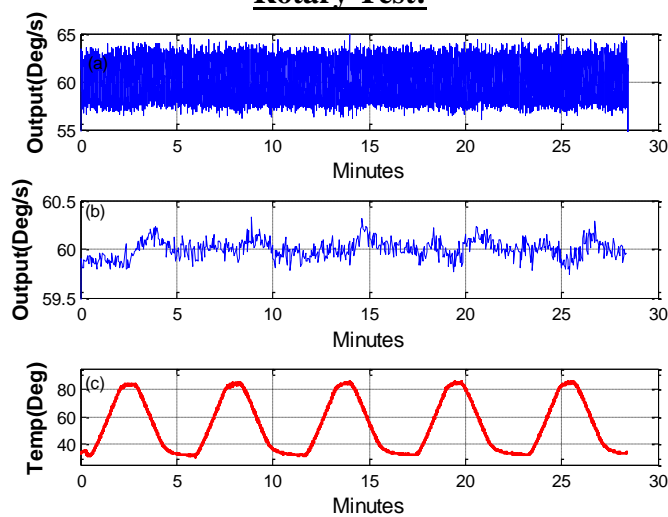


Figure 0-5: (a) Rotary thermal test results from 25°C to 85°C; (b) Mean of angular rate data with window size = 100; (c) Thermal cycles from 25°C to 85°C.

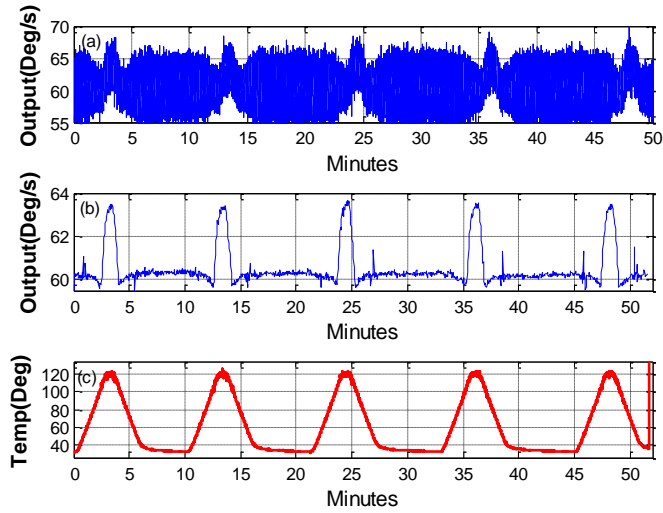


Figure 0-6: (a) Rotary thermal test results from 25°C to 125°C; (b) Mean of angular rate data with window size = 100; (c) Thermal cycles from 25°C to 125°C.

| Cycles       | Angular Velocity(Deg/s) at 125 °C | Bias (Deg/s) |
|--------------|-----------------------------------|--------------|
| First cycle  | 63.30                             | 3.3          |
| Second cycle | 63.15                             | 3.15         |
| Third cycle  | 63.40                             | 3.40         |
| Fourth cycle | 63.25                             | 3.25         |
| Fifth cycle  | 63.25                             | 3.25         |
| Avg.         | 63.27                             | 3.27         |

Table 0-3: Angular velocity and temperature dependent bias of five rotary thermal cycles from 25°C to 125°C.

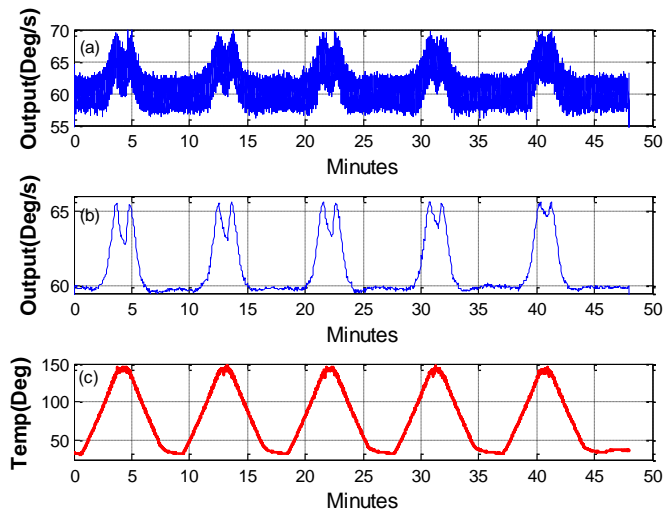


Figure 0-7: (a) Rotary thermal test results from 25°C to 150°C; (b) Mean of angular rate data with window size = 100; (c) Thermal cycles from 25°C to 150°C.

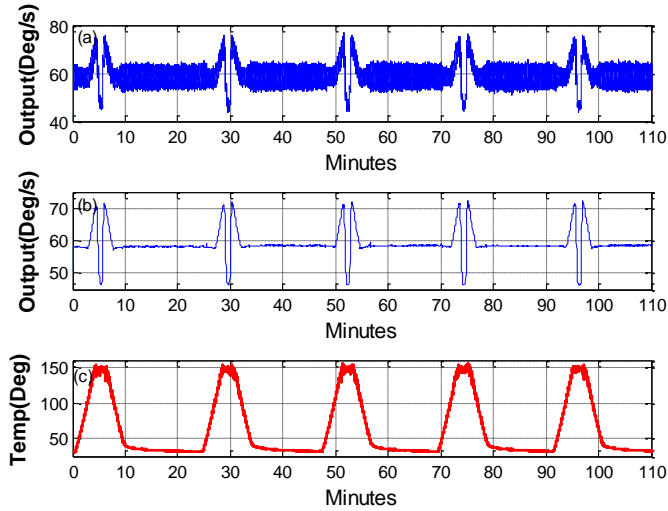


Figure 0-8: (a) Rotary thermal test results from 25°C to 175°C; (b) Mean of angular rate data with window size = 100; (c) Thermal cycles from 25°C to 175°C.

| No | Tests                       | Mean (°/s) | Standard Deviation (°/s) |
|----|-----------------------------|------------|--------------------------|
| 1  | First Rotary baseline test  | 59.92      | 0.93                     |
| 2  | Second Rotary baseline test | 59.98      | 1.05                     |
| 3  | Third Rotary baseline test  | 59.85      | 1.20                     |
| 4  | Fourth Rotary baseline test | 59.79      | 1.33                     |
| 5  | Fifth Rotary baseline test  | 59.88      | 1.01                     |

Table 0-4: Mean and Standard Deviation of Rotary Baseline Test

Unit-C  
Stationary Test:

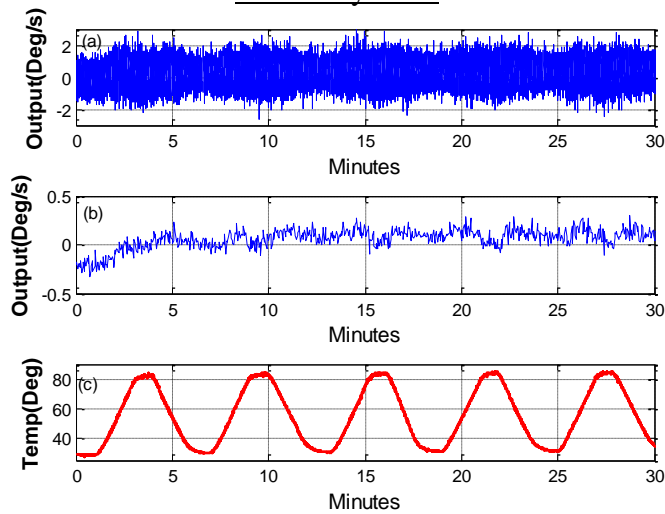


Figure 0-9: (a) Stationary thermal test results from 25°C to 85°C; (b) Mean of angular rate data with window size = 100; (c) Thermal cycles from 25°C to 85°C.

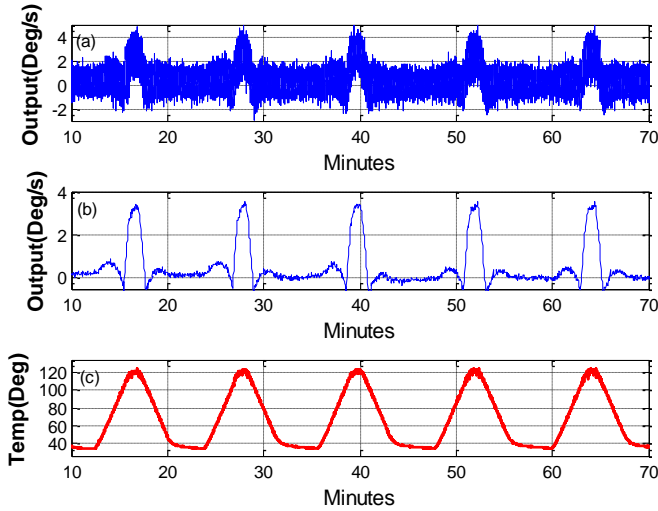


Figure 0-10: (a) Stationary thermal test results from 25°C to 125°C; (b) Mean of angular rate data with window size = 100; (c) Thermal cycles from 25°C to 125°C.

| Cycles       | Temperature Dependent Bias (°/s) |
|--------------|----------------------------------|
| First cycle  | 3.20                             |
| Second cycle | 3.25                             |
| Third cycle  | 3.35                             |
| Fourth cycle | 3.30                             |
| Fifth cycle  | 3.30                             |
| Avg.         | 3.28                             |

Table 0-5: Temperature dependent bias values of five stationary thermal cycles from 25°C to 125°C.

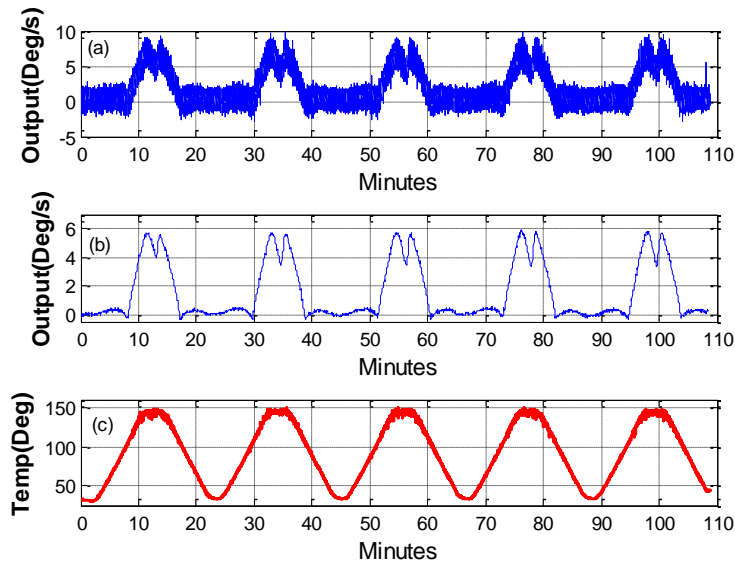


Figure 0-11: (a) Stationary thermal test results from 25°C to 150°C; (b) Mean of angular rate data with window size = 100; (c) Thermal cycles from 25°C to 150°C.

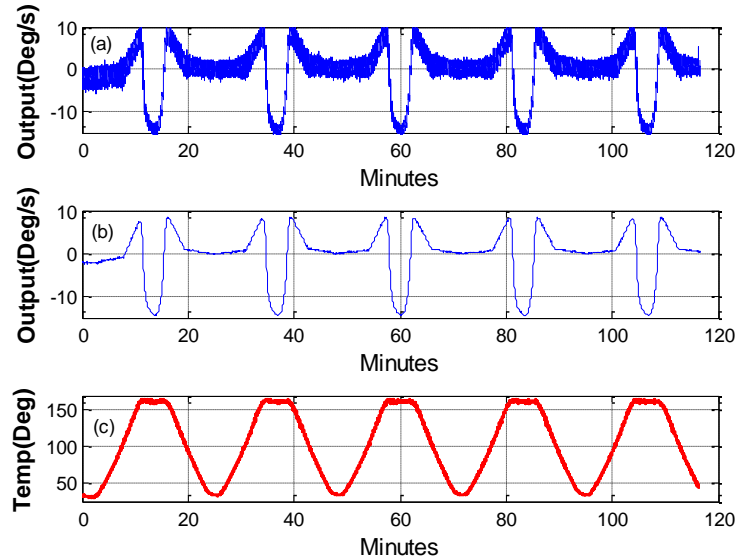


Figure 0-12: (a) Stationary thermal test results from 25°C to 175°C; (b) Mean of angular rate data with window size = 100; (c) Thermal cycles from 25°C to 175°C.

| No | Tests                           | Mean (°/s) | Standard Deviation (°/s) |
|----|---------------------------------|------------|--------------------------|
| 1  | First stationary baseline test  | 0.01       | 0.46                     |
| 2  | Second stationary baseline test | 0.01       | 0.48                     |
| 3  | Third stationary baseline test  | 0.01       | 0.44                     |
| 4  | Fourth stationary baseline test | 0.02       | 0.45                     |
| 5  | Fifth stationary baseline test  | 0.01       | 0.45                     |

### Rotary Test:

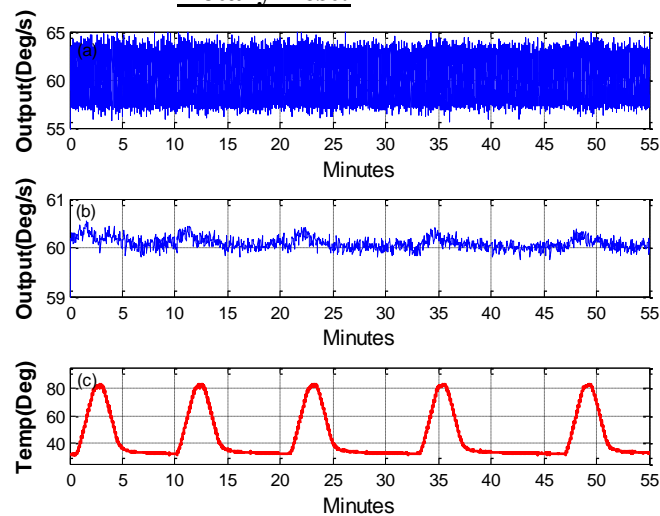


Figure 0-13: (a) Rotary thermal test results from 25°C to 85°C; (b) Mean of angular rate data with window size = 100; (c) Thermal cycles from 25°C to 85°C.

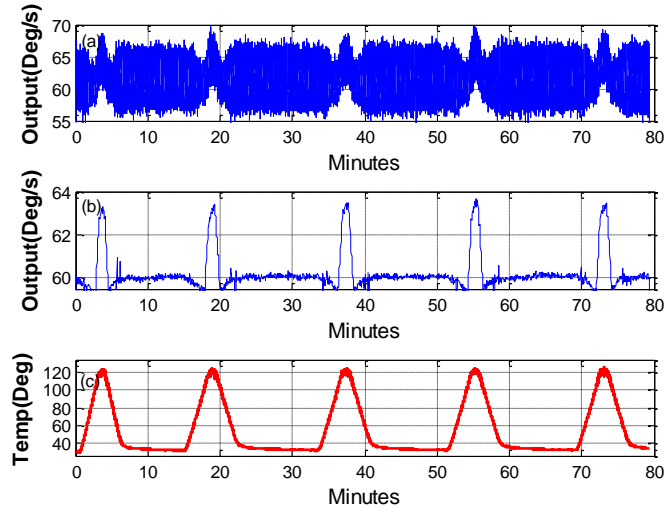


Figure 0-14: (a) Rotary thermal test results from 25°C to 125°C; (b) Mean of angular rate data with window size = 100; (c) Thermal cycles from 25°C to 125°C.

| Cycles       | Angular Velocity(Deg/s) At 125 °C | Bias (Deg/s) |
|--------------|-----------------------------------|--------------|
| First cycle  | 63.30                             | 3.30         |
| Second cycle | 63.15                             | 3.15         |
| Third cycle  | 63.30                             | 3.30         |
| Fourth cycle | 63.40                             | 3.40         |
| Fifth cycle  | 63.25                             | 3.25         |
| Avg.         | 63.28                             | 3.28         |

Table 0-6: Angular velocity and temperature dependent bias of five rotary thermal cycles from 25°C to 125°C.

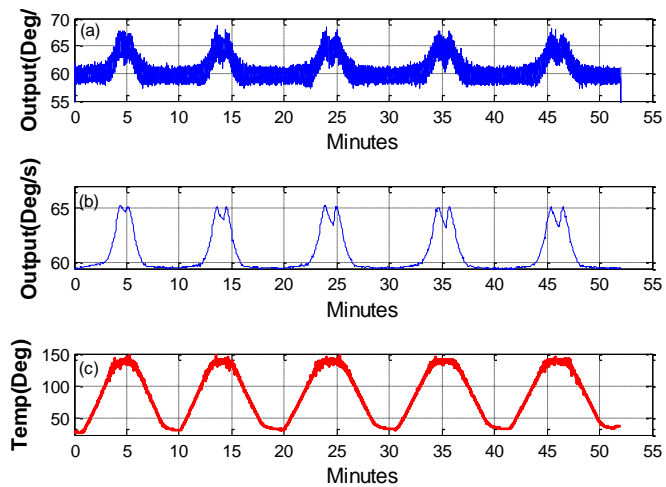


Figure 0-15: (a) Rotary thermal test results from 25°C to 150°C; (b) Mean of angular rate data with window size = 100; (c) Thermal cycles from 25°C to 150°C.



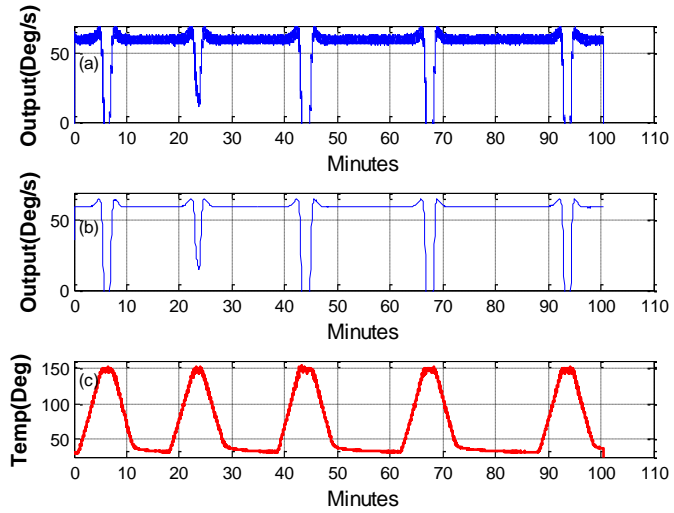


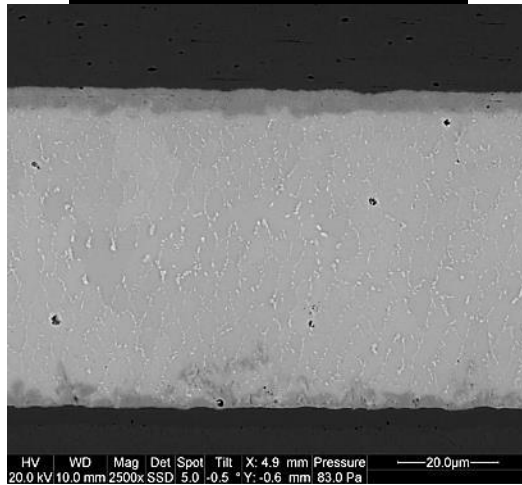
Figure 0-16: (a) Rotary thermal test results from 25°C to 175°C; (b) Mean of angular rate data with window size = 100; (c) Thermal cycles from 25°C to 175°C.

| No | Tests                       | Mean (°/s) | Standard Deviation (°/s) |
|----|-----------------------------|------------|--------------------------|
| 1  | First Rotary baseline test  | 59.94      | 1.07                     |
| 2  | Second Rotary baseline test | 59.85      | 0.91                     |
| 3  | Third Rotary baseline test  | 59.88      | 0.99                     |
| 4  | Fourth Rotary baseline test | 59.97      | 1.22                     |
| 5  | Fifth Rotary baseline test  | 59.90      | 1.23                     |

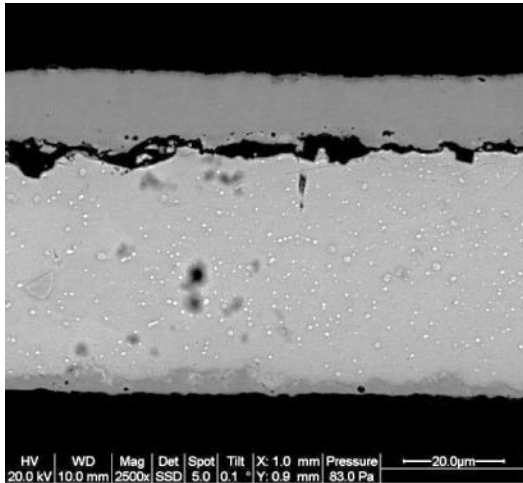
Table 0-7: Mean and Standard Deviation of Rotary Baseline Test

# Appendix-B

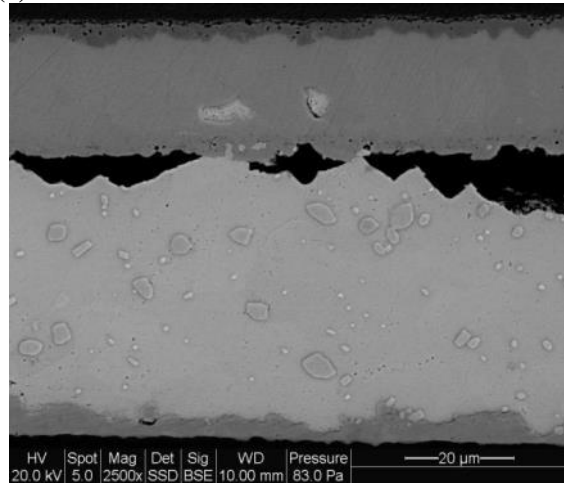
## Part-A - QFN32 185°C Aging



(a)

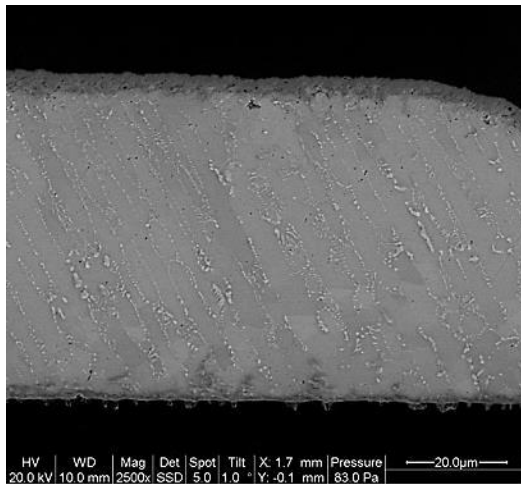


(b)

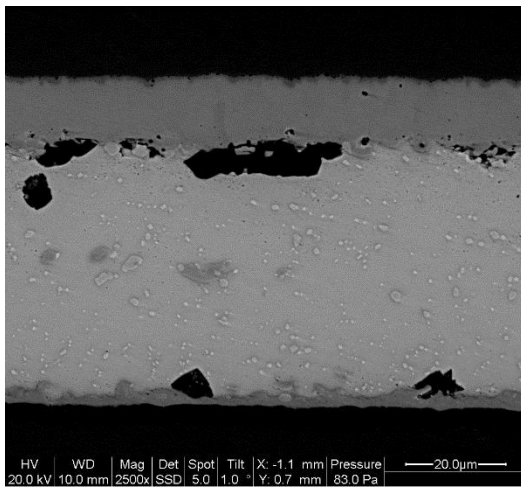


(c)

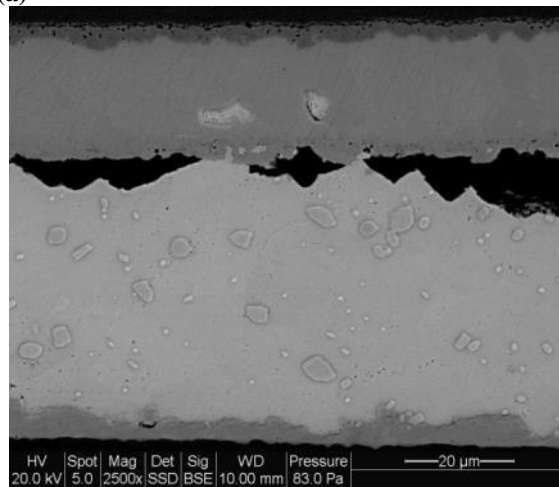
Figure 0-1: QFN32 - SAC305 Solder Joint (a) After Reflow, (b) After 100 hours/185°C Aging, (c) After 1000 hours/185°C Aging



(a)

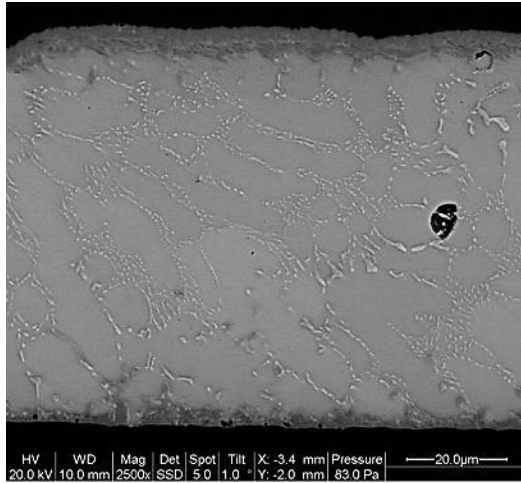


(b)

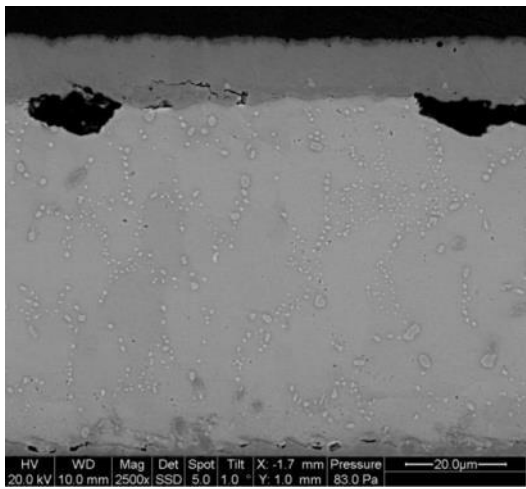


(c)

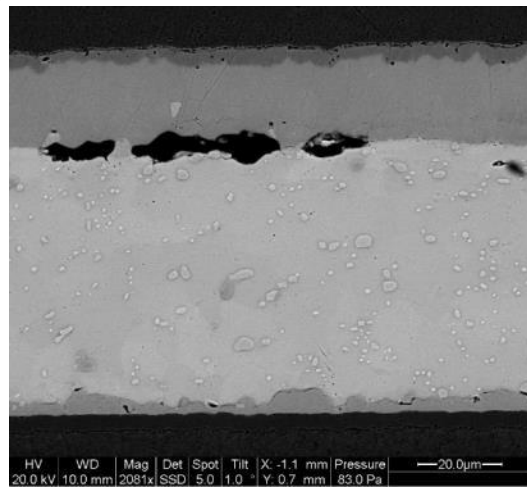
Figure 0-2: QFN32 - SAC305+0.05%Mn Solder Joint (a) After Reflow, (b) After 100 hours/185°C Aging, (c) After 1000 hours/185°C Aging



(a)

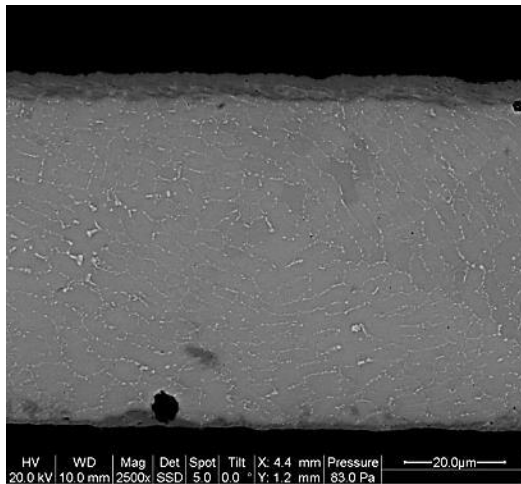


(b)

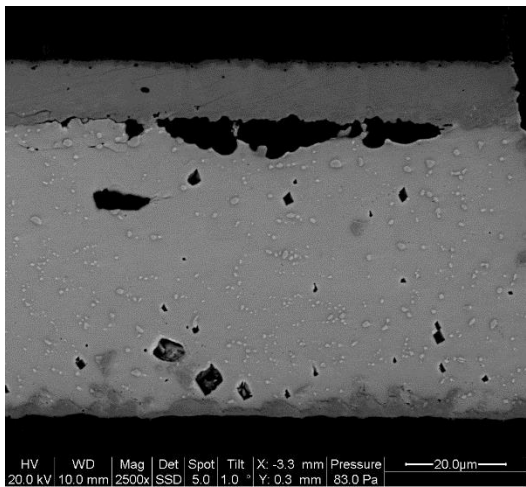


(c)

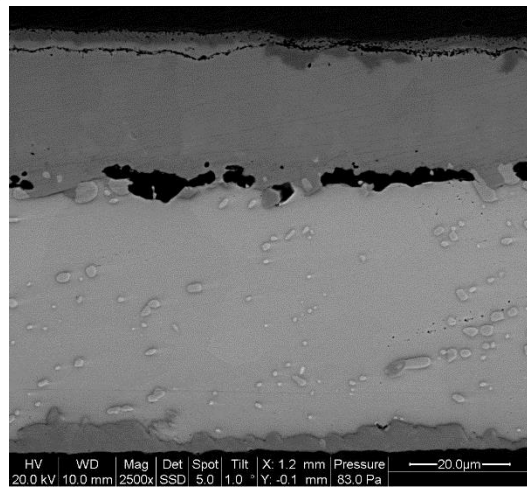
Figure 0-3: QFN32 - SAC305+0.17%Mn Solder Joint (a) After Reflow, (b) After 100 hours/185°C Aging, (c) After 1000 hours/185°C Aging



(a)

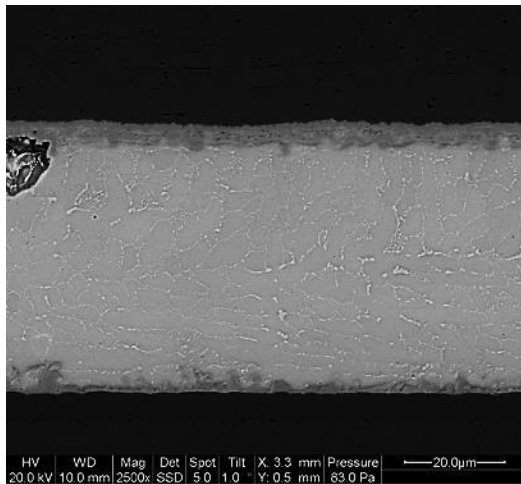


(b)

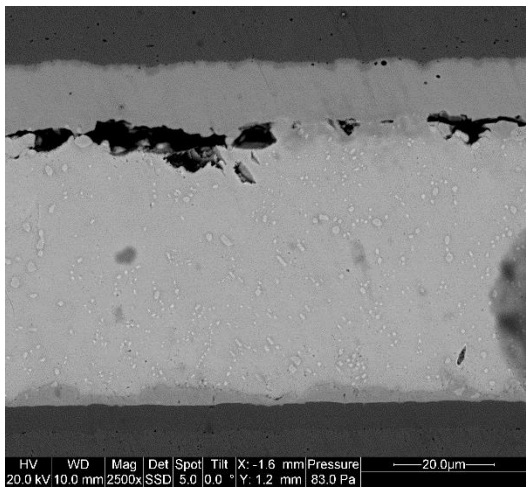


(c)

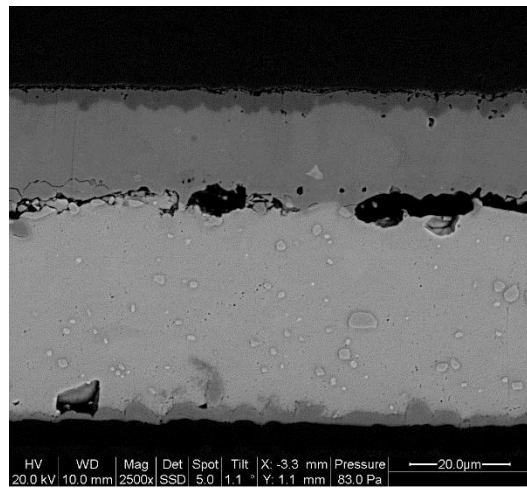
Figure 0-4: QFN32 - SAC305+0.07%Ce Solder Joint (a) After Reflow, (b) After 100 hours/185°C Aging, (c) After 1000 hours/185°C Aging



(a)



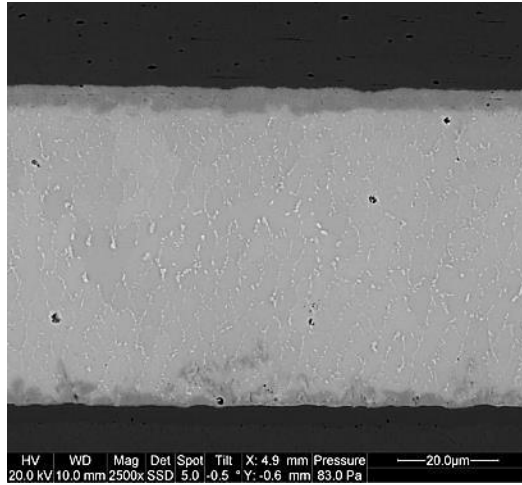
(b)



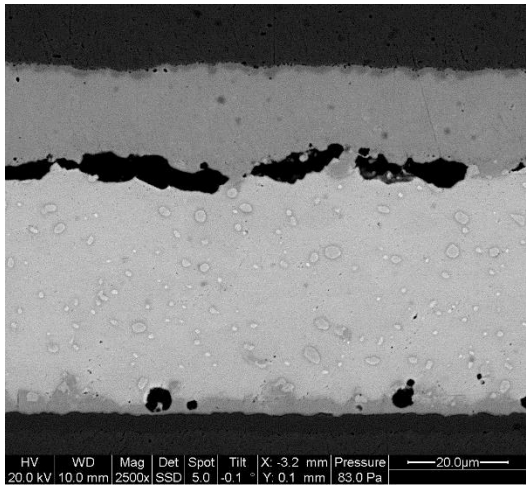
(c)

Figure 0-5: QFN32 - SAC305+0.13%Ce Solder Joint (a) After Reflow, (b) After 100 hours/185°C Aging, (c) After 1000 hours/185°C Aging

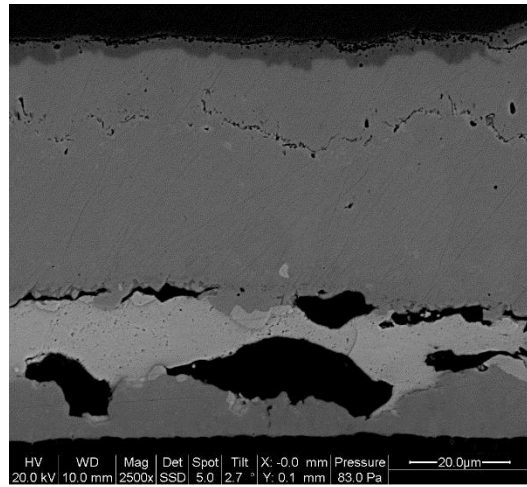
**Part-B - QFN32 200°C Aging**



(a)

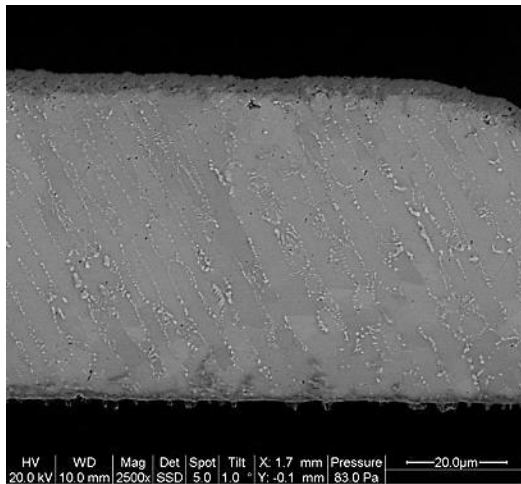


(b)

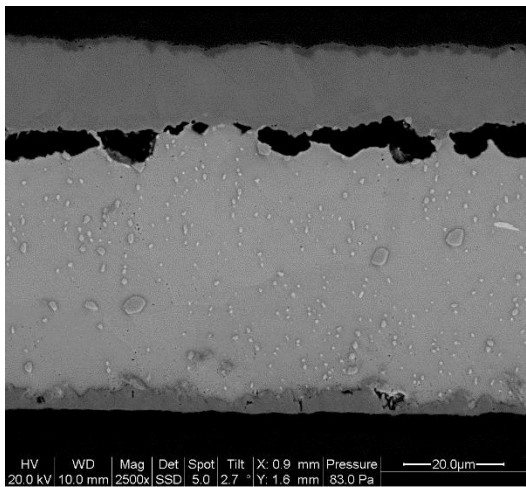


(c)

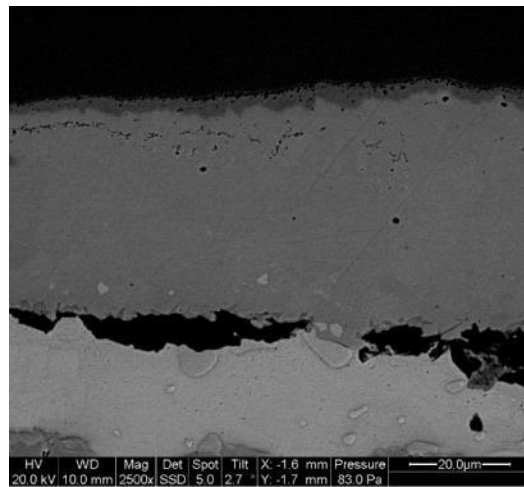
Figure 0-6: QFN32 - SAC305 Solder Joint (a) After Reflow, (b) After 100 hours/200°C Aging, (c) After 1000 hours/200°C Aging



(a)



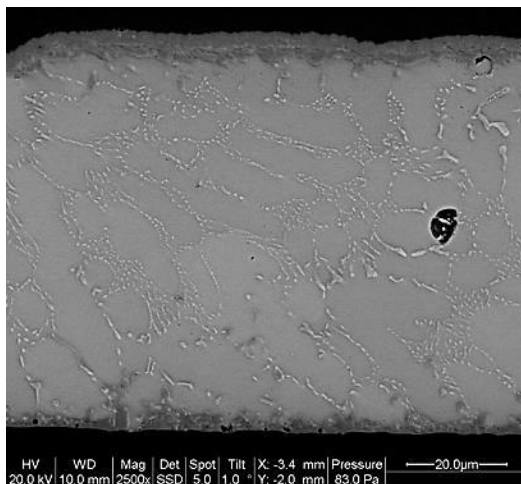
(b)



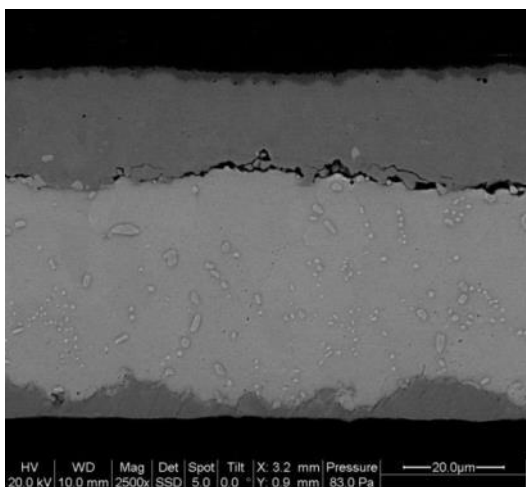
(c)

Figure 0-7: QFN32 - SAC305+0.05%Mn Solder Joint (a) After Reflow, (b) After 100 hours/200°C Aging, (c) After 1000 hours/200°C Aging

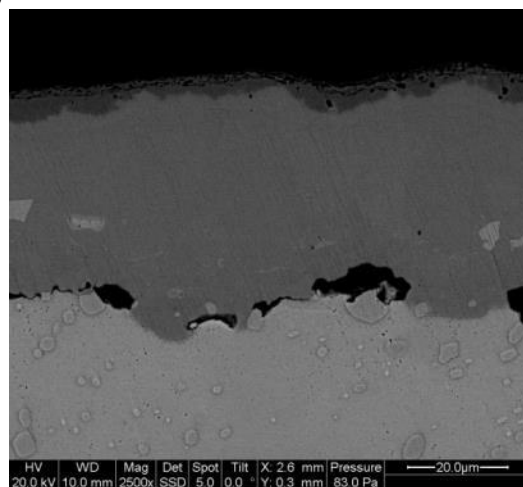




(a)

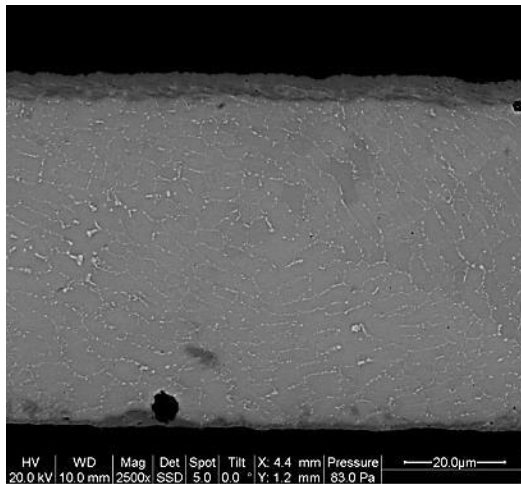


(b)

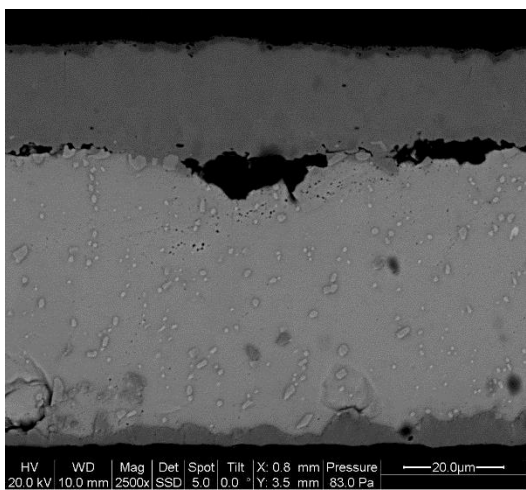


(c)

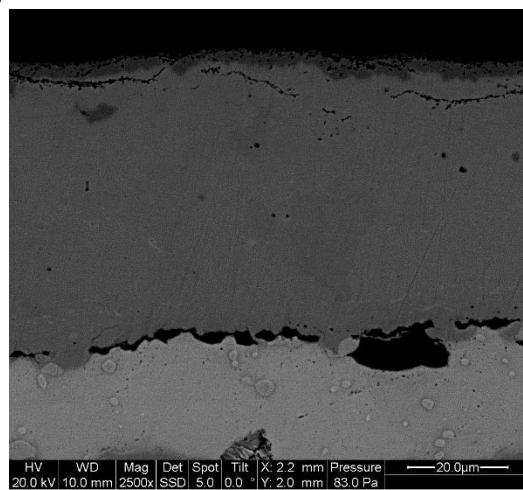
Figure 0-8: QFN32 - SAC305+0.17%Mn Solder Joint (a) After Reflow, (b) After 100 hours/200°C Aging, (c) After 1000 hours/200°C Aging



(a)

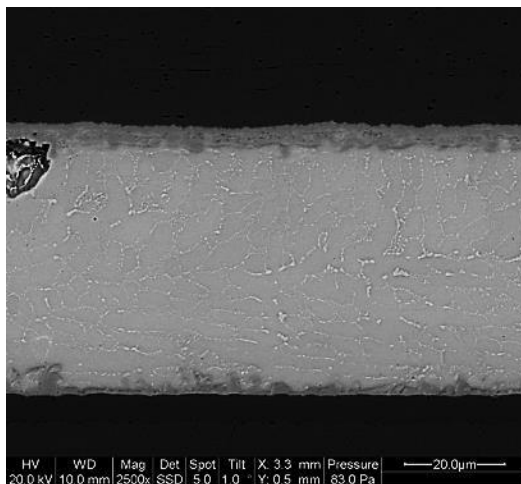


(b)

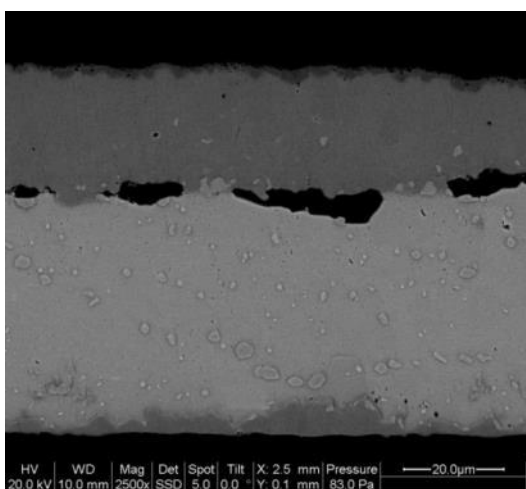


(c)

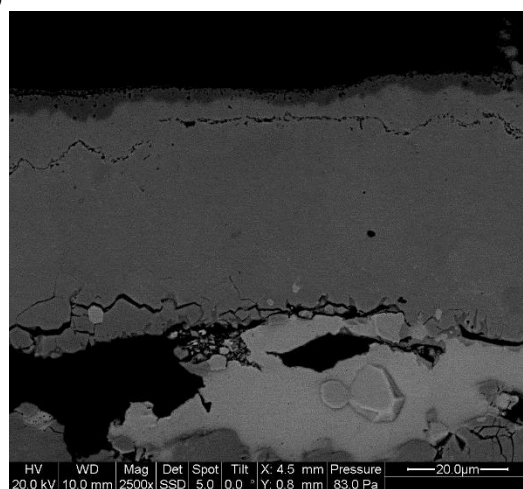
Figure 0-9: QFN32 - SAC305+0.07%Ce Solder Joint (a) After Reflow, (b) After 100 hours/200°C Aging, (c) After 1000 hours/200°C Aging



(a)



(b)



(c)

Figure 0-10: QFN32 - SAC305+0.13%Ce Solder Joint (a) After Reflow, (b) After 100 hours/200°C Aging, (c) After 1000 hours/200°C Aging

## References

- [1] S. Nasiri, "A Critical Review of MEMS Gyroscopes Technology and Commercialization Status." InvenSense Inc.
- [2] M. N. Armenise, C. Ciminelli, F. Dell'Olio, and V. M. N. Passaro, *Advances in Gyroscope Technologies*, 1st Edition. Springer, 2010.
- [3] M. P. de Boer, B. D. Jensen, and F. Bitsie, "Small-area in-situ MEMS test structure to measure fracture strength by electrostatic probing," in *Society of Photo-Optical Instrumentation Engineers (SPIE) Conference Series*, 1999, vol. 3875, pp. 97–103.
- [4] T. G. Brown, "Harsh military environments and microelectromechanical (MEMS) devices," in *Sensors, 2003. Proceedings of IEEE*, 2003, vol. 2, pp. 753 – 760 Vol.2.
- [5] T. G. Brown, B. Davis, D. Hepner, J. Faust, C. Myers, C. Muller, T. Harkins, M. Holis, and B. Placzankis, "Strap-down microelectromechanical (MEMS) sensors for high-g munition applications," *Magn. IEEE Trans. On*, vol. 37, no. 1, pp. 336 –342, Jan. 2001.
- [6] H. Hyvönen, "Thermomechanical and Mechanical Characterization of a 3-Axial MEMS Gyroscope," Aalto University School of Electrical Engineering, 2011.
- [7] R. Dean, G. Flowers, S. Hodel, K. Macallister, R. Horvath, A. Matras, and R. Glover, "Vibration isolation of MEMS sensors for aerospace applications," *SPIE Proc. Ser.*, pp. 166–170.
- [8] D. M. Tanner, J. A. Walraven, K. S. Helgesen, L. W. Irwin, D. L. Gregory, J. R. Stake, and N. F. Smith, "MEMS reliability in a vibration environment," in *Reliability Physics Symposium, 2000. Proceedings. 38th Annual 2000 IEEE International*, 2000, pp. 139 –145.
- [9] R. N. Dean, S. T. Castro, G. T. Flowers, G. Roth, A. Ahmed, A. S. Hodel, B. E. Grantham, D. A. Bittle, and J. P. Brunsch, "A Characterization of the Performance of a MEMS Gyroscope in Acoustically Harsh Environments," *Ind. Electron. IEEE Trans. On*, no. 99, pp. 1–1, 2011.
- [10] R. N. Dean, G. T. Flowers, A. S. Hodel, G. Roth, S. Castro, R. Zhou, A. Moreira, A. Ahmed, R. Rifki, B. E. Grantham, D. Bittle, and J. Brunsch, "On the Degradation of MEMS Gyroscope Performance in the Presence of High Power Acoustic Noise," in *IEEE International Symposium on Industrial Electronics, 2007. ISIE 2007*, 2007, pp. 1435–1440.
- [11] G. Roth, "Simulation of the Effects of Acoustic Noise on MEMS Gyroscopes," thesis, Auburn University, 2009.
- [12] "ADIS16135 from Analog Device Inc." .
- [13] "ISZ-1215 from InvenSense Inc." .
- [14] "MLX90609 from MELEXIS Inc." .
- [15] "LY330ALH from STMicroelectronics.Inc." .
- [16] K. Shcheglov, C. Evans, R. Gutierrez, and T. K. Tang, "Temperature dependent characteristics of the JPL silicon MEMS gyroscope," in *Aerospace Conference Proceedings, 2000 IEEE*, 2000, vol. 1, pp. 403–411.

- [17] D. Keymeulen, C. Peay, K. Yee, and D. L. Li, "Effect of Temperature on MEMS Vibratory Rate Gyroscope," in *Aerospace Conference, 2005 IEEE*, 2005, pp. 1–6.
- [18] Q. Zhang, Z. Tan, and L. Guo, "Compensation of Temperature Drift of MEMS Gyroscope Using BP Neural Network," in *Information Engineering and Computer Science, 2009. ICIECS 2009. International Conference on*, 2009, pp. 1–4.
- [19] D. Xia, S. Chen, S. Wang, and H. Li, "Microgyroscope Temperature Effects and Compensation-Control Methods," *Sensors*, vol. 9, no. 10, pp. 8349–8376, Oct. 2009.
- [20] G. Liu, A. Wang, T. Jiang, J. Jiao, and J.-B. Jang, "Effects of environmental temperature on the performance of a micromachined gyroscope," *Microsyst Technol*, vol. 14, no. 2, pp. 199–204, Oct. 2007.
- [21] Z. Hou, D. Xiao, X. Wu, P. Dong, Z. Niu, Z. Zhou, and X. Zhang, "Effect of parasitic resistance on a MEMS vibratory gyroscopes due to temperature fluctuations," in *Nano/Micro Engineered and Molecular Systems (NEMS), 2011 IEEE International Conference on*, 2011, pp. 293–296.
- [22] Z. Hou, D. Xiao, X. Wu, P. Dong, Z. Chen, Z. Niu, and X. Zhang, "Effect of Axial Force on the Performance of Micromachined Vibratory Rate Gyroscopes," *Sensors*, vol. 11, no. 1, pp. 296–309, Dec. 2010.
- [23] X.-H. Zhu, H.-J. Chu, Q. Shi, A.-P. Qiu, and Y. Su, "Experimental Study of Compensation for the Effect of Temperature on a Silicon Micromachined Gyroscope," *Proc. Inst. Mech. Eng. Part N J. Nanoeng. Nanosyst.*, vol. 222, no. 2, pp. 49–55, Jun. 2008.
- [24] L. F. Wu and F. X. Zhang, "Effect of the temperature on the performance of silicon micro-machined gyroscope using for rotating carrier," in *Control and Decision Conference, 2008. CCDC 2008. Chinese*, 2008, pp. 4876–4879.
- [25] R. Feng, A. P. Qiu, Q. Shi, X. H. Zhu, L. Yang, and Y. Su, "A Research on Temperature Dependent Characteristics of Quality Factor of Silicon MEMS Gyroscope," *Adv. Mater. Res.*, vol. 159, pp. 399–405, Dec. 2010.
- [26] B. Kim, M. A. Hopcroft, R. N. Candler, C. M. Jha, M. Agarwal, R. Melamud, S. A. Chandorkar, G. Yama, and T. W. Kenny, "Temperature Dependence of Quality Factor in MEMS Resonators," *Microelectromechanical Syst. J. Of*, vol. 17, no. 3, pp. 755–766, Jun. 2008.
- [27] R. Feng, A. P. Qiu, Q. Shi, X. H. Zhu, L. Yang, and Y. Su, "A Research on Temperature Dependent Characteristics of Quality Factor of Silicon MEMS Gyroscope," *Adv. Mater. Res.*, vol. 159, pp. 399–405, Dec. 2010.
- [28] H. Chang, Y. Zhang, J. Xie, Z. Zhou, and W. Yuan, "Integrated Behavior Simulation and Verification for a MEMS Vibratory Gyroscope Using Parametric Model Order Reduction," *Microelectromechanical Syst. J. Of*, vol. 19, no. 2, pp. 282–293, Apr. 2010.
- [29] S. Mohite, N. Patil, and R. Pratap, "Design, modelling and simulation of vibratory micromachined gyroscopes," *J. Phys. Conf. Ser.*, vol. 34, pp. 757–763, Apr. 2006.

- [30] C. C. Painter and A. M. Shkel, "Structural and thermal modeling of a z-axis rate integrating gyroscope," *J. Micromechanics Microengineering*, vol. 13, no. 2, pp. 229–237, Mar. 2003.
- [31] J. Fang and J. Li, "Improved temperature error model of silicon MEMS gyroscope with inside frame driving-- 《Journal of Beijing University of Aeronautics and Astronautics》 2006."
- [32] W. M. van Spengen, P. Czarnecki, R. Poets, J. T. M. van Beek, and I. De Wolf, "The influence of the package environment on the functioning and reliability of RF-MEMS switches," in *Reliability Physics Symposium, 2005. Proceedings. 43rd Annual. 2005 IEEE International*, 2005, pp. 337 – 341.
- [33] M. K. Yeh and C. L. Lu, "Thermal Stress and Thermal Cycling Analyses of Microgyroscope Chip Models," *Key Eng. Mater.*, vol. 462–463, pp. 622–627, Jan. 2011.
- [34] C.-L. Lu and M.-K. Yeh, "Thermal cycling analysis of microgyroscope chip embedded with through-silicon vias by finite element method," in *Microsystems Packaging Assembly and Circuits Technology Conference (IMPACT), 2010 5th International*, 2010, pp. 1 –4.
- [35] J. Cui, B. Sun, Q. Feng, and S. Zeng, "Study on MEMS board-level package reliability under high-G impact | PHM Society," presented at the Annual Conference of the Prognostics and Health Management Society 2011.
- [36] C. Acar and A. Shkel, *MEMS Vibratory Gyroscopes: Structural Approaches to Improve Robustness*, 2nd ed. Springer, 2008.
- [37] N. Patil, "Design And Analysis Of MEMS Angular Rate Sensors," Master's thesis, Indian Institute of Science, Bangalore, India., 2006.
- [38] V. Kaajakari, *Practical MEMS: Design of microsystems, accelerometers, gyroscopes, RF MEMS, optical MEMS, and microfluidic systems*. Small Gear Publishing, 2009.
- [39] S. Mohite, N. Patil, and R. Pratap, "Design, modelling and simulation of vibratory micromachined gyroscopes," *J. Phys. Conf. Ser.*, vol. 34, pp. 757–763, Apr. 2006.
- [40] R. Dean, G. Flowers, N. Sanders, R. Horvath, M. Kranz, and M. Whitley, "Micromachined vibration isolation filters to enhance packaging for mechanically harsh environments," *J. Microelectron. Electron. Packag.*, vol. 2, no. 4, pp. 223–231.
- [41] J. K. Bekkeng, "Calibration of a Novel MEMS Inertial Reference Unit," *IEEE Trans. Instrum. Meas.*, vol. 58, no. 6, pp. 1967–1974, Jun. 2009.
- [42] Fang Jiancheng and Li Jianli, "Integrated Model and Compensation of Thermal Errors of Silicon Microelectromechanical Gyroscope," *IEEE Trans. Instrum. Meas.*, vol. 58, no. 9, pp. 2923–2930, Sep. 2009.
- [43] C. Patel, P. McCluskey, and D. Lemus, "Performance and Reliability of MEMS Gyroscopes and Packaging at High Temperatures," presented at the High Temperature Electronics (HiTEC), IMAPS, 2010.
- [44] C. Patel, P. McCluskey, and D. Lemus, "Performance and reliability of mems gyroscopes at high temperatures," in *Thermal and Thermomechanical Phenomena in Electronic Systems (ITherm), 2010 12th IEEE Intersociety Conference on*, 2010, pp. 1–5.

- [45] C. Acar, A. R. Schofield, A. A. Trusov, L. E. Costlow, and A. M. Shkel, "Environmentally Robust MEMS Vibratory Gyroscopes for Automotive Applications," *IEEE Sens. J.*, vol. 9, no. 12, pp. 1895–1906, Dec. 2009.
- [46] K. Shcheglov, C. Evans, R. Gutierrez, and T. K. Tang, "Temperature dependent characteristics of the JPL silicon MEMS gyroscope," in *Aerospace Conference Proceedings, 2000 IEEE*, 2000, vol. 1, pp. 403–411 vol.1.
- [47] D. Keymeulen, C. Peay, K. Yee, and D. L. Li, "Effect of Temperature on MEMS Vibratory Rate Gyroscope," in *Aerospace Conference, 2005 IEEE*, 2005, pp. 1–6.
- [48] L. F. Wu and F. X. Zhang, "Effect of the temperature on the performance of silicon micro-machined gyroscope using for rotating carrier," in *Control and Decision Conference, 2008. CCDC 2008. Chinese*, 2008, pp. 4876–4879.
- [49] S. H. Choa, "Reliability of Vacuum Packaged MEMS Gyroscopes," *Microelectron. Reliab.*, vol. 45, no. 2, pp. 361–369, Feb. 2005.
- [50] W. N. Sharpe, Bin Yuan, R. Vaidyanathan, and R. L. Edwards, "Measurements of Young's modulus, Poisson's ratio, and tensile strength of polysilicon," in *Micro Electro Mechanical Systems, 1997. MEMS '97, Proceedings, IEEE., Tenth Annual International Workshop on*, 1997, pp. 424–429.
- [51] M. Shamshirsaz and M. B. Asgari, "Polysilicon micro beams buckling with temperature-dependent properties," *Microsyst. Technol.*, vol. 14, no. 7, pp. 957–961, Feb. 2008.
- [52] W. N. Sharpe, M. . Eby, and G. Coles, "Effect of Temperature on Mechanical Properties of Polysilicon." *Proceedings Transducers '01, Munich*, 1366-1369, 2001.
- [53] H.-T. Lee, M.-H. Chen, H.-M. Jao, and T.-L. Liao, "Influence of interfacial intermetallic compound on fracture behavior of solder joints," *Mater. Sci. Eng. A*, vol. 358, no. 1–2, pp. 134–141, Oct. 2003.
- [54] K. S. Kim, S. H. Huh, and K. Sugauma, "Effects of intermetallic compounds on properties of Sn–Ag–Cu lead-free soldered joints," *J. Alloys Compd.*, vol. 352, no. 1–2, pp. 226–236, Mar. 2003.
- [55] J.-W. Yoon, S.-W. Kim, J.-M. Koo, D.-G. Kim, and S.-B. Jung, "Reliability investigation and interfacial reaction of ball-grid-array packages using the lead-free Sn-Cu solder," *J. Electron. Mater.*, vol. 33, no. 10, pp. 1190–1199, Oct. 2004.
- [56] T. Y. Lee, W. J. Choi, K. N. Tu, J. W. Jang, S. M. Kuo, J. K. Lin, D. R. Frear, K. Zeng, and J. K. Kivilahti, "Morphology, kinetics, and thermodynamics of solid-state aging of eutectic SnPb and Pb-free solders (Sn–3.5Ag, Sn–3.8Ag–0.7Cu and Sn–0.7Cu) on Cu," *J. Mater. Res.*, vol. 17, no. 02, pp. 291–301, 2002.
- [57] D. Q. Yu, C. M. L. Wu, C. M. T. Law, L. Wang, and J. K. L. Lai, "Intermetallic compounds growth between Sn–3.5Ag lead-free solder and Cu substrate by dipping method," *J. Alloys Compd.*, vol. 392, no. 1–2, pp. 192–199, Apr. 2005.
- [58] W. K. Choi and H. M. Lee, "Effect of soldering and aging time on interfacial microstructure and growth of intermetallic compounds between Sn-3.5Ag solder alloy and Cu substrate," *J. Electron. Mater.*, vol. 29, no. 10, pp. 1207–1213, Oct. 2000.

- [59] P. Chauhan, "MICROSTRUCTURAL CHARACTERIZATION AND THERMAL CYCLING RELIABILITY OF SOLDERS UNDER ISOTHERMAL AGING AND ELECTRICAL CURRENT," 2012.
- [60] Y. H. Tian, C. Q. Wang, and W. F. Zhou, "EVOLUTION OF MICROSTRUCTURE OF Sn-Ag-Cu LEAD-FREE FLIP CHIP SOLDER JOINTS DURING AGING PROCESS," *Acta Metall. Sin. Engl. Lett.*, vol. 19, no. 4, pp. 301–306, Aug. 2006.
- [61] D.W. Henderson, P. Borgesen, P. Kondos, I. De Sousa, L. Patry, and L. Yin, "What the Electronics Industry Missed for 80 Years....Interfacial Void Formation in Solder Joints with Cu Pad Structures during Thermal Aging." Presentation at TMS 2006 Lead Free Workshop, San Antonio, Mar-2006.
- [62] L. Xu and J. H. L. Pang, "Interfacial IMC and Kirkendall void on SAC solder joints subject to thermal cycling," in *Electronic Packaging Technology Conference, 2005. EPTC 2005. Proceedings of 7th, 2005*, vol. 2, p. 5 pp.–.
- [63] F. W. Gayle, G. Becka, A. Syed, J. Badgett, G. Whitten, T.-Y. Pan, A. Grusd, B. Bauer, R. Lathrop, J. Slattery, I. Anderson, J. Foley, A. Gickler, D. Napp, J. Mather, and C. Olson, "High temperature lead-free solder for microelectronics," *JOM*, vol. 53, no. 6, pp. 17–21, Jun. 2001.
- [64] E. George, D. Das, M. Osterman, and M. Pecht, "Thermal Cycling Reliability of Lead-Free Solders (SAC305 and Sn3.5Ag) for High-Temperature Applications," *IEEE Trans. Device Mater. Reliab.*, vol. 11, no. 2, pp. 328–338, 2011.
- [65] M. A. Crandall, "Effect of Intermetallic Growth on Durability of High Temperature Solders (SnAg, SAC305, SAC+Mn, SnAg+Cu Nano) in Thermal and Vibration Environments," Thesis, 2011.
- [66] D. Y. R. Chong, F. X. Che, J. H. L. Pang, L. Xu, B. S. Xiong, H. J. Toh, and B. K. Lim, "Evaluation on Influencing Factors of Board-Level Drop Reliability for Chip Scale Packages (Fine-Pitch Ball Grid Array)," *IEEE Trans. Adv. Packag.*, vol. 31, no. 1, pp. 66–75, 2008.
- [67] T. T. Mattila and J. K. Kivilahti, "Reliability of lead-free interconnections under consecutive thermal and mechanical loadings," *J. Electron. Mater.*, vol. 35, no. 2, pp. 250–256, Feb. 2006.
- [68] W. Peng and M. E. Marques, "Effect of Thermal Aging on Drop Performance of Chip Scale Packages with SnAgCu Solder Joints on Cu Pads," *J. Electron. Mater.*, vol. 36, no. 12, pp. 1679–1690, Dec. 2007.
- [69] T.-K. Lee, W. Xie, and K.-C. Liu, "Impact of isothermal aging on Sn-Ag-Cu solder interconnect board level high G mechanical shock performance," in *Electronic Components and Technology Conference (ECTC), 2011 IEEE 61st*, 2011, pp. 547–552.
- [70] W. Liu and N.-C. Lee, "The effects of additives to SnAgCu alloys on microstructure and drop impact reliability of solder joints," *JOM*, vol. 59, no. 7, pp. 26–31, Jul. 2007.
- [71] W. Liu and N.-C. Lee, "NOVEL SACX SOLDERS WITH SUPERIOR DROP TEST PERFORMANCE," presented at the SMTA International Conference Proceedings, 2006.



- [72] M. Amagai, "A study of nanoparticles in SnAg-based lead free solders for intermetallic compounds and drop test performance," in *Electronic Components and Technology Conference, 2006. Proceedings. 56th*, 2006, p. 21 pp.–.
- [73] W. Liu, N.-C. Lee, A. Porras, M. Ding, A. Gallagher, A. Huang, S. Chen, and J. ChangBing Lee, "Achieving high reliability low cost lead-free SAC solder joints via Mn or Ce doping," in *Electronic Components and Technology Conference, 2009. ECTC 2009. 59th*, 2009, pp. 994–1007.
- [74] W. Liu, N.-C. Lee, A. Porras, M. Ding, A. Gallagher, A. Huang, S. Chen, and J. C.-B. Lee, "Shock resistant and thermally reliable low Ag SAC solders doped with Mn Or Ce," in *Electronics Packaging Technology Conference, 2009. EPTC '09. 11th*, 2009, pp. 49–63.
- [75] I. E. Anderson and J. L. Harringa, "Suppression of void coalescence in thermal aging of tin-silver-copper-X solder joints," *J. Electron. Mater.*, vol. 35, no. 1, pp. 94–106, Jan. 2006.
- [76] M. Ghosh, A. Kar, S. Das, and A. Ray, "Aging Characteristics of Sn-Ag Eutectic Solder Alloy with the Addition of Cu, In, and Mn," *Metall. Mater. Trans. A*, vol. 40, no. 10, pp. 2369–2376, 2009.
- [77] L.-W. Lin, J.-M. Song, Y.-S. Lai, Y.-T. Chiu, N.-C. Lee, and J.-Y. Uan, "Alloying modification of Sn–Ag–Cu solders by manganese and titanium," *Microelectron. Reliab.*, vol. 49, no. 3, pp. 235–241, Mar. 2009.
- [78] K. S. Kim, S. H. Huh, and K. Suganuma, "Effects of fourth alloying additive on microstructures and tensile properties of Sn–Ag–Cu alloy and joints with Cu," *Microelectron. Reliab.*, vol. 43, no. 2, pp. 259–267, Feb. 2003.
- [79] A. Boesenberg, "Development of Al, Mn, & Zn doped Sn-Ag-Cu-X solders for electronic assembly," *Theses Diss.*, Jan. 2011.
- [80] L.-W. Lin, J.-M. Song, Y.-S. Lai, Y.-T. Chiu, and N.-C. Lee, "Alloying design of Sn-Ag-Cu solders for the improvement in drop test performance," in *International Conference on Electronic Materials and Packaging, 2008. EMAP 2008*, 2008, pp. 33–36.
- [81] S. Mukherjee, A. Dasgupta, B. Zhou, and T. R. Bieler, "Multiscale Modeling of the Effect of Micro-alloying Mn and Sb on the Viscoplastic Response of SAC105 Solder," *J. Electron. Mater.*, pp. 1–12.
- [82] S. Mukherjee, T. T. Mattila, and A. Dasgupta, "Effect of addition of manganese and antimony on viscoplastic properties and cyclic mechanical durability of low silver Sn-Ag-Cu solder," in *2012 13th IEEE Intersociety Conference on Thermal and Thermomechanical Phenomena in Electronic Systems (ITherm)*, 2012, pp. 888–895.
- [83] L. Liang, Q. Wang, and Z. Zhao, "Effect of Cerium Addition on Board Level Reliability of Sn-Ag-Cu Solder Joint," in *Electronic Packaging Technology, 2007. ICEPT 2007. 8th International Conference on*, 2007, pp. 1–4.
- [84] C. M. L. Wu, D. Q. Yu, C. M. T. Law, and L. Wang, "Properties of lead-free solder alloys with rare earth element additions," *Mater. Sci. Eng. R Rep.*, vol. 44, no. 1, pp. 1–44, Apr. 2004.
- [85] C. Law, C. Wu, D. Yu, L. Wang, and J. Lai, "Microstructure, solderability, and growth of intermetallic compounds of Sn-Ag-Cu-RE lead-free solder alloys," *J. Electron. Mater.*, vol. 35, no. 1, pp. 89–93, 2006.

- [86] Z. Chen, Y. Shi, Z. Xia, and Y. Yan, "Properties of lead-free solder SnAgCu containing minute amounts of rare earth," *J. Electron. Mater.*, vol. 32, no. 4, pp. 235–243, Apr. 2003.
- [87] Z. G. Chen, Y. W. Shi, Z. D. Xia, and Y. F. Yan, "Study on the microstructure of a novel lead-free solder alloy SnAgCu-RE and its soldered joints," *J. Electron. Mater.*, vol. 31, no. 10, pp. 1122–1128, Oct. 2002.
- [88] C. M. L. Wu, D. Q. Yu, C. M. T. Law, and L. Wang, "The properties of Sn-9Zn lead-free solder alloys doped with trace rare earth elements," *J. Electron. Mater.*, vol. 31, no. 9, pp. 921–927, Sep. 2002.
- [89] C. M. L. Wu, D. Q. Yu, C. M. T. Law, and L. Wang, "Improvements of microstructure, wettability, tensile and creep strength of eutectic Sn–Ag alloy by doping with rare-earth elements," *J. Mater. Res.*, vol. 17, no. 12, pp. 3146–3154, 2002.
- [90] C. M. L. Wu, D. Q. Yu, C. M. T. Law, and L. Wang, "Microstructure and mechanical properties of new lead-free Sn-Cu-RE solder alloys," *J. Electron. Mater.*, vol. 31, no. 9, pp. 928–932, Sep. 2002.
- [91] W. Liu and N.-C. Lee, "Lead-free solder alloys and solder joints thereof with improved drop impact resistance," EP1977022 A431-Dec-2008.
- [92] "IPC-A-610D Acceptability of Electronic Assemblies - IPC Association Connecting Electronics Industries," 2005. .
- [93] "IPC 9701 A - Performance Test Methods and Qualification Requirements for Surface Mount Solder Attachments." Jan-2002.
- [94] "IPC/JEDEC-9703 - Mechanical Shock Test Guidelines for Solder Joint Reliability." Mar-2009.
- [95] "JESD-B111 - Board Level Drop Test Method of Components for Handheld Electronic Products." Jul-2003.
- [96] Z. Mei, M. Ahmad, M. Hu, and G. Ramakrishna, "Kirkendall voids at Cu/solder interface and their effects on solder joint reliability," in *Electronic Components and Technology Conference, 2005. Proceedings. 55th*, 2005, pp. 415–420 Vol. 1.
- [97] R. Aspandiar, "Voids in Solder Joints," *J. SMT Artic.*, Oct. 2006.